

The Study of Physical Processes in Circumgalactic Medium

by

Manami Roy



Jawaharlal Nehru University, New Delhi



Department of Astronomy and Astrophysics, Raman Research Institute

Supervisor : **Biman B. Nath**

May, 2023

This thesis is submitted for the degree of Doctor of
Philosophy

DECLARATION

I, **Manami Roy** (Enrolment No.: RRI/18/002), declare that the work reported in this thesis titled '**The Study of Physical Processes in Circumgalactic Medium**', is entirely original. This thesis is composed independently by me at **Raman Research Institute (RRI)** under the supervision of **Prof. Biman Nath** and is the result of my own work unless otherwise stated. I further declare that the subject matter presented in this thesis has not previously formed the basis for the award of any degree, diploma, membership, associateship, fellowship or any other similar title of any university or institution. I also declare, this thesis has been checked through the plagiarism software Ouriginal.



Signature of Supervisor

Prof. Biman Nath

Professor, RRI



Signature of Candidate

Manami Roy

Research Fellow, RRI

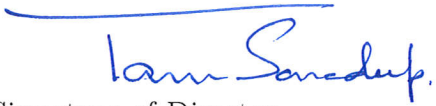
Astronomy & Astrophysics Group
Raman Research Institute (RRI)
Bengaluru 560080, Karnataka, India

Date:

Place:

CERTIFICATE

This is to certify that the work contained in the thesis titled ‘**The Study of Physical Processes in Circumgalactic Medium**’, submitted by **Manami Roy** (Enrolment No.: RRI/18/002) to the Jawaharlal Nehru University for the award of the degree of **Doctor of Philosophy (Ph.D.)** in Physical Sciences, is the bonafide record of original research work carried out by the candidate from July 2018 — May 2023, under my guidance and supervision at **Raman Research Institute (RRI)**, Bengaluru, India. The results embodied in the thesis have not been submitted to any other University or Institute for the award of any degree or diploma.



Signature of Director

Prof. Tarun Souradeep

Director & Professor, RRI



Signature of Supervisor

Prof. Biman Nath

Professor, RRI

Astronomy & Astrophysics Group
Raman Research Institute (RRI)
Bengaluru 560080, Karnataka, India

Date:

Place:

ACKNOWLEDGEMENTS

I want to thank all who have been an integral part of these five years of my endeavours. This Ph.D. journey is not only an excellent academic learning experience for me but has also enriched my life with lots of personal developments.

I am grateful to my thesis supervisor, Biman B. Nath, for his unwavering guidance and insightful feedback throughout my Ph.D. journey. His expertise and knowledge in the subject have been invaluable to me, and I am honored to have had the opportunity to work with him. He taught me not to be afraid of thinking wildly of any research idea and not to feel demotivated if one idea does not work. His constant encouragement has helped me continue my work even in difficult times like covid pandemic. I also fondly enjoyed our conversations about our shared interest in music.

I thank Shiv Shetty for highly engaging discussions regarding astrophysics and cosmology and for being the ‘go-to person’ for any problem, like regarding the courses, hostel, or institute. I am also grateful to have had such a wonderful mentor, Stephanie Tonnesen, during my visit to the Center for Computational Astrophysics (CCA), Flatiron Institute. Her guidance since then has immensely helped me in my academic endeavors, and she has always been very kind to me. I would also like to thank my collaborators Mark Voit, Ranita Jana, Kung-Yi Su, and Drummond B. Fielding for their valuable insights, advice, and suggestions that have helped me to expand my research and broaden my understanding of the subject. I also thank Prateek Sharma for sharing his expertise and knowledge, which has immensely enriched my understanding of the subject. The bi-weekly meetings with the members of his group (Alankar, Ritoli) have also been highly beneficial to me. It provided me with the opportunity to discuss and explore new ideas. I sincerely thank all my teachers from my school, bachelor’s and master’s studies. My love and passion for physics have nurtured and grown because of their teaching and motivation.

I want to express my gratitude towards several individuals and departments who have greatly assisted me during my time at RRI. Firstly, I thank the Accounts Section and Administration for their prompt handling of official documents and our Group Secretaries Harini, Mamta, and Mahima for their invaluable assistance. In addition, I have always received excellent support from the Computer Section, especially Jacob, who was always

one call away whenever I encountered any issues. I am deeply grateful for his assistance. Furthermore, I have greatly benefited from the extensive collection of printed books and online resources at the RRI library. I want to thank the Library Section for efficiently maintaining these resources. Overall, I appreciate the support and assistance from various individuals and departments at RRI, which have undoubtedly contributed to my success during my time here.

I am also grateful to my parents for their unrelenting support, love, encouragement, and sacrifice to live away from their only child. Their unwavering faith in me has strengthened and motivated me throughout my academic journey. I always look forward to our daily hour-long video calls, one of my day's highlights. Without my father's constant motivation, I would not have had the courage to live away from home. He is the one who has always encouraged me to pursue a research career in physics. I am also grateful to my dearest friend Dhrubojyoti and his family, especially his parents, for their love, care, constant support, and motivation. I would not have taken astrophysics as my research topic if not for Dhrubo. Thanks to him for introducing me to Cosmos and many other great things. I also thank my cousin brother Bittu, who is more of a dear friend to me, for his unconditional love, care, and support. I am genuinely grateful to have you in my life. I am also thankful to have a supporting family members, like my mummum, cousins, uncles, and aunties, for always having my back and appreciating even my small achievements. I am also grateful to have friends like Suchismita and Sayanika since college. They have always supported and loved me unconditionally. They never misunderstood me and made me feel unwanted, even if I could not be there on so many of their important days due to my work schedule. I also thank Ketan for his kindness, patience, care, and constant encouragement throughout the thesis writing process. Thank you for giving me company and motivation during my late thesis writing hours. He is the best 'cheerleader' that I possibly can have. Thanks to him for making my life easier when things were not easy.

I also would like to thank the feline astrophysicist of our Astro floor, Fluffy. Thanks for being my first feline friend. I will always fondly remember our friendship. I hope to find you hopping around the Astro department every time I visit RRI. Thanks to Gunjan for being a sister and giving me a home away from home during the years of my Ph.D.

journey. I appreciate her kindness and support. I sincerely appreciate the dear friends that I have made during my Ph.D. journey. Thanks to Ashwin for teaching me bash script and many other programming-related things; I will ‘not’ miss your never-ending talking. Thanks to my one and only roommate, Shreya, for being such a kind friend. Thanks to my batch mates Sukanya, Rashid, Anirban, Sandeep, and Ankur for being such amazing friends. Thanks to my group members Sourav and Mukesh for always being good friends and providing me a safe place to vent out whenever needed. Mukesh, I will miss sharing a working space with you and, of course, your great tea. Thanks to Sovan for making the workplace lively with his never-ending pranks. I will miss our pranks and ‘chit-chat’. I will also like to thank our ‘chai-pe-charcha’ group (Saurabh, Yash, Rajorshri, Aman, Rahul-da, Ajit, Manish, Sarvesh, and so many others). Our evening tea and chatting sessions have always been fun and a great escape from regular work days. Thanks to Ranita-Di, Aditi, Sidhartho-Da, Raj, Varun, Karam, Priyanka-Di, Sriju, Irla, Akash, Sebanti, and so many other seniors; I am lucky to have such great seniors like you guys who have always made me feel welcomed and always be there to help. I would also like to thank Tanuman-da and Agniva-da; I always fondly enjoyed our conversations about academics, music, and many other things. I also want to thank the amazing friends I have made during my CCA visit, Surya, Brato-Da, Sophia, Brent, Alex, and Mike; you guys are truly awesome, and without you guys, I might not have had that great time at CCA. I thank all my friends, juniors, and seniors for their moral support, understanding, and encouragement. They have been my constant source of inspiration, and I could not have completed this thesis without their unwavering support.

Finally, I want to express my gratitude to all those who have helped me in big and small ways throughout my Ph.D. journey. Their support has been invaluable to me, and I am truly blessed to have such amazing people in my life.

SYNOPSIS

Introduction

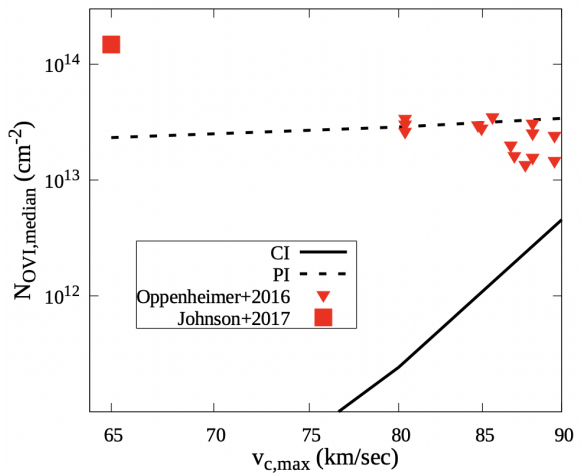
Galaxies are the building blocks of our universe, *but how do they form and evolve?* It is now apparent that the diffuse gaseous halo, known as Circumgalactic medium (CGM), surrounding galactic disks plays a crucial part in galaxy evolution. The CGM is the habitat for large-scale gas flows that fundamentally regulate the evolution of the galaxy by providing fresh and recycled gaseous fuel for star formation and regulating the galaxy's interactions with other galaxies. For example, interactions between galaxies can strip gas from them, which can lead to quenching. However, physical processes at small scales vastly affect this large-scale gaseous flow. One of the most important and theoretically uncertain small-scale physical processes in the CGM is the physics of relativistic charged cosmic ray (CR) particles. They are produced in star-formation activity and can drive these large-scale outflows in the CGM. Therefore, it is crucial to study the CGM's small-scale ($\sim 1 - 10$ pc) and large-scale structures (~ 100 s kpc) altogether. A better understanding of the CGM promises to illuminate critical unresolved issues in galaxy formation and evolution, like satellite galaxy evolution (*Is the CGM dense enough to remove gas from satellite galaxies?*), and galaxy quenching (*To what degree CR-driven outflows can sweep out the available cold gas for star-formation?*). But the diffuse nature of the CGM makes it challenging to observe it in emission, where the absorption line studies of the CGM come to the rescue. Absorption lines from the CGM point towards the multi-phase nature of the CGM. However, it is still challenging to interpret these different phases' origin and spatial location from absorption studies. Numerical simulation can go beyond these observation challenges and address relevant issues by varying different physical processes in the CGM. However, simultaneously studying small-scale and large-scale CGM in numerical simulations is computationally expensive as it requires extremely high resolution, like $10^{-3} - 10^{-5}$ of the total simulation box size. On the other hand, there exists a plethora of simple analytical models of CGM (e.g., Isothermal (IT): [Fang et al. \(2013\)](#), Precipitation (PP): [Voit \(2019\)](#)) which assume widely varying astrophysical processes, micro-physics, and compositions of the CGM.

In this thesis, we use different analytical models and numerical simulations of the CGM and compare them with multi-wavelength observations (X-ray, UV, γ -ray, radio) to explore CGM's different interactions with surroundings such as with Cosmic rays (CRs) and Satellite galaxies. These interactions give rise to the multi-phase structure of the CGM and can be traced via multi-wavelength observations. Using the analytical models of the CGM, we also investigate how small-scale temperature fluctuation and photoionization affect the multi-phase ionization structure of CGM. Our result will illuminate several exciting aspects of the CGM: i) the effect of temperature fluctuation and photoionization on OVI, OVII, and OVIII column densities of CGM, ii) the constraints on cosmic ray content and its transport mechanisms from multi-wavelength observations, and iii) the effect of satellite galaxies on the cooling of the host galaxy. Our results help us to address the bigger question of how galaxies evolve by delving into the small-scale and large-scale processes in the CGM. Below we outline our main results for the investigations undertaken in this thesis.

The Effects of the Photoionization and Temperature Fluctuations on the Ionization Structure of the CGM

A wide range of ions detected in the absorption line studies of the CGM indicates the multi-phase temperature and density structure of the CGM. But the production mechanisms of these wide-ranged ions are still a well-debated question. In this regard, we

Figure 1: This plot shows column density of OVI with the variation in maximum circular velocity, proxy for virial mass of a galaxy. The solid black line shows the model for collisional ionization and the dashed black line shows the model for photoionization (PI). Only the PI model matches with the expected OVI column densities (Oppenheimer et al., 2016a; Johnson et al., 2017) for low mass galaxies.



address whether photoionization is required to produce the observed absorption column density in addition to collisional ionization. For this, we develop a photoionized precipitation model for Milky Way (MW)-type galaxies ($M_{\text{halo}} \sim 1-2 \times 10^{12} M_{\odot}$). In this model, feedback maintains a constant ratio of cooling time to freefall time throughout the halo. Recent phenomenological studies and numerical simulations show that this ratio has a threshold value of approximately 10, below which thermally unstable perturbation in the CGM can proceed into multi-phase condensation. In addition, this model considers the photoionization (PI) by Extra-galactic Ultra-Violet background radiation, along with the collisional ionization (CI) for the production of different ions. We also extend this model to low mass galaxies ($M_{\text{halo}} < 2 \times 10^{11} M_{\odot}$) (Roy et al., 2021a). We also consider log-normal temperature fluctuations in these models. By carefully producing mock observations of ion column densities, we found that photoionization significantly affects the oxygen ion column densities (OVI, OVII, OVIII) of low-mass galaxies, unlike the MW-type galaxies. In Figure 1, we show that the PI model can successfully match the expected OVI column densities (Oppenheimer et al., 2016a; Johnson et al., 2017), which the CI model cannot do. Our finding predicts that, specifically, the observations of OVIII in low-mass galaxies can be an essential probe of photoionization in future X-ray missions. We also find that significant fluctuations in the temperature profile of the CGM are required to explain the observed oxygen column densities and their ratios for the MW and star-forming galaxies. It implies a connection between star formation in the disk and the state of the CGM, where stellar feedback could drive these temperature fluctuations.

Constraining the CR content and its transport mechanisms in the CGM using Multi-wavelength observations

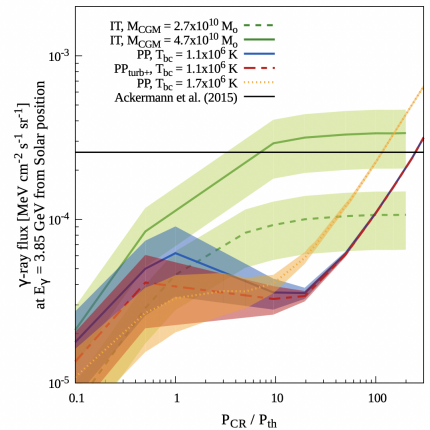
Recent simulations depict a picture that CR pressure can significantly dominate the thermal pressure in the CGM (Butsky & Quinn, 2018). CR content and transport mech-

anisms are poorly constrained at all scales, and we recognize that the impact of CR on the CGM could be used to constrain CR content and its transport physics. We consider two such effects of CRs: 1) Interaction of CRs with CGM giving rise to hadronic γ -ray and radio synchrotron emission, and 2) Inclusion of the CR component driving a decrease in thermal pressure (to which the OVIII abundance of MW is highly sensitive). Below, we will outline three chapters of the thesis, which constrain the ratio of CR pressure to thermal pressure and the CR transport mechanisms in the CGM.

Gamma-Ray and Radio Background Constraints on Cosmic Rays in Milky Way Circumgalactic Medium

To constrain CR content in the CGM, we include CR populations in the hydro-static equilibrium models of the CGM: Precipitation model and Isothermal model. In these models, CR populations are parameterized by $\eta = P_{CR}/P_{th}$. CR particles are either accelerated in disk due to star formation activities or accelerated in outflow shocks. Then they are lifted to the CGM by advection and diffusion. After that, they interact with CGM protons and give rise to neutral pions, which decay into γ -rays. In addition, the CR electron can emit synchrotron emission in the magnetic field of the CGM. Our primary goal in this chapter is to put limits on η using observations of Isotropic γ -ray background (IGRB) from the Fermi-LAT telescope and radio background from ARCADE-2 balloon observations. We compare our model prediction with the observed IGRB and radio background (Jana et al., 2020b). In Figure 2, we show the variation of γ -ray flux as a function of $\eta = P_{CR}/P_{th}$ for the PP, and IT models with varying outer boundary conditions. The solid horizontal line denoted the upper limit of IGRB observations. We find that the

Figure 2: The plot shows the γ -ray flux variation with the change in $\eta = P_{CR}/P_{th}$. The observational upper limit is shown by black horizontal line.



IGRB intensity allows $\eta < 3$ and $\eta \leq 230$ for the precipitation and isothermal models, respectively. The radio continuum limits $\eta < 400$ for the precipitation model and does not constrain the isothermal model.

Constraints on Cosmic Rays in the Milky Way Circumgalactic Medium from OVIII Observations

In this chapter (Roy & Nath, 2022b), we use the above two models, which include CR population, parameterized by η . With the inclusion of the CR component, thermal pressure in the CGM will decrease. The OVIII abundance of MW is highly sensitive to the thermal pressure of the CGM. Therefore, including CR in the model will decrease the column density of OVIII, which is traced by X-ray observations using *Chandra* and *XMM-Newton*. In Figure 3, we show the variation in OVIII column density as a function of $\eta = P_{CR}/P_{th}$ for the IT model with different temperature fluctuations along with Collisional ionization (CI) and Photoionization (PI).

The shaded horizontal region shows the observational limits. Comparing our model prediction with observed X-ray absorption column densities, we find that the pressure due to CRs can be at most ten times the gas pressure in the CGM without violating the observational signatures. We also explore the spatially varying η : rising ($\eta = Ax$) or declining ($\eta = A/x$) with radius, where A is the normalization of the profiles. In particular, the models with a declining ratio of CR to thermal pressure match the observed column densities better than those with a rising ratio with suitable temperature fluctuations.

Gamma-rays from the circumgalactic medium of M31

In this chapter, we check the observational constraints of γ -ray emission from the CGM of M31 in hydrodynamical simulation using two-fluid (thermal + CR) hydrodynamical code (PLUTO, Mignone et al. (2007))(Roy & Nath, 2022a). We consider the acceleration

of CRs by star formation activity in the disc of the M31 galaxy and *in-situ* in the shock of outflows and lifted to the CGM by star-formation driven advection and CR diffusion. Then, considering hadronic interactions of CRs with CGM, we produce a mock γ -ray emission map from the CGM of M31 with the angular resolution of Fermi-LAT telescope to compare the detected γ -ray emission from the CGM of M31 (Karwin et al., 2019). With the variation in CR physics in my simulation, we found that only the combination of advection and diffusion (with a diffusion coefficient of $10^{29} \text{ cm}^2/\text{sec}$) can match this observation (the red colored portion inside the black circle shown in the *left panel* of Figure 4), obviating the previous theory of γ -ray emission-origin by dark matter annihilation (Karwin et al., 2019). Our simulation matches the observation even with the minimal assumption of the equipartition of CR and thermal pressure. It strengthens the earlier findings in the thesis that one does not need CR-dominated CGM to explain the observations (like γ -ray emission from M31).

Seeding the CGM; How Satellites Populate the Cold Phase of Milky Way Halos

The origin of the cold phase in the CGM is a well-debated question. Recent observations in massive halos ($10^{11-13}M_{\odot}$) show the high column densities of MgII and HI, which are the tracers of the cold phase of CGM (Zhu et al. (2014); Chen et al. (2018); Zahedy et al. (2018)) even at the outer radii. In addition, the recent observations also point towards the existence of cold phase out to large radii ($> 100\text{kpc}$) (Lan & Mo, 2018, 2019). It leads to the well-debated questions: *how do these massive halos whose virial temperature is much higher than that of the cold phase (Prochaska et al., 2013) form cold gas?*, and *how does the cold gas exist at such a large radius?* Along with the cold mode accretion from the Intergalactic medium, the satellite galaxies can also populate the outer CGM with cold gas. For this, we investigate what amount satellite galaxies can contribute to the cold gas budget of the CGM. For this, we simulate a suite of MW-type host galaxies with a varying distribution of satellite galaxies using the idealized GIZMO simulation code (Hopkins,

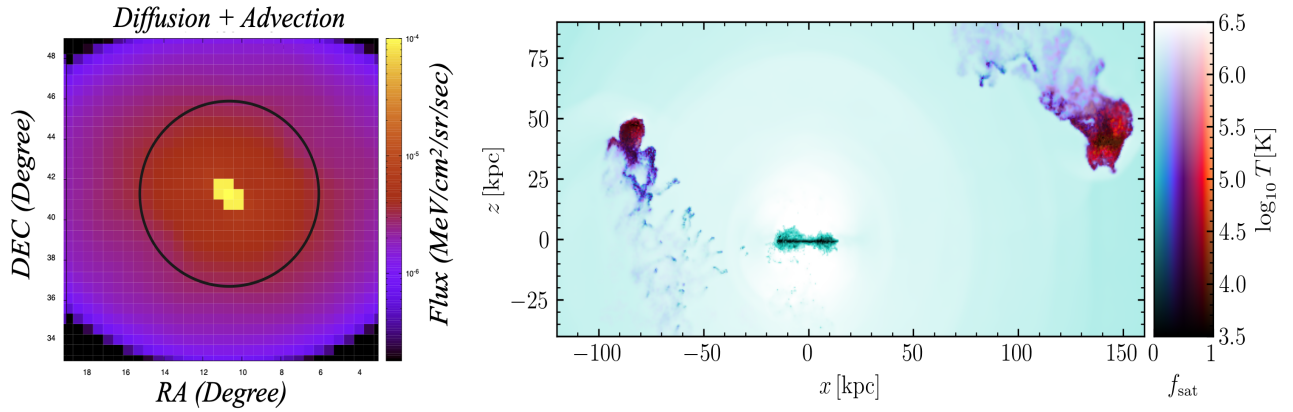
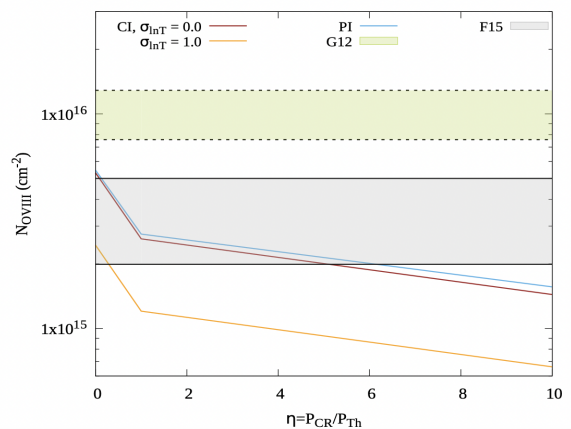


Figure 4: *Right* shows the temperature distribution of the one snapshot at 1.5 Gyr of the simulation. It is run with a setup of host galaxy of Milky Way mass and two satellites of SMC mass which are placed on circular orbit at 100 kpc and 150 kpc away, respectively, from the host galaxy. The cold gas is streaming behind the satellites and falling towards the central disk. *Left panel* shows γ -ray map of M31 with a combination of diffusive and advective transport mechanisms of CRs. This combination is required to reproduce the observed extended gamma-ray emission (the red colorbar extends to the black circle).

2015b).

We find that satellite galaxies can significantly supply cold gas to the CGM not only by direct stripping but also equally by induced cooling in the mixing layer of the stripped cold gas (*Right panel* of Figure 4). We also find that massive satellites like the Large Magellanic Cloud (LMC) continue to feed cold gas to the CGM for several Gyr. However, low-mass satellites quickly lose all of their gas since, unlike massive satellites, the low-mass satellites produce small clouds which have short cloud-crushing time and get easily destroyed (Roy+2022 in prep).

Figure 3: The plot shows the OVIII column density variation with the change in $\eta = P_{CR}/P_{th}$ for IT model with different temperature fluctuations along with Collisional ionization (CI) and Photoionization (PI). The observational limits are shown by shaded horizontal regions from Chandra and XMM-Newton telescopes.



Summary

To summarize, in my Ph.D. thesis, we use analytical models and numerical simulations of the CGM and compare them in light of multi-wavelength observations. In the first chapter, we develop the Photoionized Precipitation model and find that high-temperature fluctuations in the CGM are required to explain the oxygen column densities of the CGM of the Milky Way and star-forming galaxies. We also conclude that photoionization has a significant effect in producing oxygen ions in the CGM of low-mass galaxies, whereas it does not affect the same for Milky Way-type galaxies. In the following two chapters, we explore two hydrostatic models of CGM. We include the CR population in those models to investigate the constraint of CR content from γ -ray, X-ray, and radio observations. We find from these multi-wavelength studies that CR pressure can be at the most ten times the thermal pressure in the CGM, negating the standard lore that CR pressure in the CGM can exceed the gas pressure by two orders of magnitude (Butsky & Quinn, 2018; Dashyan & Dubois, 2020; Hopkins et al., 2021). In the next chapter, we study the interaction of CR with the CGM in numerical simulation and find out that the hadronic interaction of CRs with CGM can give rise to observed γ -ray emission from M31 by the Fermi-LAT telescope. In the last chapter, we find that the satellite galaxies can significantly contribute to the cold phase of CGM of the host galaxy by several mechanisms. Our investigations, in the thesis, about physical processes in the CGM are very important to understand the multi-phase nature of the CGM and large-scale gas flows, which in turn will enlighten us about galactic evolution.

Signature of Supervisor

Prof. Biman Nath

Professor, RRI

Signature of Candidate

Manami Roy

Research Fellow, RRI

LIST OF PUBLICATIONS

1. *Gamma-ray and radio background constraints on cosmic rays in Milky Way circumgalactic medium*
Ranita Jana, **Manami Roy**, Biman B. Nath (2020)
DOI : 10.3847/2041-8213/abbee4, arXiv:2007.11015
2. *A panoramic view of the circumgalactic medium in the photoionized precipitation model*
Manami Roy, Biman B. Nath, G.M.Voit (2021)
DOI : 10.1093/mnras/stab2407, arXiv:2108.08320
3. *Constraints on cosmic rays in the Milky Way circumgalactic medium from OVIII observations*
Manami Roy, Biman B. Nath (2022)
DOI : 10.3847/1538-4357/ac6a57, arXiv:2205.00020
4. *Gamma-rays from the circumgalactic medium of M31*
Manami Roy, Biman B. Nath (2022)
DOI : 10.1093/mnras/stac1465, arXiv:2205.12291
5. *Seeding the CGM: How Satellites Populate the Cold Phase of Milky Way Halos*
Manami Roy, Kung-Yi Su, Stephanie Tonnesen, Drummond Fielding (2022)
in preparation (soon to be submitted)



Signature of Supervisor

Prof. Biman Nath

Professor, RRI

Astronomy & Astrophysics Group

Raman Research Institute (RRI)

Bengaluru 560080, Karnataka, India

Date:

Place:



Signature of Candidate

Manami Roy

Research Fellow, RRI

Contents

1	Introduction	3
1.1	Circumgalactic Medium	3
1.2	Theoretical background	6
1.3	Methods of Investigation of the CGM	7
1.3.1	Observations	8
1.3.2	Simulations	15
1.3.3	Analytical model	17
1.4	Different phases of the CGM	21
1.4.1	Cold Phase	21
1.4.2	Cool Phase	22
1.4.3	Warm Phase	23
1.4.4	Hot Phase	24
1.4.5	Super-Virial Phase	25
1.5	Variety of interactions of the CGM	26
1.5.1	Interaction with Cosmic Rays	26

1.5.2	Interaction with Satellite Galaxies	28
1.6	Motivation of the thesis	30
1.7	Structure of the thesis	31
2	Impact of photoionization and temperature fluctuation on the highly ionized oxygen ions in the CGM	35
2.1	Introduction	37
2.2	Modelling the CGM	41
2.2.1	Effect of photoionization	43
2.2.2	Temperature Fluctuations	43
2.3	Results for the Milky Way	44
2.4	Comparison with UV and X-Ray observations	51
2.5	Discussion	56
2.5.1	CGM in galaxies like the Milky Way	56
2.5.2	CGM in low mass galaxies	58
2.6	Conclusion	60
3	Gamma-ray and radio background constraints on cosmic rays in Milky Way circumgalactic medium	63
3.1	Introduction	65
3.2	Density and temperature profiles	66
3.3	Gamma-ray background radiation	71
3.4	Synchrotron radiation	76

<i>CONTENTS</i>	xix
3.5 Discussions	78
3.6 Conclusion	79
4 Constraints on cosmic rays in the Milky Way circumgalactic medium from OVIII observations	81
4.1 Introduction	83
4.2 Density and Temperature Models	86
4.2.1 Isothermal Model	89
4.2.2 Precipitation Model	90
4.2.3 Observational constraints	92
4.2.4 Log-normal Temperature Fluctuation	94
4.3 Results	94
4.3.1 Observations To Compare With	96
4.3.2 Constraints	97
4.4 Discussion	98
4.5 Conclusion	101
5 Gamma-rays from the circumgalactic medium of M31	103
5.1 Introduction	105
5.2 Leptonic Interaction	106
5.3 Hadronic interaction	107
5.3.1 Star formation activity	107
5.3.2 In-situ formation	109

5.4	Simulation setup	111
5.4.1	Initial Condition	111
5.4.2	Injection Condition	114
5.4.3	Solver and resolution	115
5.5	Result	117
5.6	Discussion	121
5.7	Conclusion	124
6	Seeding the CGM: How Satellites Populate the Cold Phase of Milky Way Halos	125
6.1	Introduction	127
6.2	Methodology	132
6.2.1	Initial Conditions	133
6.2.2	Defining Cold CGM Gas	135
6.3	Results	136
6.3.1	Where is the cold gas?	136
6.3.2	How much cold gas is there?	138
6.3.3	How do satellite properties affect the cold gas mass in the CGM?	140
6.4	Discussion	150
6.5	Conclusion	150
7	Conclusions and future goals	155

7.1	Effects of Photoionization and Temperature Fluctuations on the Ionization Structure of the CGM	155
7.2	Constraints on CR content	156
7.3	Constraints on CR content	157
7.4	Gamma-rays from the circumgalactic medium of M31	157
7.5	Effects of Satellites on the Cold Phase of the CGM	158
7.6	Future goals	158
A	Geometry	175
B	Significance Study	179

List of Figures

1	Column density of OVI with the variation in maximum circular velocity .	viii
2	γ - ray flux variation with the change in $\eta = P_{CR}/P_{th}$	x
4	Temperature distribution of the one snapshot at 1.5 Gyr of the simulation (Right) and γ -ray map of M31 with a combination of diffusive and advective transport mechanisms of CRs (Left)	xiii
3	OVI column density variation with the change in $\eta = P_{CR}/P_{th}$	xiii
1.1	Schematic diagram for the baryon budget of the Universe at present time	4
1.2	Schematic diagram of the circumgalactic medium	5
1.3	Absorption line studies of the CGM	8
1.4	The emission measure map of Milky Way's thermal plasma component .	12
1.5	Simulated MgII surface brightness map of one of the star-forming galaxy from TNG50 simulation	18
2.1	Entropy, electron density and temperature profile for Precipitation model	40
2.2	Radiative cooling function $\Lambda_N(T)$ for gas with metallicity $0.3 Z_\odot$ and solar abundance ratios	41
2.3	OVI column density map of Milky Way from Precipitation model	45

2.4	OVII column density map of Milky Way from Precipitation model	46
2.5	OVIII column density map of Milky Way from Precipitation model	47
2.6	Radial density profiles of OVI, OVII, and OVIII for $M_{\text{vir}} = 2 \times 10^{12} M_{\odot}$	48
2.7	Column-density ratio $N_{\text{OVII}}/N_{\text{OVIII}}$ map of Milky Way from Precipitation model	50
2.8	Variation of OVI column density with sigma and comparison with observation of star forming and passive galaxies	57
2.9	Variation of OVI column density in case of CI and PI in the low mass galaxies	59
2.10	Variation of OVII, OVIII and NV, CIV column densities respectively in the case of CI and PI in the low mass galaxies	60
3.1	Density, temperature and pressure profiles from different CGM models	67
3.2	Variation of $t_{\text{cool}}/t_{\text{ff}}$ with $P_{\text{CR}}/P_{\text{th}}$	68
3.3	Variation of mean gamma-ray flux from Solar position at 3.85 GeV with $P_{\text{CR}}/P_{\text{th}}$ and the corresponding flux map for PP model	72
3.4	Variation of anisotropy (ratio of standard deviation to mean in γ -ray intensity map) with η for different models	73
3.5	Brightness temperature at 1.4 GHz for different models	77
4.1	Radial profiles of η in the case of $\eta = x$ and $1/x$	84
4.2	Total pressure, density and temperature profiles for different models	88
4.3	Variation of OVIII column density with η for IT model	90
4.4	Variation of OVIII column density with η for PP model	91
4.5	OVIII column density for different η profiles for IT and PP model	93

5.1	The density, CR pressure and γ -ray emissivity at the simulation time of 1 Gyr	112
5.2	The radial profiles of volume averaged values of density, CR pressure, emissivity and ratio of CR pressure and gas pressure	113
5.3	The γ -ray spectra for the cases without and with diffusion	116
5.4	Simulated γ -ray image in the sky at 35 GeV with respect to RA and DEC	118
6.1	The temperature distribution of three snapshots of the simulation, 2xm10fh	127
6.2	The temperature distribution of the three snapshots of the simulations, 20xm09fh	128
6.3	The temperature distribution of the three snapshots of the simulations 200xm08fh	129
6.4	The time evolution of total cold gas mass beyond 40kpc radius from the center of the host galaxy	133
6.5	The time evolution of the cold gas mass from different contributions beyond 40kpc radius from the center of the host galaxy	134
6.6	Time and mass-weighted probability distribution function and cumulative distribution function of cold-stripped cloud mass as a function of the temperature of the cloud after the stripping	143
6.7	The time evolution of the cold gas mass from different contributions beyond 40kpc radius from the center of the host galaxy for the case of no feedback in satellites and host along with no gas in the satellites for the 10^9 and $10^8 M_{\odot}$ satellites	146
6.8	2-d probability distribution function of stripped gas mass as a function of the time and temperature of the gas in the case of with feedback and without feedback for the m09 and m08 satellites	147

6.9	The time evolution of the cold gas mass from different contributions beyond 40kpc radius from the center of the host galaxy for the change in a number of satellites in the case of $10^9 M_{\odot}$ satellites	148
6.10	Radial profile of time-integrated mach number	151
A.1	Coordinate systems of M31 and Milky Way	176
B.1	Time evolution of stripped cold gas from one satellite situated at 100 kpc in the case of two different runs of m10 (2xm10fl and 2xm10nl).	180

List of Tables

2.1	Summary of the observations	54
4.1	Constraints of η on the basis of N_{OVIII} observations by G12 and F15 . . .	95
6.1	Properties of Initial Conditions for the Simulations/Halos Studied Here .	153
6.2	Summary of all the runs with different satellite distributions	154

Chapter 1

Introduction

1.1 Circumgalactic Medium

Our current knowledge of the inventory of mass-energy density of the universe is that it consists of $\sim 73\%$ dark energy and $\sim 27\%$ matter, where roughly $\sim 85\%$ of this matter is dark matter and the rest $\sim 15\%$ is baryonic matter (Planck Collaboration et al., 2016b). Dark matter and baryons are the two main components of galaxies which are the building blocks of our universe. Roughly $\sim 10\%$ of these baryons are in the central part of the galaxies in the form of stars and cold gas in the interstellar medium (ISM). Another $\sim 70\%$ of the baryons are in the form of diffuse gas around the galaxies, in circumgalactic medium (CGM), intergalactic medium (IGM) and intracluster medium (ICM) (See the schematic diagram of baryon budget in Figure 1.1 (de Graaff et al., 2019)). However, the origin of the rest $\sim 20\%$ of baryons is still debated. In addition, the available gas for star formation is supposed to deplete in a time scale, $t_{\text{dep}} \equiv \frac{M_{\text{gas}}}{\dot{M}_{\text{sfr}}} \approx 3 \text{ Gyr} \times \left(\frac{M_{\text{gas}}}{10^{10} M_{\odot}}\right) \times \left(\frac{\dot{M}_{\text{sfr}}}{3 M_{\odot}/\text{yr}}\right)$, where M_{gas} is the gas mass and \dot{M}_{sfr} is the star formation rate of a galaxy (using approximate values for Milky Way galaxy). This depletion time is much smaller than the age of the galaxies. Therefore, one might ask how galaxies continue to get their star-formation fuel. It is now apparent from several studies that a large fraction of the missing baryons are in the form of a diffuse gaseous halo, known as the Circumgalactic medium (CGM), which surrounds the central, star forming optically visible part of the galaxies (Tumlinson et al., 2017). The CGM is the ‘habitat’ for large-scale gas flows that fundamentally regulate the evolution of

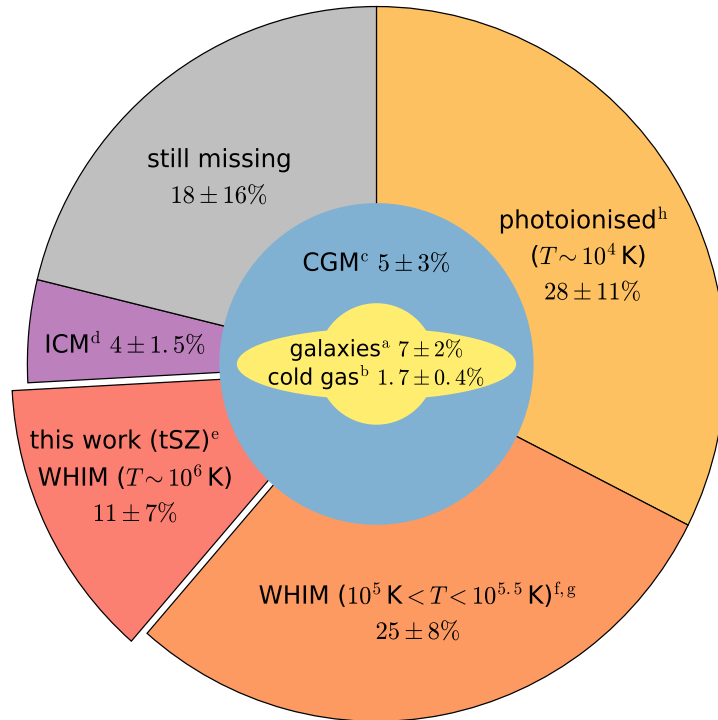


Figure 1.1: Schematic diagram for the baryon budget of the Universe at present time, taken from [de Graaff et al. \(2019\)](#). Galaxies, along with the stellar and cold gas components, comprise of 10% of the overall baryon budget. The rest 70% of the baryon budget is made up of the circumgalactic medium (CGM), intergalactic medium (photoionized and warm-hot IGM, or WHIM), and intracluster medium (ICM), with the remaining 20% yet unaccounted for.

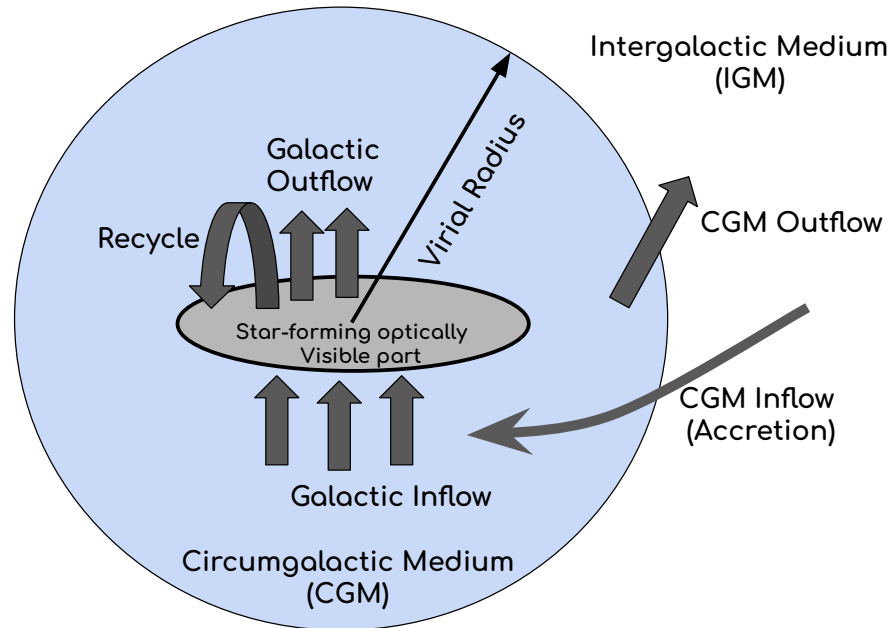


Figure 1.2: Schematic diagram of the circumgalactic medium (CGM) of a galaxy, which surrounds the central, star forming optically visible part of the galaxy. It extends roughly up to the virial radius of the galaxy. We show various large-scale gaseous flows occurring in the CGM which play important role in the evolution of the galaxies.

the galaxy by providing fresh and recycled gaseous fuel for star formation (See schematic diagram of the CGM in Figure 1.2). A better understanding of the CGM promises to illuminate key unresolved issues in the galactic evolution. For example, if the CGM of a host galaxy is dense enough to remove gas from satellite galaxies, then the satellite galaxy becomes gas deficit and quenched over time. Recent and upcoming observational data from modern facilities, including JWST, eROSITA, and the MUSE/KCWI ground-based IFU instruments will facilitate the detailed physical interpretation of the CGM undoubtedly. However, they are also challenging our current understanding of CGM. For example, recent X-ray observations have detected gas in the Milky Way CGM with a temperature much higher than the maximum temperature expected. In the upcoming years, CGM studies will be one of the exciting areas of extragalactic astrophysics and will hold critical information about galaxy evolution.

1.2 Theoretical background

In 1956, Spitzer proposed the idea of a Galactic ‘corona’ (Spitzer, 1956), the extra-planar diffuse high temperature gas, from the observation of Na I and Ca II in the spectra of hot stars at high galactic latitude (Münch & Zirin, 1961). He interpreted that it is this diffuse hot gas that keeps these extra-planar cold clouds of Na I and Ca II in pressure confinement. Thereafter, the discovery of quasar provided many bright background sources, facilitating the improvement of the spectroscopy of absorption lines from the intervening medium between background source and observer. It was anticipated that the diffuse gas in the corona of the galaxies gives rise to most of the absorption lines seen in these quasar spectra (Bahcall & Spitzer, 1969). In recent times, a wide range of spectral lines observed in quasar spectra by the Cosmic Origins Spectrograph (COS) in the Hubble Space Telescope (HST) points towards a rich multi-phase temperature, density, metallicity, and ionization structure of this diffuse galactic corona, now popularly known as the CGM (Tumlinson et al., 2011).

Density perturbations in a homogeneous and isotropic universe grow until they reach critical density¹ (Mo et al., 2010), after which they turn around and stop following the expansion of the universe and gravitationally collapse to form virialized dark matter (DM) halos. A virialized system implies a system of gravitationally interacting particles that maintain a stable system by not expanding or collapsing. For such static system, the second derivative of the system’s moment of inertia is zero (Mo et al., 1998). The small structures within the halo interact with each other, but the virialized halo does not expand or collapse. Mathematically, according to the virial theorem:

$$\frac{1}{2} \times \frac{d^2 I}{dt^2} = 2K.E + P.E, \quad (1.1)$$

where K.E is kinetic energy, P.E is potential energy, and ‘I’ is the moment of inertia of the halo structure. Then, mathematically, the system is virialized when the potential energy (P.E) is twice the negative kinetic energy (K.E). With time, these halos then grow in mass (and size), either by accretion of material (gas or dark matter) from their neighbouring

¹Critical density (ρ_c) is the mean matter density, needed for gravity to halt the expansion of the Universe: $\rho_c = \frac{3H^2}{8\pi G}$

regions or by merging with other halos. When the gas from the neighbouring region falls into the dark matter halo, it gets shocked and heated to the virial temperature of the dark matter halo to form a virialized gaseous halo. If we assume the gas to be ideal and monoatomic and the halo to be spherical, then we can calculate the temperature of this virialized halo, known as the virial temperature. For gas with mass M_{gas} in a halo of mass M_{vir} and radius r_{vir} is in virial equilibrium, the virial temperature is given by

$$\begin{aligned}
2K.E + P.E &= 0, \\
\Rightarrow 3 \frac{M_{gas}}{\mu m_p} k_B T_{vir} - \frac{3}{2} \frac{GM_{gas}M_{vir}}{r_{vir}} &= 0, \\
\Rightarrow T_{vir} &= \frac{1}{2} \frac{\mu m_p}{k_B} \frac{GM_{vir}}{r_{vir}}, \\
\Rightarrow T_{vir} &= 1.6 \times 10^6 \text{K} \left(\frac{M_{vir}}{2 \times 10^{12} M_\odot} \right) \left(\frac{r_{vir}}{200 \text{kpc}} \right).
\end{aligned} \tag{1.2}$$

However, sustaining its temperature at the virial temperature is a critical question as this gas can cool by different mechanisms such as radiative cooling including line transitions. Therefore, in this context, the interplay between cooling time and gravitational free-fall time plays a critical role in the formation of the galactic halo. If the cooling time scale is larger than the time scale for gravitational collapse, then the thermal pressure can sustain the galactic gaseous halo by giving it the required pressure to support it against gravitational collapse and sustaining this hot gaseous halo.

1.3 Methods of Investigation of the CGM

Several methods have been employed in investigating the properties and structure of the CGM. There exists a number of analytical and semi-analytical models along with numerical simulations which use a wide range of parameters to describe the CGM. Observations of the CGM, however, will be the ultimate arbiter of whether or not our simulations and theoretical models are on the correct route. The effort towards the observation of the CGM is improving day by day with the improvement in observational techniques and telescope sensitivities. In this section, we will describe the different observational techniques along with simulations and analytical models of the CGM in detail.

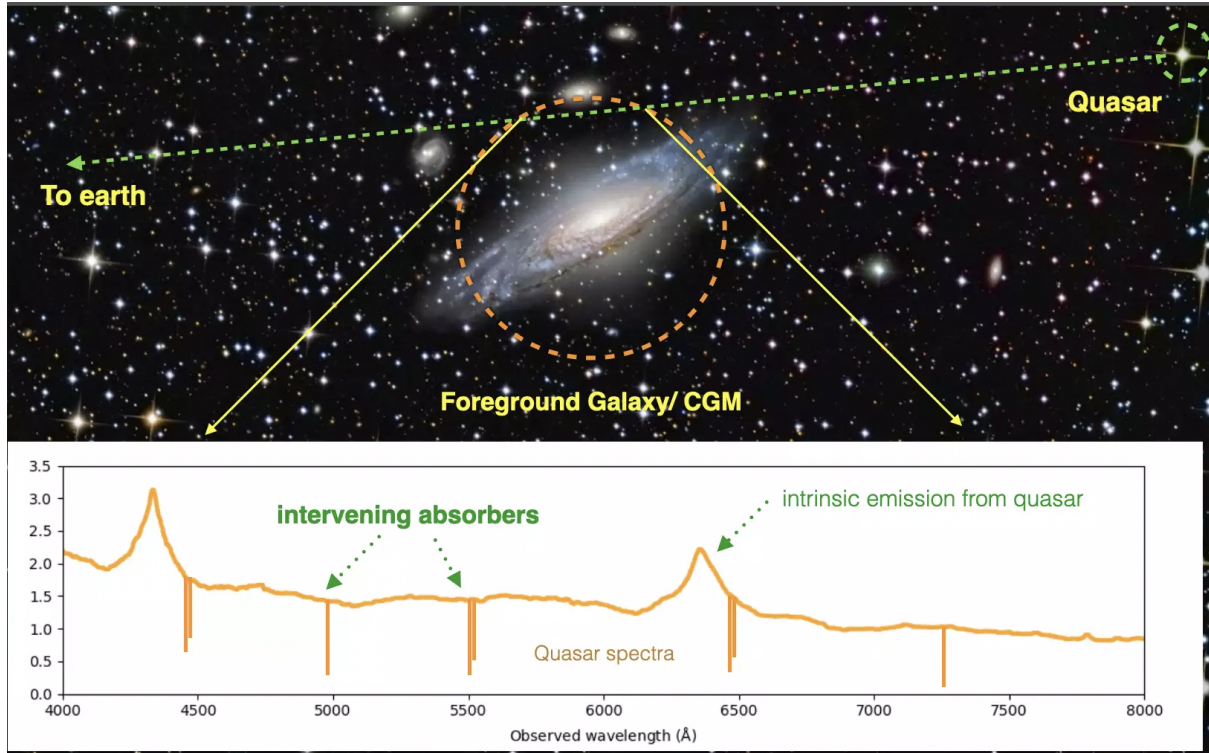


Figure 1.3: When continuum radiation from background quasar passes through the CGM of a foreground galaxy, it gives rise to multiple absorption lines in the quasar spectra. This figure depicts the schematic diagram of such quasar absorption lines, where metal species in various ionisation states trace various CGM phases. (image credit: <https://www.mpa-garching.mpg.de/964620/hl202107>).

1.3.1 Observations

There are several ongoing efforts to observe the CGM in multi-wavelength with different techniques. Using different telescope facilities, the CGM can be observed in different wavelengths, such as x-ray, ultraviolet, and infrared, even in radio and γ -rays. The observational techniques include absorption studies from background bright sources, emission studies, and stacking analysis. In addition, the Sunyaev–Zeldovich (SZ) effect, rotation measure, and dispersion measure are also used to obtain information about the pressure, electron density, and magnetic field of the CGM. In this section, we will briefly discuss these observational techniques and what information we get to know about CGM from these different observations.

1.3.1.1 Absorption Studies:

One of the most popular and convenient ways to observe CGM is the absorption of the continuum emission from background bright sources like a quasar or bright galaxy. These absorptions are caused by line transitions of different ions in the CGM (see Figure 1.3). This technique comes with several advantages: 1) it is sensitive to low column density because it is independent of distance, 2) the detection limits are independent of the luminosity and redshift of the host galaxy, and most importantly, 3) unlike emission studies, it has access to a wide range of densities as absorption column density is proportional to density whereas emission measure is proportional to the density squared:

$$N_{ion} (\text{cm}^{-2}) = \int_{s_1}^{s_2} n_{ion} ds, \quad (1.3)$$

where n_{ion} is the ion density, ds is an infinitesimal line element along the line of sight and s_1 and s_2 are the distances to the closest and furthest points of interception by the CGM. This technique, however, can not yield information regarding the absorber size, unless close pairs of lines of sight are available, which are rare. However, in the local universe (Lehner et al., 2015; Bowen et al., 2016), especially for Milky Way CGM, it is possible to have multiple sightlines, like quasars or UV-bright halo stars (Richter et al., 2017; Peek & Bish, 2020), whereas, for high redshift galaxies, one can make use of multiply-lensed images from background quasars to get multiple sightlines (Rauch & Haehnelt, 2011; Rubin et al., 2015).

There are several ways to select absorber samples, e.g. one is by blindly looking for background quasars on the basis of their properties such as brightness and redshift (Stoche et al., 2006; Rudie et al., 2012). It is also possible to select targeted samples, where the objects probe particular foreground absorbers. For example, some particular class of galaxies, galaxies with known properties like known ISM of the galaxy (Borthakur et al., 2015), L^* galaxies (Tumlinson et al., 2013) or sub- L^* galaxies (Bordoloi et al., 2014b). In general, the UV and optical spectra are used to constrain CGM gas in absorption line studies, however, x-ray spectra from *Chandra*, *XMM-Newton* telescopes (Gupta et al., 2012; Fang et al., 2015; Das et al., 2021) are also being used for this technique.

There is also the so-called ‘Down-the-barrel’ technique which detects absorption using the galaxy’s own starlight as background. In the case of galaxies with high star formation

rate, galactic inflow and outflow dominate the kinematics of the CGM, and they can be studied in optical, near UV (Martin, 2005; Bordoloi et al., 2014a; Rubin et al., 2014) and UV wavelengths (Henry et al., 2015; Heckman et al., 2015) using this method. However, this method is again limited by the fact that one can not constrain the location of the absorbing region.

1.3.1.2 Emission Studies:

The intracluster medium (ICM) can be thought of as a larger structure, analogous to the CGM, both being large reservoirs of hot gas. For the ICM, x-ray emission study is one of the well-established approaches to investigate its structure and physical processes due to its high temperature ($T \sim 10^7 \text{K}$). An emission study would also be important to investigate the structure of the CGM as it can probe the photons directly emitted from the CGM. In comparison to the projected pencil beam line of sight in absorption studies, emission maps are very useful to put more direct constraints on the physical extent, density profile, and morphology of the CGM. However, emission studies of CGM are more challenging than the absorption technique, as the emission measure (EM) is directly proportional to the square of the density of the CGM:

$$\text{EM} (\text{cm}^{-6} \text{pc}) = \int n_e^2(s) ds, \quad (1.4)$$

where n_e is the thermal electron density, and ds is the infinitesimal line element along the line of sight. Therefore, as CGM has a typical density, $n_e \leq 10^{-2} \text{cm}^{-3}$, the EM of the CGM is very low. In Figure 1.4, we show EM map of Milky Way's thermal plasma component in the X-ray spectral fits indicating the Milky Way halo emission (Kaaret et al., 2020).

The CGM can emit in different wavelengths. There has been extensive mapping of high-velocity clouds or other structures using 21-cm emission in the radio band (Putman et al., 2012). In addition, the hot gas phase of the CGM has a temperature, $T \geq 10^6 \text{K}$ and it can be probed in soft X-ray emission. There are recent detections of hot halo emission using *Chandra*, ROSAT, and *XMM-Newton* (Humphrey et al., 2011; Anderson et al., 2016; Bhattacharyya et al., 2022). Not only radio and X-ray, but CGM emissions can also be seen in UV and optical, although they are equally challenging. The emission

from extended OVI halo around low-redshift galaxies, probing the warm phase of the CGM, are detected in the UV band (Hayes et al., 2016). Moreover, extended Ly- α (Cantalupo et al., 2014; Prescott et al., 2015) and H α (Zhang et al., 2016) emissions are observed at impact parameters of 100s of kpc away from galaxies, probing the CGM of these galaxies. There has been also the detection of emission in optical from the extended filamentary structure that is connected to the galactic disk (Martin et al., 2015). Other than this, CGM also contains high energy cosmic ray particles produced by star-formation processes, which can also interact hadronically or leptonically with CGM and give rise to emission in γ -ray. These cosmic rays can also interact with the magnetic field of the CGM and give rise to synchrotron emission in the radio band. We will discuss these interactions in a later section in detail.

However, observing CGM in emission is extremely difficult due to the low surface brightness of this gas in comparison to the background and for its steep decrement with distance ($\propto 1/D^2$). These difficulties have encouraged efforts to improvise upon current detectors and build telescopes with better sensitivity. Example of such recent and ongoing facilities are eROSITA, JWST, Athena, and so on, and we will be able to probe CGM in emission in a much better way using these facilities in near future.

1.3.1.3 Sunyaev–Zel’dovich (SZ) effect:

Another well-established technique in ICM studies is probing gas using the SZ effect, which is essentially the distortion of the Cosmic Microwave Background (CMB) spectrum while photon goes through hot ionized gas. This is also becoming a technique for CGM studies. However, the SZ signal from the CGM is very faint and its detection is challenging. One needs to stack signals from a large number of galaxy populations to make a reasonable detection.

There are two kinds of SZ effect: 1) thermal SZ effect (tSZ) - where CMB photon gets scattered by high energy electrons in hot ionized gas, and 2) kinematic SZ effect (kSZ) - where CMB photon gets scattered by hot ionized gas with bulk motion and gets Doppler shifted. The SZ effect is characterized by the y -parameter, where for tSZ, it is proportional to the thermal pressure of the gas and in the case of kSZ, it is proportional

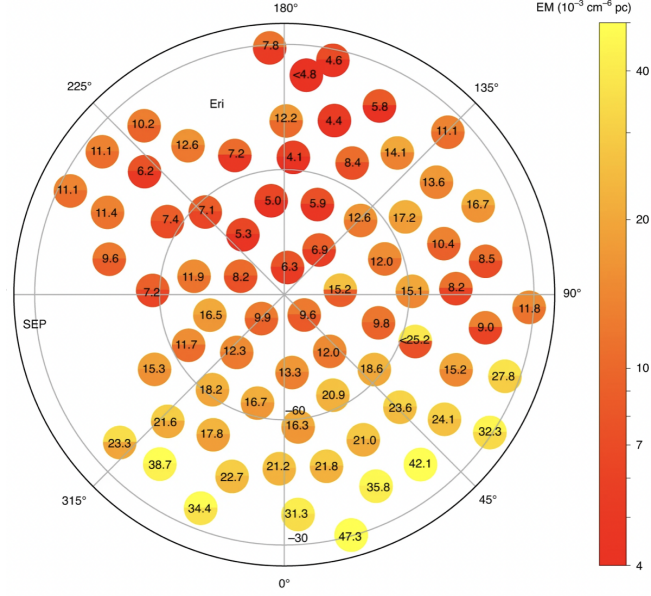


Figure 1.4: The emission measure map of Milky Way's thermal plasma component in the X-ray spectral fits which represents the Milky Way halo emission (Kaaret et al., 2020). The center of the plot denotes the Galactic south pole. The different circles denote different Galactic latitude. The lines connecting the center and perimeter of the circle indicate different Galactic longitude.

to the scattering medium's line of sight velocity and electron density of the gas:

$$y_{tSZ} = (k_b T_e n_e \sigma_T L) / (m_e c^2), \text{ and} \quad (1.5)$$

$$y_{kSZ} = (v_{los} n_e \sigma_T L) / c,$$

where T_e and n_e are the temperature and electron density of the medium, σ_T is the Thompson scattering cross section, L is the distance that photons pass through the intervening medium and v_{los} is the peculiar velocity of scattering medium projected along the line of sight. One can also estimate the integrated y -parameter for tSZ effect over a sphere of radius R_{500} ² for the CGM, which is,

$$Y_{500} = \frac{\sigma_T}{m_e c^2} \times \int_0^{R_{500}} \frac{n_e k_b T_e dV}{D_A^2(z)}. \quad (1.6)$$

This Y_{500} can be scaled to $z=0$, which is defined as,

$$\tilde{Y}_{500} = Y_{500} \times E^{-2/3}(z) \left(\frac{D_A(z)}{500 \text{ Mpc}} \right)^2 \quad (1.7)$$

For a cluster ($\sim 1 \text{ Mpc}$) with temperature of 10^8 K , density of $10^{-3} / \text{cc}$ and line of sight of velocity of 500 km/sec , one gets $y_{tSZ} \approx 10^{-5}$ and $y_{kSZ} \approx 10^{-6}$. Before the Planck survey,

² R_{500} is the radius within which the mean mass density is 500 times the critical density of the Universe.

the SZ signal only from the ICM have been discovered so far due to the sensitivity limit (Birkinshaw, 1999). For the hot phase of CGM, $T \sim 10^6$ K, tSZ signal is two orders of magnitude lower than that of ICM. However, the better sensitivity and all-sky coverage of Planck survey (Planck Collaboration et al., 2013a) enable the detection of the SZ effect down to the galaxy scale. Their recent detection of tSZ signal of $\tilde{Y}_{500} \simeq 10^{-6}$ arcmin² for galaxies down to stellar mass $M_\star \approx 9 \times 10^{10} M_\odot$ with a equivalent mean halo mass of $M_{halo} \approx 1.4 \times 10^{13} M_\odot$ by stacking signals of galaxies from the SDSS survey (Planck Collaboration et al., 2013a). Incidentally, Singh et al. (2015) analytically calculated the tSZ signal from the hot gas in these galactic halos and their predicted SZ signal is consistent with Planck's marginal detection at these mass scales for the majority of big galaxies (halo mass $> 10^{12.5} M_\odot$). They also estimated the tSZ signal from warm OVI absorbing gas to be $y \sim 10^{-8}$, which may be detected by future investigations. In addition, the kSZ signal in the galaxy scale is also detected with Atacama Cosmology Telescope (ACT) and Planck data (Hand et al., 2012; Planck Collaboration et al., 2016a).

1.3.1.4 Dispersion Measure And Rotation Measure:

Fast radio bursts (FRBs) are bright in radio wavebands with fluxes $F_\nu \sim 100$ s of Jy, and their duration is up to a few milliseconds. They have been detected in a wide frequency range from 400 MHz-400 GHz. Over 1000 FRBs (See Figure 1 of Petroff et al. (2022)) have been detected so far, with many more about to be discovered in the coming years (CHIME/FRB Collaboration et al., 2021; Niu et al., 2022). This growing number of detection of FRBs has facilitated putting constraints on the electron density of the CGM using dispersion measure (DM) along different lines of sight. The Dispersion Measure (DM) of a signal is directly proportional to the integrated electron number density along the signal's line of sight. This fundamental relationship makes DM a valuable tool for constraining the density profile of the CGM, as the CGM is predominantly ionized and contributes an excess amount to the total DM along the sightlines of observed signals. By using DM to probe the density profile of the CGM, one can gain essential insights into the distribution and properties of ionized gas in the CGM:

$$\text{DM (pc cm}^{-3}\text{)} = \int n_e(s) ds, \quad (1.8)$$

where n_e is the thermal electron density, ds is the infinitesimal line element along the line of sight and d is the distance to the FRB. When the radio signal emitted from these FRBs passes through the a plasma between the source and observer, the dispersion relation ($w = ck$) of the electromagnetic radiation becomes dependant on the plasma frequency (w_p) leading to $w^2 = k^2c^2 + w_p^2$.

Generally, if the FRB signal is extra-galactic, the observed DM is the summation of the following components:

$$\text{DM}_{\text{obs}} = \text{DM}_{\text{ISM}} + \text{DM}_{\text{CGM}} + \text{DM}_{\text{IGM}} + \text{DM}_{\text{Intervening Halos}} + \text{DM}_{\text{FRB,host}} \quad (1.9)$$

In order to calculate the excess DM just from CGM, one needs to subtract the DM contribution from the host galaxy and its environment (a few tens to a few hundreds of pc cm^{-3} ; [Kulkarni et al. \(2015\)](#); [Yang et al. \(2020\)](#); [Cordes et al. \(2022\)](#)) along with DM from the cosmic structure (hundreds of pc cm^{-3} ; [McQuinn \(2014\)](#); [Macquart et al. \(2020\)](#)). Suppose one can accurately measure the redshifts of the host galaxy and any intervening galaxies associated with Fast Radio Bursts (FRBs), which requires precise localization to an arcsecond scale. In that case, one can subtract the expected average cosmological contribution from the total DM of the FRB. This subtraction can significantly reduce the variance in the measurement. Even with the arcsecond localization, one must stack an order of ~ 100 FRBs ([McQuinn, 2014](#); [Ravi, 2019](#)) to detect excess DM from the CGM. However, to date, only around 20 Fast Radio Bursts (FRBs) have been accurately localized ([Petroff et al., 2022](#)); hence, many more FRBs are needed to put constraints on foreground CGM. The growing number of detection of FRBs is opening up a new era where DM from FRBs will put stringent limits on the gas density profile of the CGM along with emission maps and the SZ effect. Recent studies have calculated that the excess DM from Milky Way halo could be $\sim 10\text{s pc cm}^{-3}$ for a variety of CGM models ([Keating & Pen, 2020](#); [Wu & McQuinn, 2022](#)).

Another important but uncertain parameter is the magnetic field in the CGM. In addition to DM from the FRBs, one can also use Rotation Measure (RM) to put constraints on the galactic magnetic field. When a linearly polarized emission passes through a magnetized ionized medium, its polarization vectors rotate, known as the Faraday effect. The observed polarization angle (ξ) is the sum of the intrinsic polarization (ξ_0) and $\lambda^2(\text{RM})$

where λ is the observing frequency:

$$\xi(\lambda^2) = \xi_0 + \lambda^2(\text{RM}). \quad (1.10)$$

RM is defined as the integrated electron number density (n_e) and the parallel magnetic field along the line of sight (B_{par}):

$$\text{RM} = 0.812 \text{ rad m}^{-2} \int \left[\frac{n_e(s)}{\text{cm}^{-3}} \right] \left[\frac{B_{par}}{\mu\text{G}} \right] \left(\frac{ds}{\text{pc}} \right), \quad (1.11)$$

where ds is the infinitesimal line element along the line of sight. RM contribution can also be broken down to components similar to DM:

$$\text{RM}_{\text{obs}} = \text{RM}_{\text{ISM}} + \text{RM}_{\text{CGM}} + \text{RM}_{\text{IGM}} + \text{RM}_{\text{Intervening Halos}} + \text{RM}_{\text{FRB,host}}. \quad (1.12)$$

If one can measure the DM and RM along the same line of sight, the parallel magnetic field to the line of sight weighted by electron density can be estimated from the ratio of RM and DM. It is also possible to determine the column density distribution of ionized gas from absorption line measurements and use it to calculate the magnetic field from RM. Several recent works have used RM measurement from polarized radio sources and put limits on CGM magnetic field, which usually turns out to be less than several μG (Lan & Prochaska, 2020; Pandhi et al., 2022).

1.3.2 Simulations

In the previous section, we have shown that different methods of observations have ample potential to reveal the key physical state of the CGM. However, the CGM is inherently complex in nature for its dependency on many non-separable parameters such as density, temperature, ionization equilibrium, etc. Without doing controlled experiments, by varying different parameters, it is difficult to disentangle the effect of each parameter on the CGM. Simulations of the CGM can provide a stage for controlled experiments where one can have detailed knowledge about different parameters like the physical properties, history, and time evolution of the CGM. One can also vary these parameters by hand to investigate their dependencies. There are different methods used in galaxy simulations in order to study the formation of galaxies or cosmic web governed by gravity of mostly the dark matter, and hydrodynamics of baryons. For example, smooth particle hydrodynamics (SPH; e.g Gasoline (Wadsley et al., 2004), Gadget (Springel, 2005), and GIZMO

(Hopkins, 2015b)), adaptive mesh refinement (AMR, e.g Enzo (O’Shea et al., 2004)), and moving mesh (e.g Arepo Weinberger et al. (2020), Illustris (Vogelsberger et al., 2014)). make it clear

There are mainly three types of simulations that are extensively used to study the CGM, a) cosmological simulation, b) idealized simulation, and c) zoom-in simulation. Cosmological simulations consist of a roughly ~ 100 Mpc scale box simulating a part of the universe that consists of at least a few filament nodes. These simulations start with cosmological initial conditions and simulate the time evolution of different properties of the CGM from high redshift to the present day. Many physical processes of the galaxy, e.g., feedback processes, metal mixing, and transport, star formation, etc. are implemented in these simulations as sub-grid modules ³. These simulations provide physical realism to a great degree as they include as many processes as possible, and facilitate statistical investigation of different population of galaxies. However, they have a high degree of complexity, and the different physical processes behind particular CGM properties are hard to segregate. In addition, since some sub-grid models used in these cosmological simulations are tuned to recover some observed properties and not motivated physically, the predictability of these simulations is rather limited. Also, a large volume of these simulations comes with resolution limitations which makes it difficult to resolve small clouds in the CGM and study their dynamical properties and evolution. Still, various cosmological simulations have been used in recent times to investigate observational signatures (Hummels et al., 2013; Faucher-Giguère et al., 2015; Oppenheimer et al., 2016b; Hafen et al., 2017; Nelson et al., 2018) and physical properties (Oppenheimer et al., 2018; Hafen et al., 2019, 2020; Ji et al., 2020) of the CGM. However, different cosmological simulations yield very different CGM properties as these simulations are tuned to match global galaxy properties where one does not directly model the CGM. For example, Davies et al. (2020) compared two cosmological simulations, EAGLE and IllustrisTNG simulations, where they found very different median mass fractions of the CGM produced in the simulations. In addition, different cosmological simulations use different feedback

³Sub-grid modules are implemented in simulations to consider some physical processes occurring at a length-scale that are unresolved by the simulation. They are parameterised and calibrated to produce particular metrics, such as the stellar mass function at $z=0$, and the resulting properties (e.g. SFRs, morphology, quenching, CGM) are then compared with data to restrict the underlying physical processes.

prescriptions as sub-grid modules. For example, in TNG100 cosmological simulation, the AGN-decoupled wind is used as a feedback prescription (Pillepich et al., 2018; Nelson et al., 2019), whereas Joung et al. (2012) considered supernova feedback to be injected in thermal energy form using cosmological simulation Enzo.

Therefore, it is crucial to first understand the impact of different physical processes and sub-grid modules on the CGM in order to constrain CGM properties from cosmological simulations. Here, idealized simulations can play an important role by resolving finer length scale (\sim pc scale) and can hand-pick ingredients that can also be added in an incremental manner in order to isolate their effect on the structure and properties of the CGM. Many idealized simulations have been used in the investigation of the properties and physical processes of the CGM and their dependence on galaxy properties (Fielding et al., 2017; Li & Tonnesen, 2020; Stern et al., 2019, 2020; Lochhaas et al., 2020a; Su et al., 2020).

On the other hand, the ‘zoom-in’ simulations, which span these two regimes of cosmological and idealized simulations, can trace a single galaxy or a subset of galaxies chosen from a larger box by resolving further (Augustin et al., 2019; Suresh et al., 2019). However, for the ‘zoom-in’ simulations, there are also physics-related assumptions involved in the form of sub-grid modules for the unresolved scale/physics by these simulations to represent intricate phenomena like star formation, metal mixing and transport, supernova and AGN feedback, among others. Therefore, there remain some limitations in the predictability of these zoom-in simulations. However, it cannot be denied that simulating CGM can be very useful to perform controlled experiments for investigating the structure and physical processes in the CGM. In the present thesis, we use two different idealized simulations, PLUTO (Mignone et al., 2007) and GIZMO (Hopkins, 2015b) in order to address two different important issues in the CGM studies that are described in the later chapters.

1.3.3 Analytical model

There exists a lot of simple analytical models of the CGM (e.g., Isothermal (IT): Fang et al. (2013), Precipitation (PP): Voit (2019)) which assume widely varying astrophysical

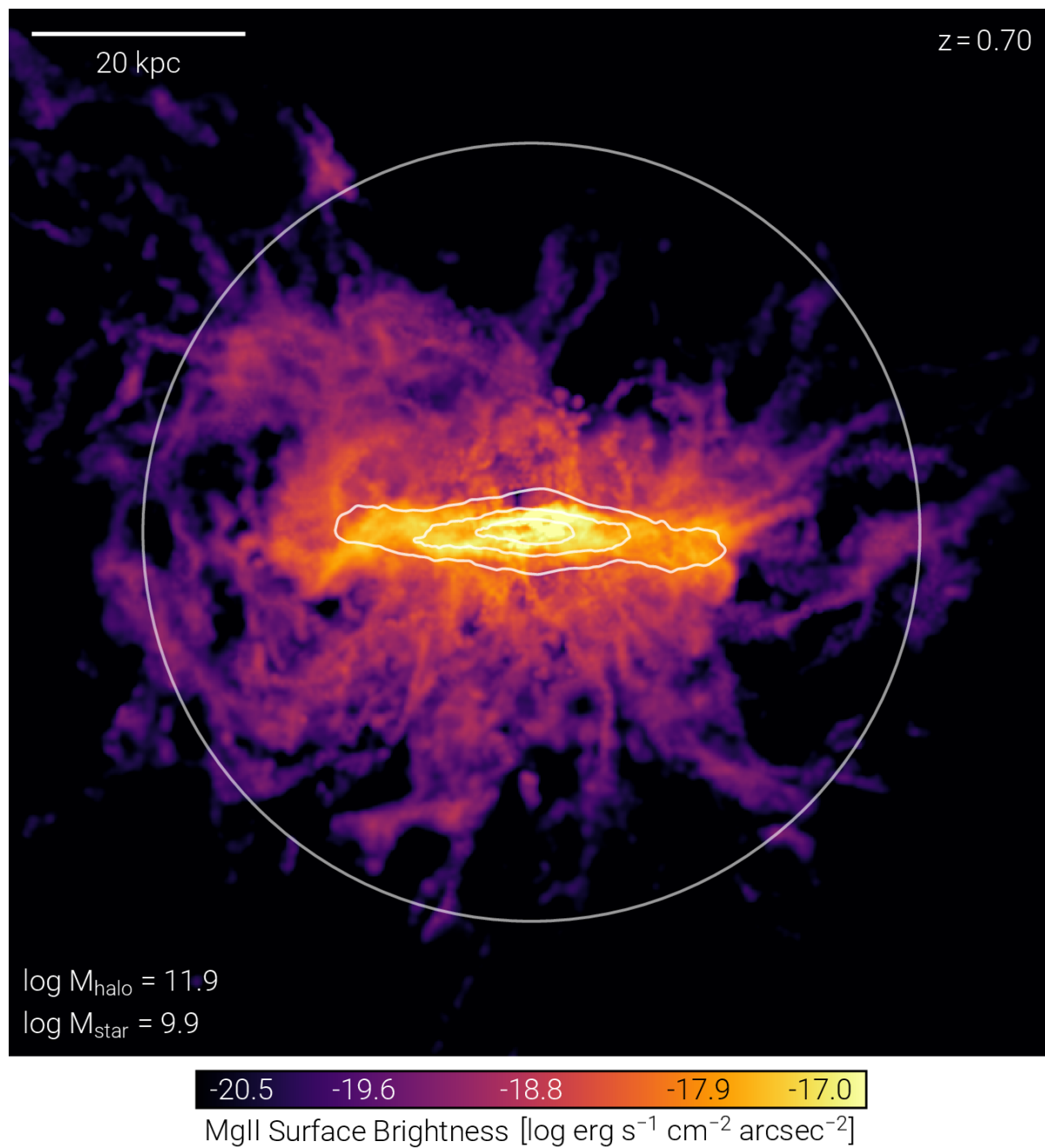


Figure 1.5: Simulated MgII surface brightness map of one of the star-forming galaxy from TNG50 simulation (Nelson et al., 2021). This plot describes that MgII emission extends to the CGM of the galaxy. This kind of simulated map can be used to compare with observational maps of different ions in the CGM to constrain different physical processes of the CGM.

processes, micro-physics, and compositions of the CGM. Despite their diverse nature, these models are very useful to study CGM due to their simple analytical approach.

The simplest starting point of these analytical models is to assume that the CGM is in hydrostatic equilibrium under the gravitational potential of the Dark Matter halo so that one has,

$$\frac{dP}{dr} = -\frac{d\phi}{dr}\rho \Rightarrow \frac{dT}{dx} = -\left(\frac{\mu m_p}{k}\right) \frac{d\phi}{dx} - \left(\frac{T}{n}\right) \frac{dn}{dx}, \quad (1.13)$$

where ϕ represents the gravitational potential, $x \equiv r/r_s$ represents radius in units of a scale radius r_s , and the other variables have standard meanings. Following [Voit \(2019\)](#), we consider a CGM confined by a modified Navarro-Frenk-White (NFW) potential well ([Navarro et al., 1996a](#)). The circular velocity $v_c \equiv [r(d\phi/dr)]^{1/2}$ is constant in the inner part of the potential, with

$$v_c(r) = v_{c,\max}, \quad r \leq 2.163 r_s,$$

to account for stellar mass near the center, and v_c declines slowly with radius at larger radii, following

$$v_c^2(r) = v_{c,\max}^2(r) \times 4.625 \left[\frac{\ln(1 + r/r_s)}{r/r_s} - \frac{1}{1 + r/r_s} \right] \quad (1.14)$$

as in a normal NFW profile. This prescription for circular velocity yields the derivative of the potential required in the first term of the equation (1.13).

At this point, there are several ways to proceed. The simplest is to consider an ‘isothermal’ model (assuming the temperature of the CGM to be constant) that would render the LHS of equation (1.13) zero ([Faerman et al., 2017](#); [Qu & Bregman, 2018](#)). Another option is to connect temperature and density by specifying the specific entropy⁴ at each radius. One choice is to assume a uniform entropy throughout. Recently [Faerman et al. \(2019\)](#) have described an ‘isentropic’ model of the CGM, in which entropy is held a constant in the halo. They include three components in their description of pressure: (a) thermal gas (b) non-thermal gas (magnetic field and CR) and (c) turbulence. They characterise turbulence by a fixed $\sigma_{turb} \approx 60 \text{ km s}^{-1}$, and define a parameter $\alpha(r) = (P_{nth} + P_{th})/P_{th}$. They fixed the boundary condition with the help of the value of α at

⁴This thesis expresses specific entropy in terms of the entropy index $K \equiv kTn_e^{-2/3}$ that is usually adopted in CGM studies.

the outer boundary (r_{200}), α_b , and varied its value between 1 (no non-thermal component) and 3 (equipartition of thermal, magnetic and CR components). In this model, the ratio $\alpha(r)$ drops from its boundary value (α_b) in the inner region.

Another approach is to consider a profile for entropy rather than considering it to be constant. [Voit \(2019\)](#), in his ‘precipitation’ model, assumes a composite entropy profile built by combining two physically motivated entropy profiles. The first is the baseline entropy profile produced by non-radiative structure formation,

$$K_{\text{base}} = (39 \text{ keV cm}^2) v_{200}^2 \left(\frac{r}{r_{200}} \right)^{1.1}, \quad (1.15)$$

taken from [Voit \(2019\)](#), in which $v_{200} = v_{c,\text{max}}/(200 \text{ km s}^{-1})$ and r_{200} is the radius encompassing a mass density 200 times the cosmological critical density. The second is based on the precipitation limit. They assume that the ratio between t_{cool} and t_{ff} is maintained at $t_{\text{cool}}/t_{\text{ff}} = 10$ by an approximate balance between radiative cooling and precipitation-regulated feedback, which fixes the electron density as,

$$n_{e,\text{pre}}(r) = \frac{3kT(r)}{10 \Lambda_{\text{N}}[T(r)]} \left(\frac{n_e n}{2n_{\text{H}}^2} \right) \frac{v_c(r)}{\sqrt{2} r}. \quad (1.16)$$

Given this density profile (equation 1.16) and a temperature profile $T(r)$, one can then write the precipitation limited entropy profile as

$$K_{\text{pre}} = \left[\frac{2kT(r)}{\mu m_p v_c^2(r)} \right]^{1/3} \left\{ \frac{10}{3} \left(\frac{2n_{\text{H}}^2}{n_e n} \right) \Lambda_{\text{N}}[T(r)] r \right\}^{2/3}. \quad (1.17)$$

Then they construct the entropy profile that goes into the integration by adding the entropy profiles in equations (1.15) and (1.17) to get

$$K_{\text{pNFW}}(r) = K_{\text{pre}}(r) + K_{\text{base}}(r). \quad (1.18)$$

The subscript indicates a precipitation-limited NFW model, as in [Voit \(2019\)](#). Using the fact that $n_e = (kT/K_{\text{pNFW}})^{3/2}$, one can write the second term on the RHS of equation (1.13) as

$$\frac{T}{n} \frac{dn}{dx} = \frac{T}{n_e} \frac{dn_e}{dx} = \frac{3}{2} \frac{dT}{dx} - \frac{3}{2} \frac{T}{K_{\text{pNFW}}} \frac{dK_{\text{pNFW}}}{dx} \quad (1.19)$$

Using equation (1.19), the hydrostatic equilibrium equation to be solved boils down to

$$\begin{aligned} \frac{dT}{dx} &= \frac{2}{5} \left[- \left(\frac{\mu m_{\text{H}}}{k} \right) \frac{d\phi}{dx} + \frac{3}{2} \frac{T}{K_{\text{pNFW}}} \frac{dK_{\text{pNFW}}}{dx} \right] \\ &= \frac{2}{5} \left[- \left(\frac{\mu m_{\text{H}}}{k} \right) \frac{d\phi}{dx} + \frac{3}{2} \frac{T}{x} \frac{d \ln K_{\text{pNFW}}}{d \ln x} \right]. \end{aligned} \quad (1.20)$$

Equation (1.20) is one that is iteratively solved to determine a temperature profile that gives $t_{\text{cool}}/t_{\text{ff}} = 10$ for $K_{\text{pNFW}} = K_{\text{pre}}(r) + K_{\text{base}}(r)$, given the boundary condition $kT(r_{200}) = 0.25 \mu m_p v_{\text{c,max}}^2$. Notably, the solution of equation (1.20) for the temperature profile is independent of the entropy profile's normalization. Variation of the boundary condition significantly changes the temperature profile only in the outer region, where $T \leq 10^6$ K. Hence, the choice of boundary condition has only minor effects on the column densities of OVII and OVIII but can have considerably more significant effects on the OVI column density. In this thesis, we use and modify these models to constrain different physical processes in the CGM.

1.4 Different phases of the CGM

Various investigations of CGM point towards the fact that the CGM is multi-phase in nature, with a wide range of temperatures, from low temperatures (T) of $T \leq 10^4 K$ to hot gas with temperatures more than the virial temperature ($T \geq 10^6 K$). Observations of different ions with a wide range of ionization potential probe gas in these different phases. In this section, we briefly describe these phases.

1.4.1 Cold Phase

This cold phase of the CGM mainly contains very dense gas at temperature $T \leq 10^4 K$. This phase is mainly probed by the ions with low ionization potentials like HI, NaI, CaII lines, and dust. [Putman et al. \(2012\)](#) observed 21 cm emission from HVCs in the CGM of Milky Way and calculated the total cold gas mass probed by these HVCs to be $\sim 3 \times 10^7 M_{\odot}$. This phase may have originated from the cooling of hotter phases by thermal instability or from the cool clouds in the disk entrained in multi-phase outflows.

1.4.2 Cool Phase

The cool phase of the CGM mainly comprises dense clouds with temperature $T \sim 10^{4-5} K$. In order to maintain pressure equilibrium with the hot and diffuse CGM gas, this cool phase is likely to have a high density: $n_{cool} = \frac{T_{hot}}{T_{cool}} n_{hot} \simeq 100 n_{hot}$, which is roughly $10^{-1}/cc$ if the hot phase density is considered to be $10^{-3}/cc$. We will come back to the question in later section whether or not this phase is actually dense. This phase is predominantly characterized by the presence of ions with low ionization potentials such as MgII, HI, SiII, CII, and so on, which can be probed by observing absorption lines originating from these ions in the continuum emission of a background source. For example, some recent studies have found the signature of this cool phase with MgII, and HI lines, at impact parameters of 100s kpc, which therefore belongs to the CGM of the galaxy (Chen et al., 2010; Thom et al., 2012). However, some exceptions exist where OVI has been used to probe the cool phase despite its higher ionization potential. It is because OVI can also be produced by photoionization in low-density gas (density roughly below 10^{-4} cm^{-3} ; for example, see Stern et al. (2016)).

There are many possible origins of the cool phase in the CGM, for example, cooling by thermal instability, uplifting by outflows, accretion of gas from IGM or satellite galaxies, etc. Several studies have investigated this phase and come up with different mass estimates. For example, Werk et al. (2014) utilized the COS-Halos survey to investigate the mass density profile and total mass of cool phase of L_* galaxies. Using photoionization equilibrium model (PIE) and low ionization potential ions like CII, SIII, NIII etc., they found that the total cool gas mass of L_* galaxies out to their virial radius is approximately $6 \times 10^{10} M_\odot$. Additionally, Stern et al. (2016) also investigated the total mass of cool CGM in L_* galaxies, and found that the total mass to be approximately $1.3 - 4 \times 10^{10} M_\odot$. However, there has been another recent estimate of the mass to $9 \times 10^{10} M_\odot$ of the cool phase of Lyman Limit Systems in COS-halos sample, which, if taken together with hot CGM mass can resolve the problem of missing baryons (Prochaska et al., 2017a). This order of magnitude scatter in the estimated mass is primarily attributed to a lack of adequate data and limitations in constraints for the physics that governs the CGM.

1.4.3 Warm Phase

Ions with intermediate ionization potentials such as CIV, NV, NeVII, and OVI mainly trace the warm phase of the CGM, which has a temperature of $T \sim 10^{5-6} K$. The cooling rate peaks at this temperature range, hence the stability of this phase is not yet fully understood. Because of its ability to efficiently cool down, it potentially serves as a transitional phase between the hot and cool phases of the CGM. As a result, the warm phase may be a transient state that exists temporarily before the gas either heats up or cools down further.

It is hard to detect this phase in X-ray emission due to its low temperature, and therefore, the prime method of probing this phase is absorption line studies. This method detects the warm phase in many galactic halos, primarily via collisionally ionized OVI ion (at temperature $\sim 3 \times 10^5$ K) (Stocke et al., 2017). For example, the OVI line is detected at impact parameters of ~ 100 kpc in a survey of 42 galaxies with a redshift span of 0.1-0.36 using the COS (Tumlinson et al., 2011). Faerman et al. (2017) recently demonstrated that this phase may originate from the cooling tail of the hot CGM, which naturally accounts for the presence of warm gas at significant distances from the galactic center. These observations have also shown that the warm phase contains a vast gas reservoir with a mass comparable to that of the galaxy's ISM. Moreover, nearly all lines of sight through the galactic halo experience absorption from OVI, as observed in studies conducted by Johnson et al. (2015); Faerman et al. (2017); McQuinn & Werk (2018). This suggests that the OVI has a covering fraction of $\simeq 100\%$. However, sub- L_* galaxies can be generally observed at low redshifts $z < 0.1$, where it is not easy to probe the warm phase by OVI. At these redshifts, it is hard to efficiently detect the doublet lines of O VI (1031.93 Å and 1037.62 Å) using the high-resolution COS FUV gratings⁵. Therefore, CIV lines (1548 Å and 1550 Å) are used to detect the warm phase in these low-mass galaxies (Bordoloi et al., 2014b). Also, in super- L_* non-star-forming galaxies, the absence of OVI line (Tumlinson et al., 2011) in the spectra points towards their hotter halo or non-equilibrium cooling. Although some recent studies have used extreme-UV lines from

⁵Best sensitivities for these gratings are at wavelengths greater than 1150 Å (Osterman et al., 2002)). The OVI lines are not redshifted enough to be detected with high sensitivity ($\lambda_{obs} = \lambda_{em}(1+z)$, where λ_{obs} is observed wavelength and λ_{em} is emitting wavelength).

the NeVIII ion (Tripp et al., 2011; Meiring et al., 2013), the warm phase detection in these high-mass galaxies is not yet fully constrained.

However, the specific ionization mechanism that produces ionic tracers of the warm phase is plagued by a great deal of uncertainty. For example, if any of these ions, say OVI, is partially photoionized, it can trace the gas with a lower temperature than the warm phase and contribute some mass to the cool phase. However, large ‘b’⁶ values of the lines, in particular, seem to naturally support the notion that the most of the OVI is in a hotter phase based on the kinematics of the OVI in comparison to the low-ions (Tumlinson et al., 2011; Werk et al., 2016).

1.4.4 Hot Phase

The CGM hot phase contains the diffuse gas that falls into the dark matter halo and shock heated to the virial temperature of the galaxy ($T \sim T_{vir} = 10^{6-6.5} K$ for Milky Way type galaxy). It surrounds the galactic stellar component and is the volume-filling phase of the CGM. This phase is mainly traced by ions with high ionization potential like OVII, OVIII. It can emit in X-rays due to its high temperature, however, the low density of this phase causes faintness in the emission ($\propto n^2 T$). Thus, most of the emission from this gas still lies below the sensitivity limit in current X-ray telescopes. Therefore, one needs X-ray telescopes with high sensitivity for detecting faint CGM emissions.

Some studies, such as those conducted by Wang et al. (2001, 2003); Hagihara et al. (2010), have suggested that most of the X-ray emission observed in the Milky Way originates within a few kiloparsecs of the galactic center. However, there is now an increasing agreement that the hot phase of the CGM extending till 100s kpc is likely to be responsible for the most of the observed X-ray emission. Therefore, one requires high resolution observations in order to resolve the diffuse X-ray emission from the central region (\sim few kpc) of the galaxy (most probably due to galactic outflows) and extract the CGM emission.

⁶b denotes the Doppler parameter, or Doppler broadening parameter, which is used to characterize the width of observed spectral lines. It is defined as $b = \sqrt{2}\sigma$, where σ denotes 1-d velocity dispersion.

Recently, some observations have (e.g. Gupta et al. (2012); Fang et al. (2015)) detected this hot phase in multiple sightlines of the Milky Way using spectral signatures of high ionization potential ions like OVII and OVIII from Chandra and XMM-Newton. Also, recent detection of X-ray emissions (Anderson & Bregman, 2011; Bogdán et al., 2013a,b; Walker et al., 2015) have been made extending to an impact parameter of ~ 100 kpc from the center of massive elliptical galaxies. This sample also includes passive galaxies, which rule out the possible contamination by stellar winds. In addition, stacking emission maps from multiple galaxies can increase the signal-to-noise ratio and help detect faint signals. Using this technique, Anderson et al. (2013) detected emission from extended hot halos of nearby galaxies of both early and late-type. The hot gas content of CGM can also be constrained at the galactic scale by the thermal (Planck Collaboration et al., 2013a) and kinetic (Hand et al., 2012; Planck Collaboration et al., 2016a) SZ signals, which are proportional to the density and temperature of this hot phase.

1.4.5 Super-Virial Phase

As mentioned in the previous section, the Milky Way has a virialized halo and is expected to have volume-filling gas at virial temperature, supported by observations and theory. However, in recent studies (Das et al., 2021; Bhattacharyya et al., 2022), an even hotter gas in the Galaxy has been discovered in X-ray emission and absorption (XMM-Newton and Chandra), which has been termed as the ‘super-virial gas’. It has a temperature of $T \approx 10^{6.5-7.5} K > T_{vir}$. Its origin, location, distribution, and other physical properties are still uncertain. This super-virial gas has two distinguishing characteristics: (a) significant non-thermal broadening and (b) super-solar abundance (as evidenced by the Neon to Oxygen ratio). Although the first feature suggests turbulence, it does not necessarily indicate where it might originate or be located. However, the second feature is consistent, along with the signatures of α -enhancement, with core-collapse supernovae enrichment. Along with these observations, using HaloSat all-sky survey, Bluem et al. (2022) have also found the proof of at least two hot gas model components that are needed to explain the observed emission, where the hotter component has a temperature more than the virial temperature.

1.5 Variety of interactions of the CGM

The CGM of a galaxy is not at all an isolated entity. It interacts with its host galaxy and surroundings such as the intergalactic medium (IGM) and satellite galaxies. These interactions mainly occur through gaseous exchanges, where outflows from the galactic disk dump material into the CGM, and cold gas accretes to the CGM from the IGM and satellite galaxies. Additionally, the CGM can interact with highly energetic cosmic ray particles, which, when interacting with the CGM gas and magnetic field, produce multi-wavelength emissions. Other modes of interactions of the CGM include gravitational (e.g., with orbiting satellites within the CGM of a host galaxy) Dark Matter annihilation (where two dark matter particles can interact to give rise to γ -rays) and radiation (e.g., radiation from star-light or extra-galactic UV background can photoionize the CGM gas) modes.

These interactions are of paramount importance in shaping the structure and multiphase nature of the CGM, as well as the evolution of the host galaxy. They may also lead to emissions in various wavelengths, which can serve as critical probes for studying the CGM's structure and the host galaxy's properties. This section will focus on two such interactions, specifically with cosmic rays and satellite galaxies, which have been the primary focus of investigation in the present thesis.

1.5.1 Interaction with Cosmic Rays

One of the essential components of the CGM is the highly energetic cosmic ray particles. These particles were first discovered by Victor Hess in 1911 from balloon-borne experiments. In these experiments, with an onboard electroscope, he detected charged particles whose abundance increased with altitude. He named this background radiation 'cosmic radiation', later known as Cosmic Rays (CR). CR particles mainly consist of protons ($\sim 90\%$), with $\sim 9\%$ being Helium nuclei and $\sim 1\%$ being other heavy nuclei and leptons. These particles have energy ranging from $10^9 - 10^{20}$ eV, roughly following a power-law energy spectrum of $n(E) \propto E^{-p}$ with the index ' p ' being approximately 2.7 in the Galaxy. The origin and acceleration of these particles have been discussed for over

half a century. In 1949, Fermi proposed that repeated reflections from ISM magnetic field in moving interstellar clouds could accelerate these charged particles (Fermi, 1949). Almost 30 years later, in 1978, Bell demonstrated how magnetic anomalies around a supernova shock might energize the particles by repeatedly reflecting them back and forth, known as the diffuse shock acceleration mechanism (Bell, 1978).

Therefore, in the standard picture, CRs are believed to be accelerated in supernova shocks triggered by star formation activity in the galactic disk. One may ask if they can be lifted to the CGM from the galactic disk. Unfortunately, the transport mechanisms of CRs still need to be better constrained. After being accelerated in the supernovae shocks, CRs can be lifted to the CGM by advection due to star-formation-driven outflow. They can also diffuse through magnetic field to reach the CGM. Once they are lifted to the CGM, they can interact with the CGM in several ways. For example, they can interact with the CGM protons and give rise to neutral pions that decay into high-energy γ -ray photons. They can also give rise to synchrotron emission in the magnetic field of the CGM.

Not only this, but CRs may also propel large-scale outflows (Jana et al., 2020a; Butsky & Quinn, 2018). If CR pressure supports the galaxy's gaseous component against the galaxy's inward gravitational pull, the outward CR diffusion can inhibit the gas inflow. Calculating CR pressure from the CR flux, which is related to the star formation rate, one gets for an isothermal sphere Socrates et al. (2008),

$$P_{CR} \simeq 3 \times 10^{-10} \tau_3 \epsilon_6 \dot{m}_{SF} R_{kpc}^{-2} \text{ erg cm}^{-3}, \quad (1.21)$$

where, τ_3 , ϵ_6 , \dot{m}_{SF} and R_{kpc} denote CR proton optical depth (in units of 10^3), the conversion efficiency of rest mass into CR energy (in units of 10^6), SFR (in units of M_\odot/year), and galactic radius (in units of kpc) respectively. For the density profile of an isothermal sphere, the corresponding gravitational 'pressure' would be

$$\rho \sigma^2 \simeq 3 \times 10^{-8} f_{g,0.1} R_{kpc}^{-2} \sigma_{300}^4 \text{ erg cm}^{-3}, \quad (1.22)$$

where f_g is the gas fraction (in the units of 0.1) and σ_{300} is the velocity dispersion (in the units of 300 km/sec). Now, if one assumes hydrostatic equilibrium between the CR pressure and gravitational inward pull, the required star formation rate to inhibit the

inflow of gas is given by,

$$\dot{m}_{SF} \simeq 10^3 \tau_3^{-1} \epsilon_6^{-1} f_{g,0.1} \sigma_{300}^4. \quad (1.23)$$

The required SFR is clearly huge; therefore, CR can only propel outflows in rapidly star-forming galaxies (Socrates et al., 2008). In the case of galaxies with moderate SFR, the role of CRs vis-à-vis is not straightforward to discern. However, we will not discuss this aspect of CRs in this thesis.

As we discussed in the earlier section, the cool gas density is expected to be 100 times larger than the density of the hot diffuse phase. However, Werk et al. (2014) observed the cool gas density profile to be similar to that of hot gas density, suggesting the existence of an additional pressure component, which is non-thermal in nature. This non-thermal pressure component can arise from CRs, and it can contribute to the overall pressure along with the thermal pressure. Therefore, CR pressure can give additional non-thermal pressure support to the cool phase of the CGM against the diffuse hot phase to maintain total pressure equilibrium. Therefore, to understand the CGM, we need to study in detail the cosmic ray content in the CGM and the different transport mechanisms of CRs. In this thesis, we put constraints on CR content and its transport mechanisms in light of multi-wavelength observations.

1.5.2 Interaction with Satellite Galaxies

The interactions between a host galaxy and its satellite galaxies have a notable impact on the properties of the host galaxy's CGM. They can interact with the CGM of the host galaxy in several ways. When a satellite galaxy passes through the diffuse gas of the CGM, the gas in the satellite galaxies experiences a headwind that causes pressure on the satellite galaxy, known as 'ram pressure'. Its magnitude depends on the relative speed (v) of the satellite with respect to the medium and the local density of the medium (ρ), i.e.,

$$\rho v^2 = 5 \times 10^{-8} \frac{n}{1 \text{ cm}^{-3}} \times \frac{v}{1700 \text{ km/sec}} \text{ dyn cm}^{-2}. \quad (1.24)$$

Gunn & Gott (1972) first pointed out that for a typical spiral galaxy, the gas material will be held back in the disk by a pressure $2\pi G \sigma_s \sigma_g$ (where σ_g and σ_s are the surface

densities of star and gas disk of the galaxies respectively), if the ram pressure does not exceed this gravitational restoring pressure. In the case of a $10^{11} M_{\odot}$ spiral galaxy, with radius 10kpc, $\sigma_s \sim 0.06 \text{ gm cm}^{-2}$. If the gas layer thickness is 200pc and gas density is 1/cc, then $\sigma_g \sim 10^{-3} \text{ gm cm}^{-2}$. These values correspond to a restoring force of $2.5 \times 10^{-11} \text{ dyn cm}^{-2}$. Therefore, the gas from such a galaxy will be stripped if the surrounding intracluster medium through which it is moving with a velocity of 1700 km/sec has a density of $5 \times 10^{-4}/\text{cc}$. This phenomenon is known as ‘ram pressure stripping’.

A similar scenario of ram pressure stripping is also valid for the satellite galaxies moving through the CGM of a host galaxy. Ram pressure stripping can be more effective for low-mass satellite galaxies than in the case of massive satellite galaxies due to their low gravitational restoring force. Also, galaxies moving through the CGM of massive halos will experience higher ram pressure due to their higher density. For example, the neighboring dwarf galaxies of the Milky Way and M31 system tend to be poorer in HI gas content than those at larger distances (Grcevich & Putman, 2009a). It is due to the fact that the gas in these neighbouring dwarfs is ram pressure stripped by the environment of the Milky Way-M31 system. Ram pressure stripping is an essential factor in the co-evolution of galaxies by regulating gas content and hence star formation of the galaxies. There is significant observational evidence that not only does ram pressure remove gas from satellite galaxies, but it also populates the CGM of the host galaxies with cold gas. For example, it is apparent from recent MUSE observations that there is a strong connection between the group environment and the ionization structure of the CGM of the member galaxies. These observations showed that the group environment significantly increases the column densities and covering fractions of MgII, HI ions of the CGM of member galaxies (Muzahid et al., 2021; Dutta et al., 2021). It is mainly due to the increase of cold gas in the CGM through accretion from the satellite galaxies in a group environment.

Moreover, the gas can also be ejected from the satellites due to the stellar wind or other feedback processes and it can accumulate behind the satellites in the form of a wake (Ostriker, 1999; Bernal & Sánchez-Salcedo, 2013). Moreover, the cold gas stripped from the satellites tries to mix with the hot CGM; subsequently, significant cooling can occur in the mixing layer of this stripped cold gas. The satellites can also stir the CGM gas

and create local perturbations, leading to the condensation of cold gas out of hot CGM gas. In this thesis, we study in detail how the satellite galaxies can contribute to the cold phase of the CGM.

1.6 Motivation of the thesis

Galaxies are the building blocks of our universe. It is however a moot question as to how galaxies form and evolve. It is now apparent that the Circumgalactic medium (CGM) plays a crucial part in galaxy evolution by supplying fresh and recycled gaseous fuel for the formation of stars. The CGM also regulates the central galaxy's interactions with other nearby galaxies. For example, interactions between galaxies can cause ram-pressure stripping, gas removal, and eventual quenching of star formation.

However, physical processes at small scales vastly affect this large-scale gaseous reservoir. For example, one of the most important, and most theoretically uncertain small-scale physical processes in the CGM, is the physics of the relativistic charged cosmic ray (CR) particles that are produced during star formation. As mentioned earlier, these CRs can propel large-scale outflows. Therefore, it is crucial to form a comprehensive theoretical picture of both the small-scale ($\sim 1 - 10$ pc) and large-scale structure (~ 100 kpc) of the CGM together. In this thesis, we not only address small-scale physical processes like cooling processes, interaction of CR proton with CGM gas, but we also investigate large-scale interaction of satellite galaxies with the CGM of host galaxy.

A better understanding of the CGM promises to illuminate key unresolved issues in galaxy evolution, including satellite galaxy evolution (*Is the CGM dense enough to remove gas from satellite galaxies?*), star-formation in the galaxy (*How does the hot gas of the CGM cool down and the cool gas accrete onto the galaxy to provide star-forming fuel?*). Our motivation for this thesis is to understand the small-scale and large-scale structure and physical processes of the CGM. With the help of simulations, and analytical models along with using observational data, we address the following pressing scientific questions:

- How important is the process of photoionization by extra-galactic UV background

radiation in producing different ions in the CGM of the Milky Way and low-mass galaxies? How much small-scale temperature fluctuation is needed to produce observed column density of different ions in the CGM of the Milky Way?

- Recent simulations depict a picture that cosmic ray (CR) pressure can significantly dominate over the thermal pressure in the CGM (Butsky & Quinn, 2018; Dashyan & Dubois, 2020). CR content and transport mechanisms are poorly constrained at all scales and we use the interactions between CRs and the CGM to constrain CR content and CR transport physics. How much CR can there be in the CGM without violating multi-wavelength observational constraints?
- How can the physics of CR, such as acceleration, transport mechanisms be constrained using simulation and multi-wavelength observational data?
- The origin of the cold phase in the CGM is a debated question. Recent observations in massive halos ($10^{11-13}M_{\odot}$) show high column densities of MgII and HI (which are the tracers of the cold phase of CGM) even at the outer radii (Zhu et al., 2014; Chen et al., 2018; Zahedy et al., 2018). Recent observations by Lan & Mo (2018, 2019) also point towards the existence of cold phase out to large radii ($> 100\text{kpc}$). This leads to questions, such as, how do these massive halos whose virial temperature is much higher than that of the cold phase (Prochaska et al., 2013) form cold gas? Also, how does cold gas exist at such large radii? It is possible that ram-pressure stripping from satellite galaxies, and/or accretion from IGM can significantly contribute cold gas to the outer CGM. In this thesis, we address the question: to what degree and by what processes can satellites populate the cold phase of the CGM of their host galaxy?

1.7 Structure of the thesis

This thesis is arranged according to the chapters as follows :

- **Chapter 2:** In this chapter, we develop a photoionized precipitation model for Milky Way (MW)-type galaxies ($M_{\text{halo}} \sim 1-2 \times 10^{12} M_{\odot}$). In this model, feedback

maintains a constant ratio of cooling time to freefall time throughout the halo. Recent phenomenological studies and numerical simulations (Sharma et al., 2012; Voit et al., 2015) showed that this ratio has a threshold value of approximately 10 ($\frac{t_{\text{cool}}}{t_{\text{ff}}} \sim 10$), below which thermally unstable perturbations in the CGM can proceed into multi-phase condensation. In addition, our model considers photoionization (PI) by the Extra-galactic Ultra-Violet background radiation, along with collisional ionisation (CI) for the production of different ions. We also extend this model to low mass galaxies ($M_{\text{halo}} < 2 \times 10^{11} M_{\odot}$) (Roy et al., 2021a). By producing mock observations of ion column densities, we find that photoionization has a significant effect on the ion column densities of low mass galaxies, unlike in MW-type galaxies. Further, we show how observations of OVIII in low-mass galaxies can be an important probe of photoionization in the future X-ray missions like ARCUS, LEM, and Athena. Including log-normal temperature fluctuation in these models, we find that large fluctuations in temperature profile of the CGM are required to explain the observed oxygen column densities and their ratios for MW, and for star-forming galaxies in general. This implies a connection between star formation in the disk and the state of the CGM. Such temperature inhomogeneities in the CGM could be due to star-formation driven outflows.

- **Chapter 3:** In this chapter, we develop two-pressure-component (Thermal + CR) hydrostatic equilibrium models (IT model and PP model) of the CGM. Our model parameterises CR content as $\eta \equiv P_{\text{CR}}/P_{\text{th}}$, the ratio between CR and thermal pressure. We consider the interaction of CRs with CGM, which gives rise to γ -rays and radio synchrotron emission. Comparing our model prediction with radio background and Isotropic γ -ray background (IGRB) (Jana et al., 2020b), we find that the radio continuum constrains $\eta \lesssim 400$ for the PP model and does not constrain the IT model. However, the IGRB intensity allows $\eta \lesssim 3$ and $\eta \lesssim 230$ for IT and PP models, respectively.
- **Chapter 4:** In this chapter, we develop two-pressure-component (Thermal + CR) hydrostatic equilibrium models of the CGM. The inclusion of CRs in a CGM model of hydrostatic equilibrium necessarily decreases the thermal pressure. As a result, the OVIII abundance declines due to its strong temperature sensitivity. Comparing

our model prediction with X-ray OVIII absorption line data (Roy & Nath, 2022b), we find that the pressure due to CRs can be at most ten times the gas pressure in the CGM without violating the observational signatures, negating the picture by some recent simulations of CGM (Butsky & Quinn, 2018; Dashyan & Dubois, 2020; Hopkins et al., 2021) that CR pressure in the CGM can exceed the gas pressure by many orders of magnitude.

- **Chapter 5:** In this chapter, we check the observational constraints of γ -ray emission from the CGM of M31 in hydrodynamical simulation using a two-fluid (thermal + CR) hydrodynamical code (PLUTO, Mignone et al. (2007))(Roy & Nath, 2022a). we consider acceleration of CRs by star formation activity in the disc of the M31 galaxy, as well as *in-situ* acceleration in outflow shocks. We also consider CRs to be lifted to the CGM by star-formation driven outflow and CR diffusion. Then, considering hadronic interactions of CRs with the CGM, we produce mock γ -ray emission maps from the CGM of M31 with the angular resolution of the Fermi-LAT telescope to compare the detected γ -ray emission from the CGM of M31 (Karwin et al., 2019). Varying the parameters of CR physics in our simulation we find that the combination of advection and diffusion with a diffusion coefficient of $10^{29} \text{ cm}^2 \text{ sec}^{-1}$ can match these observations. This conclusion is based only on the equipartition of CR and thermal pressure in the initial condition, obviating the hypothesis that the origin of the γ -ray emission is dark matter annihilation (Karwin et al., 2019). It also strengthens the fact that one does not require a CR dominated CGM in order to explain the observations (like γ -ray emission from M31).
- **Chapter 6:** In this chapter, we investigate how satellite galaxies can contribute to the cold gas budget of the CGM. To this end, we simulate a suite of MW-type host galaxies with a varying distribution of satellite galaxies using the GIZMO code (Hopkins, 2015b). We find that satellite galaxies can supply significant amounts of cold gas to the CGM not only by direct stripping but equally also by induced cooling in the mixing layer of the stripped cold gas. We also find that massive satellites like the Large Magellanic Cloud (LMC) continue to feed cold gas to the CGM for several Gyr. However, low-mass satellites quickly lose all of their gas since, unlike massive satellites, the low-mass satellites produce small clouds which

have short cloud-crushing time and get easily destroyed ([Roy+2022 in prep](#)).

Chapter 2

Impact of photoionization and temperature fluctuation on the highly ionized oxygen ions in the CGM

Based on:

“Panaromic View of CGM in a photoionized Precipitation model”

Manami Roy, Biman B. Nath, G. M. Voit

MNRAS, Volume 507, Issue 3, November 2021, Pages 3849–3859,

[Roy et al. \(2021a\)](#)

We consider a model of the circumgalactic medium (CGM) in which feedback maintains a constant ratio of cooling time to freefall time throughout the halo, so that the entire CGM is marginally unstable to multiphase condensation. This ‘precipitation model’ is motivated by observations of multiphase gas in the cores of galaxy clusters and the halos of massive ellipticals. We derive from the model density and temperature profiles for the CGM around galaxies with masses similar to the Milky Way.

Key Results:

- After taking into consideration the geometrical position of our solar system in the Milky Way, we show that the CGM model is consistent with observed OVI, OVII and OVIII column densities only if temperature fluctuations with a log-normal dispersion $\sigma_{\ln T} \sim 0.6\text{--}1.0$ are included.
- We show that OVI column densities observed around star-forming galaxies require systematically greater values of $\sigma_{\ln T}$ than around passive galaxies, implying a connection between star formation in the disk and the state of the CGM.
- Photoionization by an extra-galactic UV background does not significantly change these CGM features for galaxies like the Milky Way but has much greater and significant effects on the CGM of lower-mass galaxies.

2.1 Introduction

The circumgalactic medium (CGM) is a reservoir of diffuse gas that fills the region surrounding the optically visible part of a galaxy, extending up to its virial radius (Tumlinson et al., 2017). It has been inferred that the CGM contains a substantial amount of baryons, thereby possibly mitigating the problem of missing baryons (Tumlinson et al., 2017). This gaseous halo may date back to the epoch of formation of the host galaxy, but its properties have likely evolved due to various feedback processes (White & Frenk, 1991). The CGM is believed to play a big role in the evolution of a galaxy by supplying gaseous fuel that triggers star formation (Kereš et al., 2005, 2009; Sancisi et al., 2008), by acting as the ‘waste dump’ for outflows of gas, and also by helping to recycle this gas (Tumlinson et al., 2017).

The density, temperature, metallicity structure, ionization state, and total mass of the CGM are yet to be determined with accuracy. These open questions are being addressed through both analytical and semi-analytical theoretical models, as well as numerical simulations. However, the relevant length scale for studying some of the processes such as cooling, metal mixing and transport, feedback that determine the physical state of the CGM is a few tens of parsecs and is difficult to achieve in a numerical simulation also containing the virial radius of a Milky Way-sized galaxy. Alternatively, theoretical modelling offers a simple, flexible, physically motivated and efficient approach to exploring those issues. In this regard, Faerman et al. (2017) considered an isothermal model with constant metallicity and two phases of gas (warm and hot) with a log-normal distribution of dispersion $\sigma_{\ln T}$ around each of those (constant) mean temperatures. They concluded that a metallicity of $0.5 Z_{\odot}$ and $\sigma_{\ln T}$ of 0.3 are needed to match the OVI column density observations. Qu & Bregman (2018) have recently built an analytical model with $0.3 Z_{\odot}$, based on balancing the star formation rate and cooling rate, that predicts CGM column densities for OVI, OVII, and OVIII. They compared the calculated column densities at $0.3 R_{\text{vir}}$ with observed values and could not find a suitable match. Then they modified the model to have a metallicity $0.55 Z_{\odot}$ and a temperature that is nearly twice the virial temperature in order to match their model values with observations. Faerman et al. (2019) have proposed a newer CGM model that is isentropic without any temperature

fluctuations and in which photoionization affects the ion abundances in such a way that the observed column densities of OVI, OVII and OVIII are reproduced.

The existence of lines of different ionization species in the absorption spectra of the CGM strongly points towards a multiphase (temperature and density) structure (Gupta et al., 2012; Fang et al., 2015). Various instabilities and radiative cooling cause cool gas to condense out of the hot CGM, leading to a multiphase structure in which there are large and non-radial variations in specific entropy. Approximate pressure equilibrium then ensures a multiphase structure in temperature and density.

Field (1965) showed that local thermal instability is possible in a diffuse medium in which the cooling curve has a negative slope and a region with higher density and lower temperature than the surrounding medium has formed. Local thermal instability occurs in the CGM when a region of slightly overdense gas starts to cool faster than its surroundings, because the cooling time

$$t_{\text{cool}} \equiv \frac{3}{2} \frac{nkT}{n_{\text{H}}^2 \Lambda_{\text{N}}(T)} , \quad (2.1)$$

where $n_{\text{H}}^2 \Lambda_{\text{N}}$ is the radiative cooling per unit volume, generally decreases with increasing density. Local pressure equilibrium then implies an isobaric cooling process, causing the density in the clump to increase and the cooling time to decrease further, until efficient radiation emission by atomic lines is not possible ($T \lesssim 10^4$). However, gravity can interfere with the growth of thermally unstable perturbations, if buoyancy causes the overdense gas to sink faster than it can shed its thermal energy (e.g., Binney et al., 2009). Recent phenomenological studies and numerical simulations (e.g., McCourt et al., 2012; Sharma et al., 2012; Voit et al., 2015) show that there is a threshold value for the ratio of radiative cooling time to free fall time, below which thermally unstable perturbations can proceed into multiphase condensation. Buoyancy strongly suppresses multiphase condensation in stratified media with a cooling time more than an order of magnitude greater than the local free-fall time, $t_{\text{ff}} \equiv (2r/g)^{1/2}$. But numerical simulations show that thermal instability can produce multiphase condensation (also known as precipitation) in stratified media with $t_{\text{cool}}/t_{\text{ff}} \lesssim 10$, as long as moderate disturbances can suppress the damping effects of buoyancy (e.g., Voit et al., 2017; Voit, 2018, 2021). Our physically motivated analytical model of the CGM is therefore a ‘precipitation model’ based on assuming $t_{\text{cool}}/t_{\text{ff}} \approx 10$ (e.g., Voit, 2019).

In this chapter, we extend the work of (Voit, 2019) by presenting the angular dependence of OVI, OVII and OVIII column densities on Galactic coordinates for a precipitation-limited CGM model and considering the effects of photoionization on a precipitation-limited CGM model. We study the CGM density and temperature profiles that result from the ‘precipitation model’ in light of the observed column densities of highly ionized oxygen lines through the CGM of the Milky Way (MW), as well as those of other galaxies. We calculate the column density for a general line of sight and show the variation with Galactic latitude and longitude. We consider both collisional ionization and photoionization for calculating the ionization fractions of OVI, OVII, and OVIII. We also extend our analysis to low mass galaxies to study the effect of photoionization on the precipitation-limited CGM model around these galaxies. In addition, we incorporate small scale temperature fluctuations at each radius and compare our model with the UV and X-ray observations of these absorption lines by *COS-Halos*, *Far-Ultraviolet Spectroscopic Explorer (FUSE)*, *XMM-Newton*, and the *Chandra* X-ray observatory. Lastly, we use our results to compare the column density observations of star forming and passive galaxies, and ask if star formation in the central galaxy affects the physical state of its CGM.

The structure of this chapter is as follows: Section 2.2 describes a precipitation-limited model for CGM density and temperature that accounts for photoionization and allows for small-scale temperature fluctuations with a log-normal distribution. Section 2.3 applies the model to calculate column densities of highly ionized oxygen through the Milky Way’s CGM over the full range of Galactic latitude and longitude. Section 2.4 compares those results with UV and X-ray absorption-line observations of the Milky Way’s CGM. Section 2.5 discusses what those results imply about CGM temperature fluctuations and extends the analysis to OVI observations of other galaxies like the Milky Way, showing star formation is correlated with greater CGM fluctuations. It also considers the effects of photoionization on precipitation-limited models of the CGM around lower-mass galaxies, showing that including photoionization dramatically increases their OVI column density as well as affects the column densities of other ions . Section 2.6 summarizes our results.

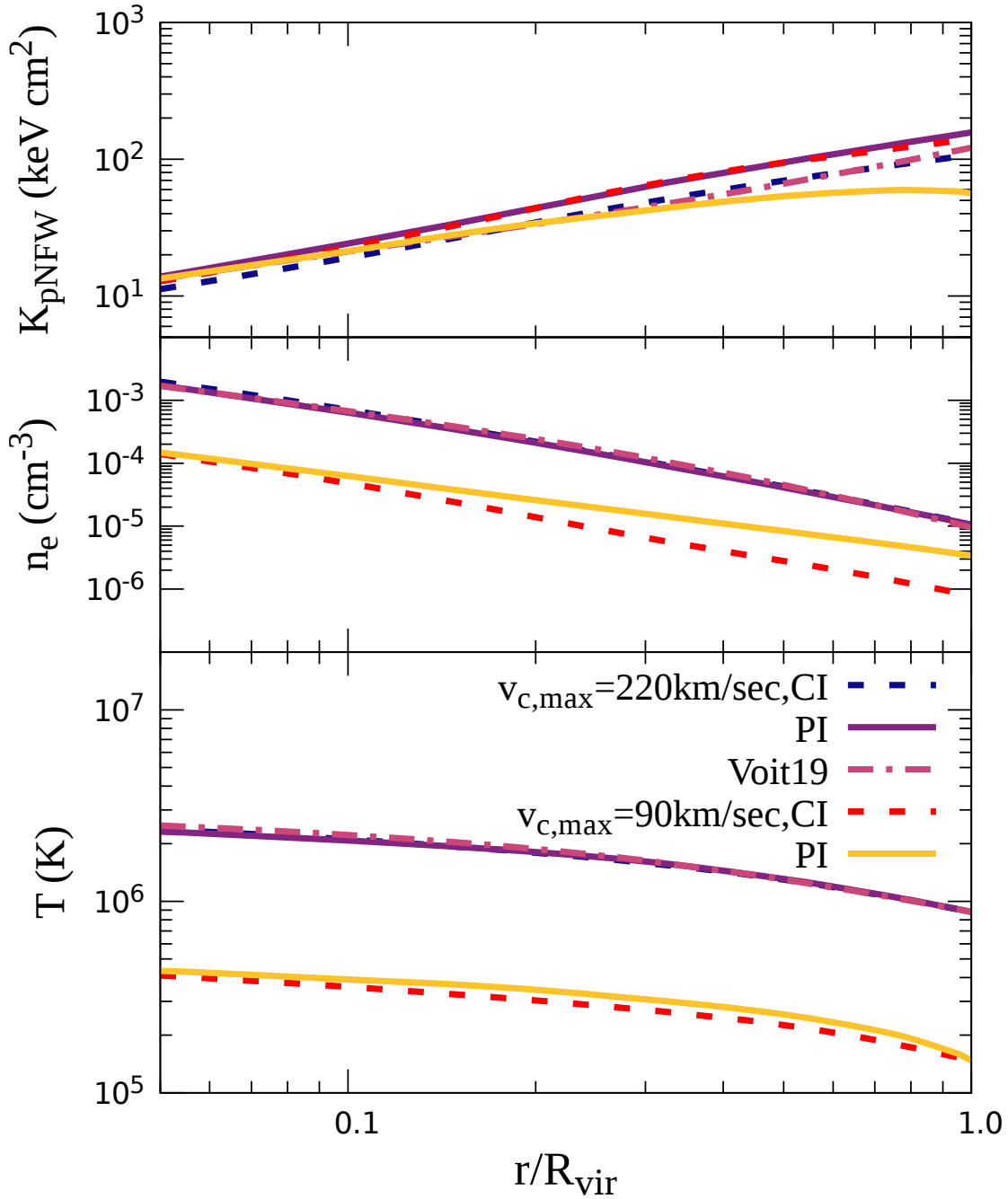


Figure 2.1: (a) Entropy profile K_{pNFW} , (b) the corresponding pNFW electron density profile, and (c) the pNFW temperature profile for both CI and PI precipitation-limited model in the case of two different halo masses ($v_{\text{c,max}} = 90, 220 \text{ km s}^{-1}$). The profiles of [Voit \(2019\)](#) are also shown for comparison.

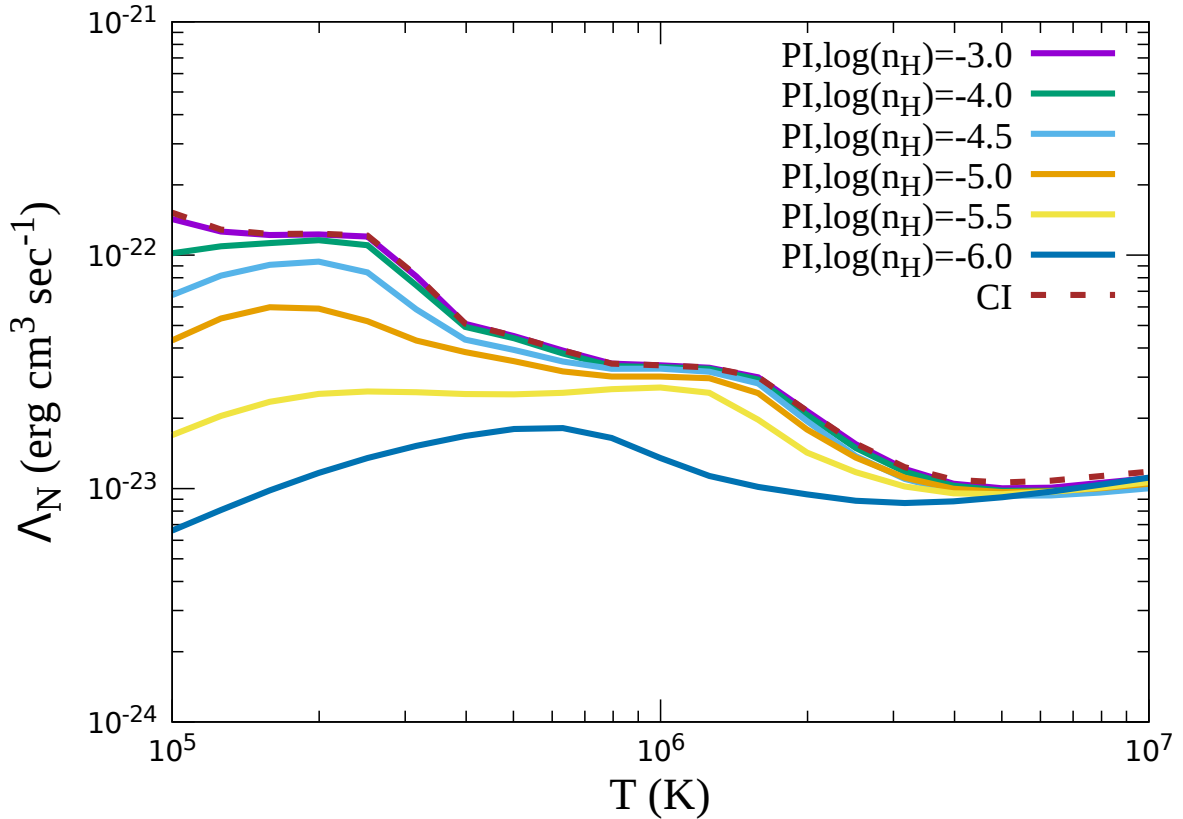


Figure 2.2: Radiative cooling function $\Lambda_N(T)$ for gas with metallicity $0.3 Z_\odot$ and solar abundance ratios (Grevesse et al., 2010) in pure collisional ionization (CI) equilibrium and with additional density-dependent photoionization by the Haardt & Madau (2012) extragalactic UV background at redshift $z=0$.

2.2 Modelling the CGM

We first present a precipitation-limited CGM model that assumes $t_{\text{cool}}/t_{\text{ff}} = 10$ in a galactic potential well. This model is briefly described above in Section 1.3.3. We use CLOUDY (Ferland et al., 2017) to determine $\Lambda_N(T)$ in Equation 1.17, assuming a metallicity of $0.3 Z_\odot$, motivated by CGM absorption-line observations (Prochaska et al., 2017a). Note that equation (1.17) differs from the corresponding equation in Voit (2019), where K_{pre} was approximated assuming that $T(r)/v_c^2(r)$ remains nearly constant and that $\Lambda_N(T) \approx \Lambda_N(2T_\phi)$, where $kT_\phi \equiv 0.5\mu m_p v_c^2$. Voit (2019) then used the resulting entropy profile to obtain a more accurate temperature profile through integration of the

hydrostatic equilibrium equation, given a boundary condition

$$kT(r_{200}) = 0.25 \mu m_p v_{c,\max}^2 \quad (2.2)$$

inspired by direct observations of galaxy clusters (e.g., [Ghirardini et al., 2019](#)).

[Esmerian et al. \(2020\)](#) have recently critiqued the approach of [Voit \(2019\)](#), because they find that $T(r) \propto v_c^2(r)$ is not a good approximation for the median CGM temperature near the virial radii of the simulated galaxies they analyse. Their precipitation limited CGM models instead rely on a custom temperature profile for each galaxy, derived from the simulations, to determine the entropy profile that gives $t_{\text{cool}}/t_{\text{ff}} = 10$ in hydrostatic equilibrium. However, CGM temperature profiles are not generally available for real galaxies, requiring some sort of assumption to be made about them.

Here we follow [Voit \(2019\)](#) by applying the boundary condition in equation (2.2) but iteratively solve the hydrostatic equilibrium equation (Equation 1.20) using a 4th-order Runge-Kutta scheme to determine the temperature profile at which $t_{\text{cool}}/t_{\text{ff}} = 10$, given our assumed entropy profile. Figure 2.1 shows that the CGM temperature and density profiles we obtain differ by only $\approx 8 - 10\%$ from the profiles of [Voit \(2019\)](#). Consequently, the approach of [Voit \(2019\)](#) is adequate for the assumed boundary condition, but is less accurate for the galaxies in [Esmerian et al. \(2020\)](#), which have $kT(r_{200}) \ll 0.25 \mu m_p v_{c,\max}^2$.

Equation (1.20) is the one that we iteratively solve to determine a temperature profile that gives $t_{\text{cool}}/t_{\text{ff}} = 10$ for $K_{\text{pNFW}} = K_{\text{pre}}(r) + K_{\text{base}}(r)$, given the boundary condition $kT(r_{200}) = 0.25 \mu m_p v_{c,\max}^2$. Notably, the solution of equation (1.20) for the temperature profile is independent of the entropy profile's normalisation. Variation of the boundary condition significantly changes the temperature profile only in the outer region, where $T \leq 10^6$ K. Hence, the choice of boundary condition has only minor effects on the column densities of OVII and OVIII but can have considerably larger effects on the OVI column density.

Our standard model for a galaxy like the Milky Way assumes $v_{c,\max} = 220 \text{ km s}^{-1}$, which corresponds to a halo mass of $2 \times 10^{12} M_{\odot}$. It assumes that collisional ionisation equilibrium (CI) in the CGM at the temperature $T(r)$ determines all the ionisation fractions. However, we also consider two modifications to the standard model, one in which photoionization (PI) by extragalactic background radiation alters the CGM ionisation

states and another in which log-normal fluctuations in gas temperature alter the CGM ionisation states.

2.2.1 Effect of photoionization

For photoionization, we use the Extra-galactic UltraViolet background radiation (UVB) model at redshift $z=0$ from [Haardt & Madau \(2012\)](#). This background radiation alters our CGM model because cooling functions with PI can differ from the pure CI case. [Figure \(2.2\)](#) shows how PI changes the CGM cooling function in gas of differing density. The differences from CI are small for $n_{\text{H}} \gtrsim 10^{-4.5} \text{ cm}^{-3}$ but can be large in gas of lower density, particularly for $T < 10^6 \text{ K}$. These results are consistent with the time independent cooling curves of CI and PI from previous studies ([Gnat, 2017](#); [Qu & Bregman, 2018](#)) in the presence of the same Extra-galactic UVB model.

Our PI models therefore use a 2-dimensional interpolation scheme (in density and temperature) to the Λ_{N} curves in [Figure \(2.2\)](#) to iteratively solve for n_e using [equation \(1.16\)](#). We apply the outer temperature boundary condition to calculate the density there. Then we advance inward using 4th-order Runge-Kutta integration for [equation \(1.20\)](#) as in the CI case. [Figure 2.1](#) shows the differences between the CI and PI model for our standard Milky Way-sized galaxy and also a low-mass galaxy ($v_{\text{c,max}} = 90 \text{ km s}^{-1}$, $M_{\text{vir}} = 10^{10} M_{\odot}$). As the curves show, the differences are small for massive galaxies, in which $n_{\text{H}} \gtrsim 10^{-4.5} \text{ cm}^{-3}$ at most radii, and are considerably larger for low-mass galaxies, in which $n_{\text{H}} \lesssim 10^{-4.5} \text{ cm}^{-3}$ at most radii.

2.2.2 Temperature Fluctuations

We allow for the possibility of an inhomogeneous CGM by considering a log-normal temperature distribution around the median $T(r)$ at each radius. The observed widths and centroid offsets of OVI absorption lines in the CGM suggest dynamical disturbances that may lead to temperature fluctuations. There can be several sources for these fluctuations. Outflows or high-entropy bubbles can lift low-entropy gas, and adiabatic cooling of these uplifted gas parcels as they maintain pressure balance gives rise to temperature and den-

sity fluctuations. Alternatively, turbulence-driven nonlinear oscillations of gravity waves in a gravitationally stratified medium can also lead temperature fluctuations as well as condensation resulting in multiphase gas.

[Faerman et al. \(2017\)](#) considered an isothermal, two-phase model, one phase with temperature $\sim 1.5 \times 10^6$ K and another (designed to reproduce OVI measurements) at $\sim 3 \times 10^5$ K. They assumed temperature fluctuations with a log-normal distribution around these two median temperatures. They found that $\sigma_{\ln T} \approx 0.3$ can account for the observed OVI column density in the context of their two-component CGM model.

[Voit \(2019\)](#) applied a similar fluctuation distribution around a single median gas temperature and showed that for the case of $M_{200} \geq 10^{11.5} M_{\odot}$, temperature fluctuations enhance the OVI column density by altering the ionization fraction at each radii. He also showed that each ion is generally present over a broader range in median temperature when temperature fluctuations are considered. Comparing with data of [Werk et al. \(2016\)](#), he concluded that broad OVI absorption lines in the CGM of galaxies like the Milky Way are consistent with $\sigma_{\ln T} \approx 0.7$.

In this chapter, we follow [Voit \(2019\)](#) and consider how different values of $\sigma_{\ln T}$ around a single median temperature affect the predicted absorption-line column densities of highly ionized oxygen and estimate $\sigma_{\ln T}$ through comparisons with observations.

2.3 Results for the Milky Way

Here we use the ingredients described so far to calculate the absorption-line column densities of highly-ionized oxygen along different lines of sight through the Milky Way's CGM that all start at the solar system. Some previous calculations have considered CGM column density as a function of impact parameter through the CGM and have chosen a particular value of impact parameter for comparisons with observations. [Qu & Bregman \(2018\)](#) have taken $0.03 R_{\text{vir}}$ (≈ 8 kpc) as their chosen impact parameter, while comparing with column density data for $b > 60^\circ$, because the column density at this impact parameter would be twice the value of column density seen at $b = 90^\circ$ (the distance of the Galactic centre from solar system being ≈ 8 kpc). However, while

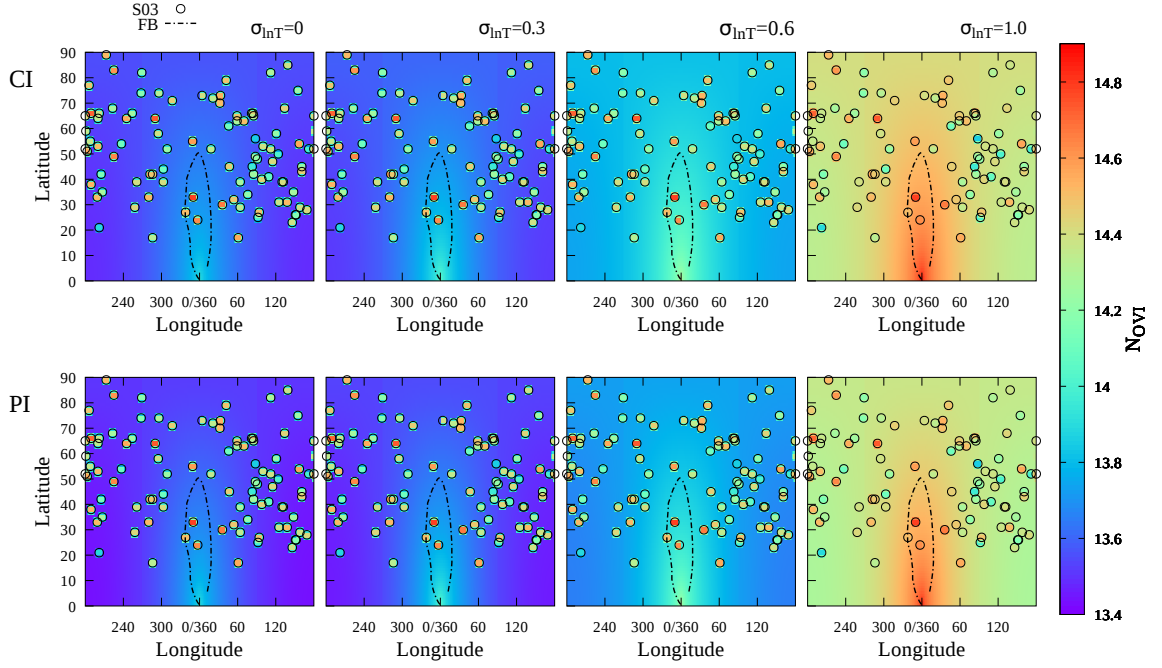


Figure 2.3: Dependence of OVI on galactic latitude (l) and longitude (b) in the case of pure collisional ionization (CI, top row) and additional photoionization (PI, bottom row) by the UV background, given different $\sigma_{\ln T}$. The observed value of N_{OVI} by [Savage et al. \(2003\)](#) from *Far-Ultraviolet Spectroscopic Explorer (FUSE)* spectra of 100 extragalactic objects and two distant halo stars have been shown by circles with appropriate colours. The observation along negative latitudes are shown as positive latitudes. We have excluded data points that give only upper-limits. The gamma-ray edge of the Fermi bubble is superposed on this plot, denoted by dashed lines.

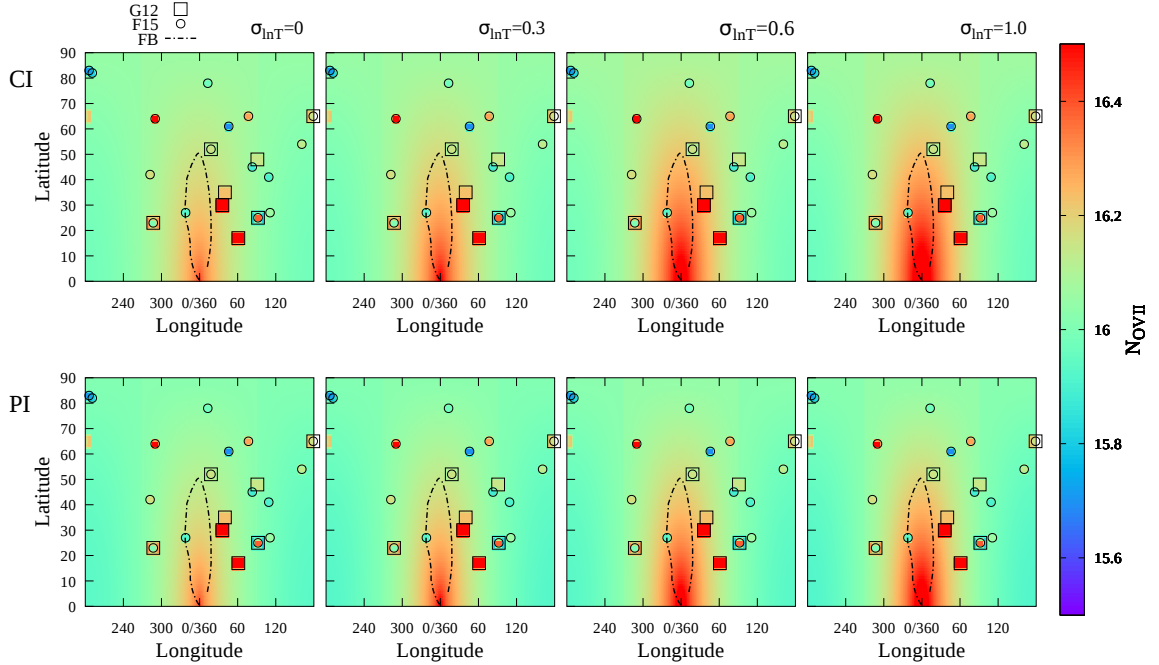


Figure 2.4: Dependence of OVII on galactic latitude (l) and longitude (b) in the case of pure collisional ionization (CI, top row) and additional photoionization (PI, bottom row) by the UV background, given different $\sigma_{\ln T}$. The observed values of N_{OVII} by Gupta et al. (2012) and Fang et al. 2015 have been shown by squares and circles respectively with appropriate colours. The observation along negative latitudes are shown as positive latitudes. The observational uncertainties in the observations of Gupta et al. (2012) are typically a factor of 1.5 – 3 whereas same is larger (factor of 1.6 to even 500) in the case of Fang et al. (2015) as their saturation corrections are more uncertain. We plotted 16 lines of sight out of 33 from Fang et al. (2015) as their observed OVII column density distribution peaks around ($\log \text{OVII}$) 16.0, with half the data points (16 out of 33) in the range of 15.5 – 16.5 (the right panel of fig 12 from their paper). The gamma-ray edge of the Fermi bubble is superposed on this plot, denoted by dashed lines.

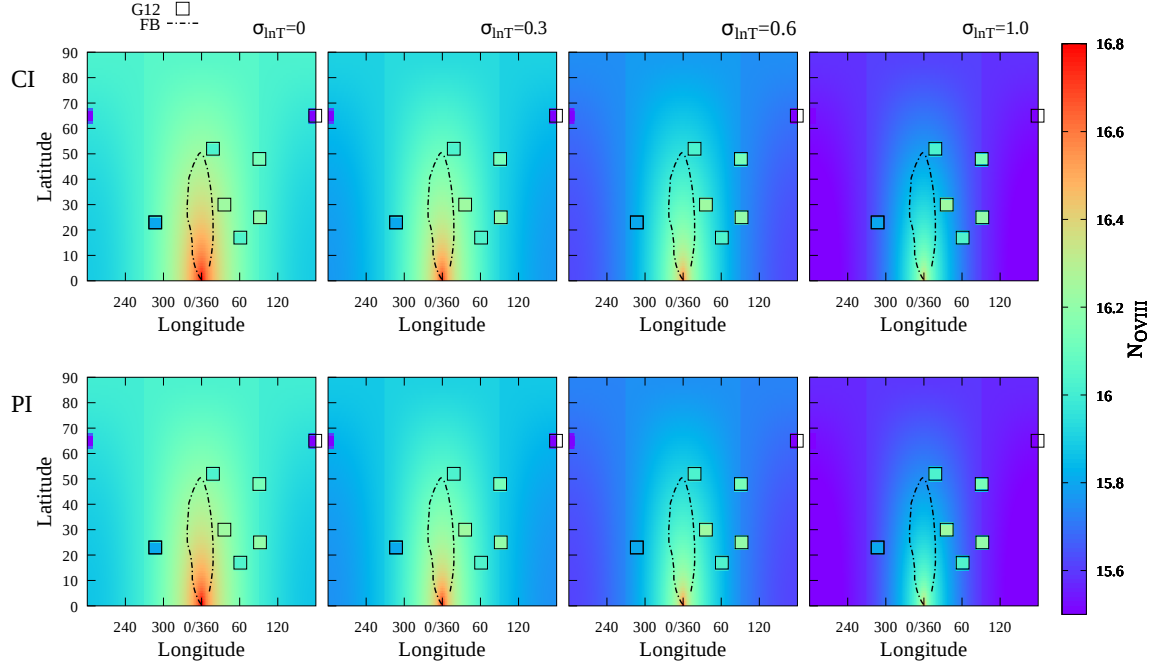


Figure 2.5: Dependence of O VIII on galactic latitude (l) and longitude (b) in the case of pure collisional ionization (CI, top row) and additional photoionization (PI, bottom row) by the UV background, given different $\sigma_{\ln T}$. The derived values of $N_{\text{O VIII}}$ (assuming no saturation) from observed equivalent widths by Gupta et al. (2012) have been shown by squares with appropriate colours. The observation along negative latitudes are shown as positive latitudes. The gamma-ray edge of the Fermi bubble is superposed on this plot, denoted by dashed lines.

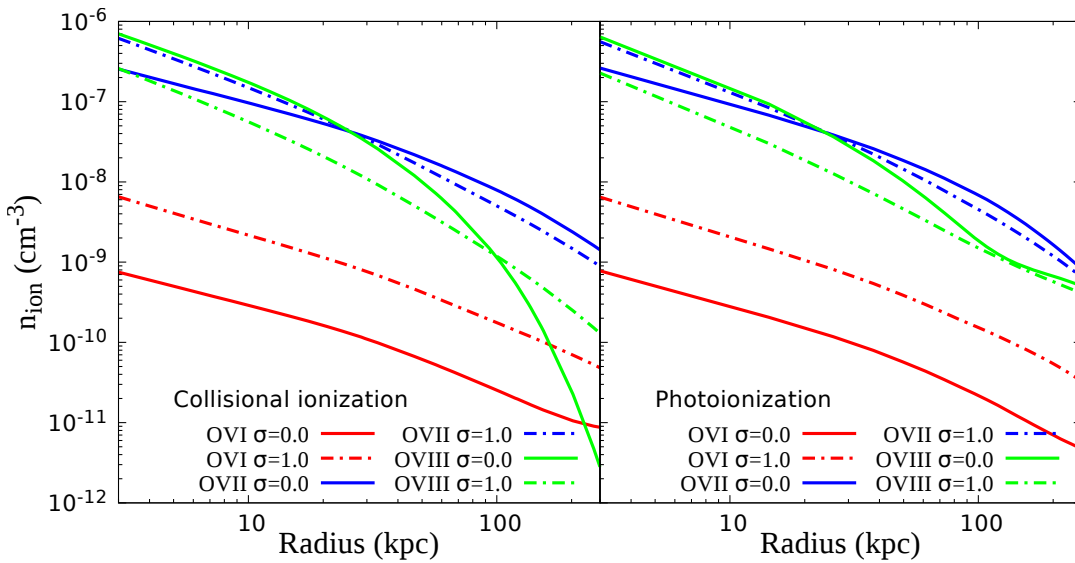


Figure 2.6: Radial density profiles of OVI, OVII, and OVIII for $M_{\text{vir}} = 2 \times 10^{12} M_{\odot}$.

comparing the predicted column density at this impact parameter, they used the median value of the whole data set, which includes data from low Galactic latitudes. We note that [Faerman et al. \(2017\)](#) and [Faerman et al. \(2019\)](#) have shown the variation of column density with respect to the angle from Galactic Centre for an observer at solar position. However, for comparison with observations they used the value of column density which is half of its total value up to r_{CGM} .

[Miller & Bregman \(2013\)](#) have analyzed a sample of 29 sightlines with absorption line observations of OVII and OVIII. They considered two isothermal models, a spherical model and a flattened model, and attempted to fit the observed column densities by transforming the galactocentric density profile to a coordinate system centered on the Sun.

Since the observations with which we wish to compare our results involve different lines of sight through the CGM as seen from our location, we also calculate predicted column densities from the Sun's location as a function of Galactic latitude (l) and longitude (b). The predicted OVI, OVII, and OVIII column densities are presented in figures (2.3), (2.4) and (2.5) respectively. In each figure, the upper rows show the case of only collisional ionization (CI) and the lower rows include photoionization (PI) by the extragalactic UVB. The leftmost columns of both figures show results when temperature

fluctuations are not included ($\sigma_{\ln T} = 0$) and the columns to the right show the effects of increasing $\sigma_{\ln T}$ to 0.3, 0.6, and 1.0.

The figures show substantial variations in the column densities of OVI, OVII, and OVIII with both longitude l and latitude b . Temperature fluctuations also have significant effects. For example, the range of OVI column density predicted by CI models changes from $13.5 \leq \log N_{\text{OVI}} \leq 13.8$ for $\sigma_{\ln T} = 0$ to $14.4 \leq \log N_{\text{OVI}} \leq 14.8$ for $\sigma_{\ln T} = 1.0$. OVII column density ranges between $15.9 \leq \log N_{\text{OVII}} \leq 16.4$ for $\sigma_{\ln T} = 0$, whereas for $\sigma_{\ln T} = 1.0$, the range changes to $15.9 \leq \log N_{\text{OVII}} \leq 16.9$. For OVIII column density, the corresponding ranges change from $16.0 \leq \log N_{\text{OVIII}} \leq 16.8$ for $\sigma_{\ln T} = 0$ to $15.5 \leq \log N_{\text{OVIII}} \leq 16.8$ for $\sigma_{\ln T} = 1.0$. In other words, temperature fluctuations *decrease* the total OVIII ion density and *increase* the total OVI and OVII column densities, with most of the OVIII change coming from the inner CGM. Figure (2.6) shows this effect by plotting the density profiles of different ions for models with $\sigma_{\ln T} = 0$ and 1.0.

Figure (2.6) also shows differences between the purely collisional (CI) and photoionization (PI) cases. Around a galaxy like the Milky Way, the main effect of photoionization is on the OVIII ion, especially at outer radii in the case with no temperature fluctuations. (Section 2.5.2 shows that UVB photoionization can have considerably greater effects on precipitation-limited CGM models for low-mass galaxies.) The effects on OVIII arise because the ionization potential of OVII is much greater than that of OVI. Therefore, collisionally ionized gas in the temperature range we are concerned with here (a few times 10^5 K to $\sim 2 \times 10^6$ K), has a relatively small OVIII number density (n_{OVIII}) at large radii. But the inclusion of UVB photons (which can have energies of a few hundred eV) can increase the OVIII number density. This effect becomes particularly significant when the density is low, which happens at the outer radii. It was also pointed out by [Faerman et al. \(2019\)](#) in their isentropic model. However, here we show that the effect of temperature fluctuations can compensate for the effects of photoionization. The resulting increase in OVIII number density in the case of PI (green solid line, without temperature fluctuation) is seen in Figure 2.6, when the corresponding two panels are compared. But when temperature fluctuation is included (green dotted lines), the radial profiles of OVIII number density for PI and CI cases are similar at large radii.

Going back to Figures (2.4) and (2.5), we note that column densities can be rather

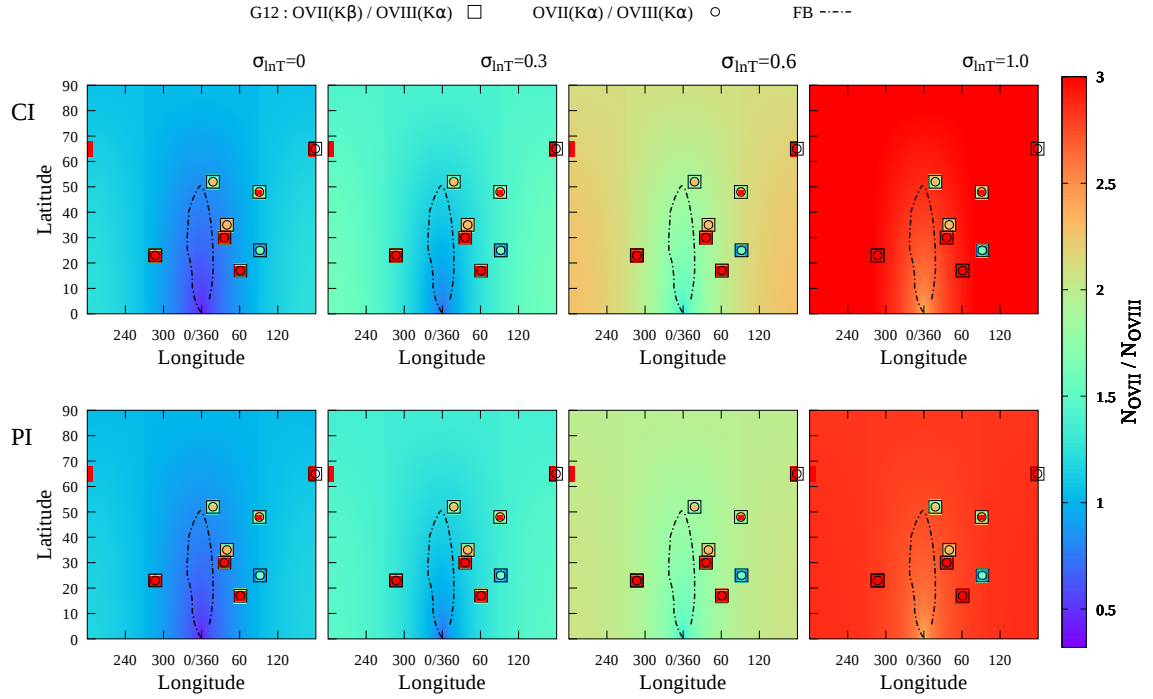


Figure 2.7: Dependence of the column-density ratio $N_{\text{OVII}}/N_{\text{OVIII}}$ on galactic latitude (l) and longitude (b) in the case of pure collisional ionization (CI, top row) and additional photoionization (PI, bottom row) by the UV background, given different $\sigma_{\ln T}$. The derived values of ratio between N_{OVII} and N_{OVIII} from observation of [Gupta et al. \(2012\)](#) have been shown by squares and circles with appropriate colours. The observation along negative latitudes are shown as positive latitudes. The gamma-ray edge of the Fermi bubble is superposed on this plot, denoted by dashed lines.

large for $l \sim 0, b \leq 50^\circ$. However, sight lines passing close to the Galactic centre are not well suited for comparison with observations, owing to the Fermi bubbles in this range of latitudes and longitudes. Dot-dashed lines outline the gamma-ray edge of the Fermi bubbles, following [Su et al. \(2010\)](#), in order to exclude these sightlines from our present consideration.

Figure (2.7) shows the predicted ratio of OVII to OVIII column density as a function of Galactic latitude and longitude for both CI (upper panels) and PI (lower panels) and different values of $\sigma_{\ln T}$. Temperature fluctuations significantly decrease N_{OVIII} compared to N_{OVII} , thereby increasing the value of the ratio, as can be seen by looking from left to right in figure (2.7). The predicted $N_{\text{OVII}}/N_{\text{OVIII}}$ ratios span a large range, from ~ 0.5 for $\sigma_{\ln T} = 0$ (along sightlines toward the Galactic centre) to ~ 3.0 for $\sigma_{\ln T} = 1.0$ (along sightlines away from the Galactic centre). Comparing the CI and PI cases for a given value of $\sigma_{\ln T}$, shows that the $N_{\text{OVII}}/N_{\text{OVIII}}$ ratio slightly decreases from the CI to PI case, because of the PI increase in OVIII density explained above.

2.4 Comparison with UV and X-Ray observations

This section compares our model predictions for the Milky Way's CGM with UV and X-ray observations. [Savage et al. \(2003\)](#) used the observation of *FUSE* far-UV spectra of 100 extragalactic objects and two halo stars to measure the OVI column density along different lines of sight through the Milky Way. We compare our model predicted values with these observations and superpose them on our OVI map of the Milky Way (Figure 2.3). Note that we have not plotted data points that give only upper limits and the observation along negative latitudes are shown as positive latitudes. The observed values of $\log(N_{\text{OVI}})$ are mostly large (14.8 – 14.9) in the vicinity of Fermi bubble region whereas at larger longitudes their values are mostly smaller (14.4 – 14.6). This trend along with the observational range of $\log(N_{\text{OVI}})$ agrees with the prediction of our model for $\sigma_{\ln T} = 1.0$.

The emission-line intensities of OVII and OVIII are similar to the predictions of [Voit \(2019\)](#), which presents a comparison with the data on X-ray emission. So, we here focus only on absorption data in order to compare with our model. Table 2.1 summarises the

reported measurements of OVII and OVIII lines in X-ray absorption spectra. However, some explanations are in order regarding the values in the table.

[Gupta et al. \(2012\)](#) have reported measurements of N_{OVII} and N_{OVIII} with *Chandra* along eight sight lines. Their observed values of $\log(N_{\text{OVII}})$ range from 15.82 to 16.7 with a weighted sample mean of 16.19. [Miller & Bregman \(2013\)](#) have studied OVII lines toward 26 AGNs along with one detection of an OVIII line with a ratio $N_{\text{OVII}}/N_{\text{OVIII}}=0.7 \pm 0.2$. [Fang et al. \(2015\)](#) have also measured OVII column density from data on 43 AGNs, including the sample of [Miller & Bregman \(2013\)](#), observed with *XMM-Newton*. They found that most of their OVII lines had column densities centered around 10^{16} cm^{-2} with a wide range, $10^{15.5} - 10^{16.5} \text{ cm}^{-2}$. The observed values of N_{OVII} by [Gupta et al. \(2012\)](#) and [Fang et al. \(2015\)](#) have been shown in Figure 2.4 by circles and squares respectively with appropriate colours. We plotted 16 lines of sight out of 33 from [Fang et al. \(2015\)](#) as their observed OVII column density distribution peaks around $(\log \text{OVII})$ 16.0, with half the data points (16 out of 33) in the range of 15.5 – 16.5 (the right panel of fig 12 from their paper). The derived values of N_{OVIII} (assuming no saturation) from observed equivalent widths by [Gupta et al. \(2012\)](#) have been shown in Figure 2.5 by squares with appropriate colours. Note that the observations along negative latitudes are marked as positive latitudes.

However, [Faerman et al. \(2017\)](#) increased [Gupta et al. \(2012\)](#)'s observed values of OVII and OVIII equivalent widths (EW) by 30% in order to correct for systematic error and re-calculated the median as 16.34(16.25–16.46). For 10 objects in [Fang et al. \(2015\)](#)'s sample, they could derive only upper limits and calculated the range of the OVII column density by ignoring those sight lines. [Faerman et al. \(2017\)](#) took into account the upper limits for the non-detections and added those upper limits to the group of detected absorption lines. This addition reduced the median column density of the [Fang et al. \(2015\)](#) sample to 16.15(16 – 16.3). The third and fourth columns of table 2.1 show both the original measurements and the revised values by [Faerman et al. \(2017\)](#) of N_{OVII} and of N_{OVIII} respectively.

[Fang et al. \(2015\)](#) did not report any OVIII observations, and [Gupta et al. \(2012\)](#) gave only equivalent widths for OVIII absorption. [Faerman et al. \(2017\)](#) calculated the corresponding column densities (and the median value thereof) assuming that the OVII

and OVIII lines arise in similar physical conditions. These values are shown in the 4th column of table 2.1. Faerman et al. (2017) then derived a median value of 4.0 for the ratios of column densities along individual sight lines from Gupta et al. (2012). They used this value of the ratio to estimate the OVIII column densities in Fang et al. (2015) sample, which are shown in the second row of the 4th column.

In the second row of 5th column, we show the median ratio estimated by Faerman et al. (2017). Note that this is the median of ratios of corrected column densities along each of the eight sight lines from Gupta et al. (2012). Also note that the ratio of the medians (2.1) is different from the median of ratios (4.0). The ranges of values shown for Faerman et al. (2017) refer to a $1\text{-}\sigma$ uncertainty around the median, although it is the standard deviation around the mean which they applied to the median.

We can, however, obtain the ratio of column densities of OVII and OVIII from the observations by Gupta et al. (2012) in a slightly different manner, which might be physically more meaningful. Along 6 out of 8 lines of sight in Gupta et al. (2012), the EW of OVII K_β and OVIII K_α are essentially the same, given the observational uncertainties. The lines also have similar wavelengths. Therefore, the optical depths of those lines are similar, which implies that they experience approximately the same amount of saturation. If both the optical depths and the wavelengths are similar, then the ratio of column densities is approximately equal to the inverse of the ratio of oscillator strengths, *i.e.* $N_{\text{OVII}}/N_{\text{OVIII}} \approx 2.8$. However, one should consider the large uncertainties in the EW ratios. For the 6 lines of sight with detected OVII K_β , we get a weighted mean of the ratio of EWs of 0.7 ± 0.2 . Dividing this mean EW ratio by the ratio of oscillator strengths gives $N_{\text{OVII}}/N_{\text{OVIII}} \approx 2.0 \pm 0.6$. The ratios along each sightline calculated from OVII K_β and OVIII K_α lines are shown in Figure 2.7 by squares with appropriate colours. If we consider the OVII K_β and OVIII K_α instead, we find the weighted mean of EW ratios to be 2.3 ± 0.2 which gives $N_{\text{OVII}}/N_{\text{OVIII}} \approx 1.1 \pm 0.1$. This is, however, only a lower limit because the actual ratio is greater, if the lines are saturated. A mean saturation correction can be derived from the OVII EW ratios $\text{EW}(K_\beta)/\text{EW}(K_\alpha)$ measured by Gupta et al. (2012), which have a weighted mean of 0.43 ± 0.06 . Comparing with the expected ratio of 0.156 for the optically thin case, this implies a saturation correction factor of 2.7 ± 0.4 . If we apply this correction to the ratio of column densities we get $N_{\text{OVII}}/N_{\text{OVIII}} \approx 3.0 \pm 0.5$.

Table 2.1: Summary of the observations

Data set		$\log(N_{\text{OVII}})$	$\log(N_{\text{OVIII}})$	$N_{\text{OVII}}/N_{\text{OVIII}}$
Gupta et al. (2012)	original	16.19(15.82-16.5)	–	2.6(2.2-3.0)
	Faerman et al. (2017)	16.34(16.25-16.46)	16.0(15.88-16.11)	4.0(2.8-5.62)
Fang et al. (2015)	original	16.0(15.5-16.5) *	–	0.7(0.5-0.9) **
	Faerman et al. (2017)	16.15(16.0-16.3)	15.5(15.3-15.7)	–

*Reported previously by Miller & Bregman (2013) for smaller sample size.

**Reported ratio by Miller & Bregman (2013) for one OVIII observation.

The ratios along each sightlines calculated from OVII K_α and OVIII K_α lines are shown in Figure 2.7 by circles with appropriate colours. Please note that the observation along negative latitudes are shown as positive latitudes. The ratio of these two estimates can also be averaged to give the $N_{\text{OVII}}/N_{\text{OVIII}} \approx 2.6 \pm 0.4$. This value is quoted in the 1st row of the 5th column of table 2.1.

Comparing our models with the observational data from table 2.1 shows that the models with greater temperature fluctuations are in better agreement with the observations. It can be seen that $\log(N_{\text{OVIII}})$ in our model ranges from 15.5 to 15.7 for $\sigma_{\ln T} = 1.0$, and $\log(N_{\text{OVII}})$, ranges between 16.0 to 16.2 for the same value of $\sigma_{\ln T} = 1.0$, for both CI and PI models, excluding the Fermi Bubble region. It is clear from Figures 2.4 and 2.5 that there is not much difference in the predicted column densities of OVII and OVIII between CI and PI. The predicted ratio of N_{OVII} to N_{OVIII} for $\sigma_{\ln T} = 1.0$ is between 2.8 and 3.0 and is therefore within the 1σ uncertainty range around the median found by Faerman et al. (2017), for both CI and PI. However, the model predictions for $\sigma_{\ln T} = 0.6$ (1.7–2.5) are a better match to the ratio of the median column densities of OVII and OVIII. Although, if we consider the ratio of column densities we have re-estimated in this chapter from the observations by Gupta et al. (2012), we find that $\sigma_{\ln T} = 0.6$ is consistent with the observations of OVII K_β and OVIII K_α lines, whereas the ratio is more consistent with our model with $\sigma_{\ln T} = 1.0$ for observations of OVII K_α and OVIII K_α lines. The weighted mean of these two ratios 2.6 ± 0.4 is consistent with the range of $\sigma_{\ln T} \approx 0.6 - 1.0$. Therefore, the observed ratios favor values of $\sigma_{\ln T} \approx 0.6 - 1.0$ in the context of our precipitation limited CGM model.

One should also consider the individual values of N_{OVII} and N_{OVIII} . If we compare our model values of N_{OVIII} with Gupta et al. (2012) observations, then $\sigma_{\ln T} = 0.6$ can provide a good match. The observed values of N_{OVIII} do not show the angular dependence predicted by the model. However, it is worth noting that one data point at high latitude and longitude ($l \sim 180$ $b \sim 65$) shows a lower $\log(N_{\text{OVIII}})$ than other 6 data points, and is in general agreement with the model predictions. But more observational data points, preferably with higher precision are required in order to draw any definite conclusion about the angular dependence of N_{OVIII} . The predicted range of $\log(N_{\text{OVIII}}) \approx 15.5\text{--}15.7$ for $\sigma_{\ln T} = 1.0$ matches the range obtained by Faerman et al. (2017) for Fang et al. (2015) using the ratio of column densities from Gupta et al. (2012). For $\log(N_{\text{OVII}})$, the predicted column density for all values of $\sigma_{\ln T}$ (excluding the Fermi Bubble region) is in the range $\approx 16.0\text{--}16.3$, which falls within the originally reported values of Gupta et al. (2012) and original as well as re-estimated values of Fang et al. (2015) by Faerman et al. (2017). Approximately 50 percent of the data points (includes Gupta et al. (2012) and Fang et al. (2015) both) are in good agreement with the angular variation predicted by our model. However, in Figure 2.4, we find deviations of the observed values from the predicted ones mainly near the Fermi Bubble and some at large longitude directions as well. Note that, the uncertainties in the observations of N_{OVII} are large; factor of $1.5 - 3$ in case of Gupta et al. (2012) and even larger (factor of $1.6 - 500$) in the case of Fang et al. (2015). However it is difficult to rule out any model solely on the basis of N_{OVII} because there is no significant change in N_{OVII} with $\sigma_{\ln T}$.

We can also compare the N_{OVII} data for different values of l and b from Fang et al. (2015) with the computed values for $\sigma_{\ln T} = 1.0$ from our model. We calculate the Pearson correlation coefficient between the model and the observed values and find the correlation to be $r \approx 0.2$. As mentioned earlier, the sight lines around $l \sim 0.0$ may not be suitable for comparison because of contamination from the Fermi Bubble, whose boundary is marked in Figure (2.4) and Figure (2.5). Performing a t-test for the data (for $N = 33$ data points) yields a value of

$$t = r \times \sqrt{\left(\frac{N - 2}{1 - r^2}\right)} \approx 1.08. \quad (2.3)$$

This t-statistic is distributed in the null case of no correlation like a Student's t distribution with $\nu = N - 2 = 31$ degrees of freedom, whose two-sided significance level is given

by $1 - A(t|\nu) = 0.28$. However, we note that the highest column density observations are mainly concentrated in three zones of l, b . Region 1 ($l \leq 30, l \geq 350, b \leq 50$) coincides with the direction of the Fermi Bubble. Region 2 ($260 \leq l \leq 300, b \leq 60$) points towards the high-temperature zone of the Local Bubble. Therefore observations of sight lines in these two regions are likely to be contaminated by foreground rather than CGM. However, column densities are also high in Region 3 ($30 \leq l \leq 90, b \leq 60$) and sight lines in these regions would provide the best diagnostic for CGM. If these sight lines are removed, and if we further focus on the sight lines that produce the column density $\leq 10^{16} \text{ cm}^{-2}$, then the correlation coefficient increases to ~ 0.3 and the probability for null case decreases to ~ 0.26 . But for both the above cases, the significance for rejecting null hypothesis is low because we have only a small number of observations to compare with. However if we compare larger N_{OVI} data set for different values of l and b from [Savage et al. \(2003\)](#) with the computed values for $\sigma_{\ln T} = 1.0$ from our model, we get correlation coefficient to be 0.35, t value to be 3.54 and probability for null case decreases to $\sim 10^{-4}$. Hence, larger observational data set improves in the significance for rejecting null hypothesis.

In summary, the range of $\sigma_{\ln T}$ that best agrees with all the observational quantities is ≈ 0.6 – 1.0 . The uncertainties in the data, However, are large, which makes it difficult to find a point-by-point match with the model. We note that the comparison shown by [Miller & Bregman \(2013\)](#) for an off-centered model of the Milky Way CGM does imply an underlying angular variation in the column density data. More data with less uncertainties will definitely help to constrain the precipitation model in the future.

2.5 Discussion

2.5.1 CGM in galaxies like the Milky Way

Encouraged by the apparent agreement between our precipitation models with $\sigma_{\ln T} \approx 0.6$ – 1.0 and OVII and OVIII column density observations for the Milky Way CGM, we now look towards extragalactic observations. Figure 2.8 compares the calculated column density of OVI from our model with OVI observations of a set of star-forming and passive

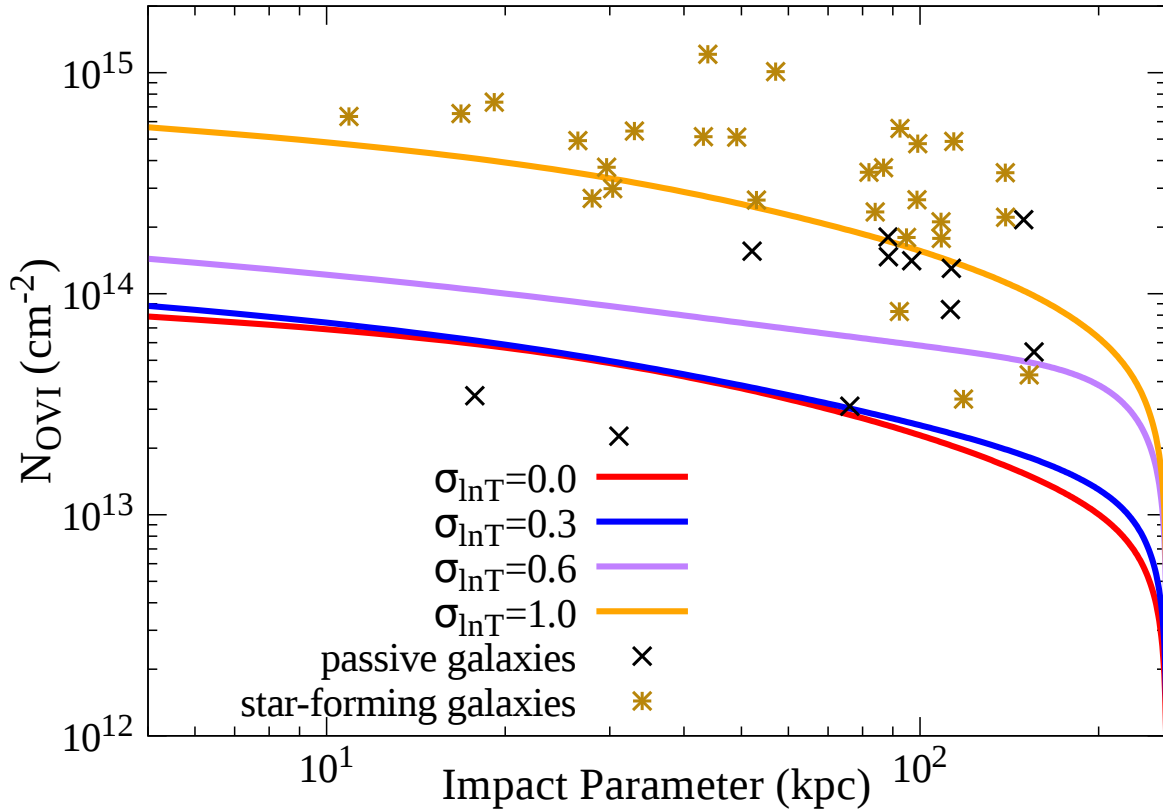


Figure 2.8: Variation of OVI column density with sigma and comparison with observation of star forming and passive galaxies from [Tumlinson et al. 2011](#).

galaxies by ([Tumlinson et al., 2011](#)). It can be seen that large-amplitude temperature fluctuations are required to fit the star-forming galaxies with the model. In the figure, log-normal fluctuations with $\sigma_{\ln T} \approx 1.0$ are needed to obtain the OVI column densities observed around star-forming galaxies, while smaller values of $\sigma_{\ln T}$ suffice for passive ones. This finding implies that star formation is somehow related to temperature fluctuations in the CGM.

We note that the values of $\sigma_{\ln T}$ inferred here from OVI absorption are somewhat larger than reported in [Voit \(2019\)](#). This finding may arise from the following causes. Firstly, the default CGM metallicity in [Voit \(2019\)](#) was solar, in contrast to $0.3 Z_{\odot}$ considered here, and N_{OVI} in precipitation-limited CGM models approximately scales as $(Z/Z_{\odot})^{0.3}$ (see Eq. 17 of [Voit 2019](#)). Secondly, uncertainty in the virial radius and mass of MW-type halos along with that in the position of the accretion shock leading to uncertainty in the CGM outer radius (r_{vir} to $1.3 r_{\text{vir}}$) can introduce differences of $\sim 10\%$ in

predicted column densities. Thirdly, differences in the rates assumed for different atomic processes can lead to different predictions for the ionization fractions. For example, the collisional ionization model of [Sutherland & Dopita \(1993a\)](#), used by [Voit \(2019\)](#), has different dielectronic recombination rate coefficients as well as solar abundances from the ones used here by CLOUDY ([Ferland et al., 2017](#)) leading to a substantial differences in the OVI ionization fraction (e.g., 6×10^{-3} using CIE model of [Sutherland & Dopita \(1993a\)](#) whereas 4.6×10^{-3} using CLOUDY at 10^6 K). One must therefore be cautious about these uncertainties while drawing conclusions on the physical state of the CGM that depend on those values.

2.5.2 CGM in low mass galaxies

The results we have presented so far indicate that photoionization does not play a significant role in determining the column densities of highly-ionized oxygen in the CGM of galaxies like the Milky Way. However, precipitation-limited CGM models of lower mass galaxies have considerably lower densities, in which photoionization becomes more important. Here we present CGM models of low-mass halos ($M_{\text{halo}} < 2 \times 10^{11} M_{\odot}$) to illustrate how photoionization affects our CGM models for those galaxies. The entropy, density and temperature profiles for low mass galaxies are shown in [figure 2.1](#).

The left panel of [figure 2.9](#) shows the variation of column densities of OVI with impact parameter in precipitation-limited models of low-mass halos with and without photoionization. The curves in this figure show that N_{OVI} greatly increases from its CI value when photoionization is included. The plot in the right panel shows that with the inclusion of photoionization, N_{OVI} tends to agree with the simulated values in [Oppenheimer et al. \(2016a\)](#) of OVI column density, while the CI value does not. However, the PI value (integrated out to R_{vir}) is not quite as large as the value of N_{OVI} observed by [Johnson et al. \(2017\)](#) in dwarf galaxies. However, if we extend the OVI column-density integration to $1.2R_{\text{vir}}$ due to the uncertainty in the CGM extent, the result then agrees with the observations of [Johnson et al. \(2017\)](#).

The left panel of [figure 2.10](#) shows that N_{OVII} also increases with the inclusion of photoionization. However, the largest effect of photoionization is on N_{OVIII} , which does

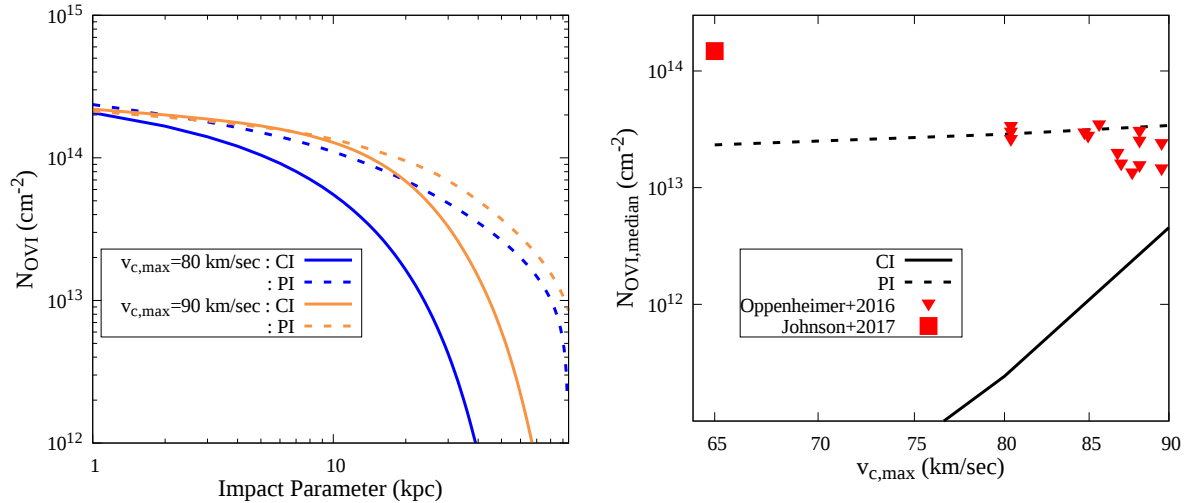


Figure 2.9: Left panel shows the variation of OVI column density in case of CI and PI in the low mass galaxies. The plot in the right panel compares variation of $N_{\text{OVI,median}}$ in both CI and PI with the simulated and observed values of N_{OVI} of [Oppenheimer et al. \(2016a\)](#) and [Johnson et al. \(2017\)](#).

not produce any measurable absorption in the CI case because the CI temperature peak for OVIII ion is considerably different from the virial temperature of a low-mass galaxy. Photoionization is required to produce significant amounts of OVIII. Thus, for low mass galaxies, N_{OVIII} can be a possible diagnostic for the effects of photoionization.

At the same time we find that CIV density decreases when photoionization is included (in the right panel of Figure 2.10), and it is not possible for this model to match COS-Halos observations of large CIV column densities in dwarf galaxies ([Bordoloi et al., 2014c](#)), who found $N_{\text{CIV}} \sim 10^{14} \text{ cm}^{-2}$ in such galaxies. However, there are only upper limits on NV for external galaxies. There can be several reasons for the mismatch between observed and predicted CIV column densities. Gas in low mass galaxies may deviate significantly from hydrostatic equilibrium ([Lochhaas et al., 2020b](#)). Also, the gas particle density in galaxies with $v_c \leq 100 \text{ km s}^{-1}$ dips down to $\sim 10^{-6} \text{ cm}^{-3}$ beyond 50 kpc. Given the recombination coefficients of CV (a few times $10^{-12} \text{ cm}^3 \text{ s}^{-1}$), the recombination time scale becomes Gyr or more. This contrasts with the larger galaxies considered in previous sections, where densities in the outskirts are of order 10^{-4} cm^{-3} , and the recombination time scale is of order $\sim 100 \text{ Myr}$. This implies non-equilibrium cooling in low mass galaxies, which means that equilibrium calculations may not succeed in explaining observations. For low mass

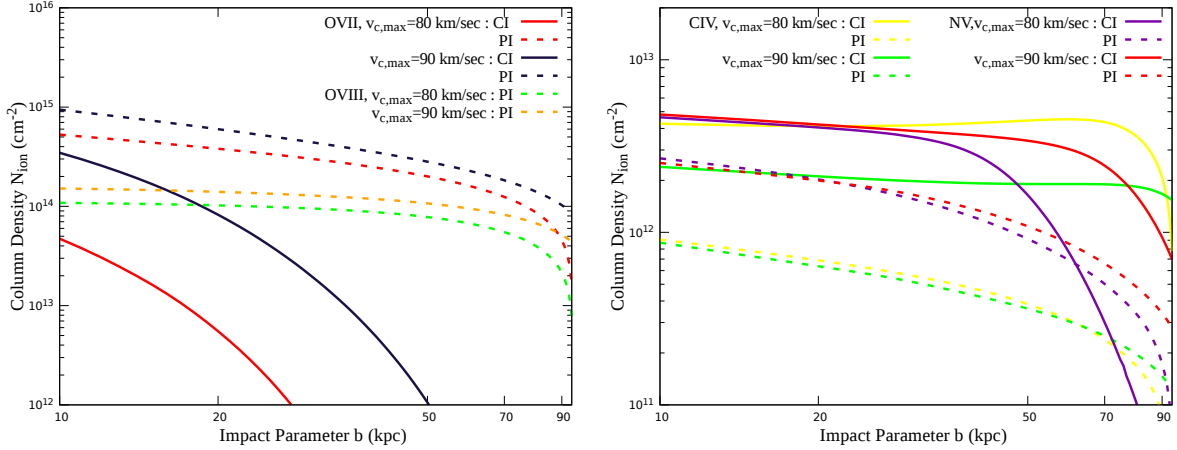


Figure 2.10: Left and right panels show the variation of OVII, OVIII and NV, CIV column densities respectively in the case of CI and PI in the low mass galaxies.

galaxies, the cooling time in the central region is much shorter than 1 Gyr (~ 0.4 Gyr for $v_{c,max} \sim 90$ km s $^{-1}$). Gas in this region is far from hydrostatic equilibrium and there can be a cooling flow in the inner CGM. However, the outer CGM, at say 50 kpc, where the column density calculations have been done, the cooling time is ~ 2.2 Gyr. Therefore our calculations are valid at least for this time scale. There is certainly a scope for refinement in this model in future by considering deviation from hydrostatic equilibrium by taking into account cooling flow or wind ejection in the inner CGM. However, our aim here has been to study the importance of photoionization in low-mass galaxies, which seems to be quite significant, in anticipation of future observations.

2.6 Conclusion

We extend the precipitation model of [Voit \(2019\)](#) for CGM and investigate the Galactic latitude and longitude variation of column density of OVI, OVII and OVIII. We include photoionization in the model to determine its effects on both Milky-way type and low mass galaxies. Our results are summarized below:

- Our precipitation model can account for OVIII observations of the Milky Way CGM for $\sigma_{\ln T} \sim 0.6$ – 1.0 , and OVI observations for $\sigma_{\ln T} \sim 1.0$. The indicated ratio of OVII to OVIII column density depends on whether or not we take the median of

ratios along individual sight lines (which gives $\sigma_{\ln T} \approx 1.0$) or ratio of the medians (which gives $\sigma_{\ln T} \approx 0.6$). This range is broadly consistent with the previous findings of [Voit \(2019\)](#) who considered OVI column density for broad absorbers at different impact parameters of other galaxies and estimated $\sigma_{\ln T} \sim 0.7$.

- Photoionization does not play a significant role in CGM of Milky-way type galaxies. This is because of the fact of that the typical CGM temperatures in this case lie in the range favourable for collisional ionization of OVI, OVII, OVIII ions, if there is a wide (log-normal) distribution of temperature.
- However, photoionization has a significant effect in the case of low mass galaxies, in which the virial temperature is far from the collisional peak for OVI, OVII and OVIII ions. The calculated values from the photoionized precipitation model are similar to the observed OVI column density of low mass galaxies. The largest effect of photoionization for low mass galaxies is seen in the column density of OVIII. Hence, OVIII observations can be a probe for the effect of photoionization in low mass galaxies.
- Our precipitation model implies that star formation related processes in a halo's central galaxy are likely correlated with temperature fluctuations in its CGM. Comparing the model with observations indicates temperature fluctuations $\sigma_{\ln T} \approx 1.0$ in the CGM around star-forming galaxies.

Chapter 3

Gamma-ray and radio background constraints on cosmic rays in Milky Way circumgalactic medium

“Gamma-ray and radio background constraints on cosmic rays in Milky Way circumgalactic medium”

Ranita Jana, **Manami Roy**, Biman B. Nath

The Astrophysical Journal Letters, Volume 903, Number 1, October 2020, (ApJL 903 L9)

[Jana et al. \(2020b\)](#)

We study the interaction of CRs with the diffuse circumgalactic gas of MW galaxy, resulting in hadronic γ -ray emission and radio synchrotron emission. We aim to constrain the CR population in our CGM with the help of observed isotropic γ -ray background (IGRB), its anisotropy, and radio continuum. We modify different models of CGM gas in hydrostatic equilibrium discussed in literature by including a cosmic ray population, parametrized by $\eta \equiv P_{\text{CR}}/P_{\text{th}}$. These bounds on η are relevant for current numerical simulations that indicate a significant CR population in CGM of galaxies of MW mass.

Key Results:

- For the simplest IT model, while the IGRB intensity allows $\eta \lesssim 3$, the anisotropy resulting from the Solar system's off-center position in MW rules out all values of η .
- For the PP model, in which the cooling of the CGM gas is regulated with an optimum ratio of cooling time to free-fall time, while the observed IGRB intensity allows $\eta \lesssim 230$, the observed anisotropy allows only very large values of η , of order $\gtrsim 100$.
- The radio continuum limits $\eta \lesssim 400$ for PP model and does not constrain IT model, however these constraints are mitigated by synchrotron loss time being comparable to CR diffusion time scales.

3.1 Introduction

Recent numerical simulations have indicated that galactic outflows in Milky Way-type galaxies can populate the CGM with cosmic rays (CRs). Galactic outflows are likely to contain CR particles, either accelerated in the disk and then advected outwards, or produced by shock acceleration in the outflow. Once these CRs are lifted to the CGM, they would diffuse throughout the halo. Some of the high energy CRs may diffuse out into the intergalactic medium, but most of the CRs would remain in the CGM. For a diffusion coefficient of $D(E) \approx 2 \times 10^{29} \text{ cm}^2 \text{ s}^{-1} E_{\text{GeV}}^{1/3}$ (Berezinsky et al., 1997), and a virial radius of the MW $\approx 260 \text{ kpc}$, CRs with $E \lesssim 1.8 \text{ GeV}$ would be contained in the CGM as their escape time-scale is greater than the age of the Universe. For a shorter and more relevant time scale, the corresponding limit of CR energy would be higher.

One of the observational implications of having a CR population at large in the CGM is hadronic interaction of CRs with CGM gas and subsequent γ -ray production through pion decay. Feldmann et al. (2013) estimated the γ -ray luminosity of the CGM by solving the transport equation for CRs and assuming a star formation history of MW. They found that the γ -ray flux from the CGM would provide $\approx 3\%$ – 10% of the total IGRB flux. They did not, however, consider any violent processes such as galactic outflows produced by star formation processes. Similarly, Liu et al. (2019) used IGRB flux at $\leq 1 \text{ TeV}$ to put important limits on CR luminosity ($\leq 10^{41} \text{ erg s}^{-1}$) of MW. In a related simulation, Chan et al. (2019a) constrained the average CR diffusivity with observed γ -ray ($> \text{GeV}$) emission from galaxies. They have found that for dwarf and L_* galaxies, a constant isotropic diffusion coefficient of order $\sim 3 \times 10^{29} \text{ cm}^2 \text{ s}^{-1}$ can explain the observed relation between γ -ray luminosity and star formation rate. However, they did not compare with synchrotron observations.

In this *Letter*, we ask a related but different question, as to the degree that CRs can dominate the energy budget of the MW CGM, without violating the γ -ray and radio background limits. This is important in the context of recent galactic outflow simulations, which depict a picture of the CGM that it may even be dominated by CRs (Butsky & Quinn 2018; Dashyan & Dubois 2020; Hopkins et al. 2020). It is also claimed that

feedback efficiency of the outflowing gas increases in presence of CRs, by an increase in mass loading and suppression in star formation rate. [Butsky & Quinn \(2018\)](#) and [Hopkins et al. \(2020\)](#) found that this effect is dependent on the ratio of CR pressure to thermal pressure (which we denote here by $\eta \equiv P_{\text{CR}}/P_{\text{th}}$) in the CGM. Hence it is necessary to constrain the value of η using observational limits.

For example, while simulating a MW-sized galaxy with different CR transport prescriptions, [Butsky & Quinn \(2018\)](#) found that η can exceed the value 10 over a large portion of the halo, even extending to ~ 100 kpc for certain models (see their Fig. 10). [Dashyan & Dubois \(2020\)](#) simulated smaller galaxies, with virial mass 10^{10} and $10^{11} M_{\odot}$, and found that η can have a value ~ 100 within central 3 kpc (their Fig. 1). [Ji et al. \(2019\)](#) have found that at redshift $z \lesssim 1$ outflows in MW-mass galaxies can populate the halos with CR and as a result $\eta \approx 10$, although, in warm regions ($T \gtrsim 10^5$ K), locally η may have a value less than or comparable to 1.

We use the IGRB as observed by *Fermi-LAT* to constrain the CR population in our halo. While protons in CR population produce γ -rays, CR electrons in CGM emit synchrotron radiation in the presence of magnetic field. In this regard, we can use the result of [Subrahmanyan & Cowsik \(2013\)](#) to constrain CR population who calculated the maximum synchrotron flux that can arise from MW. They showed that a careful modelling of the Galactic components can explain the anisotropic part of the background emission as observed in *ARCADE* balloon observations by [Fixsen et al. \(2011\)](#). This gives an upper limit to the radio frequency emission that can possibly come from CR electron population in an extended halo of our galaxy. We use different density and temperature profiles that have been used in the literature to model the CGM and put bounds on the CR population in the halo.

3.2 Density and temperature profiles

We assume for analytical tractability that CGM gas is in hydrostatic equilibrium in the dark matter potential of the MW. Such models have been recently studied in order to explain the observations of several ions as absorption lines in the lines of sight through the

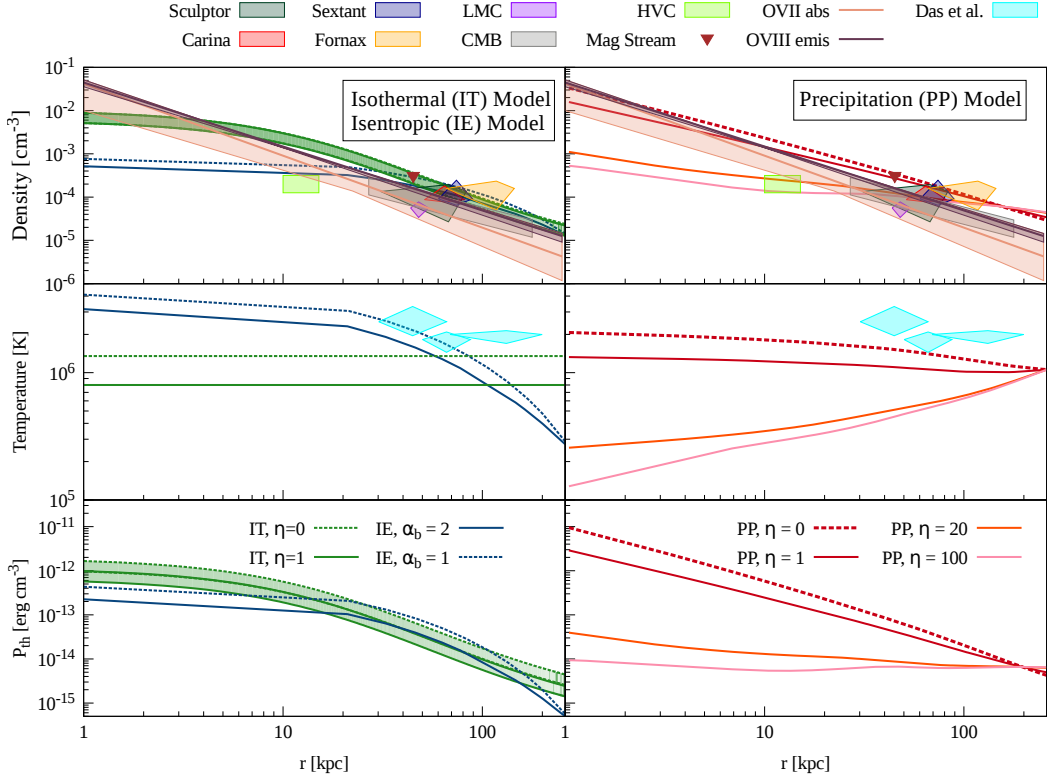


Figure 3.1: Density, temperature and pressure profiles from different models are shown with the distance (r) from the Galactic center in the left (Isothermal (IT) and Isentropic (IE)) and right (Precipitation (PP)) panels. IT model is shown for the cases of $\eta = 0$ (green, dashed) and 1 (green, solid)—the density profiles coincide in these two cases, but with two different corresponding temperature and pressure profiles. The no-CR ($\eta = 0$) profiles of PP model is shown with dashed red, and those for $\eta = 1$ (red solid), $\eta = 20$ (orange), $\eta = 100$ (pink). The profiles for IE model for $\alpha_b = 1$ (no-CR, dashed) and $\alpha_b = 2$ (solid) is shown in blue. Observational constraints are described in detail in text.

CGM. In order to explore the γ -ray production implications, we study three illustrative examples of these models: i) Isothermal model (IT), ii) Precipitation model (PP), and (iii) Isentropic model (IE).

The underlying dark matter potential in all these models is assumed to be that of Navarro-Frenk-White (NFW) profile (Navarro et al., 1997), although in some cases we assume a variation of this profile. In the modified version of NFW potential, we assume that the circular velocity v_c is constant ($= v_{c,max}$) below a radius $2.163 r_s$, where r_s is the scaling radius, as suggested by Voit (2019). We assume a virial mass $M_{vir} = 2 \times 10^{12} M_\odot$

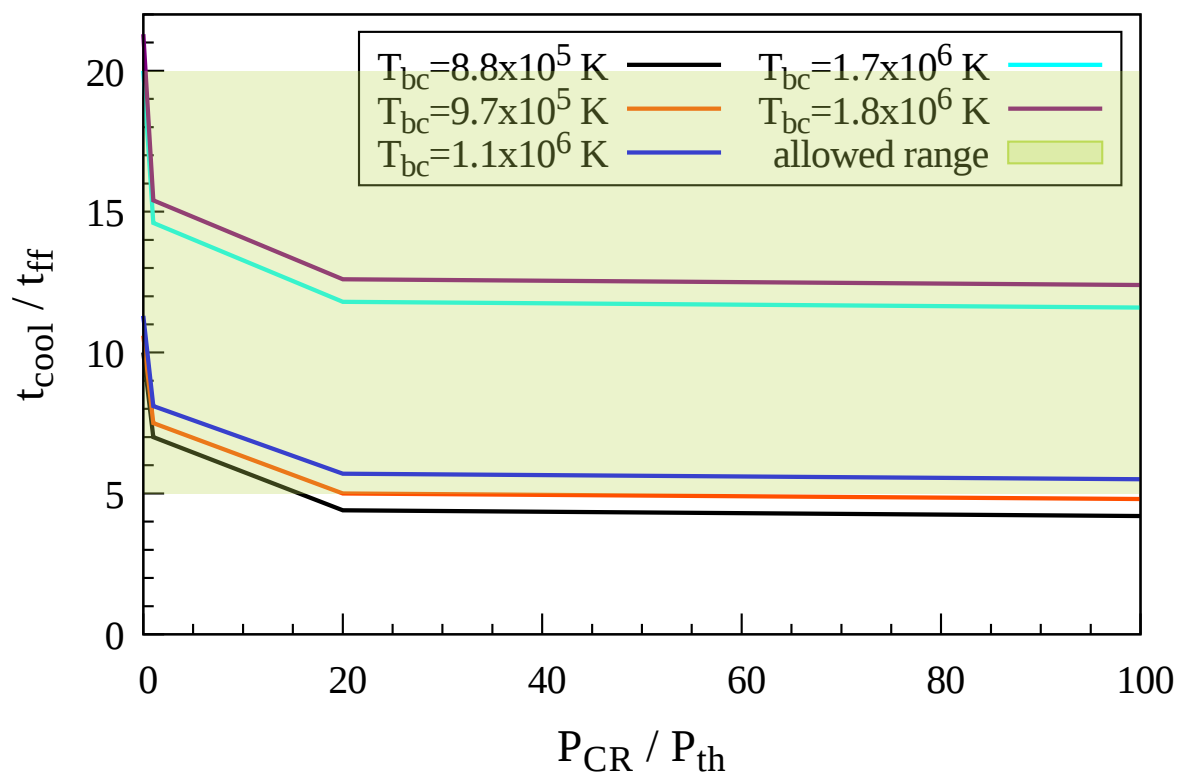


Figure 3.2: Variation of t_{cool}/t_{ff} with P_{CR}/P_{th} for different boundary conditions in the precipitation model. The shaded region indicates the allowed range for this ratio of two time scales from cluster studies.

(Bland-Hawthorn & Gerhard, 2016), with a concentration parameter $c = 10$. When we modify the temperature and density profile by including the non-thermal components, magnetic pressure and CR pressure, we ensure that the total CGM gas mass remains the same. Because of this constraint, the inclusion of a CR population in the CGM suppresses gas pressure, by suppressing the gas temperature, as has been also noted in the simulations, e.g. (Hopkins et al., 2020). The Magnetic energy is assumed to be in equipartition with the thermal energy (i.e. $P_{\text{mag}} = 0.5 P_{\text{th}}$) in the CGM in absence of any observational constraint. The question of magnetic field strength in the CGM is yet to be observationally settled. On one hand, Bernet et al. (2008) have detected magnetic field in the CGM of galaxies (at $z \sim 1.3$) of comparable strength or larger than that in disks of present-day galaxies. On the other hand, Prochaska et al. (2019) have found in the sightline of a Fast Radio Burst that the magnetic field in the CGM of a massive galaxy is less than the equipartition value. In the absence of any definitive answer, we assume an equipartition magnetic field strength, and calculate the synchrotron flux from CR population in the CGM. In other words, $P_{\text{tot}} = P_{\text{th}} + P_{\text{mag}} + P_{\text{CR}} = P_{\text{th}}(1.5 + \eta)$. Below we describe the changes wrought upon by the introduction of CR population in different models.

In the isothermal model, the temperature of the CGM gas is held uniform, and has been extensively used for its simplicity (eg. Fang et al. 2013). The observed temperature of massive halos ($M_{\text{vir}} \geq 10^{12} M_{\odot}$) (Li et al., 2015), and that of MW (Miller & Bregman, 2015a) is $\geq 2 \times 10^6$ K. In the absence of CR and magnetic field, we assume a uniform CGM temperature of 2×10^6 K. According to the isothermal model of Miller & Bregman (2015a), the hot gas mass in CGM is within a range of $(2.7\text{--}4.7) \times 10^{10} M_{\odot}$. We therefore initialize our density and temperature profiles such that the CGM contains this amount of mass. In Fig. 3.1, we show the density, temperature and pressure profiles of IT model with dashed green ($\eta = 0$) and solid green ($\eta = 1$) lines. The shaded region with the same colour between the dashed (or solid) lines signifies extent of the profiles for a CGM mass within the allowed range for $\eta = 0$ (or 1). The temperature decreases when CR is included, but the density profile practically remains the same, since the CGM mass is held a constant. The temperature falls below the temperature of the photoionized gas ($\sim 10^4$ K) in case of $\eta \geq 200$ for this model, hence we only consider $\eta \leq 200$ in case of isothermal model.

In the precipitation model (Voit, 2019), the ratio of cooling time to free-fall time ($t_{\text{cool}}/t_{\text{ff}}$) is assumed to be uniform throughout the halo. The underlying idea is that heating and cooling of CGM is regulated in such a manner to keep this ratio at an optimum range. If the ratio becomes too small, cooling would dominate, which would usher in more star formation and stellar feedback would start heating CGM and it would increase the ratio. If the ratio is too large, then reduced feedback would decrease heating, ultimately to pave way for cooling and a reduction of the ratio. The boundary condition used by Voit (2019) is such that the temperature (T_{bc}) at r_{200} is $kT_{\text{bc}} = 0.25\mu m_p v_{c,\text{max}}^2$. We use the cooling function (Λ_{N}) of CLOUDY, for a metallicity of $Z = 0.3Z_{\odot}$. The total CGM mass in this model for this metallicity is $\approx 6 \times 10^{10} M_{\odot}$, and we use the same value here. We keep the temperature at the outer boundary (T_{bc} , at r_{200}) fixed for a particular case when CR is included. Hence the gas temperature in the inner region drops, which increases the cooling rate, and consequently, in order to maintain the same gas mass, the ratio $t_{\text{cool}}/t_{\text{ff}}$ has to be decreased. According to the simulations for gas in galaxy clusters and massive ellipticals, the optimum range of this ratio is believed to be 5–20 (Voit, 2018). This means that the outer boundary temperature can be varied within a small range, so that this condition is satisfied. We found this range to be 1.1×10^6 – 1.7×10^6 K, as shown in Fig. 3.2. If the boundary temperature is larger (smaller) than this range, then $t_{\text{cool}}/t_{\text{ff}}$ becomes larger than ≈ 20 (smaller than ≈ 5). We have also included an additional pressure due to turbulence as in the isentropic model, which is described below, and studied its effect on our final results.

The corresponding density, temperature and pressure profiles for PP model are shown in Fig. 3.1 with dashed red ($\eta = 0$), solid red ($\eta = 1$), orange ($\eta = 20$) and pink ($\eta = 100$) lines. The boundary temperature used for this plot is 1.1×10^6 K. The curves show that with an increasing presence of CR, the temperature drops in the inner region, as has also been noted in the simulations of Ji et al. (2019) (their Fig. 5).

Recently Faerman et al. (2019) have described an ‘isentropic’ model of the CGM, in which entropy is held a constant in the halo. They include three components in their description of pressure: (a) thermal gas (b) non-thermal gas (magnetic field and CR) and (c) turbulence. They characterise turbulence by a fixed $\sigma_{\text{turb}} \approx 60 \text{ km s}^{-1}$, and define a parameter $\alpha(r) = (P_{\text{nth}} + P_{\text{th}})/P_{\text{th}}$. They fixed the boundary condition with the help

of the value of α at the outer boundary (r_{200}), α_b , and varied its value between 1 (no non-thermal component) and 3 (equipartition of thermal, magnetic and CR components). In this model, the ratio $\alpha(r)$ drops from its boundary value (α_b) in the inner region.

In addition to the density and temperature profiles of these three models, with and without CR, we also show a few observational constraints on density and temperature in Fig. 3.1 : (a) OVII and OVIII observations (Miller & Bregman, 2015a), (b) CMB/X-ray stacking (Singh et al., 2018), (c) limits on density (assuming a temperature of 2.2×10^6 K from ram pressure stripping of LMC (Salem et al., 2015), Carina, Sextans (Gatto et al., 2013), Fornax, Sculptor (Grcevich & Putman, 2009b), (d) pressure equilibrium of high-velocity clouds (assuming the above mentioned temperature) (Putman et al., 2012), and Magellanic stream (Stanimirović et al., 2002). The observed temperature profile (Das et al., 2020) of a L_* galaxy NGC 3221 is shown for comparison along with the profiles used here. These constraints show that the density profiles including a CR component are reasonable, although there remains uncertainty regarding the temperature profiles.

3.3 Gamma-ray background radiation

Once the density and temperature profiles for these models are calculated, we determine the γ -ray flux resulting due to the hadronic interaction between CR protons and CGM protons. We use the prescription of Dermer's model (Dermer 1986; Pfrommer & Enßlin 2004) for these calculations. The γ -ray flux can be estimated using the source function \tilde{q}_γ which when multiplied by the number density of target nuclei (n_{CGM}), CR energy density (ϵ_{CR}) and photon energy (E_γ), gives the photon energy per unit time from a particular volume element. The diffuse flux at the Solar position in units of $\text{erg cm}^{-2} \text{s}^{-1} \text{sr}^{-1}$ is then given by

$$J_\gamma = \int 4\pi x^2 dx \frac{1}{4\pi x^2} \left[n_{\text{CGM}}(x) \epsilon_{\text{CR}}(x) E_\gamma \frac{\tilde{q}_\gamma(E_\gamma)}{4\pi} \right]. \quad (3.1)$$

where x is the line-of-sight distance from the position of Solar system. The lower limit ($|b| > 30^\circ$) of the line of sight integration is chosen in a way such that the contri-

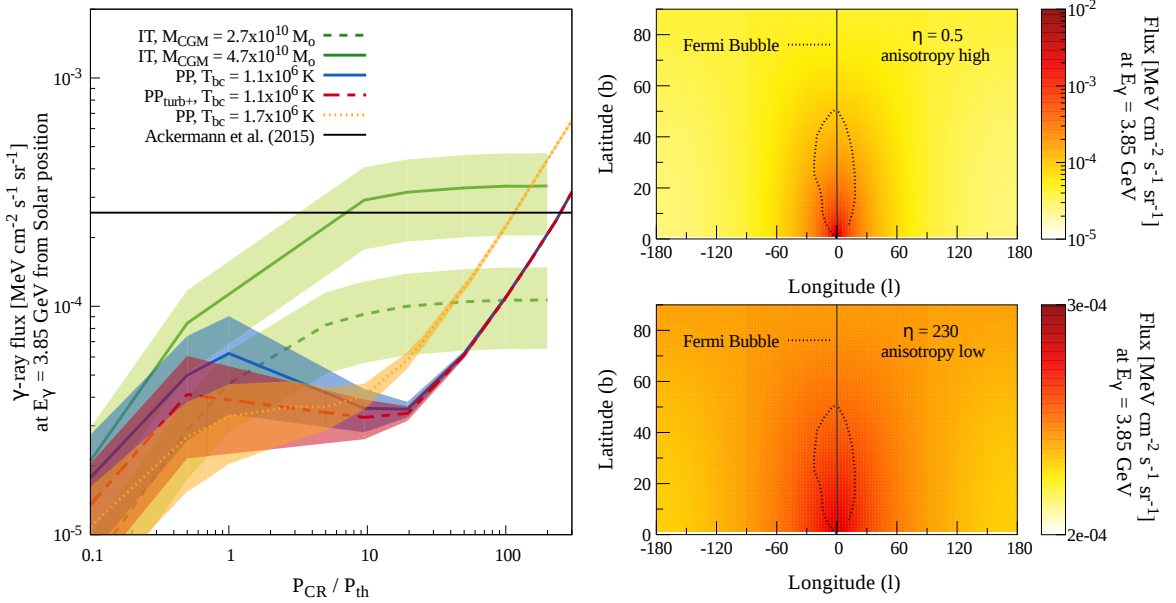


Figure 3.3: *Left panel* shows the variation of mean gamma-ray flux from Solar position at 3.85 GeV with $P_{\text{CR}}/P_{\text{th}}$ for different models and boundary conditions. The black horizontal line shows the observed flux (Ackermann et al., 2015) at $E_{\gamma} = 3.85$ GeV. The curves show the mean flux for $|b| > 30^{\circ}$ and the shaded region around each curve indicates the standard deviation. The case of IT model is shown with a green solid ($M_{\text{CGM}} = 4.7 \times 10^{10} M_{\odot}$) and dashed ($M_{\text{CGM}} = 2.7 \times 10^{10} M_{\odot}$) line, and PP model with blue solid line ($T_{\text{bc}} = 1.1 \times 10^6$ K), red dashed line ($T_{\text{bc}} = 1.1 \times 10^6$ K, with turbulence) and yellow dotted line ($T_{\text{bc}} = 1.7 \times 10^6$ K). *Right panel* shows the corresponding flux map for PP model ($T_{\text{bc}} = 1.1 \times 10^6$ K) in Galactic coordinates for $\eta = 0.5$ and $\eta = 230$, made with the angular resolution (0.6°) of *Fermi-LAT* (Atwood et al., 2009), and in which the dotted line demarcates the region of Fermi Bubble (Su et al., 2010).

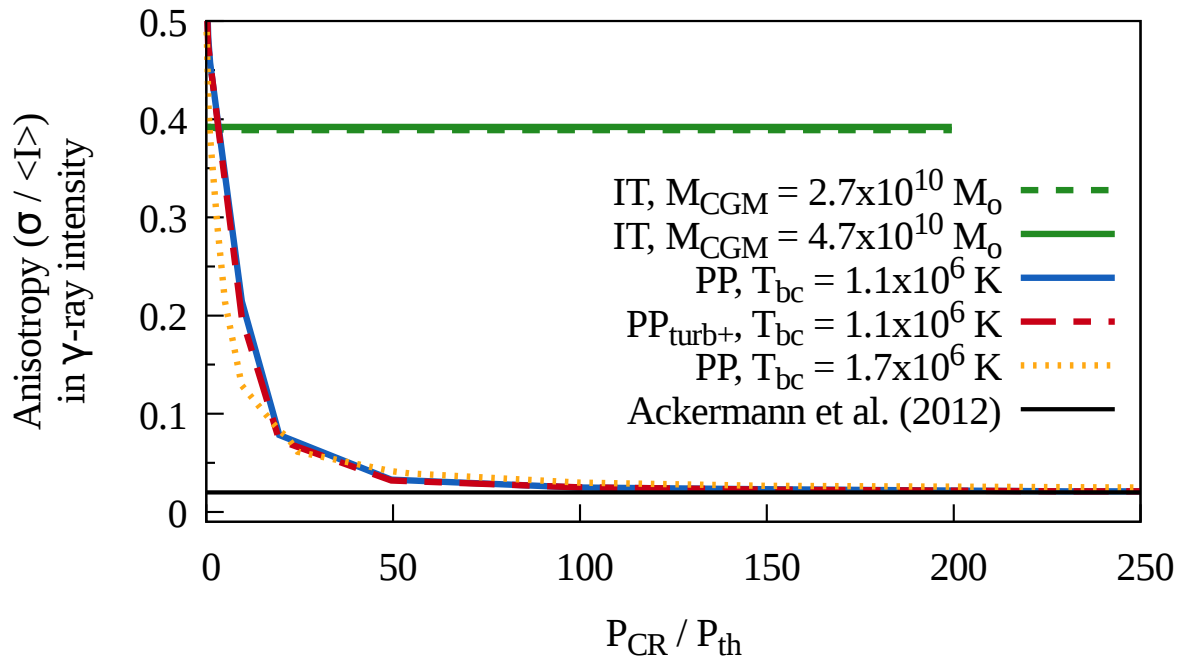


Figure 3.4: Variation of anisotropy (ratio of standard deviation to mean in γ -ray intensity map) with η for different models. The observed value of the ratio (as derived in eqn. 3.4) (Ackermann et al., 2012) is shown with black horizontal line.

bution from lower latitude, where the Galactic inter-stellar matter dominates over the circumgalactic medium, is excluded. The omnidirectional source function \tilde{q}_γ (Gupta et al., 2018) is given as,

$$\tilde{q}_\gamma = \left[\frac{\sigma_{\text{pp}} c \left(\frac{E_{\pi^0}}{\text{GeV}} \right)^{-\zeta_\gamma} \left[\left(\frac{2E_\gamma}{E_{\pi^0}} \right)^{\delta_\gamma} + \left(\frac{2E_\gamma}{E_{\pi^0}} \right)^{-\delta_\gamma} \right]^{-\zeta_\gamma/\delta_\gamma}}{\xi^{\zeta_\gamma-2} \left(\frac{3\zeta_\gamma}{4} \right) \frac{E_p}{2(\zeta_p-1)} \left(\frac{E_p}{\text{GeV}} \right)^{1-\zeta_p} \text{B}\left(\frac{\zeta_p-2}{2}, \frac{3-\zeta_p}{2}\right)} \right]. \quad (3.2)$$

Here $\xi = 2$ is the multiplicity factor, E_p and E_{π^0} are the rest mass energy of protons and pions (π^0), ζ_p and ζ_γ are the spectral indices of the incident CR protons and emitted γ -ray photons respectively, $\delta_\gamma = 0.14\zeta_\gamma^{-1.6} + 0.44$ is the spectral shape parameter, $\sigma_{\text{pp}} = 32(0.96 + e^{4.4-2.4\zeta_\gamma})$ mbarn (see Equations (8), (19)-(21) in Pfrommer & Enßlin 2004) and B stands for beta function. We use $\zeta_p = \zeta_\gamma = 2.3$ in our calculations following the spectral fit of Ackermann et al. (2015).

CR electrons can also produce GeV γ -ray flux by boosting CMB photons via inverse Compton scattering. Such electrons will have TeV range energy. The inverse Compton loss time scale of these high energy electrons is short, $t_{\text{comp}} \approx 1.2 \text{ Myr} (\text{GeV}/E_\gamma)^{1/2}$ where E_γ is the scattered γ -ray energy. In light of this short time scale, we do not consider leptonic process here.

We choose the energy band of 3.2–4.5 GeV as a representative band for our comparison of model fluxes with observations since the *Fermi-LAT* spectral fit of IGRB with index -2.3 fits well the data in this band. We compute fluxes at the midpoint of this band 3.85 GeV for different models and compare with observed flux in the band.

The γ -ray flux scales as $\epsilon_{\text{CR}} n \propto (\eta \times n^2 T)$, an increase in η suppresses the thermal pressure, so the resultant flux depends on the competition between η and $n^2 T$ terms. For the isothermal model, the more CR there is in CGM, the lower is the gas temperature, but the density profile remains approximately unchanged. This makes the γ -ray flux increase with the increase in η . For higher values of η (i.e. $\eta \gtrsim 10$) the curve flattens because the increase in η is compensated by the decrease in temperature (flux $\propto \eta T$ for IT model).

The case of PP model is interesting, since the density profile is coupled to the tem-

perature and cooling function by $n \propto T(r)^{\frac{3}{2}}/\Lambda_{\text{N}}(T(r))$. The initial rise of γ -ray flux with increasing η results from the fact that the temperature is in a range where the cooling function has a plateau and the density profile does not change with η , but the γ -ray flux does. This is followed by a decrease in the flux when the temperature is lowered further, and the steep portion of the cooling function suppresses the density, decreasing the γ -ray flux. For larger η , the density profile becomes almost flat and any further increase in η increases the γ -ray flux.

The anisotropy in IGRB can also give additional bounds on η . The fluctuation in IGRB intensity can be decomposed in spherical harmonics as $\frac{\delta I(\theta)}{\langle I \rangle} = \sum_{l,m} a_{l,m} Y_{l,m}(\theta)$, where $\delta I(\theta) = I(\theta) - \langle I \rangle$ is the difference in intensity between the mean intensity and the intensity in direction θ . With $C_l = \langle |a_{lm}|^2 \rangle$, the correlation function between lines of sight related through $\mathbf{k}_1 \cdot \mathbf{k}_2 = \cos \theta$ is given by,

$$C(\theta) = \left\langle \frac{\delta I(\mathbf{k}_1)}{\langle I \rangle} \frac{\delta I(\mathbf{k}_2)}{\langle I \rangle} \right\rangle = \sum_l \frac{2l+1}{4\pi} C_l P_l(\cos \theta). \quad (3.3)$$

Since the Legendre polynomials $P_l(1) = 1$, we have from the auto-correlation ($C(\theta = 0)$), the ratio of standard deviation to mean intensity,

$$\frac{\sigma}{\langle I \rangle} = \left(\sum_l \frac{2l+1}{4\pi} \frac{C_l}{\langle I \rangle^2} \right)^{1/2} \approx 0.02, \quad (3.4)$$

where the sum is dominated by C_l at $l = 30$ (Ackermann et al., 2012).

We show in the right panel of Fig. 3.3 two simulated maps in Galactic coordinates for γ -ray intensity at 3.85 GeV for $\eta = 0.5$ and $\eta = 230$ of precipitation model ($T_{\text{bc}} = 1.1 \times 10^6$ K), made with Fermi-LAT angular resolution of 0.6° at 3.85 GeV. The ratio of standard deviation to mean intensity for $|b| > 30^\circ$ as a function of η is shown in Fig. 3.4 for different models. For PP model, the decrease in anisotropy with the increasing η results from the flattened out density and temperature profiles. In contrast, anisotropy does not change with η for IT model due to unchanged density profile.

The above discussion leads us to two constraints on the CR population in CGM. Firstly, if we consider a 1σ spread around the mean intensity, then we get a limit from the observed intensity itself, ruling out those values of η for which the intensity (mean+ 1σ) exceeds the observed value. This leads to an upper limit of $\eta \lesssim 3$ for IT model, and

$\eta \lesssim 230$ for PP model. Secondly, one can limit η considering the anisotropy, requiring the ratio of standard deviation to mean intensity to be ≤ 0.02 . This rules out all varieties of IT models. For PP model, the anisotropy asymptotically reaches the observed limit for large values of η ($\gtrsim 100$). Hence, one can conclude that IGRB intensity and anisotropy allow $100 \lesssim \eta \lesssim 230$ for PP model.

The isentropic model has to be dealt separately, since their model already predicts a non-thermal component in its profile. In order to put a limit, we have not included any magnetic pressure and assume $P_{\text{CR}} = P_{\text{nth}}$ as their model does not allow equipartition of magnetic field in the inner region of halo for the $\alpha_b < 4$, and calculate the corresponding γ -ray flux at 3.85 GeV, as a function of the boundary value (α_b) of their model. We find that for the isentropic model, the γ -ray flux never exceeds the *Fermi-LAT* data, and at the most has a value $\sim 10\%$ of the flux as this model does not admit a CR dominated CGM in inner region of halo.

3.4 Synchrotron radiation

CR electrons radiate synchrotron emission in the presence of magnetic field. We assume an equipartition magnetic field in the CGM for our calculation, since its value is still a debatable issue. We take the fiducial value of the ratio of CR electrons to protons energy to be 0.01. Its value is rather uncertain, both theoretically and observationally. From observations in the Solar system, at CR energy ~ 10 GeV, where solar modulation effects are low, the ratio is known to be 1%.

We assume that the CR electrons have a power-law energy distribution, with the same power-law index ζ_p as for protons. The observed radio spectrum has an index of -0.599 ± 0.036 (Table 6 of [Fixsen et al. \(2011\)](#)), which would imply $\zeta_p \sim 2.2$ which is not very different from our assumed value. The corresponding radio flux can be calculated using the emissivity (eqn. 6.36 of [Rybicki & Lightman \(2004\)](#)) and then performing a similar integral as in the case of γ -ray flux. Finally the brightness temperature is calculated at 1.4 GHz, in order to compare with observations.

As explained earlier, [Subrahmanyan & Cowsik \(2013\)](#) devised a model of the MW

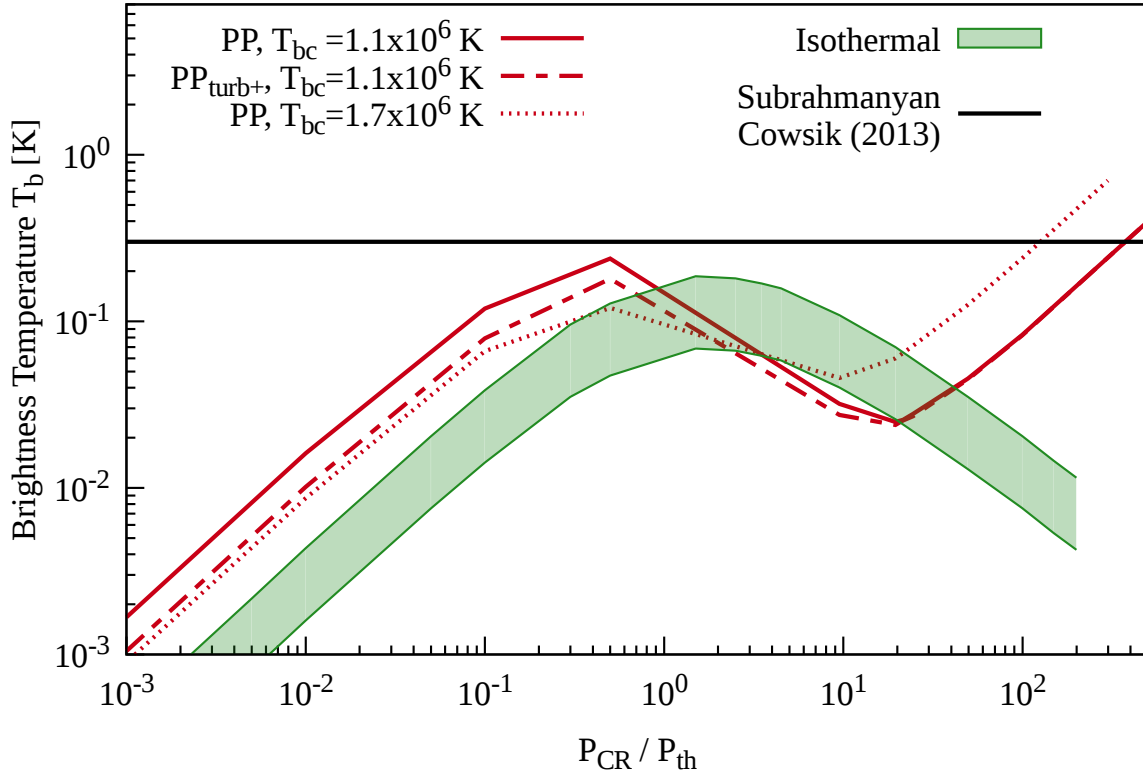


Figure 3.5: The (solid, dashed and dotted red) curves show the brightness temperature at 1.4 GHz for precipitation model for different boundary conditions, and the green band shows the same for isothermal model for the range of CGM mass mentioned in the text. The horizontal black line is the brightness temperature from the halo model of [Subrahmanyan & Cowsik \(2013\)](#).

synchrotron emitting halo in such a way as to explain the observed radio background towards the Galactic pole, by *ARCADE-2*. The purpose of the model of [Subrahmanyan & Cowsik \(2013\)](#) was to maximally explain the radio observations with the help of MW halo. This particular model, therefore, gives the maximum possible radio continuum emission that can be attributed to MW halo, and becomes useful for our purpose of putting limits on CR electrons in CGM.

We show the comparison of synchrotron flux from different models as a function of η , with the observed limit, in Fig. 3.5. The trends of radio flux with η are different from the case of γ -ray, because here the magnetic field is pegged to the thermal pressure. We find that in the isothermal model all values of η are allowed. Although in the precipitation model only $\eta \lesssim 400$ keeps the brightness temperature within limit.

The magnetic field in different models range between $(0.2\text{--}10)\mu\text{G}$ (from outer to inner regions), for $\eta = 1$. For higher values of η the range would be lower. The synchrotron loss time of electrons (responsible for radiating at 1.4 GHz, with energy $\approx 17.4 B_{\mu\text{G}}^{-1/2}$ GeV) is $\approx 700 \text{ Myr } B_{\mu\text{G}}^{-3/2}$. The diffusion time scale for the CR electrons to cross 50 kpc radius is $\approx 630 \text{ Myr } E_{\text{GeV}}^{-1/3} \approx 243 \text{ Myr } B_{\mu\text{G}}^{-1/6}$. For low values of η ($\eta \sim 1$) most of the contribution to the radio flux comes from within 50 kpc, hence a spectral break at 1.4 GHz is not expected for lower values of η . For higher values of η ($\eta \sim 100$) a spectral break at 1.4 GHz will appear at ~ 2 Gyr (synchrotron loss time) when CR diffuses beyond ~ 150 kpc from where half of the radio emission occurs. This will decrease the radio flux for large η , which should be noted with regard to our limits on η above.

3.5 Discussions

The variations of radio and γ -ray fluxes with η for different boundary conditions in Fig. 3.3 and 3.5 show that our constraints are rather robust. We also show the result of inclusion of turbulence support in the CGM (red dashed lines), which indicate, again, the robustness of our constraints. However, it is possible that non-linear processes such as CR streaming instability may change the density profile ([Ruszkowski et al., 2017](#)) and change the conclusions.

We note that the γ -ray and radio flux, hence the limit of η , depend on CGM gas mass. A 10% increase (decrease) in CGM mass would result \lesssim 30% increase (decrease) in both the fluxes.

The limit on CR electrons through synchrotron emission depends on the assumption of equipartition strength of magnetic field. If the magnetic field strength were to be a fraction ψ of the equipartition value, then the synchrotron flux would scale as $\propto \psi^{(\zeta_p+1)/2}$. For $\psi = 0.1$, *e.g.*, the flux would decrease by a factor 0.02, for $\zeta_p = 2.3$ considered here, thereby making the synchrotron limits on η practically irrelevant.

3.6 Conclusion

We have pointed out that IGRB and radio continuum background can act as important checks for models that populate CGM with a significant amount of CR. Using various density and temperature profiles from literature we have shown that resulting γ -ray background and the associated anisotropy constrain the CR pressure to thermal pressure ratio $100 \lesssim \eta (\equiv P_{\text{CR}}/P_{\text{th}}) \lesssim 230$ in the precipitation model, the lower limit arising from anisotropy due to the off-center position of the Solar system in MW, and the upper limit, from IGRB intensity measurements. Although the isothermal model allows $\eta \lesssim 3$ considering the intensity (mean + 1σ), but anisotropy considerations rule out all values of η in this model. Limits from radio background ($\eta \lesssim 400$ for precipitation model) are rather weak in comparison.

Chapter 4

Constraints on cosmic rays in the Milky Way circumgalactic medium from OVIII observations

“Constraints on cosmic rays in the Milky Way circumgalactic medium from OVIII observations”

Manami Roy, Biman B. Nath

The Astrophysical Journal, Volume 931, Number 2, June 2022, (ApJ 931 125)

[Roy & Nath \(2022a\)](#)

We constrain the CR population in the CGM of MW by comparing the observations of absorption lines of OVIII ion with predictions from analytical models of CGM PP and IT model. For a CGM in hydrostatic equilibrium, the introduction of CR suppresses thermal pressure, and affects the OVIII ion abundance. We explore the allowances given to the ratio of CR pressure to thermal pressure ($P_{\text{CR}}/P_{\text{th}} = \eta$), with varying boundary conditions, CGM mass content, photoionization by extra-galactic ultraviolet background and temperature fluctuations. These limits on η , combined with the limits derived from γ -ray and radio background, can be useful for building models of Milky Way CGM including CR population. However, the larger amount of CR can be packed in cold phase which may be one way to circumvent these constraints.

Key Results:

- We find that the allowed maximum values of η are : $\eta \lesssim 10$ in the PP model and $\eta \lesssim 6$ in the IT model.
- We also explore the spatial variation of η : rising ($\eta = Ax$) or declining ($\eta = A/x$) with radius, where A is the normalisation of the profiles. In particular, the models with declining ratio of CR to thermal pressure fare better than those with rising ratio with suitable temperature fluctuation (larger $\sigma_{\ln T}$ for PP and lower for IT).
- The declining profiles allow $A \lesssim 8$ and $A \lesssim 10$ in the case of IT and PP models, respectively, thereby accommodating a large value of η ($\simeq 200$) in the central region, but not in the outer regions.

4.1 Introduction

Galaxies have two components: galactic disk surrounded by a gaseous and a dark matter halo. The gaseous halo, which extends up to the virial radius (sometimes even beyond) is known as the circumgalactic medium (CGM). It is a reservoir for most of the baryons and plays a crucial role in galaxy formation and evolution by various feedback processes such as outflowing, recycling of gas (Tumlinson et al., 2017). Soft X -ray observation of OVII and OVIII absorption (Gupta et al., 2012; Fang et al., 2015) and emission lines (Henley et al., 2010; Henley & Shelton, 2010), and SZ effect (Planck Collaboration et al., 2013b; Anderson et al., 2015) indicate the presence of a hot phase ($T \geq 10^6$ K) of CGM. Recently, a warm ($10^5\text{K} < T < 10^6\text{K}$) and a cool phase ($10^4\text{K} < T < 10^5\text{K}$) of CGM have also been discovered through absorption lines of low and intermediate ions¹ (Tumlinson et al., 2017) at low redshifts (Stocke et al., 2013; Werk et al., 2014, 2016; Prochaska et al., 2017b) and Ly α emission at high redshifts (Hennawi et al., 2015; Cai et al., 2017). It is not yet clear how this cool phase coexists with the hot phase and survives the destructive effects of various instabilities (McCourt et al., 2015; Ji et al., 2018), but this discovery has led to a picture of multiphase temperature and density structure of the CGM (Tumlinson et al., 2017; Zhang, 2018). It also partially solves the problem of missing baryon in the galaxies (Tumlinson et al., 2017). If the CGM is considered to be in hydrostatic equilibrium by means of only thermal pressure, then in order to maintain pressure equilibrium the cold component ($\sim 10^4$ K) of CGM is expected to have a higher density than the hot component ($\sim 10^6$ K). However, Werk et al. (2014) found the density of cold gas to follow the hot gas density distribution. This has given rise to the idea of a non-thermal pressure component, consisting of cosmic-ray (CR) and magnetic pressure which can add to the thermal pressure. Without a non-thermal component, the abundances of low and mid-ions (seen in cool and warm phases, respectively) are under-estimated even in high-resolution simulations (van de Voort et al., 2019; Hummels et al., 2019; Peebles et al., 2019). Ji et al. (2019) have suggested that CR can explain these two problems. It has been suggested that CR can provide pressure support to cool diffuse gas (Salem et al., 2015; Butsky & Quinn, 2018), help in driving galactic outflows (Ruszkowski et al., 2017;

¹Low Ions: Ionization Potential (IP) < 40 eV, $T = 10^{4-4.5}$ K; Intermediate Ions: $40 \gtrsim \text{IP (eV)} \lesssim 100$, $T = 10^{4.5-5.5}$ K; High Ions: $\text{IP} \gtrsim 100$, $T > 10^{5.5}$ K.

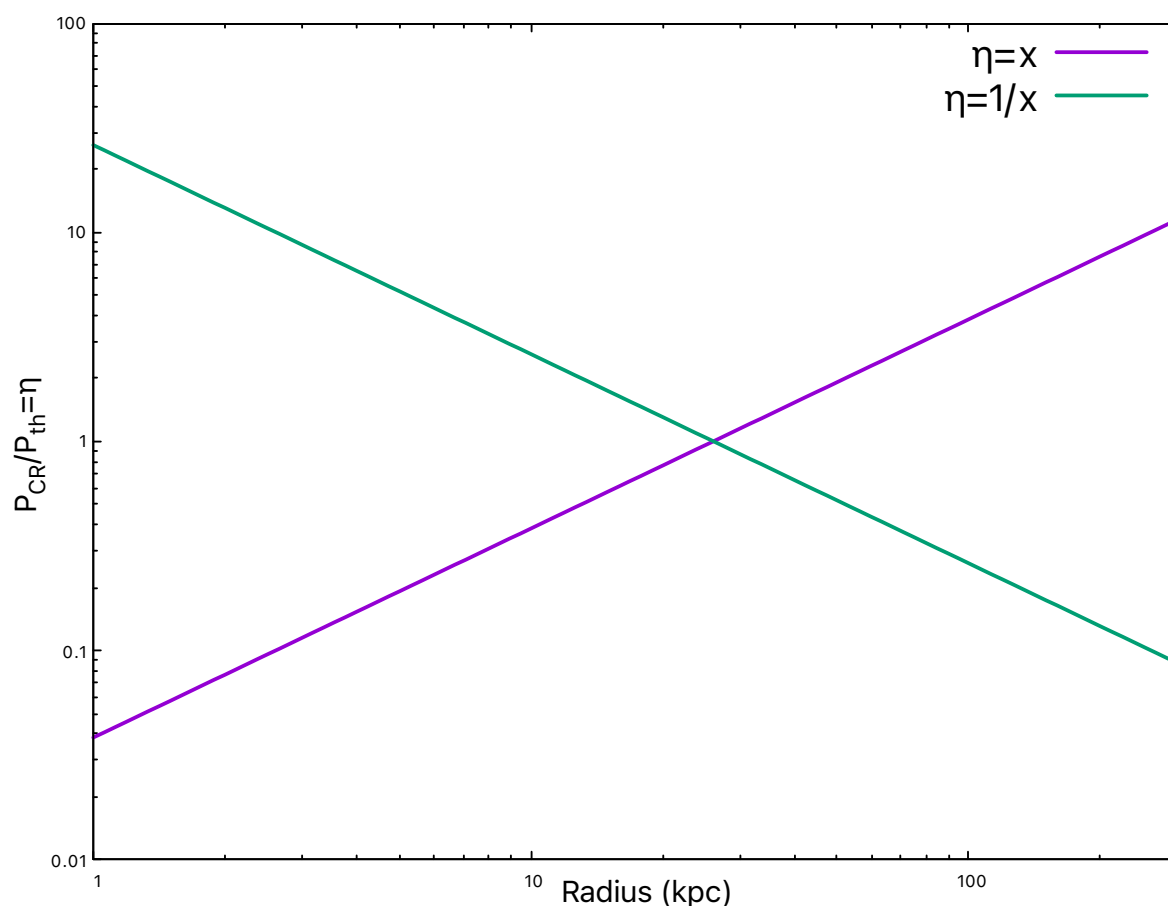


Figure 4.1: Radial profiles of η in the case of $\eta =x$ and $1/x$.

Wiener et al., 2017), as well as excite Alfvén waves that can heat the CGM gas (Wiener et al., 2013).

The magnitude of the CR population in the CGM is, however, highly debated. Some simulations (Butsky & Quinn, 2018; Ji et al., 2019; Dashyan & Dubois, 2020) claimed a CR dominated halo, which increases feedback efficiency of the outflowing gas by increasing the mass loading factor and suppressing the star formation rate. The ratio of CR pressure and thermal pressure ($P_{\text{CR}}/P_{\text{th}} = \eta$) controls this effect and can reach a large value exceeding 10 over a huge portion of Milky-way sized halo (Butsky & Quinn, 2018). Another simulation claimed that MW-sized halo at low redshift ($z < 1$) can be CR populated with η nearly 10 in outflow regions, although in warm regions ($T=10^5$ K) of halo, $\eta \leq 1$ (Ji et al., 2019). Dashyan & Dubois (2020) found in their simulation that dwarf galaxies, with virial mass $10^{10} - 10^{11} M_{\odot}$, can have a high value of η (~ 100) at 1 – 5 kpc from the mid-plane when isotropic diffusion is incorporated (their figure 1 and 2).

It is therefore an important question as to how much CR can be accommodated in the CGM in light of different observations. One of the most obvious effects of CR population in CGM is to suppress the thermal pressure of the hot phase which is also seen in the simulation of Ji et al. (2019). The recent work by Kim et al. (2021) pointed out that this reduction in thermal pressure would lower the thermal SZ (tSZ) signal, as tSZ probes the integrated thermal pressure in the halo. This diminished value of thermal pressure would also significantly change the abundance of high ionization species, and thereby jeopardise the interpretation of their column densities. In a recent work by Faerman et al. (2021), they modified their previous isentropic model Faerman et al. (2019) with significant non-thermal pressure ($\alpha = (P_{\text{nth}}/P_{\text{th}}) + 1.0 = 2.9$) and found that the gas temperature in the central region for the non-thermal model becomes lower than the value at which OVIII CIE temperature peaks, which in turn results in a lower OVIII column density. At low CGM masses, photoionization compensated for this effect by the formation of OVIII at larger radii, but for large gas masses and large mean densities (as in the Milky Way), photoionization effect is negligible and the total OVIII column density is low. In a previous work (Jana et al., 2020b), we constrained the CR pressure ($\eta = P_{\text{CR}}/P_{\text{th}}$) in the CGM in light of the isotropic γ -ray background (IGRB) and radio background,

using different analytical models (Isothermal Model: IT, Precipitation Model: PP) of CGM. In the case of IT model, the value of IGRB flux puts an upper limit of 3 on η , whereas all values of η are ruled out if one considers the anisotropy of the flux due to off-center position of solar system in Milky Way. However, in the case of PP model, IGRB flux value and its anisotropy allow a range of η from 100 to 230. In comparison, the constraints from radio background are not quite robust. In this chapter, we use the same analytical models (IT and PP) and put limits on CR population in the CGM of Milky Way by comparing the predicted OVIII absorption column densities (N_{OVIII}) with the available observations.

It might still be asked, why use OVIII as a probe? Previous works (Faerman et al., 2017; Roy et al., 2021b) explained the observed OVII, OVIII absorption column densities in the Milky Way without the incorporation of CR component using the analytical models of CGM used here. It is, therefore, important to study the effect of CR on these column densities with the inclusion of CR component in these models. Whereas the OVII ion has a plateau of favourable temperatures (5×10^5 K - 1×10^6 K), the suitable temperature for OVIII production (2×10^6 K) peaks near the temperature of the hot halo gas of Milky Way CGM. This particular fact makes OVIII abundance a sensitive probe of the CGM hot gas and motivates the choice of OVIII column density for comparison with the observations in order to constrain CR population in Milky Way CGM.

4.2 Density and Temperature Models

We study two widely discussed analytical models: 1) Isothermal Model (IT), 2) Precipitation Model (PP). These models have previously been studied in the context of absorption and emission lines from different ions (Faerman et al., 2017; Voit, 2019; Roy et al., 2021b). We assume the CGM to be in hydrostatic equilibrium within the potential of dark matter halo (ϕ_{DM}), with a metallicity of $0.3 Z_{\odot}$ (Prochaska et al., 2017a), so that,

$$\frac{dP_{\text{total}}}{dr} = -\frac{d\phi_{\text{DM}}}{dr}\rho, \quad (4.1)$$

where P_{total} is the total pressure and ρ and r are the density and radius, respectively. We consider the Navarro-Frenk-White (NFW) (Navarro et al., 1996a) profile as the underlying

dark matter potential in the IT model. However we slightly modify this potential in the case of the PP model as suggested in [Voit \(2019\)](#) by considering the circular velocity (v_c) to be constant ($v_{c,\max} = 220 \text{ km s}^{-1}$) up to a radius of $2.163 r_{\text{vir}}/c$ for a halo with $M_{\text{vir}} = 2 \times 10^{12} M_{\odot}$ and concentration parameter $c = 10$. We include non-thermal pressure support with CR population and magnetic field along with thermal pressure in these models. We consider the magnetic energy to be in equipartition with thermal energy ($P_{\text{mag}}=0.5P_{\text{th}}$) so that the total pressure $P_{\text{total}} = P_{\text{th}}(1.5 + \eta)$, which leads to,

$$\frac{dT}{dr} = - \left(\frac{1}{1.5 + \eta} \right) \left(\frac{\mu m_p}{k} \right) \frac{d\phi_{\text{DM}}}{dr} - \left(\frac{T}{n} \right) \frac{dn}{dr}. \quad (4.2)$$

Note that the magnitude of magnetic field in CGM is rather uncertain. While [Bernet et al. \(2008\)](#) claimed the magnetic field in CGM of galaxies at $z = 1.2$ to be larger than that in present day galaxies, the observations of [Prochaska et al. \(2019\)](#) suggested a value less than that given by equipartition. Yet another study claimed near-equipartition value after correlating the rotation measures of high- z radio sources with those in CGM of foreground galaxies ([Lan & Prochaska, 2020](#)).

The inclusion of non-thermal pressure suppresses the thermal pressure, and in turn the temperature or density or both of the CGM gas (also seen in recent simulation of [Ji et al. \(2019\)](#)). Our goal is to determine the effect of the inclusion of CR population on N_{OVIII} therefore constrain the CR population in Milky Way CGM. In addition to models with uniform η , we have studied the effect of varying η as a function of radius. For this, we have explored two contrasting variations, $\eta = A \times x$ (rising profile) and $\eta = A/x$ (declining profile) where $x=r/r_s$, where A is normalization of the profiles. We primarily studied the case with $A=1$, where the maximum value (for $\eta = x$) is $r_{\text{vir}}/r_s=c=10$. For $\eta = 1/x$, to avoid divergence at $r=0$ kpc we have started our calculation from $r=1$ kpc, therefore the maximum value in this case is $r_s/1 \text{ kpc} = 26$. We have shown the profiles of $\eta = x, 1/x$ in the figure [4.1](#). We have explored the effects of scaling up and down the values with these profiles as well (e.g., $\eta = Ax, B/x$, with $A, B \geq 1$). Although η can vary in a more complicated manner, we study these two particular cases (increasing and decreasing linearly) as the simplest representatives of a class of models in which η is allowed to vary with radius. It should be noted that the η here denotes the CR pressure in the diffuse hot gas with respect to thermal pressure of the hot gas.

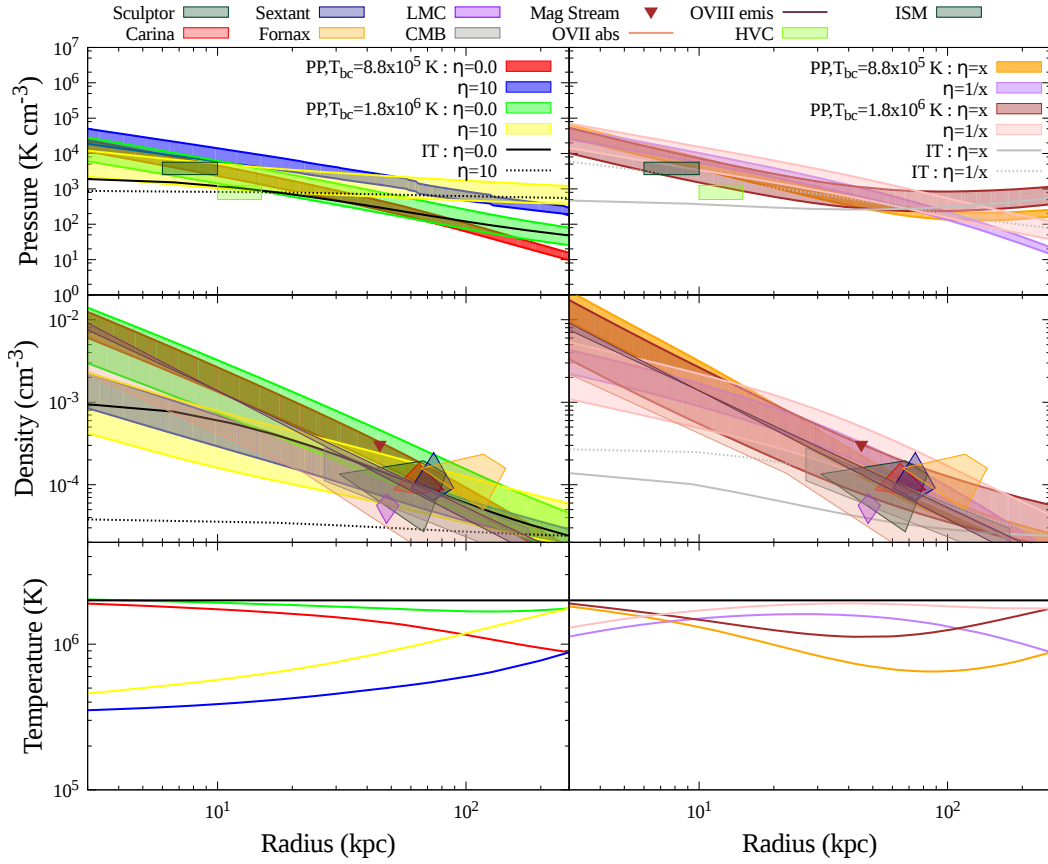


Figure 4.2: Total pressure (top panel), density (middle panel) and temperature (bottom panel) profiles for different models (IT and PP model) without ($\eta = 0$), with constant CR population ($\eta = 10$) and CR profile ($\eta = x$ and $1/x$), where $x=r/r_s$. Different observational constraints of pressure and density are also shown.

There are several ways to proceed, starting from equation 4.2. One way is to simply consider the temperature all over the CGM to be constant, which implies the LHS of the equation 4.2 to be zero. Another way is to use specific entropy to relate the two unknown quantities in the equation 4.2, temperature and density. We discuss these two ways in details in the following subsections.

4.2.1 Isothermal Model

The IT model provides the simplest model for the CGM gas with a constant temperature, so that,

$$\frac{dn}{dr} = - \left(\frac{1}{1.5 + \eta} \right) \left(\frac{\mu m_p}{kT} \right) \frac{d\phi_{\text{DM}}}{dr} \times n. \quad (4.3)$$

Previously hot gas has been modelled using isothermal profile by [Miller & Bregman \(2015b\)](#) where they fitted their model with the OVIII emission line observations which determined the hot gas mass to be within the range of $\sim 2.7 - 4.7 \times 10^{10} M_{\odot}$. Therefore, we normalize the density profile isothermal model without any non-thermal component such that the hot gas mass is $5 \times 10^{10} M_{\odot}$. It should be noted that the single temperature IT model does not represent the multiphase nature of the CGM. However, OVIII abundance is sensitive mostly to the hot phase of CGM which is well described by the single phase model. Therefore, our limits from the IT model will not change even if we have a two or three temperature model. Another way of incorporating multi-phase in IT model is to consider temperature distribution around the single mean temperature. We will show below that incorporation of such distribution in IT model will tighten our limit on CR. We can, therefore, treat the limit from our single temperature IT model as an upper limit. We then include a non-thermal pressure component in our model along with the thermal pressure. At this point, there are again several ways to proceed. One can fix the mass, and hence the density profile of the hot gas, and compensate for the decrease in thermal pressure by reducing the temperature ([Jana et al., 2020b](#)). Another way is to fix the temperature and reduce the density by keeping the boundary value same. However, for massive galaxies ($M_{\text{vir}} \geq 10^{12} M_{\odot}$) ([Li et al., 2015](#)) as well as Milky Way ([Miller & Bregman, 2015b](#)), the halo temperature is observed to be $\geq 2 \times 10^6$ K. This motivates us to assume a constant CGM temperature of 2×10^6 K for all the IT model (without and with non-thermal pressure) ([Miller & Bregman, 2015b](#)). We therefore vary the density

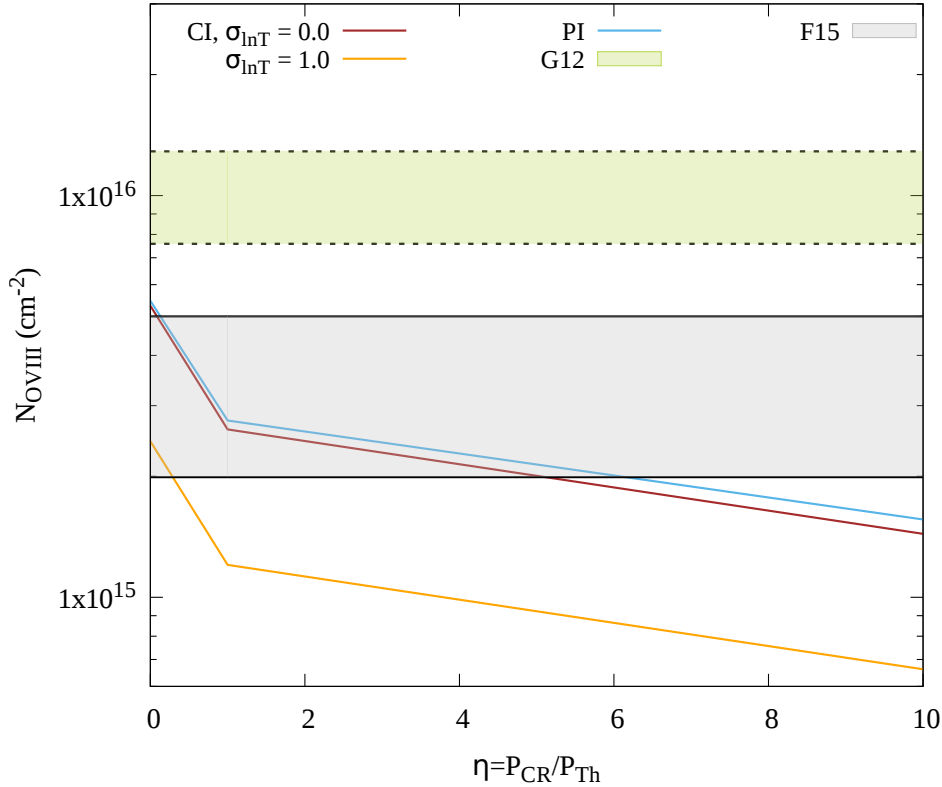


Figure 4.3: Variation of O VIII column density with η for IT model with different cases like CI without fluctuation (brown), with fluctuation (orange) and inclusion of PI (blue) with observational constraints by shaded regions from G12 (green) and F15 (grey).

profile for different values of η by keeping the density at the outer boundary fixed. This lowers the inner density for increasing value of η , and for $\eta = 10$, the hot gas mass becomes $2.7 \times 10^{10} M_{\odot}$ - the lower limit of hot gas mass obtained by [Miller & Bregman \(2015b\)](#). We, therefore, do not consider larger values of $\eta \geq 10$ for IT model. In the left panel of Figure 4.2, density profiles for IT model are shown by black solid ($\eta = 0$) and dotted lines ($\eta = 10$). The grey solid and dotted lines in the right panel of Figure 4.2 denote the $\eta = x$ and $1/x$ cases respectively.

4.2.2 Precipitation Model

The PP model is a physically motivated CGM model which uses the specific entropy as a connection between density and temperature. This model is briefly described in Section 1.3.3. A recent study by [Butsky et al. \(2020\)](#) has shown the effect of cosmic ray pressure

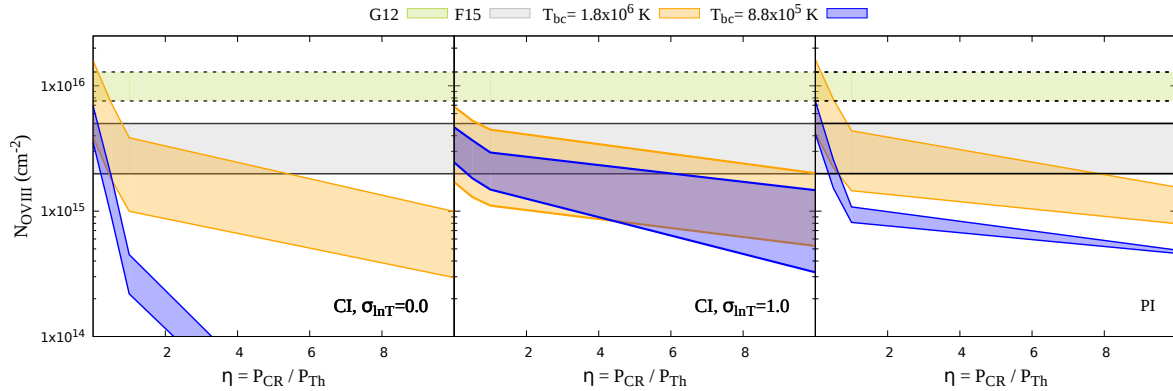


Figure 4.4: Variation of OVIII column density with η for PP model with different cases such as CI without fluctuation (left panel), with fluctuation (middle panel) and with PI (right panel). The observational constraints are shown by shaded regions from G12 (green) and F15 (grey). Different temperature boundary conditions are shown by orange ($T_{bc} = 1.8 \times 10^6$ K) and blue ($T_{bc} = 8.8 \times 10^5$ K) shaded regions where shades denote the mass range for each case.

on thermal instability and precipitation for different values of the ratio $t_{\text{cool}}/t_{\text{ff}}$. In their study, they found that large cosmic ray pressure decreases the density contrast of cool clouds. In our model, we keep $t_{\text{cool}}/t_{\text{ff}}$ to be constant throughout the halo. Although observations and simulations of intercluster medium point towards a value of this ratio between 5 – 20, it is a rather uncertain parameter in case of CGM studies and can have a wide range. We explore a range of the temperature boundary condition (T_{bc}) at the virial radius, between $T_{bc1} = 0.5\mu\text{m}_p v_c^2 = 1.8 \times 10^6$ K (\simeq virial temperature of the Milky-way) to $T_{bc2} = 0.25\mu\text{m}_p v_c^2 = 8.8 \times 10^5$ K (used originally by [Voit \(2019\)](#)). The inclusion of non-thermal pressure in the model suppresses the temperature and in turn the density. However we keep the mass of the CGM gas constant by decreasing $t_{\text{cool}}/t_{\text{ff}}$ ratio. The variation of $t_{\text{cool}}/t_{\text{ff}}$ with η for different values of temperature boundary condition can be seen in [Figure 3.2](#). We have taken the mass of the CGM in a range of $6 \times 10^{10} M_{\odot}$ (from the original model of [Voit \(2019\)](#) without CR) to $2.0 \times 10^{11} M_{\odot}$ (for cosmic baryon fraction) in case of T_{bc1} . However the mass range for T_{bc2} is $6 \times 10^{10} - 1.0 \times 10^{11} M_{\odot}$ since beyond this upper limit of mass, the value of $t_{\text{cool}}/t_{\text{ff}}$ falls below 1. We use the cooling function from CLOUDY ([Ferland et al., 2017](#)) for a metallicity of $0.3Z_{\odot}$.

We show the temperature and density profiles for PP in Figure 4.2 as shaded regions, bracketing the range of CGM mass mentioned above. In the left panel of Figure 4.2, the temperature and density profiles are shown in green and red for the PP model with no CR component whereas yellow and blue denotes $\eta = 10$ for T_{bc1} and T_{bc2} respectively. In the right panel of Figure 4.2, the temperature and density profiles are shown in brown and orange for the PP model with $\eta = x$ whereas pink and purple denote $\eta = 1/x$ for T_{bc1} and T_{bc2} respectively.

4.2.3 Observational constraints

Figure 4.2 also shows observational limits on pressure, density from (a) observations of OVII and OVIII (Miller & Bregman, 2015b), (b) CMB/X-ray stacking (Singh et al., 2018), (c) ram pressure stripping of LMC (Salem et al., 2015), Carina, Sextans (Gatto et al., 2013), Fornax, Sculptor (Grcevich & Putman, 2009b), (d) high-velocity clouds (Putman et al., 2012), (e) Magellanic stream (Stanimirović et al., 2002) and (f) ISM pressure (Jenkins & Tripp, 2011). We find that the obtained profiles including non-thermal components are within the observational limits. We can also compare the temperature and density profiles with those from simulations that include CR. In the PP model, the distinguishing feature is a rising temperature profile from the inner to the outer region. CR simulations also show such profiles, e.g., as shown in Figure 5 of Ji et al. (2019), especially beyond the galacto-centric radius of ~ 10 kpc. This particular profile from Ji et al. (2019) shows a decrease in temperature by a factor ~ 7 from the virial radius to ~ 10 kpc, similar to that shown in Figure 4.2 for $\eta = 10$ cases, although the outer boundary temperature is different in two cases. The difference in the profiles inward of ~ 10 kpc is not significant because the difference caused in the column density is small. The curves on the RHS of Figure 4.2 for declining η cases are similar to the simulation results expect at the outer radii, where PP models predict a declining temperature profile, which is not seen in CR-inclusive simulations. In brief, PP models with with constant or declining η profiles appear to capture the CR-simulation temperature (and consequently) density profiles.

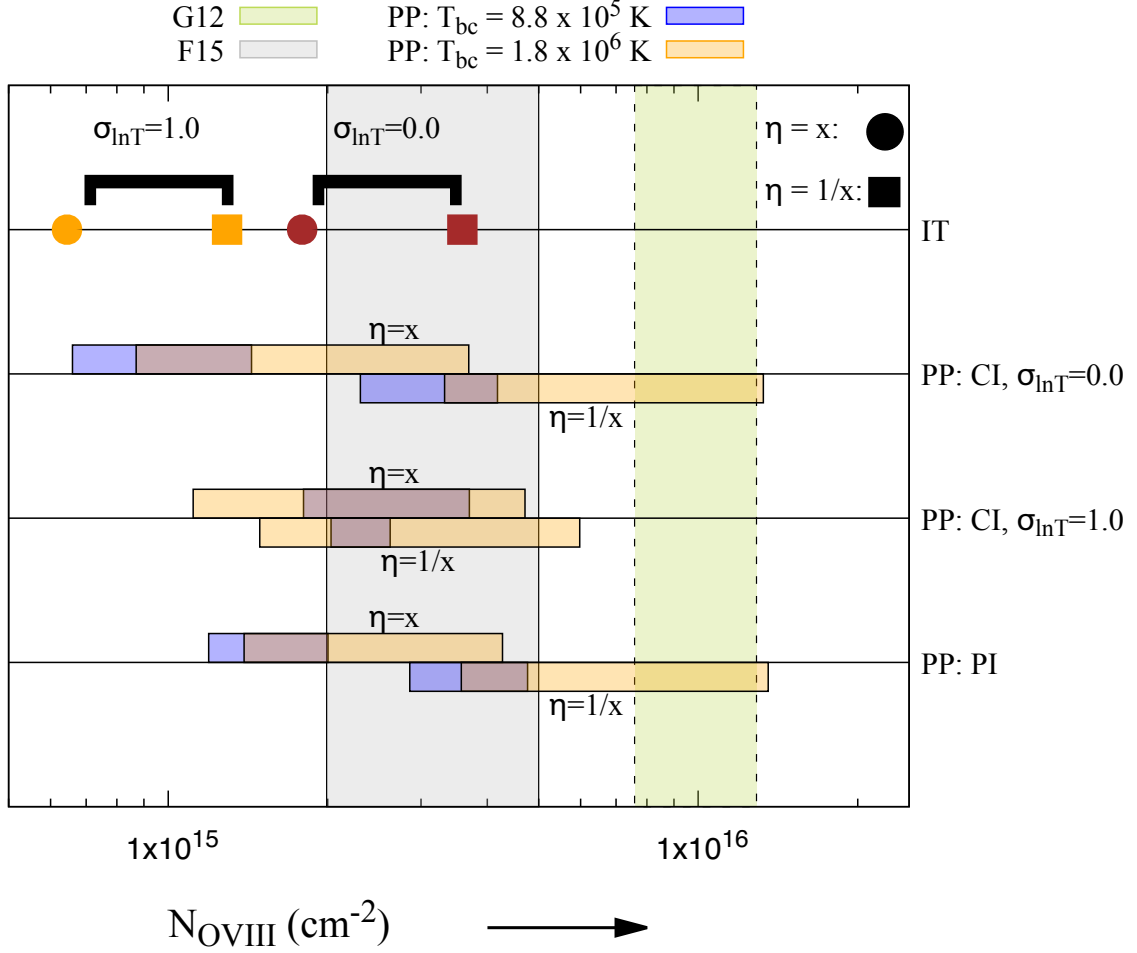


Figure 4.5: O VIII column density for different η profiles for IT and PP model with different cases like CI without fluctuation, with fluctuation and inclusion of PI with observational constraints by shaded regions from G12 (green) and F15 (grey). Different temperature boundary conditions are shown by orange ($T_{bc} = 1.8 \times 10^6$ K) and blue ($T_{bc} = 8.8 \times 10^5$ K) shaded regions where shaded region (above the lines for $\eta=x$ and below the lines for $\eta=1/x$) denote the mass range for each case in PP model. For IT model, brown and orange colours are used to denote $\sigma_{\ln T} = 0.0$ and 1.0 respectively whereas circles denote $\eta=x$ and squares denote $\eta=1/x$.

4.2.4 Log-normal Temperature Fluctuation

The observed widths and centroid offsets of OVI absorption lines in the CGM motivate us to consider dynamical disturbances causing temperature fluctuations in the CGM which results in a multiphase CGM gas. Low entropy gas parcels uplifted by outflows or high entropy gas can cool down adiabatically to maintain pressure balance and give rise to temperature and density fluctuations. Turbulence-driven nonlinear oscillations of gravity waves in a gravitationally stratified medium can be an alternative source for these fluctuations. Therefore, we consider an inhomogeneous CGM by including a log-normal temperature distribution (characterized by $\sigma_{\ln T}$) around the mean temperature.

Previous studies have considered a log-normal temperature fluctuation for CGM and successfully matched with CGM observations. [Faerman et al. \(2017\)](#) considered log-normal distribution for their two-temperature ($1.5 \times 10^6\text{K}$ and $5 \times 10^5\text{K}$) CGM model. They found the best fit value of $\sigma_{\ln T}$ to be 0.3 in order to explain the observed OVI column density. We have taken a similar approach. However we have a single temperature IT model. Therefore we consider a log-normal distribution of temperature around the single halo temperature in the case of IT model. In case of PP model, instead of a single temperature, we have a temperature profile $T(r)$. [Voit \(2019\)](#); [Roy et al. \(2021b\)](#) took into account temperature fluctuation in PP model by considering log-normal distributions with constant value of $\sigma_{\ln T}$ around the mean temperature $T(r)$ at each radius. [Voit \(2019\)](#) found that $\sigma_{\ln T} = 0.7$ satisfies the observed OVI column, whereas [Roy et al. \(2021b\)](#) concluded a range of $\sigma_{\ln T} = 0.6 - 1.0$ in order to explain the observed OVII, OVIII and their ratio. In the PP model, we follow the similar approach as in [Voit \(2019\)](#); [Roy et al. \(2021b\)](#).

4.3 Results

We calculate the ionization fraction of OVIII using CLOUDY ([Ferland et al., 2017](#)) with the input of density and temperature profiles derived from the CGM models. In order to incorporate temperature fluctuation, we calculate the ionization fraction for all the

Table 4.1: Constraints of η on the basis of N_{OVIII} observations by G12 and F15

Model	CI (without fluctuations)		CI (with fluctuations)		PI		
	G12	F15	G12	F15	G12	F15	
PP	T_{bc1}	0.5	6	–	10	0.5	8
	T_{bc2}	–	0.5	–	6	–	1
IT	–	5	–	1	–	6	

temperatures in a log-normal distribution using CLOUDY and integrate them over the corresponding log-normal distribution to get a mean ionization fraction. That means, for IT model we get a single mean ionization fraction corresponding to the log-normal distribution around the single temperature of the halo. But for PP model, we will get mean ionization fractions at each radius corresponding to the log-normal distributions with constant value of $\sigma_{\ln T}$ around the mean temperature $T(r)$ at each radius. We consider two cases: collisional ionization and photoionization along with collisional ionization. We use the extragalactic UV background (Haardt & Madau, 2012) at redshift $z = 0$ for photoionization. We take into account our vantage point of observation i.e the solar position and calculate the variation of column density with the Galactic latitude and longitude. We consider the median of the column densities for each value of η in order to compare with the observations.

In Figures 4.3 (for IT model) and 4.4 (for PP model), we show the variation of N_{OVIII} with η , considering collisional ionization (CI) and photoionization (PI) for different models. One can clearly see from these figures that with an increase in η , the value of N_{OVIII} decreases due to the decrease in the temperature. In Figure 4.3, the brown and blue lines denote the cases with CI and PI respectively in the IT model. In this figure, the orange colours denote the effect of log-normal fluctuations ($\sigma_{\ln T} = 1.0$). The cases of CI and PI do not differ for $\eta \leq 1$, since at $T \sim 10^6\text{K}$, CI dominates over PI. However, for $\eta \geq 1$, PI leads to slightly larger values of OVIII column density than the CI case, as further decrease in temperature leads to more production of OVIII by PI. It should be noted that if one considers temperature fluctuation around a single favourable

temperature of OVIII, there is less OVIII production with the increase in $\sigma_{\ln T}$.

In Figure 4.4 the orange shaded region indicates the boundary temperature near to virial temperature of halo 1.8×10^6 K (T_{bc1}) in PP model, whereas the blue shaded region denotes the boundary condition of 8.8×10^5 K (T_{bc2}) at virial radius. For the PP model, we show the cases with CI without ($\sigma_{\ln T} = 0.0$) and with fluctuation ($\sigma_{\ln T} = 1.0$) and PI in left, middle and right panel of Figure 4.4. The shaded regions in this figure refer to the CGM mass range mentioned earlier in the case of PP model. A boundary temperature that is close to the favourable temperature for OVIII yields more OVIII than one gets with lower boundary temperatures. However, with the inclusion of temperature fluctuations, one gets almost similar OVIII for both cases. With lower boundary temperature, the production of OVIII decreases for $\eta \geq 2$, because the inclusion of η shifts the temperatures from the CI peak of OVIII. However, considering PI in this case can increase the amount of OVIII.

In Figure 4.5, we show N_{OVIII} with different η profiles for both of the models. For IT model, we use brown and orange colours to denote $\sigma_{\ln T} = 0.0$ and 1.0 respectively whereas circles denote $\eta = x$ and squares denote $\eta = 1/x$. For PP model, different temperature boundary conditions are shown by orange ($T_{bc} = 1.8 \times 10^6$ K) and red ($T_{bc} = 8.8 \times 10^5$ K) shaded regions where shaded region (above the lines for $\eta=x$ and below the lines for $\eta=1/x$) denote the mass range for each case in PP model. One important point to notice here is that declining η profiles produce more OVIII than rising profiles.

4.3.1 Observations To Compare With

There are some soft X-ray observations of N_{OVIII} of Milky Way by Gupta et al. (2012), Miller & Bregman (2013) and Fang et al. (2015) (Hereafter referred as G12, MB13 and F15 respectively). G12 have measured N_{OVIII} along eight sight lines with *Chandra* telescope. They have quoted the equivalent width (EW) of OVIII instead of N_{OVIII} in their paper. However, their measured values of EW of OVIII are increased by 30% for the correction of systematic error and column densities were therefore re-calculated by Faerman et al. (2017). The re-calculated values of $\log(N_{\text{OVIII}})$ are 16.0(15.88 – 16.11) respectively. The green shaded region in Figures 4.3, 4.4 and 4.5 show the ranges of N_{OVIII} of G12 as re-

calculated by [Faerman et al. \(2017\)](#).

OVII lines have been studied by MB13 with *XMM-Newton* along the 26 sight-lines of distant AGNs as well as only one detection of OVIII with ratio of $N_{\text{OVII}}/N_{\text{OVIII}}=0.7\pm 0.2$. F15 observed the OVII absorption line for a broader sample of 43 AGNs which includes the sample from MB13. They reported a wider range of N_{OVII} ($10^{15.5-16.5} \text{ cm}^{-2}$) with the central value at 10^{16} cm^{-2} . However they have arrived at these values by setting aside the non-detection along 10 sight-lines. Adding these upper limits to the detected sample, [Faerman et al. \(2017\)](#) have come up with a new range of value of $\log(N_{\text{OVII}})$: 16.15(16.0 – 16.3). Although F15 did not report OVII lines, [Faerman et al. \(2017\)](#) calculated the median of ratio of N_{OVII} and N_{OVIII} from G12 observations. Using this ratio and re-calculated value of N_{OVII} from F15, they calculate $\log(N_{\text{OVIII}})$ which ranges from 15.3 to 15.7 with a median value of 15.5. The grey shaded regions in Figures 4.3, 4.4 and 4.5 show the ranges of N_{OVII} and N_{OVIII} of F15 as re-calculated by [Faerman et al. \(2017\)](#). Note that these re-derived ranges of N_{OVIII} indicate $1-\sigma$ uncertainty around the median value.

4.3.2 Constraints

We have tabulated the constraints on η for different models in Table 4.1. It is evident from Figures 4.3, 4.4 and 4.5 N_{OVIII} can help in putting upper limits on η . For IT model, we find that $\eta \leq 5$ if one consider only CI with no temperature fluctuations. The inclusion of PI slightly changes this constraint to $\eta \leq 6$. We can also clearly see that introducing log-normal fluctuations makes these constraints even stronger ($\eta \leq 1$) (Figure 4.3). Interestingly, we find that the models with varying η with radius can be accommodated within observational limits by suitably decreasing $\sigma_{\ln T}$ (Figure 4.5). For example, in the Figure 4.5, the model of increasing η with radius for $\sigma_{\ln T} = 0$ is fairly close to the bottom range of F15's data, and for the opposite case ($\eta = 1/x$), decreasing $\sigma_{\ln T}$ sufficiently can put in the ballpark of F15's data.

A larger upper-limit ($\eta \leq 8$) is allowed for the case of PP model with T_{bcI} if one considers of observations of F15. In general, we find that the inclusion of temperature fluctuation relaxes these limits in all the cases by allowing larger value of η (≤ 10)

(Figure 4.4). Furthermore, spatial variation of η (Figure 4.5) can be allowed within the observational limits by increasing temperature fluctuations and using suitable mass range in PP model. In particular, models with declining ratio of CR to thermal pressure with radius (as hinted in the simulations of, e.g., [Butsky & Quinn \(2018\)](#)) predict OVIII column densities within observational limits. Note that, in the PP case the requirement for $\sigma_{\ln T}$ for varying η models runs opposite to that in IT, where varying η models require smaller $\sigma_{\ln T}$ in order to be viable.

To see the effect of normalization for the cases $\eta = Ax$ or $= A/x$, we have increased the value of A , which increases the CR pressure. This leads to a decrease in the density or temperature or both, and consequently decreases the OVIII column density. Therefore, all the plots in Figure 4.5 will shift towards left with the increment of the normalization. That implies that $\eta = A \times x$ cases are not allowed for both IT and PP models even with the inclusion of photoionization and temperature fluctuations. However, in the case of the PP model, for $\eta = A/x$ with $A \geq 1$, all the cases do not satisfy the observational constraints except for the case with boundary temperature 1.8×10^6 K, for $A \leq 10$. On the other hand, in the case of IT, for the $\eta = A/x$ profiles, the OVIII column densities are within the observational constraints for the cases $A \leq 8$. That implies these models allow the central region to have large CR pressure even $\eta = 200$, but not in the outer halo. This result differs from the findings by previous simulations which shows CR dominated outer halo ([Butsky & Quinn, 2018](#)). As normalization increment shifts all the plots towards left, the inclusion of temperature fluctuations are ruled out for the models with $\eta = A/x$ profiles except for a very small range with high CGM mass in the PP model with boundary temperature 1.8×10^6 K and $A \leq 2$.

4.4 Discussion

Our constraints allow larger values of η for most of the cases in comparison to the isentropic model by [Faerman et al. \(2019\)](#); [Faerman et al. \(2021\)](#). In their recent work ([Faerman et al., 2021](#)), they have considered three cases for their model : 1) with only thermal pressure i.e, $\alpha = (P_{nth}/P_{th}) + 1.0 = ((P_{CR} + P_B)/P_{th}) + 1.0 = 1.1$, 2) with standard case as considered in [Faerman et al. \(2019\)](#) i.e, $\alpha = 2.1$ and 3) with significant

non-thermal pressure where $\alpha = 2.9$. Note that the the above mentioned values of α are the values at the outer boundary and the profiles of α will follow a declining pattern as radius decreases (see blue curve in the right panel of Figure 2 by [Faerman et al. \(2019\)](#)). With our definition of η , along with the magnetic field value used by us, we can convert these α values to $\eta \sim 0, 0.6, 1.4$, respectively, for their three cases. The thermal case matches N_{OVIII} observations up to CGM mass of $10^{11}M_{\text{solar}}$, and for the standard case, the value of N_{OVIII} is comparable to the observed value. However, for the significant non-thermal case, the OVIII value is lower than the observations by a factor of ~ 10 for a CGM mass of $10^{11}M_{\text{solar}}$. Therefore, one can say that $\eta < 0.6$ is allowed for the isentropic model. For PP model, we get upper limit of $\eta \sim 0.5$ for two cases which are therefore in agreement with the constraint from the isentropic model. However, for most of our models, the upper limits derived in the present work are larger than the isentropic model.

It should be noted that the limits of η derived here translate to constraints on cosmic ray pressure in the hot diffuse CGM, and one may wonder about the CR pressure in the cold gas. CR pressure scales with density ($P_{\text{CR}} \propto \rho^{\gamma_{c,eff}}$, where $\gamma_{c,eff}$ is the effective adiabatic index of the CR) of the gas, where the adiabatic index depends on the transport mechanism ([Butsky et al., 2020](#)), the limits of CR pressure in the cold gas would be different from what we have found for the hot gas. If CRs are strongly coupled to the gas, then in the limit of slow CR transport, *i.e.*, if the only CR transport mechanism is advection, $\gamma_{c,eff} = \gamma_c = 4/3$. In this case, CR pressure can be higher in cooler, denser gas than in the hot gas. However, in the limit of efficient CR transport *i.e.*, if there are CR diffusion, streaming along with advection, the CR pressure will be redistributed from high density, cold region to diffuse, hot region of CGM which will lower the $\gamma_{c,eff}$. In this limit, $\gamma_{c,eff} \rightarrow 0$, and the limits of CR pressure in the cold phase are nearly equal to the CR pressure in hot phase. In the context of a single phase temperature with temperature gradient, if one considers CR pressure in the hot phase to scale as $\rho_g^{\gamma_{c,eff}}$ then η is proportional to $\rho_g^{\gamma_{c,eff} - (5/3)}$, as adiabatic index for gas is $5/3$. Then η will be proportional to $\rho_g^{-1/3}$ and $\rho_g^{-5/3}$ respectively depending on slow and effective transport mechanism. This implies that η is smaller in denser gas and hence mimic a rising profile of η in case of the single hot phase gas, which we have shown in this chapter.

However, these scaling relations are for adiabatic situations, which is not the case for

PP model which involves energy loss. In the context of cold gas that may have condensed out of the hot gas, it is possible for the cold gas to contain a significant amount of CR pressure, with a large value of η for cold gas. Simulations by [Butsky et al. \(2020\)](#) (their figure 10) showed that in the limit of slow cosmic ray transport, the value of η is quite different for hot and cold gas. In the limit of efficient transport, cosmic ray pressure is decoupled from the gas, and η has similar values in hot and cold gas. If we recall the observation by [Werk et al. \(2014\)](#), that the cold phase of CGM nearly follows the hot gas density profile then for small density contrast, the CR pressure in the cold phase and hot phase may not differ much even with different transport mechanisms. But even with small density contrast, thermal pressure of cold gas will be smaller than hot phase by two order of magnitude due to the temperature difference, which allows for a larger upper limit on η . However, packing more CR in cold gas will not have any effect on the constraints derived here. In fact, this may be one way to circumvent the constraints on η described here.

We have not included any disc component in the present work. A recent work by [Kaaret et al. \(2020\)](#) took into account an empirical disc density profile motivated by the measured molecular profile of MW along with the halo component. They pointed out that the high density disc model can well fit the MW's soft X-ray emission, whereas it under predicts the absorption columns. Their conclusion is that the dominant contribution of X-ray absorption comes from the halo component due to large path length. Also this difference in contribution comes from the fact that the absorption is proportional to density whereas emission measure is proportional to density square. Therefore, considering only the halo component and making the comparison with the absorption column is justified.

Note that the limits derived here are sensitive to some of the parameters such as the magnetic field and metallicity. Increase (decrease) in the magnetic pressure would increase (decrease) the total non-thermal pressure, which would decrease (increase) the limit on η . However, given the uncertainty in the magnetic field strength in the CGM, equipartition of magnetic energy with thermal energy is a reasonable assumption. For a collisionally ionized plasma, which we assume for the CGM gas, the column density is

proportional to the metallicity (Z) in the case of IT model, whereas it is proportional to $Z^{0.3}$ for the PP model (see eq 17 of [Voit \(2019\)](#)). In the photoionized case, the dependence on metallicity will be stronger since the ion abundance would also depend on the metallicity. Also note that the limits derived here refer to CR population spread extensively in the CGM. Localized but significant CR population may elude the above limits. However, we also note that most of the contribution of the limits come from the inner region, where OVIII exists otherwise and is suppressed due to CR. Therefore, our limits also pertain to localized CR populations in the inner regions.

4.5 Conclusion

We have studied two analytical models of CGM (Isothermal and Precipitation model) in hydrostatic equilibrium in light of the observations of N_{OVIII} in order to constrain the CR population in the Milky Way CGM. We found that $\eta \leq 10$ in the case of no photoionization and including temperature fluctuations in the PP model whereas IT model allows $\eta \leq 6$ with inclusion of PI. However, it should be noted that IT is an extremely simplistic model and the inclusion of non-thermal component leads to a very low density. The limits from IT may therefore be only of academic interest.

Combined with the limits derived from γ -ray background [Jana et al. \(2020b\)](#), our results make it difficult for a significant CR population in our Milky Way Galaxy. However, models in which the ratio of CR to thermal pressure varies with radius (preferably declining with radius) can be accommodated within observational constraints, if they include suitable temperature fluctuation (larger σ_{lnT} for PP and lower for IT), although making allowances for large value of η only in the central region.

Chapter 5

Gamma-rays from the circumgalactic medium of M31

Based on:

“Gamma-rays from the circumgalactic medium of M31”

Manami Roy, Biman B. Nath

MNRAS, Volume 514, Issue 1, July 2022, Pages 1412–1421,

[Roy & Nath \(2022a\)](#)

We discuss the production of γ -rays from cosmic rays (CR) in the circumgalactic medium (CGM) of Andromeda (M31) in light of the recent detection of γ -rays from an annular region of $\sim 5.5 - 120$ kpc away from the M31 disc. We consider the CRs accelerated as a result of the star-formation in the M31 disk, which are lifted to the CGM by advection due to outflow and CR diffusion. The advection time scale due to bulk flow of gas triggered by star formation activity in the M31 disc is comparable (\sim Gyr) to the diffusion time scale with diffusion coefficient $\geq 10^{29}$ cm² s⁻¹ for the propagation of CR protons with energy ~ 412 GeV that are responsible for the highest energy photons observed.

Key Results:

- We show that a leptonic origin of the γ -rays from cosmic ray (CR) electrons has difficulties, as the inverse Compton time scale (\sim Myr) is much lower than advection time scale (\sim Gyr) to reach 120 kpc.
- Invoking CR electrons accelerated by accretion shocks in the CGM at $\sim 100 - 120$ kpc does not help since it would lead to diffuse X-ray features that are not observed.
- We, therefore, study the production of γ -rays via hadronic interaction between CR protons and CGM gas with the help of numerical two-fluid (thermal + CR) hydrodynamical simulation. We find that a combination of these mechanisms, that are related to the star formation processes in M31 in the last \sim Gyr, along with diffusion and hadronic interaction, can explain the observed flux from the CGM of M31.

5.1 Introduction

The discovery of π -meson in 1947 and the consequent $\pi^0 \rightarrow 2\gamma$ decay pointed towards the fact that γ -rays can be a useful probe of charged high energetic cosmic ray (CR) particles (Morrison, 1958). Unlike CR particles, which gets easily deflected by magnetic field and lose its source information, the γ -rays retain their directionality. Therefore, sources such as supernova remnants, the Galactic plane and Galactic halo where CR particles are born or confined to, can be observed in γ -rays. Beginning with the very first γ -ray telescope carried into orbit, on the Explorer 11 satellite in 1961 to very recent launched Fermi-LAT telescope in 2008, γ -ray astronomy has come a very long way.

There have been attempts to observe our nearest neighbour galaxy Andromeda (M31) in γ -rays since 1970s. Observation by Ackermann et al. (2017) showed that the inner galaxy (IG) (at galacto-centric distance < 5.5 kpc) of M31 has γ -ray luminosity of $(5.0 \pm 3.0) \times 10^{38}$ erg s^{-1} in $0.1 - 100$ GeV. But a recent analysis of 7.6 years of Fermi-LAT data by Karwin et al. (2019) has revealed a very interesting signature of γ -ray emission. Their analysis includes observations from a projected distance of ~ 200 kpc from M31's centre. They have noticed an excess (positive residual) in the γ -ray flux after subtracting the contribution from the Milky Way foreground emission as well as the isotropic component (*e.g.* unresolved extra-galactic diffuse γ -ray emission), residual instrumental back-ground, and possible contributions from other Galactic components with a rough isotropic distribution. In order to explain this excess emission they added M31-related components by considering a uniform spherical template centering the M31, consisting of three regions a) Inner galaxy (IG) : < 5.5 kpc, b) Spherical halo (SH) : $5.5-120$ kpc c) Outer halo (OH) $120-200$ kpc. They found that the positive residual can be flattened by adding emission from these three spherical regions of M31. They concluded that if this excess originated from M31, it is extended up to $120 - 200$ kpc from the centre of M31.

This observation has triggered a few plausible ideas to explain this extended γ -ray excess. Karwin et al. (2021) suggested dark matter annihilation for the origin of this excess. For their model, cold dark matter particles (weakly interacting massive particles (WIMP)) annihilated to bottom quark giving rise to γ -ray emission. They concluded

that DM particles with mass 45–70 GeV are favourable to produce the observed γ -ray excess in the SH region. [Recchia et al. \(2021a\)](#) proposed a different scenario in which the CRs are produced in the galactic centre of M31 and transported to the SH region by means of buoyant bubble(s). They also suggested *in-situ* acceleration of CRs at strong shocks in the SH region. These CRs can produce the extended γ -ray emission through hadronic interaction with protons in the circumgalactic medium (CGM), as well as through inverse Compton scattering of CMB photons by high energy CR electrons. Another recent work by [Zhang et al. \(2021\)](#) considered the production of CRs due to the star formation activity in the disc and propagation to the SH region by diffusion. The hadronic interaction of those CR protons with CGM protons would give rise to observed γ -ray emission at SH region. Incidentally, they have not considered advection by outflow for CR transport.

In this chapter, we study the case of CRs being produced as a consequence of star-formation activity in the disc and *in-situ* acceleration in the shocks of outflowing gas. Our approach is different from the previous studies in that we consider the CR particles to be lifted to the SH region by the combination of advection via the outflow as well as diffusion. Then they interact with CGM protons and give rise to the observed γ -ray signature in the SH region. We use two fluids (thermal component and non-thermal component: cosmic ray) hydrodynamical numerical simulation *PLUTO* ([Mignone et al., 2007](#)), in order to simulate a γ -ray image of M31 as observed from the solar position of Milky Way and compare with the above mentioned γ -ray observation.

5.2 Leptonic Interaction

Consider first the case of leptonic origin for the observed γ -ray excess, where CMB photon can give rise to γ -rays by inverse Compton (IC) scattering by CR electrons. However the IC loss time scale is short (a few Myr), making it difficult to use CR electrons produced in the galactic centre or disk for the purpose of γ -ray production at a distance of ~ 120 kpc. [Recchia et al. \(2021b\)](#) explored a scenario in which accretion shock due to infalling material can produce the necessary CRs by *in-situ* acceleration. This necessitates a shock speed of ≈ 400 km s⁻¹, and gas density, $\approx 10^{-4}$ cm⁻³. However, this scenario poses a problem. Such a shock would also produce diffuse soft X-ray emission, since the

post-shock temperature is $\approx 3 \times 10^6$ K. Considering the shocked gas region (width) to be $\Delta r \sim r_{\text{kpc}}$ kpc, a shell of radius $r \sim 100$ kpc has volume $4\pi r^2 \Delta r \approx 3.4 \times 10^{69} (\Delta r_{\text{kpc}}) \text{ cm}^3$ and would subtend a solid angle of $2\pi r \Delta r / D^2 \approx 10^{-3} (\Delta r_{\text{kpc}}) \text{ sr}$. The free-free surface brightness, in $\sim 0.2\text{--}1$ keV band, is $\approx 10^{-6} \text{ erg s}^{-1} \text{ cm}^{-2} \text{ sr}^{-1}$. The post-shock density is assumed to be 4 times the ambient, since the cooling time is ≈ 3 Gyr, and the shock is, therefore, not radiative. Note that the surface brightness estimate is independent of the width Δr because it appears in the expressions for both volume and solid angle. The corresponding count rate in the ROSAT PSPC would be¹ $2.5 \times 10^{-3} \text{ counts s}^{-1} \text{ arcmin}^{-2}$, and therefore would have been rather bright in ROSAT all-sky survey in the region, but there is no such feature in the survey map (Snowden et al., 1997) (their figure 2f). Therefore, leptonic origin of the γ -ray excess does not seem to be a plausible scenario. This prods us to focus on the hadronic origin for the observed γ -ray.

5.3 Hadronic interaction

In the hadronic interaction, a fraction ~ 0.17 of proton energy goes to pion (e.g. Reynoso et al. (2008)), which then decays into two γ -ray photons. For the production of 35 GeV γ -rays, the highest energy photon observed in the γ -ray excess, the proton energy should be at least $35 \times 2/0.17 \text{ GeV} = 412 \text{ GeV}$. The source of such CR protons, responsible for the observed γ -ray excess, can be either the star formation (SF) activity in the disc of M31, or *in-situ* formation of CRs in the CGM due to shocks present there. We consider these two possibilities below.

5.3.1 Star formation activity

Considering the mechanical power associated with supernovae (assuming Salpeter initial mass function and stellar masses in the range of $0.1\text{--}100 M_{\odot}$) and assuming a fraction $\eta \approx 0.1$ of this power being deposited in CRs, the CR luminosity is given by,

$$L_{\text{CR}} = 1.12 \times 10^{41} \text{ erg s}^{-1} \frac{\eta}{0.1} \times \frac{\text{SFR}}{(4.8 M_{\odot}/\text{year})}. \quad (5.1)$$

¹using <https://heasarc.gsfc.nasa.gov/cgi-bin/Tools/w3pimms/w3pimms.pl>

As the sound crossing time is ≈ 1 Gyr for a 10^6 K gaseous halo of 120 kpc radius, any activities in the disk before 1 Gyr would have left the region of 120 kpc radius by now. Therefore, we consider that the star formation history of the last 1 Gyr of M31, as given in [Williams et al. \(2017\)](#) (tabulated 1st, 2nd and 3rd columns in table 3 : 3rd column should be multiplied by 3 for scaling to total M31 star-formation rate) would have an effect on the observed γ -ray excess at SH. Here, we have scaled the star formation rate (SFR) in terms of $4.8 M_{\odot}$ /year, which is the highest value in the last 1 Gyr. The CR protons are accelerated in the central region and advected to the CGM by galactic outflow. The advection time scale to a distance 120 kpc (the outer boundary of SH) is

$$t_{\text{adv}} = \left(\frac{154\pi}{125}\right)^{1/3} \left(\frac{R^5 \rho_0}{L}\right)^{1/3} \approx 1.0 \text{ Gyr} \left(\frac{R}{120 \text{ kpc}}\right)^{5/3} \left(\frac{SFR}{4.8 M_{\odot}/\text{yr}}\right)^{-1/3} n_{-3}^{1/3}. \quad (5.2)$$

Here, the ambient density is written as $n = 10^{-3} n_{-3} \text{ cm}^{-3}$. However, the diffusion time scale for protons responsible for 20 GeV photons to reach a distance of ~ 120 kpc is ($\approx R^2/6D$)

$$t_{\text{diff}} \approx 1.0 \text{ Gyr} \left(\frac{R}{120 \text{ kpc}}\right)^2 \left(\frac{D_{1 \text{ GeV}}}{10^{29} \text{ cm}^2 \text{ s}^{-1}}\right)^{-1} \left(\frac{E}{412 \text{ GeV}}\right)^{-1/3}. \quad (5.3)$$

Therefore, if we use the star formation history of M31 in the last ~ 1 Gyr, then the CRs accelerated in this period would be confined within the SH region. Also, the above estimate shows that diffusion can compete with advection if the GeV scale diffusion coefficient is $\geq 10^{29} \text{ cm}^2 \text{ s}^{-1}$. However, note that if the diffusion coefficient is smaller than this, say $10^{28} \text{ cm}^2 \text{ s}^{-1}$, the diffusion time scale increases to 10 Gyr and can not compete with advection, as we will also show in our simulation below.

However, the time scale for pion production by interaction between CR proton and CGM proton is $t_{\pi} = \frac{1}{\sigma_{pp} n_H c} = 30 \times \left(\frac{n}{10^{-3}}\right)^{-1} \text{ Gyr}$, which is larger than the escape (diffusion) time. Therefore, M31 (and its CGM) cannot be considered a calorimeter for CR protons. The calorimetric fraction ($f_{\text{cal}}(E)$) would be $1 - e^{-(t_{\text{res}}/t_{\pi})} \sim 0.04$ (considering diffusion coefficient at 1 GeV to be $10^{29} \text{ cm}^2 \text{ s}^{-1}$). Incidentally, [Krumholz et al. \(2020\)](#) has recently developed a model for the calorimetric fraction, by balancing the CR streaming instability and ion-neutral damping. For Milky Way (with similar order of magnitude of

star formation rate as in M31), they have estimated $f_{\text{cal}}(E)$ to be $\sim 0.04 - 0.05$ in the case of 100 GeV CR protons, similar to our estimate derived above.

Roughly a fraction of ≈ 0.3 of CR energy is emitted in γ -rays through π_0 decay. Hence the expected γ -ray luminosity is

$$L_{\gamma, \text{H}} = 1.86 \times 10^{39} \text{ erg s}^{-1} \left(\frac{\eta}{0.1} \right) \left(\frac{f_{\text{cal}}}{0.05} \right) \frac{\text{SFR}}{(4.8 \text{ M}_{\odot}/\text{yr})} \quad (5.4)$$

This estimate matches with the calculated the total γ -ray luminosity from SH by [Recchia et al. \(2021b\)](#) which is 1.7×10^{39} and 1.9×10^{39} erg/sec by using the spectral fit of power-law with exponential cut-off and power law respectively obtained by [Karwin et al. \(2019\)](#). Note that we have taken the highest SFR over the past 1 Gyr for this estimate. Consideration of the true SF history can change these calculations a little bit. These estimates are to motivate the idea that it is indeed possible to create CR protons by the SF activity that can give rise to observed γ -ray excess in the SH region.

5.3.2 In-situ formation

Next, we explore the case of CR protons acceleration at a spherical shock located at 120 kpc i.e. the position of SH of M31, ultimately giving rise to 35 GeV γ -ray photons. For this to occur, the acceleration time scale should be smaller than the pion decay time scale. The acceleration time scale is $ar_L c / (3 \times v_{\text{sh}}^2)$ ([Drury, 1983](#)) (assuming Bohm diffusion), where r_L refers to the Larmor radius and $a \sim 10$ is a numerical factor that takes into account the compression of gas and magnetic field behind the shock, v_{sh} is shock speed, $B = 10^{-6} B_{\mu\text{G}}$ is the magnetic field. Equating this with the pion-decay loss time for protons, one gets a maximum energy of protons as,

$$E_{\text{max}} \sim 2.4 \times 10^8 \text{ GeV } B_{\mu\text{G}} \left(\frac{v_{\text{sh}}}{100 \text{ km s}^{-1}} \right)^2 n_{-3}^{-1} \left(\frac{a}{10} \right)^{-1}. \quad (5.5)$$

The maximum CR proton energy can also be calculated according to the Hillas criterion ([Hillas, 1984](#)), according to which the accelerating region (L) should be larger than $2r_L(c/v_{\text{sh}})$. This yields,

$$E_{\text{max}} \approx \frac{1}{2} 10^6 \text{ GeV } L_{\text{kpc}} B_{\mu\text{G}} \left(\frac{v_{\text{sh}}}{100 \text{ km s}^{-1}} \right), \quad (5.6)$$

where L_{kpc} is the size of the acceleration region in kpc. These estimates imply that protons with energy 412 GeV (corresponding to 35 GeV γ -ray photons) can be produced at 120 kpc i.e. in the SH region. The equipartition B field is of order 0.01 μG , if the ambient thermal pressure is $\sim 10^{-14} \text{ erg cm}^{-3}$ (corresponding to, say, $T \sim 10^6 \text{ K}$ and $n \sim 10^{-4} \text{ cm}^{-3}$). Therefore, *in-situ* acceleration of CR protons to $\sim 412 \text{ GeV}$ that is required to explain the observations is possible even if the size of the accelerating region is $\sim 80 \text{ pc}$.

Suppose a fraction f of the shock energy density (ρv_{sh}^2 , where the velocity of shock at that instant is $v_{\text{sh}} = 3R/5t$), is transferred to CR protons. The CR energy density is then given by

$$\begin{aligned} \epsilon_{CR} \approx & 7.7 \times 10^{-15} \text{ erg cm}^{-3} \left(\frac{R}{120 \text{ kpc}} \right)^{-4/3} \left(\frac{SFR}{4.8 M_{\odot}/\text{yr}} \right)^{2/3} \\ & \times n_{-3}^{1/3} \times \left(\frac{f}{0.1} \right). \end{aligned} \quad (5.7)$$

The γ -ray luminosity due to hadronic interaction between CR proton and CGM proton is

$$L_{\gamma} = \int E_{\gamma} \tilde{q}_{\gamma}(E_{\gamma}) dE_{\gamma} \int dV \left[n_{\text{CGM}} \epsilon_{\text{cr}} \right], \quad (5.8)$$

where the source function \tilde{q} is given by,

$$\tilde{q}_{\gamma} = \left[\frac{\sigma_{\text{pp}} c \left(\frac{E_{\pi^0}}{\text{GeV}} \right)^{-\zeta_{\gamma}} \left[\left(\frac{2E_{\gamma}}{E_{\pi^0}} \right)^{\delta_{\gamma}} + \left(\frac{2E_{\gamma}}{E_{\pi^0}} \right)^{-\delta_{\gamma}} \right]^{-\zeta_{\gamma}/\delta_{\gamma}}}{\xi^{\zeta_{\gamma}-2} \left(\frac{3\zeta_{\gamma}}{4} \right) \frac{E_{\text{p}}}{2(\zeta_{\text{p}}-1)} \left(\frac{E_{\text{p}}}{\text{GeV}} \right)^{1-\zeta_{\text{p}}} \beta \left(\frac{\zeta_{\text{p}}-2}{2}, \frac{3-\zeta_{\text{p}}}{2} \right)} \right]. \quad (5.9)$$

Here $\xi = 2$ is the multiplicity factor, E_{p}/E_{π^0} is the rest mass energy of proton/pions (π^0), ζ_{p} and ζ_{γ} are the spectral indices of the incident CR protons and emitted γ -ray photons respectively, $\delta_{\gamma} = 0.14\zeta_{\gamma}^{-1.6} + 0.44$ is the spectral shape parameter and $\sigma_{\text{pp}} = 32(0.96 + e^{4.4-2.4\zeta_{\gamma}}) \text{ mbarn}$ (see Equations (8), (19)-(21) in [Pfrommer & Enßlin 2004](#)). We use $\zeta_{\text{p}} = \zeta_{\gamma} = 2.3$ in our calculations following the spectral fit of [Ackermann et al. \(2015\)](#).

For CRs produced at the shock front, the corresponding shell volume is $4\pi R^2 \Delta R \approx 5.8 \times 10^{71} \text{ cm}^3$, for $R \approx 120 \text{ kpc}$ and $\Delta R \approx 100 \text{ kpc}$. From Eq 5.8, the γ ray luminosity

within the energy range of 0.1–100 GeV is given by,

$$L_\gamma = 4.5 \times 10^{38} \text{ erg/sec} \left(\frac{R}{120 \text{ kpc}} \right)^{-4/3} \left(\frac{SFR}{4.8 \text{ M}_\odot/\text{yr}} \right)^{2/3} \times n_{-3}^{1/3} \times \left(\frac{f}{0.1} \right). \quad (5.10)$$

This is $\sim 25\%$ of the observed γ -ray luminosity. However, the shock speed 120 kpc is

$$v \sim 67 \text{ km/s} \left(\frac{R}{120 \text{ kpc}} \right)^{-2/3} \left(\frac{SFR}{4.8 \text{ M}_\odot/\text{yr}} \right)^{1/3} n_{-3}^{-1/3}. \quad (5.11)$$

which is roughly equal to the local sound speed for CGM at virial temperature $\approx 10^6$ K. In other words, the outflow at this distance is subsonic. Therefore, although the estimated γ -ray luminosity is comparable to the observed value, the shock at SH region can not be expected to accelerate CRs. At the same time, there would be shocks due to the formation of cold clouds from cooling of the gas behind the shock front, and their turbulent motion. These shocks can accelerate CR protons, which is, however, difficult to estimate analytically. We therefore perform hydrodynamical simulations to build a complete scenario by capturing this process and estimate the γ -ray luminosity of M31 CGM.

5.4 Simulation setup

5.4.1 Initial Condition

The initial galaxy setup for M31 used here is similar to that of [Sarkar et al. \(2015\)](#). We consider two components: a halo with gas at 3×10^6 K temperature around a disk of 4×10^4 K temperature. The halo gas contains 11% of virial mass whereas the stellar disk consists of 5% of virial mass ([Mo et al., 1998](#)). We take into account a rotating disk gas of solar metallicity and a non-rotating halo gas with 0.1 of solar metallicity under the gravitational potential by stellar disk (Miyamoto & Nagai potential [Miyamoto & Nagai \(1975\)](#)) and dark matter halo (modified Navarro-Frenk-White Model [Navarro et al. \(1997\)](#)). We use the cooling function of [Sutherland & Dopita \(1993b\)](#) for radiative cooling of the warm disc and hot halo gas, and the metallicity dependence is taken into account by linear interpolation of the cooling function between two metallicities (Z_\odot and

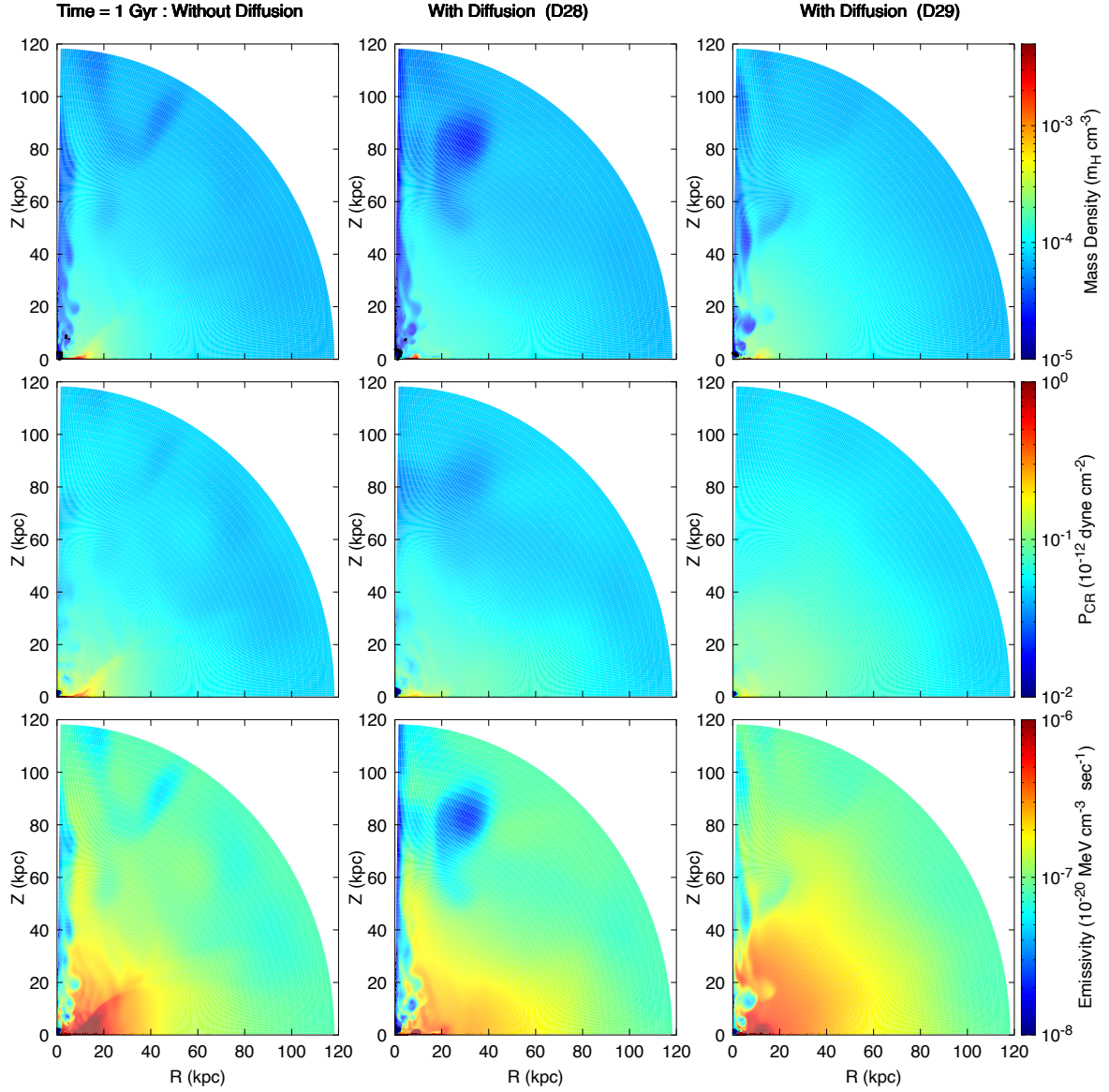


Figure 5.1: The density, CR pressure and γ -ray emissivity at the simulation time of 1 Gyr for the cases of without diffusion (left) and with diffusion : D28 (middle) and D29 (right). Black dots show the shock locations where we inject *in-situ* CR particles.

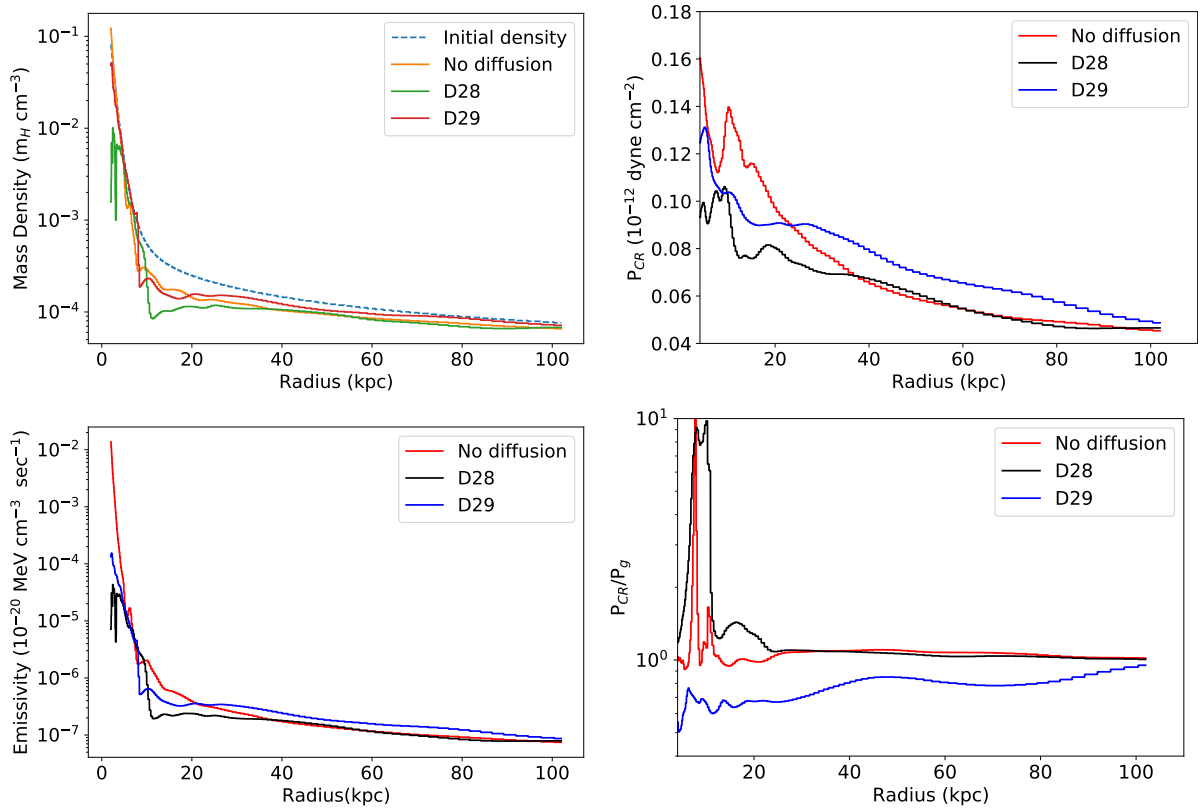


Figure 5.2: The radial profiles of volume averaged values of density (Top left panel), CR pressure (Top right panel), emissivity (Bottom left panel) and ratio of CR pressure and gas pressure (Bottom right panel).

0.1 Z_{\odot}). Due to its high density and metallicity, the disk gas will cool faster but the stellar radiation, which is not considered here, will maintain the disk temperature at 10^4 K. To mimic that effect, we exclude the cooling of disk gas by turning off the cooling in the 15kpc \times 2kpc box whereas we allow cooling of the injected material. All the parameters used in the galaxy setup are mentioned in table 1 of [Sarkar et al. \(2015\)](#). In addition, we include cosmic-ray as another fluid component and solve the following two-fluid CR hydrodynamical equations using *PLUTO* code ([Mignone et al., 2007](#); [Gupta et al., 2018](#)) where we initially assume thermal pressure to be in equipartition with CR pressure. The equations are as follows:

$$\frac{\partial \rho}{\partial t} + \nabla \cdot (\rho \mathbf{v}) = S_{\rho} \quad (5.12)$$

$$\frac{\partial(\rho \mathbf{v})}{\partial t} + \nabla \cdot (\rho \mathbf{v} \otimes \mathbf{v}) + \nabla(p_{th} + p_{cr}) + \rho \nabla \Phi_t - \frac{\rho v_{\phi}^2}{R} \hat{\mathbf{R}} = 0 \quad (5.13)$$

$$\begin{aligned} \frac{\partial(\rho v^2/2 + e_{th} + e_{cr})}{\partial t} + \nabla \cdot [(\rho v^2/2 + e_{th} + e_{cr}) \mathbf{v}] \\ + \nabla \cdot [(p_{th} + p_{cr}) \mathbf{v}] = S_{th} - q_{cool} \end{aligned} \quad (5.14)$$

$$\frac{\partial e_{cr}}{\partial t} = -\nabla \cdot (e_{cr} \mathbf{v}) - \nabla \cdot \mathbf{F}_{cr,diff} - p_{cr} \nabla \cdot \mathbf{v} + S_{cr} \quad (5.15)$$

where ρ , v , p_{cr} and p_{th} denote density, velocity, CR and thermal pressure respectively. S_{ρ} , S_{th} and S_{cr} signify the mass and energy sources. e_{cr} and e_{th} are thermal and CR energy densities respectively. The thermal energy lost by radiative cooling is denoted by q_{cool} . In the equation 5.15, first two terms in R.H.S denotes CR energy density change due to advection and diffusion respectively where $F_{cr,diff}$ is the CR flux linked to isotropic diffusion process. The third term in the R.H.S of equation 5.15 takes into account the adiabatic losses in the CR energy density.

5.4.2 Injection Condition

We consider multiple supernova explosions from a large OB association as a continuous source of mechanical energy and mass in the central region of 60 pc, following the criteria that energy deposition rate should be larger than the cooling rate ([Sharma et al., 2014](#)).

The metallicity of the injected material is considered to be the same as disk metallicity. We use the star formation history of the last 1 Gyr of M31, as given in [Williams et al. \(2017\)](#), because it is the time in which the sound crosses 120 kpc radius through a medium of 10^6 K gas and any activity in the center beyond this time would have left its signature out of the simulation box of 120 kpc by this time. Considering Salpeter initial mass function ([Salpeter, 1955](#)), 0.1-100 M_{\odot} stellar mass range, 10^{51} erg/sec energy injection by each supernova and efficiency of heating the gas to be 0.3 ([Strickland & Heckman, 2007](#)), we calculate the mechanical energy injection to be

$$\dot{E} = 7 \times 10^{40} \text{erg/sec} \left(\frac{\text{SFR}}{M_{\odot}/\text{yr}} \right) \quad (5.16)$$

The mass injection rate is assumed to be $\dot{M} = 0.1$ SFR.

We also consider 10% of supernova energy is channelled to CRs. In addition to this (central injection of CRs), we also consider shock injection of cosmic rays. Shocks are detected following the criteria described in [Gupta et al. \(2018\)](#) and we redistribute the total pressure equally between thermal pressure and cosmic ray pressure whenever a shock is detected.

5.4.3 Solver and resolution

HLL Riemann solver is used to solve the two-fluid hydrodynamical equations and we consider piece-wise linear spatial reconstruction for all variables. Time evolution has been solved with Runge-Kutta 2nd order scheme. The simulation is executed in 2D spherical geometry (r, θ) with three velocity components. We consider the computational box from 40 pc to 120 kpc in r direction with uniform grid up to 110 pc (20 grid points) and logarithmic grid (236 grid points) afterwards. In θ direction, we consider 0 to $\pi/2$ with uniform 256 grid points. We have also performed higher resolution runs with 512 grid points in both directions for convergence study.

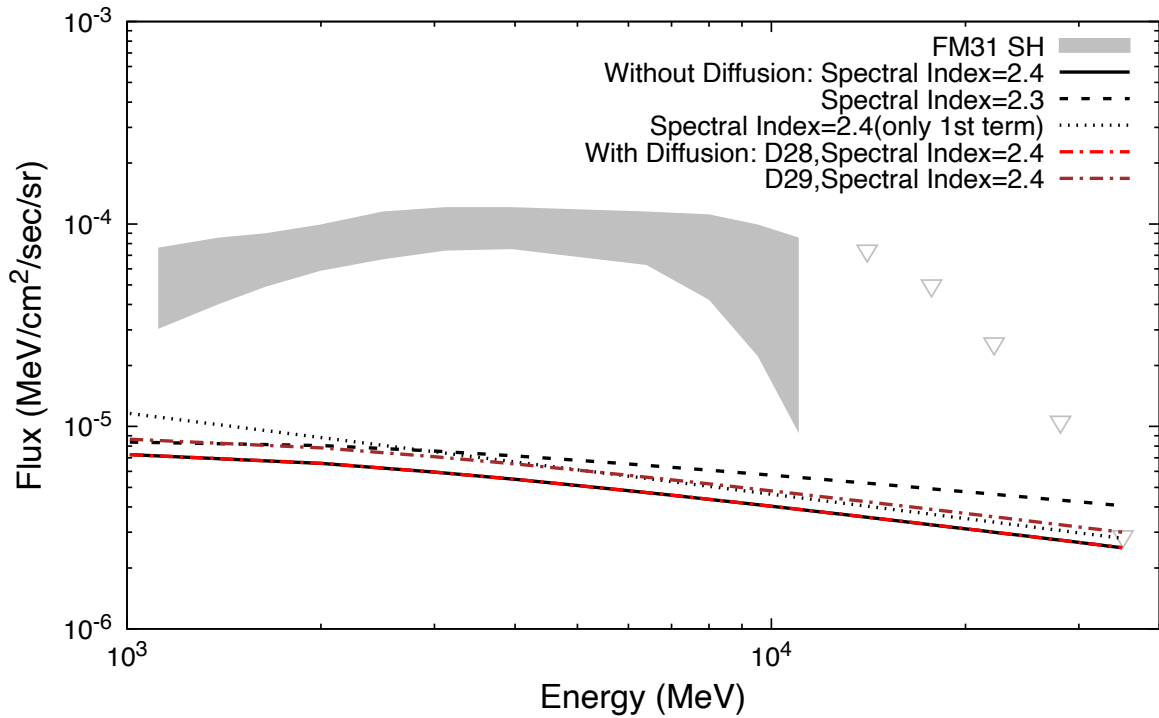


Figure 5.3: The γ -ray spectra for the cases without and with diffusion (D28,D29). The variation of γ -ray flux with differing spectral index is also shown here (black solid, dashed and dotted lines). We also plot the spectra for the case where one consider entirely a negative slope up to 1 GeV. The grey band denotes the observation by [Karwin et al. 2019](#) including the grey triangles which indicate the upper limits of the observation (Figure 31 of their paper).

5.5 Result

In this section, we describe how we use output of our simulation in order to produce γ -ray map and calculate the γ -ray flux. We have used the number densities and CR energy densities from each grid point of the simulation snapshot at 1 Gyr in order to calculate the γ -ray emissivity of the M31 (eq. 5.8 without the volume integral). In Figure 5.1, we have shown the density, CR pressure and γ -ray emissivity (top to bottom) at snapshot of 1 Gyr with left panel showing no diffusion case, and middle and right panels showing with diffusion cases for $D = 10^{28} \text{ cm}^2 \text{ s}^{-1}$ (D28) and $D = 10^{29} \text{ cm}^2 \text{ s}^{-1}$ (D29). We have indicated the position of shocks in the density plot (top) by black dots where we have injected *in-situ* CR particles. Due to low resolution, we do not seem to resolve shocks in the outer CGM and we will discuss this in the last paragraph of this section. The figure shows that the forward shock has faded out at 120 kpc (as expected from the Mach number estimates in section 3.2). However the advection by outflowing gas has lifted the CRs injected at the central region due to star-formation as well as the *in-situ* CRs to ≈ 120 kpc, the outer region of the simulation box, in 1 Gyr, as anticipated by eqn 5.2. The inclusion of diffusion with D28 does not have much effect with respect to advection as we show above that the diffusion time scale is much larger than the advection time scale in this scenario. However, the enhanced diffusion of CR in the D29 case compared to D28, increases the emissivity of the CGM around M31 as it has comparable time scale as advection time scale, thereby increasing the flux, as we will show below.

The effect of CR diffusion is clear from the comparison of the leftmost and the rightmost panels, especially in the distribution of CR energy density (middle and bottom columns), which is less patchy and more uniform in the cases with diffusion (D29). Whereas the resultant emissivity in no-diffusion case is largest surrounding the outflowing gas, along the polar direction, diffusion increases the overall emissivity throughout the CGM. If we also compare D28 and D29 cases, we can see that in the case of D29, CR energy density is more uniform than the case of D28 : diffusion makes CR distribution smoother in small scale. An increase in the diffusion coefficient by an order of magnitude increases the diffusive length by $10^{1/2}$, which is reflected in the figure, *e.g.* the size of the enhanced CR pressure region above the disk extending up to ~ 40 kpc in D28 case,

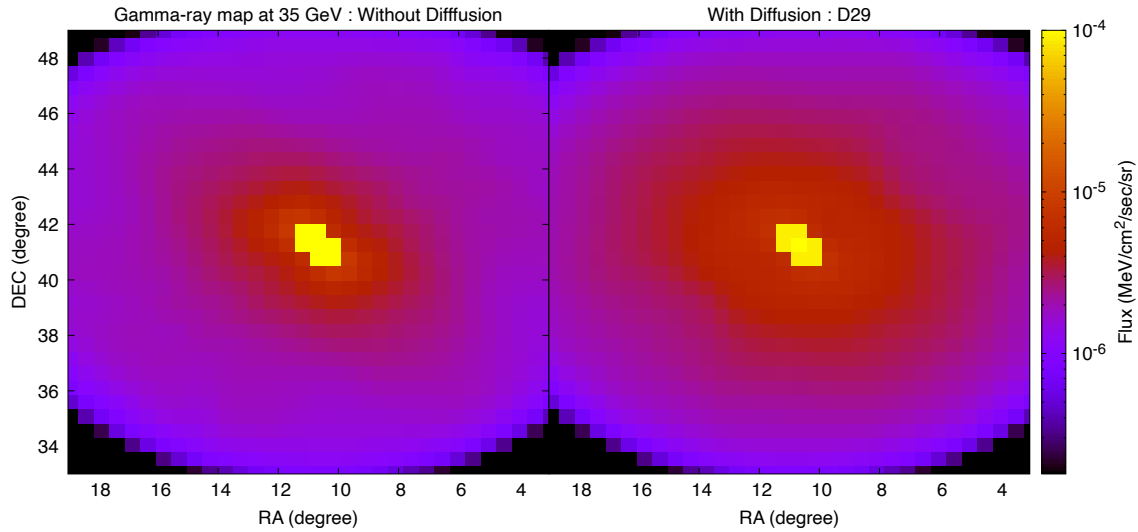


Figure 5.4: Simulated γ -ray image in the sky at 35 GeV with respect to RA and DEC. We show two cases here : 1) without any diffusion (left), 2) with diffusion D29 (right). The central point of the map is at the centre of M31 and the yellow portion in the center represents galactic disc of M31 which has a position angle of 37.7° and inclination angle of 77.5° . The details of the calculation by which the simulation box is rotated, is explained in the Appendix A. In the case of without diffusion, the high γ flux of $\approx 10^{-5}$ MeV cm $^{-2}$ s $^{-1}$ sr $^{-1}$ extends up to 2° , whereas diffusion (D29) extends it up to $3 - 4^\circ$.

reaches a distance of ~ 100 kpc in the D29 case.

We show in Figure 5.2 the radial profiles of volume averaged values of density, CR pressure, emissivity and ratio of CR pressure to gas pressure. The top left panel shows the density profile in the initial stage (dashed line), and for the cases of no diffusion and D28 as well as D29. Given the disk geometry, the volume average of annuli at galactocentric distances ≤ 10 kpc gets diluted in comparison with the disk density. Effectively, the ratio of the average density in the IG to the SH regions turn out to be $\sim 10^{-2}$, with the density in the SH region being $\approx 10^{-4}$ cm $^{-3}$. The CR pressure run would have scaled as $1/r$ in the limit of steady injection of energy (the diffusion coefficient being a constant), but advection makes the profile shallower, by transporting CR into the CGM. These two factors work together to make the ratio of the emissivity in the IG to the SH region $\sim 10^{-3}$. We note that this is consistent with the ratio estimated by [Recchia et al. \(2021b\)](#) to explain the surface brightnesses in the IG and SH region. We also note

that the emissivity marginally increases with increase in diffusion from D28 to D29. The bottom right panel of Figure 5.2 shows the profiles of the ratio of CR pressure to gas pressure for all the cases which are qualitatively similar to Figure 11 of (Butsky & Quinn, 2018). The ratio in the case of D29 is slightly smaller than D28 and no diffusion case although the CR pressure is larger in D29 than other two cases. This is due to the fact that density hence gas pressure is slightly higher for D29 than D28 and no diffusion case at outer radii. It is reassuring to see that the CR pressure is of the order of gas pressure in the outer halo for all the cases which is also seen in the simulation of (Butsky & Quinn, 2018).

We show the simulated γ -ray spectrum for different cases in figure 5.3 for the energy range 1 – 35 GeV. We have superimposed the observational data points, corresponding to the power law with exponential cut-off (PLEXP) fit (grey-shaded curve) and upper-limits (grey triangles) from 1 to 35 GeV for comparison (Figure 31 of Karwin et al. (2019)). Note that these data points have been obtained after the subtraction of foregrounds from MW and isotropic components, which are model dependent, based on assumed templates. Although Karwin et al. (2019) have demonstrated the robustness of the result, it should be noted that these procedures, each loaded with uncertainty, can introduce systematic errors in the residuals that are larger than shown here. Therefore, instead of trying to explain the exact spectrum of the residuals, we aim to reproduce the flux value within a factor of order unity. Furthermore, since the low energy CRs bring more uncertainty to the calculation as they suffer scattering due to streaming instability which leads adiabatic cooling. Therefore, we choose 35 GeV γ -ray flux to compare with our model, as has also been done by (Zhang et al., 2021).

Figure 5.3 shows that the simulated flux matches the observed values at 35GeV. The flux in the presence of diffusion, with D28, does not differ from the case of without diffusion, but the flux for the case of D29 significantly increases from the case with no diffusion. The decrease in spectral index from 2.4 to 2.3 also increases flux value. All these parameters are rather uncertain and adjusting them can change the value of the flux, however not significantly. Note that the γ -ray spectrum has an index similar to the CR spectral index at very high energies, and the spectrum flattens at low energies, near the pion rest mass energy, below which the spectrum has a positive index. We use

the full spectrum with these variation, as determined by equation 5.9. Note that Zhang et al. (2021) considered the spectrum to have a negative slope, down to ~ 1 GeV, which artificially increases the flux at these energies. We have also a done a similar exercise, and the result is shown with dotted lines in the figure.

We have considered the M31 coordinates (R.A and DEC) and alignment of M31 such as the position angle, inclination angle to produce a realistic rotated γ -ray map (see Appendix A for the rotation calculations), observed from the position of the solar system. These maps are made with nearly similar resolution of *Fermi-Lat* at 35 GeV $\sim 0.5^\circ$. We have considered the γ -ray spectral index to be 2.4 and the CR spectral index to be equal to the γ -ray spectral index for the production of these maps as well as for the flux calculations. Figure 5.4 shows the γ -ray map of M31 at 35 GeV for the cases of without diffusion (left) and with diffusion: D29 (right). We do not show other map with diffusion D28 as for D28, diffusion does not change the flux in a significant manner as we have seen above. However for D29, we can see there is a significant change from the case of without diffusion. For D29, CRs significantly diffuse out to the outer CGM, making it brighter in γ -rays. The diffusion D29 increased high intensity region with flux of $\approx 10^{-5}$ MeV cm $^{-2}$ s $^{-1}$ sr $^{-1}$ at 35 GeV from ≈ 2 – 2.5° to ≈ 3 – 4° away from the disc. However, it is difficult to compare the observed flux with the simulated map by just eye, so for comparison, we have calculated the average flux value with an angular shell of 0.4° – 8.5° from the centre of M31. The average γ -ray fluxes calculated for different cases at 35 GeV are 2.05×10^{-6} , 2.14×10^{-6} and 2.4×10^{-6} MeV cm $^{-2}$ s $^{-1}$ sr $^{-1}$, for no diffusion, D28 and D29 cases respectively. The fluxes with $D = 10^{28}$ cm 2 s $^{-1}$ and without diffusion do not differ much, whereas, there is 17% change in γ -ray flux with diffusion coefficient $D = 10^{29}$ cm 2 s $^{-1}$. Diffusion increases the emissivity as it allows CRs to interact with a larger volume of CGM, and consequently, a larger number of CGM protons. To investigate the contribution from the *in-situ*, we turned off the injection of energy to CRs in shocks and found a flux $\approx 1.73 \times 10^{-6}$ MeV cm $^{-2}$ s $^{-1}$ sr $^{-1}$ at 35 GeV. That implies the *in-situ* injection contributes $\sim 15\%$ of total flux.

Doubling the resolution in the case of no-diffusion increases the luminosity from 2.05×10^{-6} MeV cm $^{-2}$ s $^{-1}$ sr $^{-1}$ to 2.2×10^{-6} MeV cm $^{-2}$ s $^{-1}$ sr $^{-1}$. In other words, a two-fold increase in resolution increases the γ -ray flux by 7 – 9%. This is due to the

fact that the higher resolution in the SH region allows us to resolve more shocks in the CGM, thereby increasing the contribution from the *in-situ* CR acceleration. Therefore, we consider our result as a limit in the sense that the diffusion coefficient considered here can explain the observed results, and larger diffusion coefficient and/or higher resolution may require a smaller CGM mass to explain the same result.

5.6 Discussion

Previous studies have advocated a variety of proposals to explain the observed γ -ray excess in the M31 CGM. While [Karwin et al. \(2021\)](#) invoked the exotic physics of Dark Matter annihilation, [Recchia et al. \(2021b\)](#) put forward a scenario of leptonic origin for the γ -ray and *in-situ* acceleration of CR in the accretion shock due to in-falling matter. The scenario in [Zhang et al. \(2021\)](#), on the contrary, relies on hadronic γ -ray production and CR acceleration due to star formation activity in M31 going back to 14 Gyr, but excluding the effect of advection by bulk flow of gas. Our proposal differs from these in that both CR diffusion and advection is shown to be important, with some contribution from *in-situ* CR acceleration in shocks in the CGM.

Our results are roughly consistent with the conclusions drawn by [\(Salem et al., 2016\)](#), who had included CR pressure and diffusion in their cosmological run of galactic winds driving into the CGM of M31-like halos. They found that a diffusion coefficient of $\sim 3 \times 10^{28} \text{ cm}^2 \text{ s}^{-1}$ could explain the γ -ray luminosity of M31. Although theirs was a cosmological simulation from $z = 99$ to present day, and with self-regulated star formation in the disc, the concordance is encouraging. In their analytical study, [Zhang et al. \(2021\)](#) had presented a constraint on the baryonic CGM mass of M31 for different values of the diffusion constant, given the γ -ray luminosity of the SH region. Their limit on the CGM mass (outside 50 kpc) is $\leq 5 \times 10^9 M_{\odot}$ for $D_{1\text{GeV}} \approx 1.5 \times 10^{29} \text{ cm}^2 \text{ s}^{-1}$. The limit increases with the increase in the diffusion coefficient, going to $\sim 5 \times 10^{10} M_{\odot}$ for $D_{1\text{GeV}} \sim 1.5 \times 10^{30} \text{ cm}^2 \text{ s}^{-1}$. This is to be compared with the *AMIGA* estimate of the M31 CGM mass, of $\geq 4 \times 10^{10} M_{\odot}$ within the virial radius ([Lehner et al., 2020](#)). Our setup has CGM mass of $1.4 \times 10^{10} M_{\odot}$ for the region between 50 kpc to 120 kpc. One marked difference between our approaches is that we have limited our simulations

to a look-back time of 1 Gyr, reason for which has been argued above, whereas their calculation takes into account the star formation history going back to 14 Gyr, and in particular, an enhanced SFR before a look-back time of 8 Gyr. The other difference is the lack of advection by bulk flow initiated by star formation process in their calculation. It is possible that these two factors have increased the CGM emissivity for a given CGM mass in their case, and has led to a rather restrictive limit on the CGM mass. Also note that we have not considered contribution from nuclear activity of the central black hole in M31 which can also enhance the emission. However, that will introduce more free parameters in the calculation which we did not attempt in this chapter for the matter of simplicity.

[Recchia et al. \(2021b\)](#) have argued that the observed γ -ray intensity at ~ 100 Kpc cannot be explained by propagation of CRs produced in the disk, with CR diffusion or advection by galactic outflow. They have first argued that the ratio of emissivities in the IG and SH region is $\sim 10^{-3}$, based on the observed intensities in these regions. Incidentally, this is consistent with the bottom left panel of Figure 5.2. However, their discussion of CR galactic outflow is based on assumptions of magnetic field geometry, for stationary wind, and on the assumption of increasing diffusion coefficient with distance. The profiles of cosmic ray pressure, and its ratio to thermal pressure, from our simulations are qualitatively and quantitatively consistent with other recent simulations that do not make these assumptions, as explained in section 3. The distance dependence of diffusion coefficient comes from the assumption that if CRs excite waves through streaming instability in the ionized galactic halo, the diffusion coefficient would be smaller where the source density is larger enhancing the CR density in the inner galaxy and it would be larger in the spherical halo region. However this argument may not be relevant in our case as streaming instability is dominant in low energy CR protons and does not apply to 400 GeV CR protons which are responsible for 35 GeV γ -ray flux that we described in the chapter. In fact, Figure 10 of [Recchia et al. \(2016\)](#) clearly shows that the difference in diffusion coefficient with distance decreases as one increases the energy and it is almost negligible at CR energy of 400 GeV. These considerations lead us to conclude that CR diffusion and advection can indeed explain the observed γ -ray emission from the CGM of M31. If, however, the diffusion coefficient turns out to be increasing with distance as described in [Recchia et al. \(2021b\)](#), then it would be difficult for advection-diffusion

processes to explain the observed flux.

In a recent paper, [Blasi & Amato \(2019\)](#) have pointed out that if the diffusion coefficient is very large, then the CGM magnetic field of strength $\approx 0.01 \mu\text{G}$ will be amplified by a CR driven instability, thereby producing a large gradient in CR pressure, and moving the gas by advection with speed 10–100 km s^{-1} . This is one of the reasons we have not explored larger values of diffusion coefficient in our simulation. The close connection between diffusion and advection that is the crux of our result, will be more intimate in this scenario.

Our result of a brighter CGM in the case of enhanced diffusion, with D (1 GeV) $\geq 10^{29} \text{ cm}^{-2} \text{ s}^{-1}$, is potentially testable, if the SH region is further divided into two shells and the observed flux from the outer part of the SH shell is compared with simulation result. Taking the total region between 5.5 kpc to 120 kpc as a whole does not allow one to discuss the distribution of flux in this region, whether or not the outer part of SH is as bright as the inner part of SH, which will be needed to test our results. Our result shows that increasing the diffusion coefficient beyond $10^{29} \text{ cm}^2 \text{ s}^{-1}$ would render the intensity of a region $> 3\text{--}4^\circ$ away from the disc to be $\approx 10^{-5} \text{ MeV cm}^{-2} \text{ s}^{-1} \text{ sr}^{-1}$ at 35 GeV. Future analysis may be able to test this prediction.

Incidentally, since the scenario advocated here requires CR protons in the CGM of M31, one can ask if the corresponding CR electrons would emit observable synchrotron radiation, assuming the CGM to be magnetized. We can use eqn 5.8 to the CR proton energy density corresponding to the observed γ -ray luminosity. For a volume of $4\pi R^2 \Delta R$ (with $R \approx 120 \text{ kpc}$ and $\Delta R \approx 100 \text{ kpc}$), the CR proton energy density is $1 \times 10^{-15} n_{-3}^{-1} \text{ erg/cc}$. Typically, CR electrons carry $\approx 1\%$ of the total CR energy density. This implies CR electron energy density of $\epsilon_{cr,e} \approx 10^{-17} n_{-3}^{-1} \text{ erg cm}^{-3}$. For a power law distribution of electron ($N(E)dE = AE^{-p}dE$, with $p = 2.5$), the emissivity at 400 MHz (eqn 6.36 in [Rybicki & Lightman \(1986\)](#)) is $2 \times 10^{-36} \times B^{1.75} n_{-3}^{-1} \text{ erg s}^{-1} \text{ cm}^{-3} \text{ sr}^{-1} \text{ Hz}^{-1}$. The equipartition value of the magnetic field (with the thermal energy density) is $B \approx 3\mu\text{G} n_{-3}^{1/2} (T/10^6 \text{ K})^{1/2}$. This implies an emissivity at 400 MHz of $4 \times 10^{-46} n_{-3})^{-0.125} (T/10^6 \text{ K})^{0.875} \text{ erg s}^{-1} \text{ cm}^{-3} \text{ sr}^{-1} \text{ Hz}^{-1}$. Therefore, the expected radio flux is $\approx 2.5 \mu\text{Jy}$ per arcmin², which is difficult to observe. For example, the beam size of GMRT telescope for this waveband is $2 \times 2 \text{ arcmin}^2$, implying a signal in a single beam

of $8\mu\text{ Jy}$, whereas the noise is roughly $13\mu\text{ Jy}$ for GMRT.

5.7 Conclusion

We investigate the plausible origin of recently detected γ -ray signature in the CGM (at $\sim 120\text{ kpc}$) of M31 by Karwin et al. (2019) using hydrodynamic simulation with two fluid (thermal + CR). We consider CR produced in stellar disk by star-formation activity that diffuse and also get advected outwards and produce γ -ray by hadronic interaction. We argue that since acoustic wave propagation timescale to 120 kpc in the CGM gas of 10^6 K gas is $\approx 1\text{ Gyr}$, any disturbance in the disc before 1 Gyr would have departed the 120 kpc halo and has little effect in observed γ -ray. We therefore use the star-formation history of M31 over the past 1 Gyr in our simulation. We also include *in-situ* acceleration of CR in shocks in the outflow regions, as well as CR diffusion. We find that advection and diffusion of CR produced in the M31 disc (due to star formation activity) and in CGM shocks can explain the observed flux, with CR diffusion coefficient (at 1 GeV) $\approx 10^{29}\text{ cm}^2\text{ s}^{-1}$, for a CGM mass that is $\approx 10\%$ of the total halo mass of M31. We estimate the contribution of *in-situ* accelerated CR in the CGM to be of order $\sim 15\%$ towards the γ -ray luminosity. Increasing the diffusion coefficient beyond this increases the flux, especially towards the outer parts of the SH region, making a region of $> 3\text{--}4^\circ$ around the M31 disc shine with a diffuse flux of $\approx 10^{-5}\text{ MeV s}^{-1}\text{ cm}^{-2}\text{ sr}^{-1}$ at 35 GeV. Our work emphasises the hadronic nature of the observed γ -ray excess in M31 CGM, as well as the comparable contribution of advection and diffusion of CR towards CR propagation in the M31 CGM.

Chapter 6

Seeding the CGM: How Satellites Populate the Cold Phase of Milky Way Halos

“Seeding the CGM: How Satellites Populate the Cold Phase of Milky Way Halos”

Manami Roy, Kung-Yi Su, Stephanie Tonnesen, Drummond B. Fielding

Soon to be submitted

The origin of the cold phase in the CGM is a highly debated question. In this chapter, we investigated the contribution of satellite galaxies to the cold gas budget in the circumgalactic medium (CGM) of a Milky Way-like host galaxy. We performed controlled experiments with three different satellite mass distributions.

Key Results:

- We found that satellite galaxies can contribute to the cold gas budget of the CGM.
- We identified several mechanisms by which satellites can add cold gas to the CGM, including ram pressure stripping, and induced cooling in the mixing layer of the stripped cold gas.
- We found out that these two mechanisms contribute a comparable amount of cold gas to the host CGM.
- We found that the less massive satellites not only lose all of their cold gas in a short period ($\sim 0.5\text{-}1$ Gyr), but their stripped cold clouds also mix with the hot CGM gas and get heated up quickly. However, the LMC, SMC-like massive satellites can add cold gas to the total gas budget of the host CGM for several Gyrs.

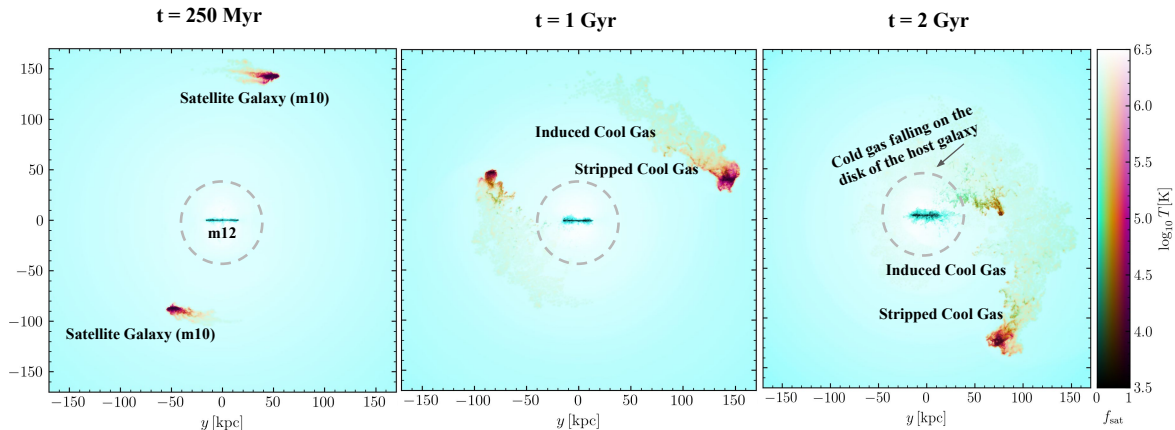


Figure 6.1: The temperature distribution of three snapshots of the simulation (2xm10fh, see Table 6.2). The colorbar varies both color and saturation based on f_{sat} and temperature, respectively. The parameter f_{sat} represents the satellite and host gas such that $f_{\text{sat}} = 1$ is entirely composed of satellite gas and $f_{\text{sat}} = 0$ is entirely host gas. The stripped cool gas is streaming behind the satellites and falling towards the central disk. There is also induced cool gas in the mixing layer of stripped cool gas and hot host gas.

6.1 Introduction

A significant portion of galactic baryonic content resides in the form of a diffuse gaseous halo, known as the Circumgalactic medium (CGM), which surrounds the galactic disk and extends up to the virial radius and even beyond (Tumlinson et al., 2017). Recent absorption and emission observations of the CGM make it abundantly clear that the gas in the CGM is multiphase in nature. On the basis of their temperatures, these phases are roughly divided into hot ($T > 10^6 \text{ K}$), warm ($10^5 - 10^6 \text{ K}$) and cold phases ($< 10^4 \text{ K}$). Recent observations in massive halos ($10^{11-13} M_{\odot}$) showed high column densities of MgII and HI, which are the tracers of the cold phase of CGM (Zhu et al., 2014; Chen et al., 2018; Zahedy et al., 2018), even out to the virial radius. The recent observations by Lan & Mo (2018, 2019) also pointed towards the existence of a cold phase out to large radii ($> 100 \text{ kpc}$). This leads to two highly debated questions: *how do these massive halos whose virial temperature is much higher than that of the cold phase (Prochaska et al., 2013) form cold gas?* and *how does the cold gas exist at such large radii?*

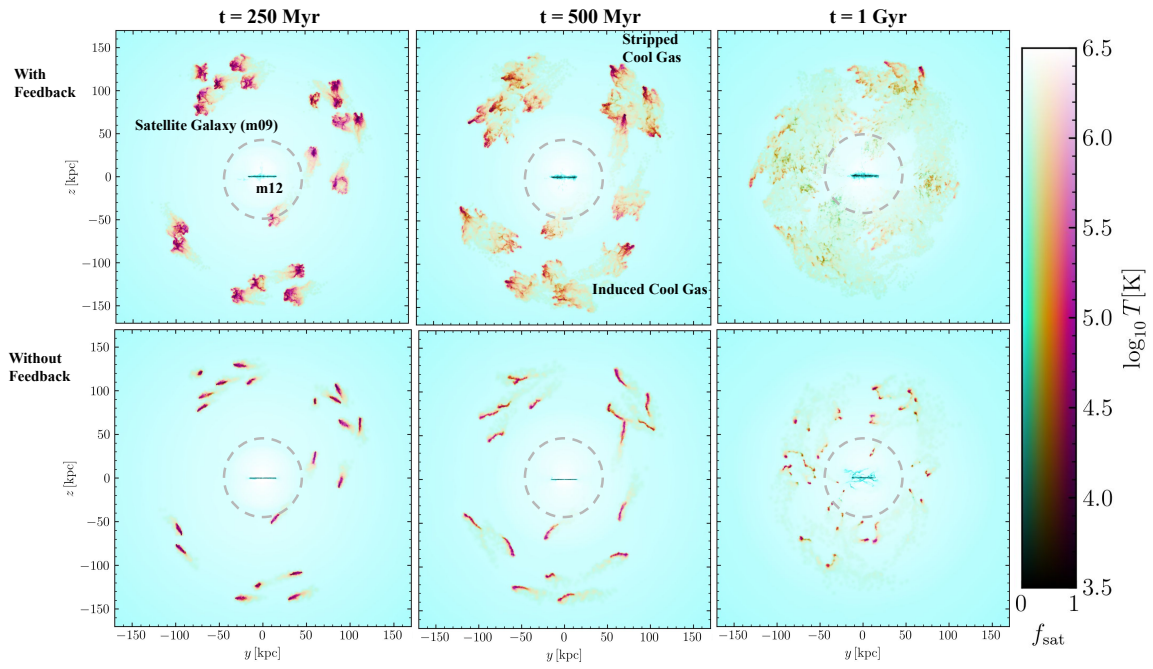


Figure 6.2: The temperature distribution of the three snapshots of the simulations (20xm09fh, see Table 6.2), with the upper and lower panels showing the runs with and without the inclusion of feedback, respectively. The colorbar is as described in Figure 6.1. Each orange galaxy tail is shorter than for the m10 satellites, but because there are more satellites the high f_{sat} gas covers more area.

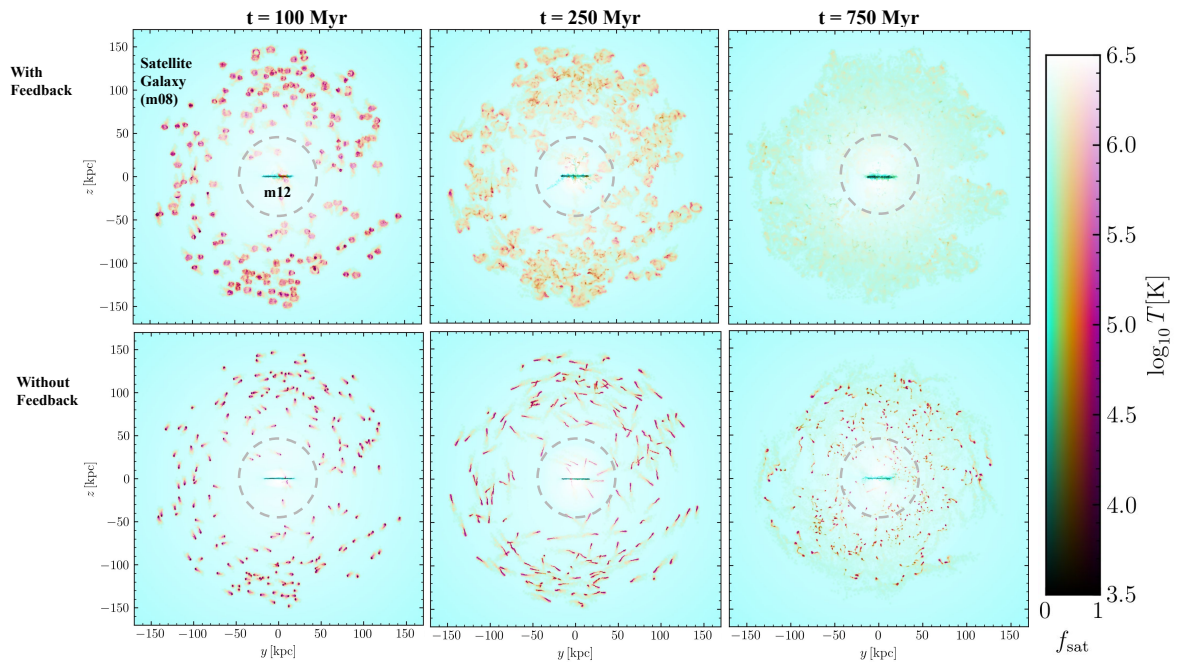


Figure 6.3: The temperature distribution of the three snapshots of the simulations (200xm08fh, see Table 6.2), with the upper and lower panels showing the runs with and without the inclusion of feedback, respectively. The colorbar is as described in Figure 6.1. The impact of feedback is clear in the more diffuse distribution of satellite gas in the upper panels.

Recent studies have shown that thermally unstable perturbations can drive cooling in the CGM, proceeding into multiphase condensation, if the ratio of the radiative cooling time to free-fall time falls below a threshold value (Maller & Bullock, 2004; McCourt et al., 2011; Sharma et al., 2012; Voit et al., 2015; Voit, 2019). Star-formation-driven outflows can also uplift cold gas to the CGM from the galactic disc (Faucher-Giguère et al., 2016; Liang et al., 2016). However, the time taken for cold clouds to reach $> 100\text{kpc}$ distance from the disc is greater than 10 Myr, which is much larger than the cloud crushing time for a typical 100 pc cloud (< 1 Myr; See Equation 6.2). Therefore, it is quite a challenge for star-formation-driven outflows to populate the outer CGM with cold gas. However, galaxies can accrete fresh cold gas directly from cold dense filaments of Intergalactic medium (IGM), known as the cold mode accretion (Birnboim & Dekel, 2003; Kereš et al., 2005) Along with this cold mode accretion, satellite galaxies can also populate the outer CGM with cold gas.

A recent study (Fielding et al., 2020) has compared the results from different idealized and cosmological simulations and found that more cold gas in the outer CGM has been seen (their Figure 3) in cosmological simulations (Joung et al., 2012; Marinacci et al., 2018; Nelson et al., 2018) than in isolated galaxy simulations (Fielding et al., 2017; Li & Tonnesen, 2020; Su et al., 2020). The idealized simulations did not include either cold mode IGM accretion or satellite galaxies, either of which could be responsible for adding cold gas to the outer CGM in cosmological simulations. However, in cosmological simulations, it is challenging to distinguish the amount of cold phase in the CGM contributed only by satellite galaxies from feedback-driven cold clouds or cold filamentary inflows. In this chapter, we run a suite of high-resolution idealized simulations of Milky Way-type host galaxies, varying the mass and spatial distribution of satellite galaxies in each run. This will allow us to explicitly determine the amount and processes by which satellites can populate the cold-phase of the CGM of their host galaxy.

When a satellite galaxy passes through the diffuse gas of the CGM, it experiences a headwind that causes pressure on the galaxy, known as ‘Ram Pressure’. Its magnitude depends on the relative speed of the satellite with respect to the medium and the local density of the medium. If this ram pressure exceeds the local gravitational restoring pressure of the satellite galaxy, its gas can be stripped (Gunn & Gott, 1972). This

is known as ‘Ram Pressure Stripping’. In lower-mass galaxies, ram pressure stripping becomes an effective mechanism for removing gas due to their lower gravitational restoring force. Also, galaxies moving through the CGM of massive halos will experience higher ram pressure due to a combination of higher CGM density and faster orbital velocities. Ram pressure stripping is also an important factor in the evolution of the satellite galaxies by regulating gas content and hence their star formation.

There is significant observational evidence that ram pressure not only removes gas from satellite galaxies, but it also populates the CGM of the host galaxies with cold gas. For example, the neighboring dwarf galaxies of the Milky Way and M31 system tend to be poorer in HI gas content than those at larger distances (Grcevich & Putman, 2009a; Putman et al., 2021). In addition to this, it is also apparent from the recent MUSE observations that there is a strong connection between the group environment and the ionization structure of the CGM. These observations showed group environment leads to a significant increase in the column densities and covering fractions of MgII, HI ions of the CGM of host galaxies (Muzahid et al., 2021; Dutta et al., 2021). Therefore, the group environment contributes more cold gas in the galaxies than the isolated systems. Along with this, cold gas can be stripped from the satellites due to the ejecting wind, and can be segregated behind the satellites in the form of a wake (Ostriker, 1999; Bernal & Sánchez-Salcedo, 2013). Now the question is: *Can satellites populate the CGM with cold gas only directly, via ram pressure stripping, or are there other mechanisms by which satellites can induce cooling in the host CGM?* The cold gas stripped from the satellites will mix with the hot CGM, and in the mixing layer of this stripped cold gas significant cooling can occur (Tonnesen & Bryan, 2021). The satellites can also stir the CGM gas and create local perturbation which can lead to the condensation of cold gas out of hot CGM gas (Voit, 2018). In this chapter, we will separate these different mechanisms and investigate the amount of cold gas contributed by these different mechanisms.

This chapter is structured as follows. In section 2, we will describe the methodology of our simulation. In section 3, we will discuss our results from the simulation and we will summarize the result in section 4.

6.2 Methodology

Our simulations use GIZMO¹ (Hopkins, 2015a), in its meshless finite mass (MFM) mode, which is a Lagrangian mesh-free Godunov method, capturing the advantages of grid-based and smoothed-particle hydrodynamics (SPH) methods. Numerical implementation details and extensive tests are presented in a series of methods papers for, e.g., hydrodynamics and self-gravity (Hopkins, 2015a), magnetohydrodynamics (MHD; Hopkins & Raives, 2016; Hopkins, 2016), anisotropic conduction and viscosity (Hopkins, 2017; Su et al., 2017), and cosmic rays (Chan et al., 2019b).

All of our simulations except for the runs with no feedback, have the FIRE-2 implementation of the Feedback In Realistic Environments (FIRE) physical treatments of the ISM, star formation, and stellar feedback, the details of which are given in Hopkins et al. (2018a,b) along with extensive numerical tests. Cooling is followed from $10 - 10^{10}$ K, including the effects of photo-electric and photo-ionization heating, collisional, Compton, fine structure, recombination, atomic, and molecular cooling.

Star formation is treated via a sink particle method, allowed only in molecular, self-shielding, locally self-gravitating gas above a density $n > 100 \text{ cm}^{-3}$ (Hopkins et al., 2013). Star particles, once formed, are treated as a single stellar population with metallicity inherited from their parent gas particle at formation. All feedback rates (SNe and mass-loss rates, spectra, etc.) and strengths are IMF-averaged values calculated from STARBURST99 (Leitherer et al., 1999) with a Kroupa (2002) IMF. The stellar feedback model includes (1) Radiative feedback, including photo-ionization and photo-electric heating, as well as single and multiple-scattering radiation pressure tracked in five bands (ionizing, FUV, NUV, optical-NIR, IR), (2) OB and AGB winds, resulting in continuous stellar mass loss and injection of mass, metals, energy, and momentum (3) Type II and Ia SNe (including both prompt and delayed populations) occurring according to tabulated rates and injecting the appropriate mass, metals, momentum, and energy to the surrounding gas. All the simulations also include MHD, fully anisotropic conduction, and viscosity with the Spitzer-Braginski coefficients.

¹A public version of this code is available at <http://www.tapir.caltech.edu/~phopkins/Site/GIZMO.html>

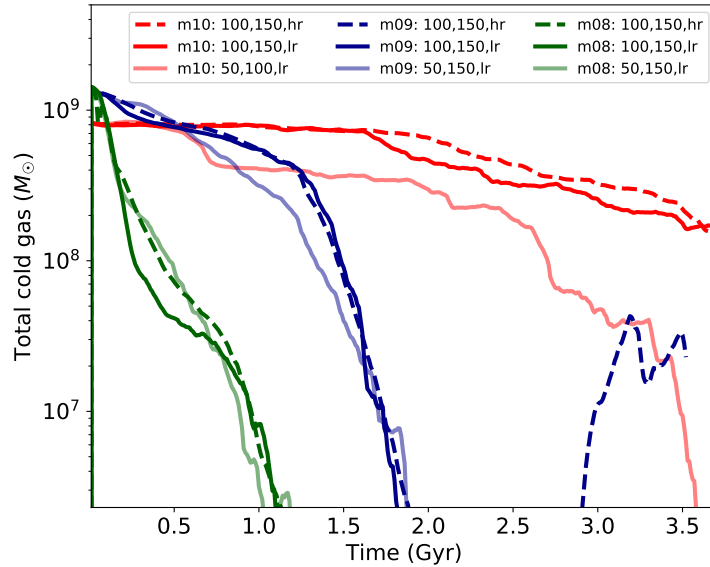


Figure 6.4: The time evolution of total cold (Temperature, $T \leq 3 \times 10^4 \text{K}$) gas mass beyond 40kpc radius from the center of the host galaxy. This total cold gas mass includes cold gas inside the satellites, cold gas stripped from the satellites, and cold gas in the host CGM.

6.2.1 Initial Conditions

The initial conditions studied here mostly follow what is described in detail in [Su et al. \(2019\)](#). To further stabilize the host CGM, we expand the simulation region to 3 times the virial radius, and the simulations are run adiabatically (no cooling or star formation) for 4.5 Gyr to relax any initial transients before the satellites are placed into the CGM. Their properties are summarised in [tab:ic](#). In this chapter, our study will focus on the **m12** halo. The dark matter (DM) halo, bulge, black hole, and gas+stellar disk are initialized following [Springel & White \(1999\)](#); [Springel \(2000\)](#). We assume a spherical, isotropic, [Navarro et al. \(1996b\)](#) profile DM halo; a [Hernquist \(1990\)](#) profile stellar bulge; an exponential, rotation-supported disk of gas and stars (10^9 and $5 \times 10^{10} M_\odot$ respectively) initialized with Toomre $Q \approx 1$; a BH with mass $\sim 1/300$ of the bulge mass (e.g. [Haring & Rix, 2004](#)); and an extended spherical, hydrostatic gas halo with a β -profile ($\beta = 1/2$) and rotation with constant angular momentum at 35 kpc. The initial metallicity drops from solar ($Z = 0.02$) to $Z = 0.001$ with radius as $Z = 0.02 (0.05 + 0.95/(1 + (r/20 \text{ kpc})^{1.5}))$. Initial magnetic fields are azimuthal with $|\mathbf{B}| = 0.03 \mu\text{G}/(1 + (r/20 \text{ kpc})^{0.375})$.

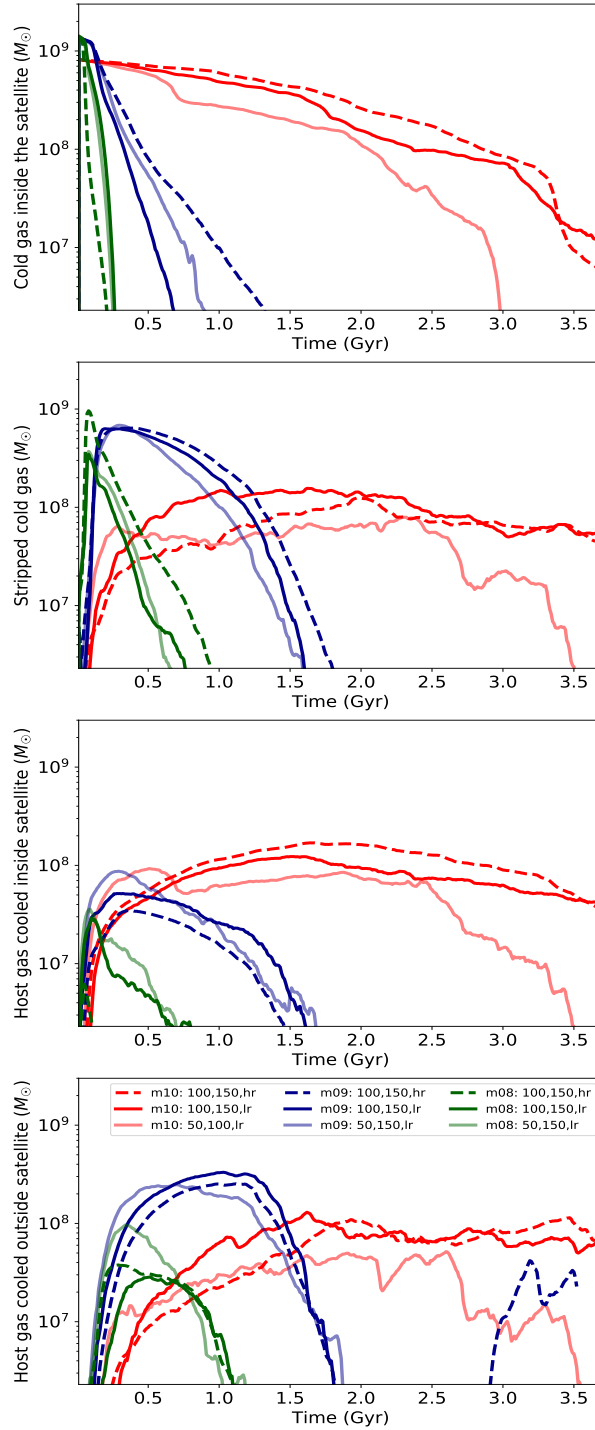


Figure 6.5: The time evolution of the cold (Temperature, $T \leq 3 \times 10^4 \text{K}$) gas mass from different contributions beyond 40kpc radius from the center of the host galaxy. From top to bottom, the panels respectively describe cold gas inside the satellites, cold gas stripped from the satellites that are cold satellite gas which falls beyond 6 times scale radius of the satellites, cold gas induced inside of the satellites, and the host gas cooled outside of the satellites.

We consider three different distributions of the satellites with different masses ranging from very small satellites of DM halo mass $2 \times 10^8 M_\odot$ to SMC-like satellites of mass $2 \times 10^{10} M_\odot$. We balance the satellite mass and number distributions such that the total DM halo mass of the satellites are same for all the cases. The three distributions that we simulate are the following: 1) 2 satellites of $2 \times 10^{10} M_\odot$ (m10), 2) 20 satellites of $2 \times 10^9 M_\odot$ (m09), 3) 200 satellites of $2 \times 10^8 M_\odot$ (m08). In addition, we vary the number of satellites in our fiducial run of m09 by considering number of satellites to be 10 and 40. We also run a fiducial setup (m09) with no gas at all inside the satellite. Also to study feedback, we have two fiducial runs (m08 and m09) with no stellar feedback in the host and the satellites. We summarize all of our runs in Table 6.2.

The satellites are initialized with the same method as the host described above except for there being no separate CGM gas halo. The properties are also summarized in tab:ic. The m10 galaxy properties are set following the SMC in Besla et al. (2010); Hopkins et al. (2011); Besla (2015); Su et al. (2017), with most of the stellar mass in the disk. For m09 and m08, the dark matter scale radius roughly follows Wang et al. (2020), with the stellar population modeled as a bulge with mass following Read et al. (2017) and size following a constant surface density ($\sim 5 M_\odot \text{pc}^{-2}$; Sánchez Almeida 2020), and the ISM gas is set so that the baryon fractions and the gas surface density are the same as m10.

6.2.2 Defining Cold CGM Gas

In this section, we define cold gas in the CGM before going into the question of how much cold gas is contributed by satellites. We consider gas to be cold if it has a temperature of less than 3×10^4 K. As we are interested in the contribution to the cold phase of the CGM by satellite galaxies, we exclude the ISM of the host galaxy by excluding all gas within a radius of 40 kpc ($\sim 0.15 R_{\text{vir}}$) from the center of the host galaxy for our analysis.

In addition, we distinguish among different origins of the cold gas in our simulation, such as ram-pressure stripping, induced cooling in the mixing layer, and turbulence-driven cooling. The gas surface density (Σ) of the satellites becomes much lower than the central gas surface density (Σ_0) at the gas scale radius, r_{gd} ($r_{gd} \sim 2.7 \times r_d$, where r_d is stellar scale radius) as $\Sigma = \Sigma_0 \times e^{r/r_d}$ (Kravtsov, 2013). Hence, we choose 6 times the gas scale radius

of the satellite to be the radius beyond which the gravitational pull from the satellites is negligible. We consider the satellite gas to be stripped if it moves from within to outside of 6 times the satellite gas scale radius. To distinguish between induced cooling inside and outside of the satellite, we also track host gas particles that are cooled outside of the satellite (which is defined above as beyond 6 times the satellite gas scale radius).

6.3 Results

The main goals of this chapter are to find how much cold gas ($T < 3 \times 10^4$ K) is contributed by satellite galaxies to the CGM of the Milky Way-type host galaxy, by what mechanisms the satellites increase the cold gas mass, and how satellite properties affect the cold gas mass. Here we present our findings, first grounding our intuition with snapshots from the simulations, then discussing quantitative measures of the cold gas mass.

6.3.1 Where is the cold gas?

In this section, we will give an overview about what happens surrounding these satellites using snapshots from several simulations. We show snapshots of the square of density weighted temperature distribution for three runs of m10, m09, and m08 in Figure 6.1, 6.2, and 6.3 respectively. To illustrate the effect of feedback, we show in the top and bottom panels of Figure 6.2 and 6.3, the runs with feedback and without any feedback respectively. Satellite and host gas are indicated by parameter ‘satellite fraction’ (f_{sat}), which is weighted by density. $f_{sat} = 1$ indicates purely satellite gas, while $f_{sat} = 0$ denotes the host gas. The temperature is shown via color saturation. These all are y-z slices of different simulation snapshots. At the center (0,0), the thin blue strip is nothing but the host ISM and around that the circle with 40 kpc radius denotes our radial cut to exclude the host ISM.

Although these figures all show snapshots from different times, they follow the same general trends. At the earliest time, we can see that most of the cold gas is associated with individual satellites with short tails of cold gas streaming behind them. As we

step forward in time, the tails become longer, and the cold gas becomes free from the satellite's gravitational pull and falls towards the central galaxy. In addition, the gas becomes more mixed with the host CGM, illustrated by the color change from red to orange. Importantly, we note that cold gas is found either near the central disk or supernova-driven outflows or near the stripped tails of gas. As we move along stripped tails of gas the f_{sat} value smoothly decreases, indicating mixing. Even where the color indicates that the gas largely originated in the host halo, there is a clear spatial correlation with stripped tails.

We can use this visual inspection as a first step in determining how host CGM gas cools in these simulations. There are two likely ways this can happen: satellites can stir the CGM of the host galaxy and create local thermal instability which can subsequently lead to cooling (turbulence-driven cooling). In addition, cold-stripped satellite gas will mix with hot host gas resulting in a high cooling rate (mixing layer cooling). These processes can occur either within the satellites (less than 6 times gas scale radii) or in the wider CGM.

In these diagrams, we can see there are lots of induced cool gas in the host CGM. Most of them, however, are spatially overlapping with the stripped cold gas and orange in color, indicating mixing. At later times, we can see in all of these diagrams that much of this cold gas (directly stripped from satellites and cooled from the halo) eventually goes within 40 kpc and falls onto the host ISM.

The morphology of this cold gas in these different satellite distributions is hugely different. We can see in these figures that the cold clouds from m10 are larger in size, whereas the less massive satellites of m09, m08 produce small cold clouds. The small clouds mix with the hot CGM and heat up in short time period as seen in the top right panel in Figure 6.3, where within roughly 1 Gyr all the clouds are destroyed and mix with CGM or have fallen into the central galaxy (as seen in the central top panel). However, even at 2 Gyr (right panel of Figure 6.1), the larger clouds of m10 survive, are clearly connected to the satellites, and continue to contribute to CGM cold gas budget.

The location of the satellite also plays an important role. Closer satellites not only feel more ram pressure due to the higher density of the CGM, but the cold clouds from

them also fall faster on the host ISM. In the right panel of Figure 6.1, we can see that the satellite at 150 kpc has more cold gas than the satellite at 100 kpc at 2 Gyr, as most of the gas from the closer satellites is stripped faster due to the higher ram pressure and the stripped gas falls within the 40 kpc inner radius more quickly.

Feedback also changes the morphology of the clouds. In the top panels of Figure 6.2 and 6.3, we can see that the clouds are more dispersed and have larger surface areas, therefore there is more induced cooling in their mixing layers. These clouds have generally lost their coherent structure by the final panel (1 Gyr and 750 Myr in m09 and m08, respectively) However, in the bottom panels, it can be seen that the clouds are elongated and narrow without the energy from supernovae, hence offering less surface area for mixing-induced cooling. These clouds survive longer period of time. They also fall within the 40 kpc faster due to their higher mass. This difference between satellites with and without feedback is most clearly seen in the right panels of Figure 6.3: in the top panels all the cold clouds are dispersed and mixed with CGM by the 750 Myr, whereas in the bottom panel, there are still lots of cold clumps, with some of them falling inside 40 kpc. We will discuss this in more detail later in Section 6.3.3.

6.3.2 How much cold gas is there?

In this section, we quantify the cold gas content of the CGM that is ≥ 40 kpc away from the center of the host galaxy. In Figure 6.4, we show the time evolution of total cold gas mass in the case of three different mass distributions of satellites: 1) 2 satellites of $2 \times 10^{10} M_{\odot}$ (m10: red), 2) 20 satellites of $2 \times 10^9 M_{\odot}$ (m09: blue), 3) 200 satellites of $2 \times 10^8 M_{\odot}$ (m08: green).

Therefore, this total budget includes cold gas inside the satellite ISM, cold stripped gas from the satellites, and cold gas from the host CGM. The cold gas mass starts with nearly a value of $10^9 M_{\odot}$, as initially it only includes the satellite ISM. The total ISM mass of m10 is slightly different than the same of m09 and m08 (see Table 6.1), hence initially they start off with different values of the total cold gas mass. For the run with no satellites, there is a very little cold gas mass (3 orders of magnitudes lower than the satellite runs) beyond 40 kpc from the center of the host galaxy throughout the entire

simulation. Therefore we conclude that in the runs with satellites, the origin of cold gas outside 40 kpc is due to the cold gas inside the satellites, stripping from satellites and the induced cooling by the satellites. After a certain time, we can see a decline in the total cold gas budget in Figure 6.4. This is due to the fact that at late times, all the cold gas either falls into the host ISM or gets destroyed by heating up. Additionally, the satellite ISM in m09 and m08 loses all of its gas at later times which leaves little gas in the ISM for stripping.

We study the cold gas in more detail by breaking up all the different contributions in Figure 6.5 where, we show the time evolution of instantaneous mass contributed by the satellites in the case of three different mass distributions of satellites. The top-to-bottom panels show the time evolution of mass of initial satellite cold ISM, stripped cold gas, host gas cooled inside of the satellite, and host gas cooled outside of the satellite respectively. All the panels sum to Figure 4. In the first panel of Figure 6.5, we can see that the initial satellite cold ISM mass decreases with time as cold gas from the satellites get stripped via ram pressure. In the second panel of Figure 6.5, we show the time evolution of these stripped cold gas. At early times we see an increasing amount of cold gas being stripped from the satellites until the stripped cold gas mass reaches an early peak. Thereafter, the stripped cold gas mass starts declining slowly over time. There are two reasons for this decline. First, all cold stripped gas from the satellites that falls to within 40 kpc and reaches the host ISM over time is removed from our instantaneous CGM count. The second reason is that most of the cold gas inside the satellites is stripped by this time. That is clear in the top panel of Figure 6.5, where the cold gas inside the satellite follows a declining trend with time as the cold gas gets stripped from the satellites and makes the satellite galaxies cold-gas deficient over time.

In the third panel of Figure 6.5, we show the host gas that has cooled within the satellites. This is the hot host gas that falls inside the potential of the satellite and cools inside the satellite. The time-scale of this mass evolution follows roughly the stripping time as once all the cold gas is stripped from the satellites, it is not possible for hot host gas to cool inside of the satellite.

Finally, the fourth panel of Figure 6.5 shows the host gas that cools outside of the satellite in the mixing layer or because of turbulence-driven cooling. Importantly, by

comparing the second and fourth panel we find that the satellites induce a similar amount of cold gas as the stripped cold gas from the satellites. In addition, the induced cold gas outside the satellite almost mimics the shape of the stripped cold gas with a slight delay time. This agrees well with our visual impression from Figures 6.1, 6.2, and 6.3 that most of the induced cooled gas is located around the mixing layer. Together these findings imply that most of the induced cooling by the satellite occurs in the mixing layer of stripped cold gas from the satellite. Therefore, we argue that the prime mechanisms that can contribute to the cold gas budget of the CGM of host galaxies are ram pressure stripping and induced cooling in the mixing layer of this cold stripped gas.

6.3.3 How do satellite properties affect the cold gas mass in the CGM?

In our suite of simulations we have varied several parameters: satellite mass, stellar feedback, orbital distribution, number of satellites, and simulation resolution. Here we discuss the impact of these variables on the cold gas content in the CGM of the Milky Way-like host.

6.3.3.1 Different mass distribution of satellites

In the first panel of Figure 6.5, the time evolution of cold satellite ISM gas follow similar trend for different satellite masses. However, the rate at which the cold ISM gas disappears from the satellites is different for different mass distribution. While the cold ISM gas from m08 and m09 satellites disappears roughly within 0.25 Gyr and 1 Gyr, m10 satellites lose their cold gas at much slower rate, over 3-4 Gyr time scale.

Similar scenario also applies for the time evolution of cold stripped gas from the satellites. Although the nature of plot in the second panel of Figure 6.5 for all three cases of different mass distribution is the same, the timescales of stripping in each case is very different. The massive m10 satellites continue to feed cold gas to the CGM for a longer period of time (\sim few Gyrs) than the less massive ones (m09: \sim 0.5Gyr, and m08: \sim 1.5Gyr). Therefore, only massive satellites of SMC-like mass can contribute to

the cold gas mass budget of the CGM for several Gyrs.

In the third panel of Figure 6.5, we can see the amount of host gas cooled inside the satellite are almost same for m08 and m09 satellite distributions. From comparing the third and fourth panel, it is clear that more host-gas cooling happens outside of the satellites than inside the satellites in the m09 and m08 runs. Only in the m10 runs, this amount of cold gas is a significant fraction of the total gas in the CGM.

In the fourth panel of Figure 6.5, induced cooling of the host gas outside the satellites follows the stripped cold gas. As in the initial time, there is more stripping in m08 than m09 and m10 which leads to more induced cooling in the case of m08 initially. However, roughly after 0.5 Gyr, all the gas blows out of m08, whereas at that time, the stripping of cold gas peaks for m09. Thereafter, m09 induces more cooling outside of the satellite. Those induced cool gas follows the stripped gas till the time the satellites become cold gas deficient. However, m10 continues to induce cold gas outside the satellite for several Gyrs even if at any given time the amount of cooled host gas is smaller than at the early times in m08 and m09. This also reflects the slower stripping rate in m10.

6.3.3.2 What is the fate of the cold gas contributed by satellites?

While we have shown that satellites add gas to the CGM both directly and by inducing cooling of the host halo, it is clear from Figure 6.5 that in most cases cold gas from satellites does not survive in the CGM for the entirety of our simulations. The less massive satellites lose their cold gas quickly (within 1 Gyr and 1.5 Gyr for m08 and m09 respectively) whereas, the massive satellites (m10) continue to feed cold gas to the CGM of the host galaxy even until 4 Gyr. We now ask what is the fate of this cold gas for different satellite mass distributions. The cold stripped clouds can either fall within 40 kpc of the host galaxy or they can mix with the hot host CGM. To investigate this scenario, we track the temperature of all the cold gas that is stripped from satellites. We begin tracking cold gas particles at the time of stripping, and continue until either the end of simulation or until the time the gas particle falls to within 40 kpc of the host center. We plot the time-weighted, mass-weighted temperature distribution (left panel) and cumulative distribution function (right panel) of this stripped cold gas in the Figure

6.6. We can see that for m10 there is one big peak at temperature 10^4 K and one small one at 10^6 K. That means most of the gas that is stripped in the cold phase remains cold, which is shown by the CDF to be about 70% of the cold stripped gas. For m09, we can see two almost equal peaks at 10^4 and 10^6 K showing that 40 – 50% of the cold gas remains cold and rest is mixed and heated. For the case of m08 the much bigger peak is at 10^6 K which implies most of the cold stripped gas is being heated and destroyed. One can calculate the ratio of cooling time (t_{cool}) to cloud crushing time (t_{cc}) with the variation in galacto-centric distance by using this expression:

$$t_{cool} = \frac{2.5 \times (k_b \times T_{mix})^2 \times (\mu_H/\mu)^2}{P_{CGM}(r) \times \Lambda(n_{mix}, T_{mix}, Z(r))}. \quad (6.1)$$

and

$$t_{cc} = \sqrt{\frac{T_{CGM}(r)}{T_{sat}}} \times \frac{R_{scale}}{v_{sat}} = \sqrt{\frac{\rho_{sat}}{\rho_{CGM}(r)}} \times \frac{R_{scale}}{v_{sat}}. \quad (6.2)$$

where temperature and density are inversely proportional at constant pressure. Here R_{scale} is the gas scale radius of satellite, which is proportional to satellite mass, $M_{sat}^{1/3}$, r is the initial positions of the satellites and $T_{mix} = \sqrt{T_{sat} \times T_{CGM}(r)}$. Using the cooling rate from [Wiersma et al. \(2009\)](#), and considering $T_{sat} = 10^4$ K, and $v_{sat} = 200$ km/sec (taken from the simulation values), we found that this ratio is much larger in m08 than in m10. As we visually also see from [Figure 6.3](#), the clouds are smaller in size for m08, hence have a small mixing time and gets easily heated up in small period of time. However, the clouds from m10 are larger ([Figure 6.1](#)) and have larger mixing time. Therefore those clouds survive longer time by retaining their temperature.

While there is much more physics included in our simulations, such as self gravity, star formation and feedback, it is reassuring that the size of the cold gas “cloud” may still correlate well with its survivability.

6.3.3.3 Dependence of cold gas on spatial location of the satellites in the CGM

In addition, we vary the distance of the satellites from the center of the host galaxy. In the [Figure 6.5](#), the lighter shade color indicates the runs with satellite galaxies distributed closer to the center of the host. A satellite that is closer to the center of the host feels

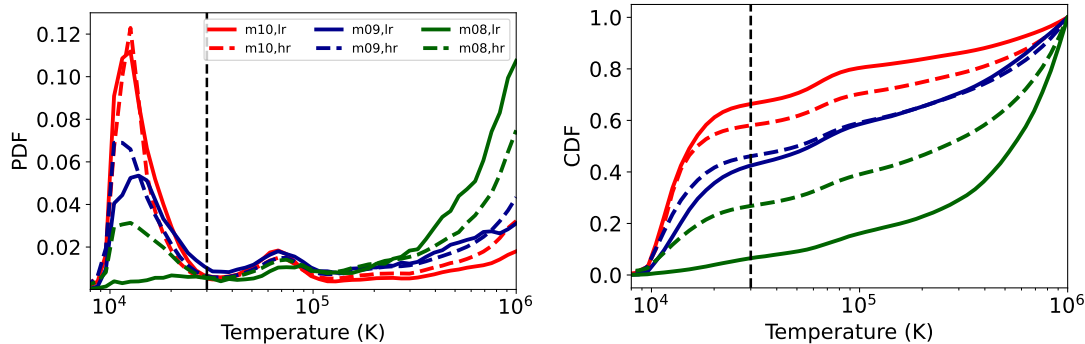


Figure 6.6: The left and the right panels respectively show the time and mass-weighted probability distribution function (PDF) and cumulative distribution function (CDF) of cold-stripped cloud mass as a function of the temperature of the cloud after the stripping. The time over which the PDF and CDF are weighted is from the time of stripping to the time at which the cloud enters 40 kpc or the end of the simulation whichever is earlier.

more ram pressure than the farther one as the density of the host is inversely related to halocentric radius. Therefore, more gas should be stripped from galaxies closer to the halo center. This effect is also clear from Figure 6.1 (rightmost; 2 Gyr snapshot), 6.2 (top right; 1 Gyr snapshot), and 6.3 (top middle; 250 Myr snapshot), where we can see that closer satellites get rid of their gas faster than the further ones. However, another competitive fact which plays a role here is that the stripped gas from the closer satellites falls to within 40 kpc of the host galaxy faster. Therefore, as time progresses, the stripped gas from the closer satellite will fall faster within 40 kpc and therefore more gas is not being accounted for in the stripped cold gas budget.

We clearly see these competing effects in the m10 runs. In the top panel of Figure 6.5, we see that the cold gas inside the closer satellites is always less than in the more distant pair. In the second panel we see that the stripped cold gas increases more quickly in the run with the closer satellites, due to the faster gas removal observed in the first panel. However, because gas from the closest satellite (50 kpc from the host center) quickly falls to within 40 kpc from the host center, the amount of stripped cold gas in the CGM from the closer satellites flattens early, and more stripped cold gas is found in the CGM from the more distant satellites. Again, the mass of host gas that cools either inside or outside the satellites follows similar trends to the cold satellite gas mass. These trends with satellite distance are independent of satellite mass.

6.3.3.4 Dependence of cold gas on stellar feedback

In this section, we investigate how stellar feedback from the host galaxy and satellites affects the contribution of cold gas to the CGM. In our run with no satellites, we find that stellar feedback from the host can contribute very little to the cold gas budget of the CGM, about 3 orders of magnitude less than what satellite galaxies would contribute. Additionally, we note that this contribution is not continuous, as cold gas in the CGM appears randomly for small duration (~ 100 Myr) due to the stellar feedback from the host.

However, the stellar feedback in satellite galaxies has a significant effect on the temperature of the gas added to the CGM. To study the effect of feedback, we also investigate runs without any feedback in the satellites and host in Figure 6.7. From the top panel, we can see that there is little effect of feedback on the cold gas inside the satellite, which implies the rate at which the cold gas disappears from the satellites are same in both cases of feedback (fb) and no feedback (nfb) runs. However, for m09, we can see that the cold gas gets stripped faster because of feedback, reaches a higher peak, and subsequently also loses the stripped cold gas faster. This is because feedback also removes hot gas, which can later cool down and add to the cold gas budget in the CGM, hence reaching a higher peak. Also without feedback, we can see more massive and narrower clouds (Bottom panels Figure 6.2, 6.3), which will survive longer than the small clouds in the feedback case. Similar trend has been observed in the time evolution of the stripped cold gas mass in the case of m08. However, for m08, the potential well is so shallow that it blows out all the gas in a very short period of time (~ 0.2 Gyr). Therefore, we do not see the stripped gas mass reaching a higher peak in m08 feedback case as m08 loses all of its gas very fast by feedback and those stripped gas does not get enough time to cool down.

This is also evident from Figure 6.8, where we show the 2-d probability distribution (PDF) of mass of the stripped gas from the satellite as a function of time and temperature of the gas. The top and bottom panels respectively indicate the m09 and m08 runs whereas left and right panels denote the cases with and without feedback, respectively. It is clear from the plots that, with no feedback the horizontal strip of cold gas distribution at 10^4 K exists for a long time, until ~ 1.6 Gyr for both m08 and m09, whereas, with

feedback, gas gets more sparse and averaged out at all temperatures also with the cold stripped gas being destroyed in a very short time of ~ 1 Gyr. In the right bar of each 2-d histogram plot, we show the 1-d histograms of temperature at single snapshots denoted by the similar colored vertical lines in 2-d histograms. We can infer the same scenario from these 1-d PDFs. For example, in m08 case with feedback, at the position of orange vertical line at 1.5 Gyr in the 2-d histogram, there is no cold gas. However, without any feedback, m08 case shows a distribution of cold gas at the same snapshot. This is also clearly shown in the 1-d histogram at 1.5 Gyr of m08, that with feedback case shows a single peak around 10^6 K temperature, but the no feedback case shows 1-d distribution of gas around 10^4 K as well. Moreover, until 1 Gyr, all the 1-d pdfs of temperature in the case of both m08 and m09, look similar in no feedback case, whereas with feedback, the low temperature distribution of 1-d PDFs shifts to the higher temperature, implying mixing of the cold stripped gas.

Feedback also changes the morphology of the stripped gas. Cold gas in feedback case has more surface area, whereas gas clouds in the no feedback case are elongated and massive with less surface area (see 2nd panel of Figure 6.2). More surface area induces more cold gas in the mixing layer of the satellite which is illustrated by the higher induced cold gas mass in the case of feedback than no feedback for m09. Also, the clumps are heavier in the case of no feedback, so they fall within the 40 kpc faster, hence not being accounted for in the cold gas budget. This is indicated by the higher induced cold gas mass in the case of feedback than no feedback for m09 (see 3rd panel of Figure 6.2). However, for m08, the trend is the opposite due to the gas getting rapidly blowing out and getting heated up by the strong feedback. Hence, within a very short period of time (~ 0.5 Gyr), there is no cold gas retaining in the stripped tail to induce cooling in the mixing layer. Additionally, the m08 feedback case produces very small clouds which get easily destroyed due to their small cloud-crushing time. However with no feedback, since the clouds are longer and more massive, they tend to survive longer time (see Figure 6.3).

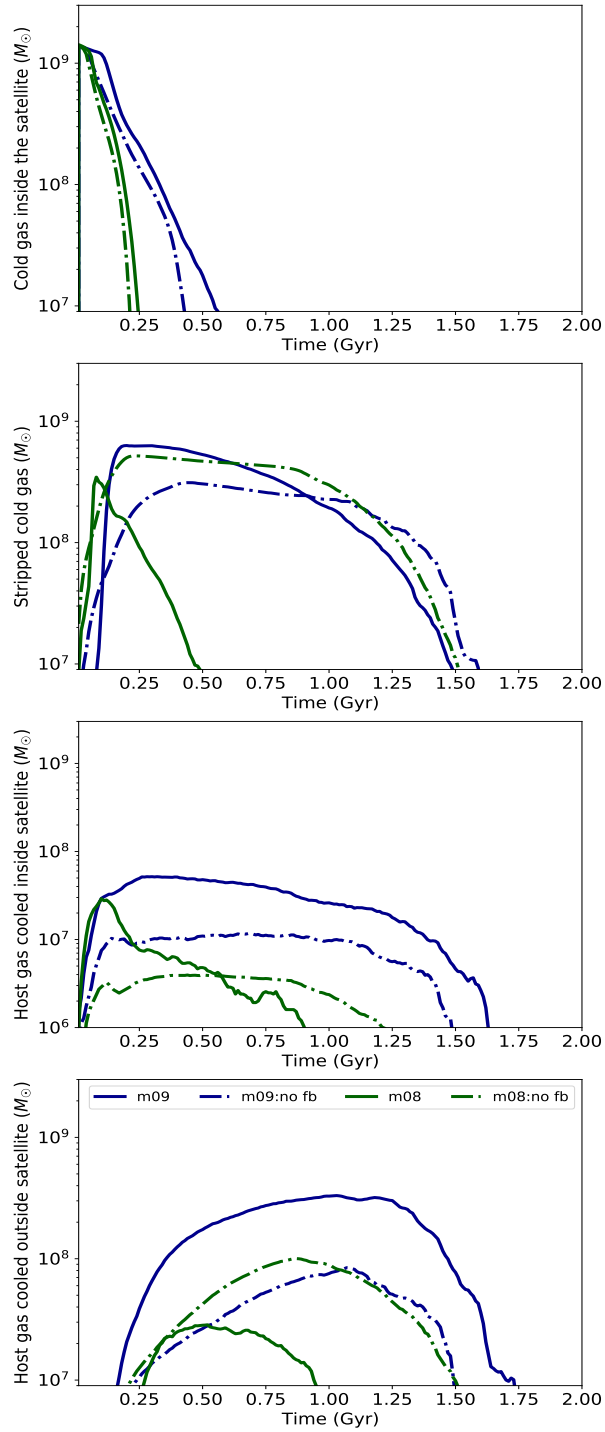


Figure 6.7: The time evolution of the cold (Temperature, $T \leq 3 \times 10^4 \text{K}$) gas mass from different contributions beyond 40kpc radius from the center of the host galaxy for the case of no feedback in satellites and host along with no gas in the satellites for the 10^9 and $10^8 M_\odot$ satellites. From left to right, the panels respectively describe cold gas stripped from the satellites which are cold satellite gas that falls beyond 6 times the scale radius of the satellites, cold gas induced inside of the satellites, and the host gas cooled outside of the satellites.

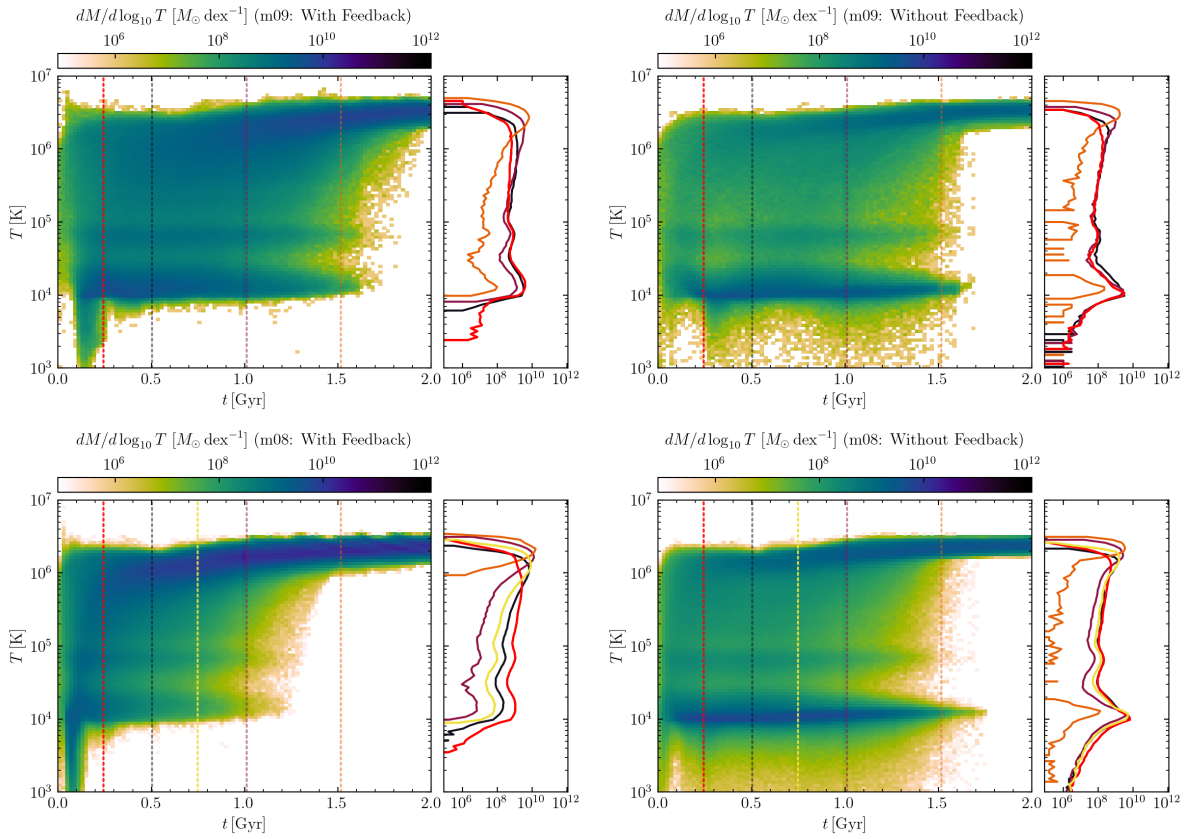


Figure 6.8: The left and the right panels show 2-d probability distribution function (PDF) of stripped gas mass as a function of the time and temperature of the gas in the case of with feedback and without feedback respectively for the m09 (top panel) and m08 (bottom panel) satellites. In the right bar of each 2-d histogram plot, we show the 1-d histograms of temperature at single snapshots denoted by the similar colored vertical lines in 2-d histograms.

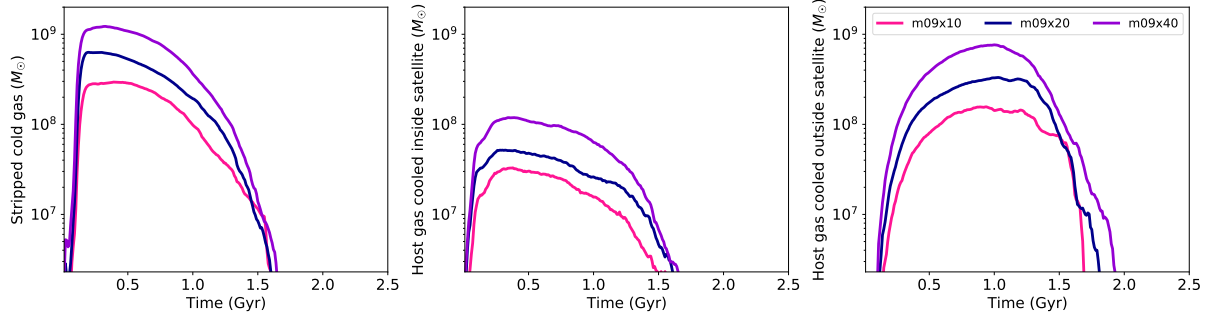


Figure 6.9: The time evolution of the cold (Temperature, $T \leq 3 \times 10^4 \text{K}$) gas mass from different contributions beyond 40kpc radius from the center of the host galaxy for the change in a number of satellites in the case of $10^9 M_\odot$ satellites. From left to right, the panels respectively describe cold gas stripped from the satellites that are cold satellite gas which falls beyond 6 times the scale radius of the satellites, cold gas induced inside of the satellites, and the host gas cooled outside of the satellites.

6.3.3.5 Dependence of cold gas on the number of satellites

We also investigate how changing the number of satellites affects the stripped gas or induced cooling contribution to the CGM. In Figure 6.9, we show three cases of m09 run with 10, 20, and 40 satellites respectively. The total amount of gas mass in the satellites in the system directly corresponds to the number of satellites. As we would expect, the contribution of stripped cold gas increases with the number of satellites (first panel). We can see from the plots, the 40 satellites run has 2 times and 4 times more stripped cold gas than the 20 satellites and 10 satellites respectively, which is roughly linear in relation. Similarly, there is about half as much cold gas in the system with 10 satellites as in the system with 20 satellites.

Given that we expect the cooling of the hot CGM gas to be dominated by mixing layer cooling, we also expect that the host gas cooled, either inside or outside the satellite, should also be related to the number of satellites. Indeed, this is what we find in the second and third panels. The increase in cold host gas is directly related to the increase in stripped gas. Therefore, increasing the number of satellites does not enhance the cold gas mass of the CGM beyond the direct correlation with the total gas mass in the satellites.

6.3.3.6 Effect of resolution

We have also performed higher resolution runs, which are shown by dashed lines in Figure 6.5. We expect that the high-resolution (hr) runs will better resolve more dense, cold gas than low resolution (lr) runs, and this can result in either harder to strip gas or more cooling in the stripped tail, which will have competing effects. Upon immediate inspection, we find that the cold gas mass in the hr runs is qualitatively similar to the lr runs and shows the same trends with satellite mass, indicating that our general results are robust to resolution.

However, running with higher resolution does not affect every simulation in the same way. For example, in the m10 case, initially stripping cold dense gas in the hr run is more difficult, therefore hr shows less cold stripped gas in the beginning than the lr run (second panel). Whereas, at later times, both of the runs show a similar amount of cold gas. This is due to the fact that at late times, when there is significant amount of stripping, the stripped hot gas can radiatively cool and the stripped cold gas can remain cool in the case of hr run due to its higher density than lr case. Therefore, they show a similar amount of stripped cold gas later on. This is also evident that there would be more cold gas inside the satellite for hr, as less gas is stripped initially and more satellite gas can radiatively cool inside the satellite as well due to the higher density in hr run. This effect is more strongly seen in the m10 run, and seen to a lesser degree in the m09 run.

For the less massive satellites of m08, in both lr and hr cases, the gas stripping occurs very rapidly and lot more quickly than from the m10 and m09 satellites due to their weaker gravitational potential. Therefore, initially they show a similar amount of stripped gas for both the cases. However, later on, more satellite gas is getting cooled in the stripped tail of hr runs for m08. The difference between hr and lr runs for the cold gas inside the satellite are not significant (for a significance study see the Appendix B) as they have very short stripping times and do not have enough time to cool more gas inside the satellite. In addition, for all the satellite distributions, the host gas that cooled inside the satellite does not show a significant difference between the hr and lr cases. Importantly, the host gas cooled outside of the satellite follows the trend of the stripped gas mass in both lr and hr cases for all the satellite distributions. Our result

holds that the more stripped gas there is, the more gas will be cooled in the mixing layer of the stripped gas.

6.4 Discussion

We have discussed in the earlier section that the host gas can be induced cool outside the satellite by the satellites in two ways: one in mixing layer cooling and another is turbulence-driven cooling. We have argued that mixing-layer cooling better matches our distribution of cold gas, but here we examine this question in more detail. We have run one case with no gas in the satellite to distinguish between the contribution of induced cool gas by these two processes. In this case there is no gas to be stripped and consequently no cooling in the mixing layer of this stripped gas. Therefore, if there is any induced cold gas outside the satellites it must be contributed by turbulence-driven cooling. Surprisingly, we do not have any induced cool gas outside the satellite in this no gas run.

In addition, we calculate the turbulent Mach number. We show the radial profile of time integrated Mach number for different satellite distribution in Figure 6.10. It turns out that the Mach number for different satellite runs do not differ from the run with no satellites. Moreover, Mach number in each case has small range of values and is much less than one, implying the velocity dispersion in the host CGM remains always subsonic. Therefore, we conclude that the induced cooling outside the satellites mainly happens in the mixing layer of the stripped cold gas from the satellites and there is not much contribution of turbulence-driven cooling.

6.5 Conclusion

We investigate the origin of the cold gas in the outer CGM and how much of this cold gas budget is contributed by satellite galaxies. For this study, we have performed controlled experiments with host galaxy of Milky Way mass along with satellite galaxies with three different satellite mass distributions (m10, m09, m08). Below, we list our main findings from this investigation.

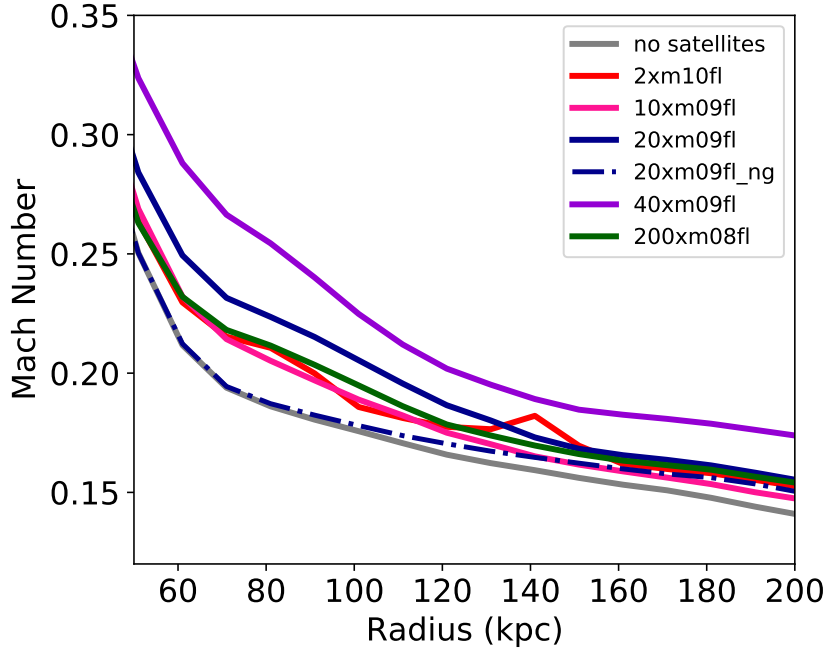


Figure 6.10: This plot shows the radial profile of time-integrated mach number which is significantly smaller than unity, implying subsonic velocity dispersion in the CGM of host galaxy even with the inclusion of different satellites.

- The satellite galaxies can contribute to the cold gas budget of the CGM of a MW-type host galaxy (Figure 6.4, 6.5, 6.9, 6.7). The setup with no satellite galaxies produce three orders of magnitude less cold gas in the CGM than the run with satellite.
- There are several mechanisms by which satellites can add cold gas to the CGM. The cold gas can be stripped from the satellite via ram pressure. Along with this, gas can also be removed from the satellites by feedback. Satellites can also induce cooling in the host CGM. We find that the most important method by which satellite induces cooling is the cooling in the mixing layer of stripped cold gas. Ram-pressure stripping and mixing layer cooling provides similar amount of cold gas to the CGM.
- The contribution of cold gas by different satellite distributions are dramatically different, even when the total gas mass brought in by the satellites is the same. The less massive satellites(m08, m09) get stripped faster and the CGM loses all of its cold gas in short period of time, the massive SMC-like satellite (m10) continues to provide cold gas to the host CGM for several Gyrs. Therefore, only LMC, SMC-

like satellites can add cold phase of roughly in the order of $10^8 M_\odot$ to the total gas budget of the MW-type host CGM even for 4 Gyr.

- The spatial location of satellites also has a significant effect on stripping and the resulting induced halo cooling. Satellites closer to the host galaxy feel more ram pressure and are stripped faster due to the higher CGM density. The larger influx of cold stripped gas then induces more cooling in the host halo.
- Stellar feedback from the host galaxy produces three orders of magnitude less cold gas than the satellite contributions. Furthermore, this contribution due to feedback from host is not continuous; cold gas in the CGM appears randomly for brief (100 Myr) time periods.
- However, supernova feedback from satellites has a significant effect on the morphology of the cold gas. Feedback makes cold clumps more diffuse and increases their surface area, which not only induces more mixing layer cooling but also speeds their destruction. However, without feedback, cold clouds have smaller surface area producing less mixing layer cooling. These clouds are denser and survive longer, even though they fall into 40kpc of host ISM faster.

Table 6.1: Properties of Initial Conditions for the Simulations/Halos Studied Here

Model	Resolution		DM halo			M_{bar} (M_{\odot})	Stellar Bulge		Stellar Disc		Gas Disc		Gas Halo	
	ϵ_g (pc)	m_g (hr/lr) (M_{\odot})	M_{halo} (M_{\odot})	r_{dh} (kpc)	V_{Max} (km/s)		M_b (M_{\odot})	a (kpc)	M_d (M_{\odot})	r_d (kpc)	M_{gd} (M_{\odot})	r_{gd} (kpc)	M_{gh} (M_{\odot})	r_{gh} (kpc)
Host galaxy														
m12	1	8e3 / 8e4	1.8e12	20	174	3.2e11	1.5e10	1.0	5.0e10	3.0	5.0e9	6.0	2.5e11	20
Satellite galaxy														
m10	1	8e3 / 8e4	2e10	4.7	35.2	7.3e8	1e7	1.5	3.0e8	0.7	4.2e8	2.1	-	-
m09	1	8e3 / 4e4	2e9	2.2	16.4	7.2e7	2e6	0.223	-	-	7e7	0.87	-	-
m08	1	8e3 / 4e4	2e8	0.9	7.62	7.3e6	8e4	0.045	-	-	7.2e6	0.27	-	-

Parameters of the galaxy models studied here : (1) Model name. The number following ‘m’ labels the approximate logarithmic halo mass. (2) ϵ_g : Minimum gravitational force softening for gas (the softening for gas in all simulations is adaptive, and matched to the hydrodynamic resolution; here, we quote the minimum Plummer equivalent softening). (3) m_g : Gas mass (resolution element). There is a resolution gradient for m14, so its m_g is the mass of the highest resolution elements. (4) M_{halo} : Dark matter halo mass within R_{vir} . (5) r_{dh} : NFW halo scale radius (the corresponding concentration of m12,m13,m14 is $c = 12, 6, 5.5$). (6) V_{max} : Halo maximum circular velocity. (7) M_{bar} : Total baryonic mass within R_{vir} . (8) M_b : Bulge mass. (9) a : Bulge Hernquist-profile scale-length. (10) M_d : Stellar disc mass. (11) r_d : Stellar disc exponential scale-length. (12) M_{gd} : Gas disc mass. (13) r_{gd} : Gas disc exponential scale-length. (14) M_{gh} : Hydrostatic gas halo mass within R_{vir} . (15) r_{gh} : Hydrostatic gas halo $\beta = 1/2$ profile scale-length.

Table 6.2: Summary of all the runs with different satellite distributions

Model	No.	Position	Resolution	Feedback	Gas	Symbol
m10	2	One at 100 kpc and one at 150 kpc	lr	Yes	Yes	2xm10fl
	2	One at 100 kpc and one at 150 kpc	hr	Yes	Yes	2xm10fh
	2	One at 50 kpc and one at 100 kpc	lr	Yes	Yes	2xm10nl
m09	20	Randomly placed between 100 kpc and 150 kpc	lr	Yes	Yes	20xm09fl
	20	Randomly placed between 100 kpc and 150 kpc	hr	Yes	Yes	20xm09fh
	20	Randomly placed between 50 kpc and 150 kpc	lr	Yes	Yes	20xm09nl
	10	Randomly placed between 100 kpc and 150 kpc	lr	Yes	Yes	10xm09fl
	40	Randomly placed between 100 kpc and 150 kpc	lr	Yes	Yes	40xm09fl
	20	Randomly placed between 100 kpc and 150 kpc	lr	No	Yes	20xm09fl_nfb
	20	Randomly placed between 100 kpc and 150 kpc	lr	Yes	No	20xm09fl_ng
m08	200	Randomly placed between 100 kpc and 150 kpc	lr	Yes	Yes	200xm08fl
	200	Randomly placed between 100 kpc and 150 kpc	hr	Yes	Yes	200xm08fh
	200	Randomly placed between 50 kpc and 150 kpc	lr	Yes	Yes	200xm08nl
	200	Randomly placed between 100 kpc and 150 kpc	hr	No	Yes	200xm08fh_nfb

Chapter 7

Conclusions and future goals

In this thesis, we have used various analytical models and numerical simulations of the CGM and compared them with multi-wavelength observations, including X-ray, UV, gamma-ray, and radio. With these tools, we have investigated several important aspects of the CGM. We have studied analytical models to examine how small-scale temperature fluctuations and photoionization affect the CGM's multi-phase ionisation structure. Additionally, we have investigated interactions of the CGM with CRs and satellite galaxies. These interactions result in the CGM's multi-phase structure, which can be probed using multi-wavelength observations. We have put constraints on the CR content and its transport mechanisms based on multi-wavelength observations. We have also explored the effects of satellite galaxies on the cooling of the CGM of the host galaxy. We outline the key findings of this thesis below and conclude with a brief summary of our future research goals.

7.1 Effects of Photoionization and Temperature Fluctuations on the Ionization Structure of the CGM

In chapter 2, we have addressed whether photoionization is needed for producing the observed absorption column density of various ions. We have developed a photoionized precipitation model for Milky Way (MW)-type galaxies ($M_{\text{halo}} \sim 1-2 \times 10^{12} M_{\odot}$). We have

also extended this model to low mass galaxies ($M_{\text{halo}} < 2 \times 10^{11} M_{\odot}$) (Roy et al., 2021a). Moreover, we have taken into account the log-normal temperature fluctuations in these models. We have found out that the observed highly ionized oxygen column densities and their ratios for the MW and star-forming galaxies can be explained if we consider significant temperature fluctuations in the CGM. We have characterised the temperature fluctuation of the CGM by dispersion of a log-normal temperature distribution, $\sigma_{\ln T}$. We have found that the range $\sigma_{\ln T} \approx 0.6 - 1.0$ is allowed by the observations mentioned earlier. We have also concluded that photoionization by extra-galactic UV background does not significantly affect the ion abundance in Milky Way Type galaxies but plays an essential role for producing different ions in the case of low-mass galaxies.

7.2 Constraints on CR content from IGRB and radio background

In chapter 3, we have put limits on CR content in the CGM of MW using observations of Isotropic γ -ray background (IGRB) from the Fermi-LAT telescope and radio background from ARCADE-2 balloon observations. We have included CR pressure component in the hydro-static equilibrium (HSE) models of the CGM: PP model and IT model. In these models, we parameterised the CR populations by $\eta = P_{\text{CR}}/P_{\text{th}}$. CR particles can interact with CGM protons and give rise to neutral pions, which decay into γ -rays. In addition, the CR electron can emit radio synchrotron emission in the magnetic field of the CGM. We have concluded that the IGRB intensity allows $\eta < 3$ and $\eta \leq 230$ for the PP and IT models, respectively. For IT model, the anisotropy that results from the Solar system's off-center position in MW rules out all values of η . For the PP model, the observed anisotropy allows only very large values of η , of order $\gtrsim 100$. The radio continuum put constraints of $\eta < 400$ for the PP model, but does not constrain η for the IT model.

7.3 Constraints on CR content from OVIII column density

In chapter 4, we have used the two models mentioned above, which incorporate the CR population and are parameterised by η . The thermal pressure in the CGM will drop with the inclusion of the CR component in the case of CGM with HSE. The thermal pressure of the CGM has a significant impact on the OVIII abundance of MW. The column density of OVIII, which is observed using X-ray data from *Chandra* and *XMM-Newton*, will therefore drop if CR is incorporated into these HSE CGM models. We have compared our model predictions with observed X-ray absorption column densities and concluded that the pressure due to CRs can be at most ten times the gas pressure in the CGM without violating the observational signatures. We have also considered models with spatially varying η : rising ($\eta = Ax$) or declining ($\eta = A/x$) with radius, where A is normalisation of the profiles. We have found that the models with a declining ratio of η match the observed column densities with suitable temperature fluctuations better than those with a rising η .

7.4 Gamma-rays from the circumgalactic medium of M31

In chapter 5, we have used two-fluid (thermal + CR) hydrodynamical code (PLUTO, Mignone et al. (2007))(Roy & Nath, 2022a) and investigated the constraints arising from the recent γ -ray observation from the CGM of M31. We have taken into account that CRs are accelerated by star formation activity in the disc of the M31 and *in-situ* in the shock of outflows. CRs can spread to the CGM, being advected by star-formation driven outflow and also through CR diffusion. Then, we have considered hadronic interactions of CRs with CGM. We have produced a mock γ -ray emission map from the CGM of M31 with the angular resolution of Fermi-LAT telescope in order to compare the detected γ -ray emission from the CGM of M31 (Karwin et al., 2019). Varying the parameters of CR physics in our simulation, we have found that the combination of advection and diffusion

(with a diffusion coefficient of 10^{29} cm²/sec) can match this observation, obviating the previous theory of γ -ray emission-origin by dark matter annihilation (Karwin et al., 2019). Our simulation matches the observation even with the minimal assumption of the equipartition of CR and thermal pressure in the initial condition. Our result strengthens the earlier findings in the thesis that one does not need CR-dominated CGM to explain the observations.

7.5 Effects of Satellites on the Cold Phase of the CGM

In chapter 6, we have investigated how much of the cold gas budget of the CGM can be contributed by satellite galaxies. Using idealised simulations (Hopkins, 2015b) of MW-type host galaxies with a varying distribution of satellite galaxies, we have concluded that the satellite galaxies can significantly supply cold gas to the CGM not only by direct stripping but also equally by induced cooling in the mixing layer of the stripped cold gas. We have also found that the massive satellites like the Large Magellanic Cloud (LMC) continue to feed cold gas to the CGM for several Gyr. However, low-mass satellites quickly lose all of their gas. This is due to the fact that the low-mass satellites produce smaller clouds than massive satellites. These small clouds have short cloud-crushing time which therefore leads to their quick destruction.

7.6 Future goals

1) What is the effect of group environment on the multiphase CGM?

Our previous work has already shown that there is a significant contribution of the cold phase to the CGM by satellite galaxies. As a next step, we plan to incorporate realistic distribution of the satellites of Milky Way and to investigate the effect on the cold gas budget of the Milky Way CGM. The presence or lack of a satellite CGM in the initial conditions can make a major differences. It is expected that isolated galaxies of similar mass as our satellites have more mass in their CGM than in their ISM (Hafen et al.,

2019), and in an analysis of the fate of satellite CGM it is also found that much of it accretes onto the central galaxy (Hafen et al., 2020). It is also seen that the satellite CGM plays a major role in cooling of CGM gas in cosmological FIRE simulations (Esmerian et al., 2021). Other idealized simulations of satellite stripping that do not include satellite CGM are unsuccessful in producing sufficient cold gas mass to match observations, and underestimate the importance of satellite galaxies for galaxy growth as a whole (Bustard et al., 2018). Our future plan is to include CGM in the satellites and investigate the change in the amount of the cold gas contributed by the satellites. However, one can take our current estimates as a lower limit of the cold gas produced in the host CGM by the satellite galaxies. We will also study the effect of CRs on the ram-pressure stripping by methodically varying the CR physics in these simulations. Using the simulation results, our goal is to build semi-analytical models of the mass of ram pressure-stripped gas, feedback-ejected gas, induced-cool gas contributed by satellite galaxies and their time evolution. Then we plan to implement these models as sub-grid modules in FIRE cosmological simulations and calculate the column density, covering fractions of different ions as a function of redshifts to compare them with different observations.

2) What is the effect of group environment on the SFR of the host galaxy and satellite galaxies?

We plan to study how the cold gas from the satellites that are falling into the host galaxy's disk affects the SFR of the host galaxy. It can be tested in light of the recent burst in SFR of MW and M31. Recent observation (Martín-Navarro et al., 2021) from a sample of 124,163 satellite galaxy pointed out that quenched satellite galaxies are less frequent along the minor axis of their central galaxy due to the fact that outflows along that axis swept out the CGM that reduces the ram pressure stripping and retain the satellite galaxy's star formation. In light of this observation, we will investigate the effect on the SFR of the satellite galaxies due to ram-pressure stripping in the group environment and how it depends on the orbital plane of satellites.

3) What is the CR content in the CGM and what are the effects of CR on CGM properties?

We plan to run two-fluid simulation code (CR + thermal) PLUTO with the variation in galactic properties (e.g SFR, mass loading factor) and CR physics (e.g CR energy distribution, transport mechanism). We will produce mock γ -ray, X-ray and radio map

from our simulation runs to constrain CR content and CR transport mechanism in the CGM by comparing them with γ -ray, X-ray, and radio observations. We will investigate how CR affect the structure and kinematics of galactic winds and how it will depend on CR transport mechanism. We also plan to study cloud size and mass distribution with the variation in CR physics in our simulations.

4) What is the amount, nature, and origin of small-scale temperature fluctuations in the CGM?

CGM is not homogeneous and there are small scale temperature fluctuations. We found in this thesis that this fluctuation is related to properties of the host galaxy like star-formation rate. We will study this fluctuation in high resolution idealised simulation with the variation in galactic properties and CR physics to investigate if we see any correlation with them. We plan to extend this project by measuring temperature fluctuations in cosmological simulations (like TNG50) and distinguish the different origin of these fluctuations. We will also investigate if this temperature fluctuation deviates from the generally assumed log-normal distribution and try to quantify the deviation.

Bibliography

Ackermann M., et al., 2012, , [85](#), [083007](#)

Ackermann M., et al., 2015, , [799](#), [86](#)

Ackermann M., et al., 2017, , [836](#), [208](#)

Anderson M. E., Bregman J. N., 2011, , [737](#), [22](#)

Anderson M. E., Bregman J. N., Dai X., 2013, , [762](#), [106](#)

Anderson M. E., Gaspari M., White S. D. M., Wang W., Dai X., 2015, , [449](#), [3806](#)

Anderson M. E., Churazov E., Bregman J. N., 2016, , [455](#), [227](#)

Atwood W. B., et al., 2009, , [697](#), [1071](#)

Augustin R., et al., 2019, , [489](#), [2417](#)

Bahcall J. N., Spitzer Lyman J., 1969, , [156](#), [L63](#)

Bell A. R., 1978, , [182](#), [147](#)

Berezinsky V. S., Blasi P., Ptuskin V. S., 1997, , [487](#), [529](#)

Bernal C. G., Sánchez-Salcedo F. J., 2013, , [775](#), [72](#)

Bernet M. L., Miniati F., Lilly S. J., Kronberg P. P., Dessauges-Zavadsky M., 2008, , [454](#),
[302](#)

Besla G., 2015, arXiv e-prints, [p. arXiv:1511.03346](#)

Besla G., Kallivayalil N., Hernquist L., van der Marel R. P., Cox T. J., Kereš D., 2010, ,
[721](#), [L97](#)

- Bhattacharyya S., Das S., Gupta A., Mathur S., Krongold Y., 2022, [arXiv e-prints](#), p. [arXiv:2208.07863](#)
- Binney J., Nipoti C., Fraternali F., 2009, , [397](#), [1804](#)
- Birkinshaw M., 1999, , [310](#), [97](#)
- Birnboim Y., Dekel A., 2003, , [345](#), [349](#)
- Bland-Hawthorn J., Gerhard O., 2016, , [54](#), [529](#)
- Blasi P., Amato E., 2019, , 122, 051101
- Bluem J., et al., 2022, , [936](#), [72](#)
- Bogdán Á., et al., 2013a, , [772](#), [97](#)
- Bogdán Á., Forman W. R., Kraft R. P., Jones C., 2013b, , [772](#), [98](#)
- Bordoloi R., et al., 2014a, , [794](#), [130](#)
- Bordoloi R., et al., 2014b, , [796](#), [136](#)
- Bordoloi R., et al., 2014c, , [796](#), [136](#)
- Borthakur S., et al., 2015, , [813](#), [46](#)
- Bowen D. V., Chelouche D., Jenkins E. B., Tripp T. M., Pettini M., York D. G., Frye B. L., 2016, , [826](#), [50](#)
- Bustard C., Pardy S. A., D'Onghia E., Zweibel E. G., Gallagher J. S. I., 2018, , [863](#), [49](#)
- Butsky I. S., Quinn T. R., 2018, , [868](#), [108](#)
- Butsky I. S., Fielding D. B., Hayward C. C., Hummels C. B., Quinn T. R., Werk J. K., 2020, , [903](#), [77](#)
- CHIME/FRB Collaboration et al., 2021, , [257](#), [59](#)
- Cai Z., et al., 2017, , [839](#), [131](#)
- Cantalupo S., Arrigoni-Battaia F., Prochaska J. X., Hennawi J. F., Madau P., 2014, , [506](#), [63](#)

- Chan T. K., Kereš D., Hopkins P. F., Quataert E., Su K. Y., Hayward C. C., Faucher-Giguère C. A., 2019a, , [488](#), [3716](#)
- Chan T. K., Kereš D., Hopkins P. F., Quataert E., Su K. Y., Hayward C. C., Faucher-Giguère C. A., 2019b, , [488](#), [3716](#)
- Chen H.-W., Helsby J. E., Gauthier J.-R., Sackett P. M., Thompson I. B., Tinker J. L., 2010, , [714](#), [1521](#)
- Chen H.-W., Zahedy F. S., Johnson S. D., Pierce R. M., Huang Y.-H., Weiner B. J., Gauthier J.-R., 2018, , [479](#), [2547](#)
- Cordes J. M., Ocker S. K., Chatterjee S., 2022, , [931](#), [88](#)
- Das S., Mathur S., Gupta A., 2020, arXiv e-prints, [p. arXiv:2003.13953](#)
- Das S., Mathur S., Gupta A., Krongold Y., 2021, , [918](#), [83](#)
- Dashyan G., Dubois Y., 2020, arXiv e-prints, [p. arXiv:2003.09900](#)
- Davies J. J., Crain R. A., Oppenheimer B. D., Schaye J., 2020, , [491](#), [4462](#)
- Dermer C. D., 1986, , [157](#), [223](#)
- Drury L. O., 1983, [Reports on Progress in Physics](#), [46](#), [973](#)
- Dutta R., et al., 2021, , [508](#), [4573](#)
- Esmerian C. J., Kravtsov A. V., Hafen Z., Faucher-Giguere C.-A., Quataert E., Stern J., Keres D., Wetzel A., 2020, arXiv e-prints, [p. arXiv:2006.13945](#)
- Esmerian C. J., Kravtsov A. V., Hafen Z., Faucher-Giguère C.-A., Quataert E., Stern J., Kereš D., Wetzel A., 2021, , [505](#), [1841](#)
- Faerman Y., Sternberg A., McKee C. F., 2017, , [835](#), [52](#)
- Faerman Y., Sternberg A., McKee C. F., 2019, Massive Warm/Hot Galaxy Coronae: II – Isentropic Model ([arXiv:1909.09169](#))
- Faerman Y., Pandya V., Somerville R. S., Sternberg A., 2021, arXiv e-prints, [p. arXiv:2107.02182](#)

- Fang T., Bullock J., Boylan-Kolchin M., 2013, , [762](#), [20](#)
- Fang T., Buote D., Bullock J., Ma R., 2015, , [217](#), [21](#)
- Faucher-Giguère C.-A., Hopkins P. F., Kereš D., Muratov A. L., Quataert E., Murray N., 2015, , [449](#), [987](#)
- Faucher-Giguère C.-A., Feldmann R., Quataert E., Kereš D., Hopkins P. F., Murray N., 2016, , [461](#), [L32](#)
- Feldmann R., Hooper D., Gnedin N. Y., 2013, , [763](#), [21](#)
- Ferland G. J., et al., 2017, The 2017 Release of Cloudy ([arXiv:1705.10877](#))
- Fermi E., 1949, [Physical Review](#), [75](#), [1169](#)
- Field G. B., 1965, , [142](#), [531](#)
- Fielding D., Quataert E., McCourt M., Thompson T. A., 2017, , [466](#), [3810](#)
- Fielding D. B., et al., 2020, , [903](#), [32](#)
- Fixsen D. J., et al., 2011, [The Astrophysical Journal](#), [734](#), [5](#)
- Gatto A., Fraternali F., Read J. I., Marinacci F., Lux H., Walch S., 2013, , [433](#), [2749](#)
- Ghirardini V., et al., 2019, , [621](#), [A41](#)
- Gnat O., 2017, , [228](#), [11](#)
- Greivich J., Putman M. E., 2009a, , [696](#), [385](#)
- Greivich J., Putman M. E., 2009b, , [696](#), [385](#)
- Grevesse N., Asplund M., Sauval A. J., Scott P., 2010, , [328](#), [179](#)
- Gunn J. E., Gott J. Richard I., 1972, , [176](#), [1](#)
- Gupta A., Mathur S., Krongold Y., Nicastro F., Galeazzi M., 2012, , [756](#), [L8](#)
- Gupta S., Nath B. B., Sharma P., 2018, , [479](#), [5220](#)
- Haardt F., Madau P., 2012, , [746](#), [125](#)

- Hafen Z., et al., 2017, , [469](#), [2292](#)
- Hafen Z., et al., 2019, , [488](#), [1248](#)
- Hafen Z., et al., 2020, , [494](#), [3581](#)
- Hagihara T., Yao Y., Yamasaki N. Y., Mitsuda K., Wang Q. D., Takei Y., Yoshino T., McCammon D., 2010, , [62](#), [723](#)
- Hand N., et al., 2012, , [109](#), [041101](#)
- Häring N., Rix H.-W., 2004, , [604](#), [L89](#)
- Hayes M., Melinder J., Östlin G., Scarlata C., Lehnert M. D., Mannerström-Jansson G., 2016, , [828](#), [49](#)
- Heckman T. M., Alexandroff R. M., Borthakur S., Overzier R., Leitherer C., 2015, , [809](#), [147](#)
- Henley D. B., Shelton R. L., 2010, , [187](#), [388](#)
- Henley D. B., Shelton R. L., Kwak K., Joung M. R., Mac Low M.-M., 2010, , [723](#), [935](#)
- Hennawi J. F., Prochaska J. X., Cantalupo S., Arrigoni-Battaia F., 2015, [Science](#), 348, [779](#)
- Henry A., Scarlata C., Martin C. L., Erb D., 2015, , [809](#), [19](#)
- Hernquist L., 1990, , [356](#), [359](#)
- Hillas A. M., 1984, , [22](#), [425](#)
- Hopkins P. F., 2015a, , [450](#), [53](#)
- Hopkins P. F., 2015b, , [450](#), [53](#)
- Hopkins P. F., 2016, , [462](#), [576](#)
- Hopkins P. F., 2017, , [466](#), [3387](#)
- Hopkins P. F., Raives M. J., 2016, , [455](#), [51](#)
- Hopkins P. F., Quataert E., Murray N., 2011, , [417](#), [950](#)

- Hopkins P. F., Narayanan D., Murray N., 2013, , [432](#), [2647](#)
- Hopkins P. F., et al., 2018a, , [477](#), [1578](#)
- Hopkins P. F., et al., 2018b, , [480](#), [800](#)
- Hopkins P. F., Chan T. K., Ji S., Hummels C., Keres D., Quataert E., Faucher-Giguere C.-A., 2020, arXiv e-prints, p. [arXiv:2002.02462](#)
- Hopkins P. F., Chan T. K., Ji S., Hummels C. B., Kereš D., Quataert E., Faucher-Giguère C.-A., 2021, , [501](#), [3640](#)
- Hummels C. B., Bryan G. L., Smith B. D., Turk M. J., 2013, , [430](#), [1548](#)
- Hummels C. B., et al., 2019, , [882](#), [156](#)
- Humphrey P. J., Buote D. A., Canizares C. R., Fabian A. C., Miller J. M., 2011, , [729](#), [53](#)
- Jana R., Gupta S., Nath B. B., 2020a, , [497](#), [2623](#)
- Jana R., Roy M., Nath B. B., 2020b, , [903](#), [L9](#)
- Jenkins E. B., Tripp T. M., 2011, [The Astrophysical Journal](#), 734, 65
- Ji S., Oh S. P., McCourt M., 2018, [Monthly Notices of the Royal Astronomical Society](#), 476, 852
- Ji S., et al., 2019, arXiv e-prints, p. [arXiv:1909.00003](#)
- Ji S., et al., 2020, , [496](#), [4221](#)
- Johnson S. D., Chen H.-W., Mulchaey J. S., 2015, , [449](#), [3263](#)
- Johnson S. D., Chen H.-W., Mulchaey J. S., Schaye J., Straka L. A., 2017, , [850](#), [L10](#)
- Joung M. R., Putman M. E., Bryan G. L., Fernández X., Peek J. E. G., 2012, , 759, 137
- Kaaret P., et al., 2020, [Nature Astronomy](#), 4, [1072](#)
- Karwin C., Murgia S., Campbell S., Moskalenko I., 2019, in 36th International Cosmic Ray Conference (ICRC2019). p. 570 ([arXiv:1903.10533](#))

- Karwin C. M., Murgia S., Moskalenko I. V., Fillingham S. P., Burns A.-K., Fieg M., 2021, [Phys. Rev. D](#), 103, 023027
- Keating L. C., Pen U.-L., 2020, , [496](#), [L106](#)
- Kereš D., Katz N., Weinberg D. H., Davé R., 2005, , [363](#), [2](#)
- Kereš D., Katz N., Davé R., Fardal M., Weinberg D. H., 2009, , 396, 2332
- Kim J., et al., 2021, arXiv e-prints, p. [arXiv:2110.15381](#)
- Kravtsov A. V., 2013, , [764](#), [L31](#)
- Kroupa P., 2002, [Science](#), 295, 82
- Krumholz M. R., Crocker R. M., Xu S., Lazarian A., Rosevear M. T., Bedwell-Wilson J., 2020, , [493](#), [2817](#)
- Kulkarni S. R., Ofek E. O., Neill J. D., 2015, [arXiv e-prints](#), p. [arXiv:1511.09137](#)
- Lan T.-W., Mo H., 2018, , 866, 36
- Lan T.-W., Mo H., 2019, , 486, 608
- Lan T.-W., Prochaska J. X., 2020, , [496](#), [3142](#)
- Lehner N., Howk J. C., Wakker B. P., 2015, , [804](#), [79](#)
- Lehner N., et al., 2020, , [900](#), [9](#)
- Leitherer C., et al., 1999, , [123](#), [3](#)
- Li M., Tonnesen S., 2020, , [898](#), [148](#)
- Li Y., Bryan G. L., Ruszkowski M., Voit G. M., O'Shea B. W., Donahue M., 2015, , [811](#), [73](#)
- Liang C. J., Kravtsov A. V., Agertz O., 2016, , [458](#), [1164](#)
- Liu R.-Y., Yan H., Wang X.-Y., Shao S., Li H., 2019, , [871](#), [40](#)
- Lochhaas C., Bryan G. L., Li Y., Li M., Fielding D., 2020a, , [493](#), [1461](#)

- Lochhaas C., Bryan G. L., Li Y., Li M., Fielding D., 2020b, , [493](#), [1461](#)
- Macquart J. P., et al., 2020, , [581](#), [391](#)
- Maller A. H., Bullock J. S., 2004, , [355](#), [694](#)
- Marinacci F., et al., 2018, , [480](#), [5113](#)
- Martin C. L., 2005, , [621](#), [227](#)
- Martín-Navarro I., Pillepich A., Nelson D., Rodriguez-Gomez V., Donnari M., Hernquist L., Springel V., 2021, , [594](#), [187](#)
- Martin D. C., Matuszewski M., Morrissey P., Neill J. D., Moore A., Cantalupo S., Prochaska J. X., Chang D., 2015, *Nature*, 524, 192—195
- McCourt M., Sharma P., Quataert E., Parrish I. J., 2011, , [419](#), [3319](#)
- McCourt M., Sharma P., Quataert E., Parrish I. J., 2012, , [419](#), [3319](#)
- McCourt M., O’Leary R. M., Madigan A.-M., Quataert E., 2015, , [449](#), [2](#)
- McQuinn M., 2014, , [780](#), [L33](#)
- McQuinn M., Werk J. K., 2018, , [852](#), [33](#)
- Meiring J. D., Tripp T. M., Werk J. K., Howk J. C., Jenkins E. B., Prochaska J. X., Lehner N., Sembach K. R., 2013, , [767](#), [49](#)
- Mignone A., Bodo G., Massaglia S., Matsakos T., Tesileanu O., Zanni C., Ferrari A., 2007, , [170](#), [228](#)
- Miller M. J., Bregman J. N., 2013, , [770](#), [118](#)
- Miller M. J., Bregman J. N., 2015a, , [800](#), [14](#)
- Miller M. J., Bregman J. N., 2015b, , [800](#), [14](#)
- Miyamoto M., Nagai R., 1975, , [27](#), [533](#)
- Mo H. J., Mao S., White S. D. M., 1998, , [295](#), [319](#)
- Mo H., van den Bosch F. C., White S., 2010, *Galaxy Formation and Evolution*

- Morrison P., 1958, *Il Nuovo Cimento*, 7, 858
- Münch G., Zirin H., 1961, , 133, 11
- Muzahid S., et al., 2021, , 508, 5612
- Navarro J. F., Frenk C. S., White S. D. M., 1996a, , 462, 563
- Navarro J. F., Frenk C. S., White S. D. M., 1996b, , 462, 563
- Navarro J. F., Frenk C. S., White S. D. M., 1997, , 490, 493
- Nelson D., et al., 2018, , 477, 450
- Nelson D., et al., 2019, , 490, 3234
- Nelson D., Byrohl C., Peroux C., Rubin K. H. R., Burchett J. N., 2021, , 507, 4445
- Niu C. H., et al., 2022, , 606, 873
- O’Shea B. W., Bryan G., Bordner J., Norman M. L., Abel T., Harkness R., Kritsuk A., 2004, [arXiv e-prints](#), pp [astro-ph/0403044](#)
- Oppenheimer B. D., et al., 2016a, , 460, 2157
- Oppenheimer B. D., et al., 2016b, , 460, 2157
- Oppenheimer B. D., Schaye J., Crain R. A., Werk J. K., Richings A. J., 2018, , 481, 835
- Osterman S. N., Wilkinson E., Green J. C., Redman K. W., 2002, in Larar A. M., Mlynczak M. G., eds, *Society of Photo-Optical Instrumentation Engineers (SPIE) Conference Series Vol. 4485, Optical Spectroscopic Techniques, Remote Sensing, and Instrumentation for Atmospheric and Space Research IV*. pp 361–369, [doi:10.1117/12.454270](#)
- Ostriker E. C., 1999, , 513, 252
- Pandhi A., Hutschenreuter S., West J. L., Gaensler B. M., Stock A., 2022, , 516, 4739
- Peek J. E. G., Bish H., 2020, in *American Astronomical Society Meeting Abstracts #236*. p. 205.03

- Peeples M. S., et al., 2019, , [873](#), [129](#)
- Petroff E., Hessels J. W. T., Lorimer D. R., 2022, , [30](#), [2](#)
- Pfrommer C., Enßlin T. A., 2004, , [413](#), [17](#)
- Pillepich A., et al., 2018, , [473](#), [4077](#)
- Planck Collaboration et al., 2013a, , [557](#), [A52](#)
- Planck Collaboration et al., 2013b, , [557](#), [A52](#)
- Planck Collaboration et al., 2016a, , [586](#), [A140](#)
- Planck Collaboration et al., 2016b, , [594](#), [A13](#)
- Prescott M. K. M., Martin C. L., Dey A., 2015, , [799](#), [62](#)
- Prochaska J. X., Hennawi J. F., Simcoe R. A., 2013, , [762](#), [L19](#)
- Prochaska J. X., et al., 2017a, , [837](#), [169](#)
- Prochaska J. X., et al., 2017b, , [837](#), [169](#)
- Prochaska J. X., et al., 2019, [Science](#), [366](#), [231](#)
- Putman M. E., Peek J. E. G., Joung M. R., 2012, , [50](#), [491](#)
- Putman M. E., Zheng Y., Price-Whelan A. M., Greevich J., Johnson A. C., Tollerud E.,
Peek J. E. G., 2021, , [913](#), [53](#)
- Qu Z., Bregman J. N., 2018, , [856](#), [5](#)
- Rauch M., Haehnelt M. G., 2011, , [412](#), [L55](#)
- Ravi V., 2019, , [872](#), [88](#)
- Read J. I., Iorio G., Agertz O., Fraternali F., 2017, , [467](#), [2019](#)
- Recchia S., Blasi P., Morlino G., 2016, , [462](#), [4227](#)
- Recchia S., Gabici S., Aharonian F. A., Niro V., 2021a, , [914](#), [135](#)
- Recchia S., Gabici S., Aharonian F. A., Niro V., 2021b, , [914](#), [135](#)

- Reynoso M. M., Romero G. E., Christiansen H. R., 2008, , [387](#), [1745](#)
- Richter P., et al., 2017, , [607](#), [A48](#)
- Roy M., Nath B. B., 2022a, , [514](#), [1412](#)
- Roy M., Nath B. B., 2022b, , [931](#), [125](#)
- Roy M., Nath B. B., Voit G. M., 2021a, , [507](#), [3849](#)
- Roy M., Nath B. B., Voit G. M., 2021b, , [507](#), [3849](#)
- Rubin K. H. R., Prochaska J. X., Koo D. C., Phillips A. C., Martin C. L., Winstrom L. O., 2014, , [794](#), [156](#)
- Rubin K. H. R., Hennawi J. F., Prochaska J. X., Simcoe R. A., Myers A., Lau M. W., 2015, , [808](#), [38](#)
- Rudie G. C., et al., 2012, , [750](#), [67](#)
- Ruszkowski M., Yang H. Y. K., Reynolds C. S., 2017, , [844](#), [13](#)
- Rybicki G. B., Lightman A. P., 1986, *Radiative Processes in Astrophysics*
- Rybicki G., Lightman A., 2004, *Radiative Processes in Astrophysics*
- Salem M., Bryan G. L., Corlies L., 2015, [Monthly Notices of the Royal Astronomical Society](#), [456](#), [582](#)
- Salem M., Bryan G. L., Corlies L., 2016, , [456](#), [582](#)
- Salpeter E. E., 1955, , [121](#), [161](#)
- Sánchez Almeida J., 2020, , [495](#), [78](#)
- Sancisi R., Fraternali F., Oosterloo T., van der Hulst T., 2008, [The Astronomy and Astrophysics Review](#), [15](#), [189](#)
- Sarkar K. C., Nath B. B., Sharma P., Shchekinov Y., 2015, , [448](#), [328](#)
- Savage B. D., et al., 2003, [The Astrophysical Journal Supplement Series](#), [146](#), [125](#)
- Sharma P., McCourt M., Quataert E., Parrish I. J., 2012, , [420](#), [3174](#)

- Sharma P., Roy A., Nath B. B., Shchekinov Y., 2014, , [443](#), [3463](#)
- Singh P., Nath B. B., Majumdar S., Silk J., 2015, , [448](#), [2384](#)
- Singh P., Majumdar S., Nath B. B., Silk J., 2018, , [478](#), [2909](#)
- Snowden S. L., et al., 1997, , [485](#), [125](#)
- Socrates A., Davis S. W., Ramirez-Ruiz E., 2008, , [687](#), [202](#)
- Spitzer Lyman J., 1956, , [124](#), [20](#)
- Springel V., 2000, , [312](#), [859](#)
- Springel V., 2005, , [364](#), [1105](#)
- Springel V., White S. D. M., 1999, , [307](#), [162](#)
- Stanimirović S., Dickey J. M., Krčo M., Brooks A. M., 2002, , [576](#), [773](#)
- Stern J., Hennawi J. F., Prochaska J. X., Werk J. K., 2016, , [830](#), [87](#)
- Stern J., Fielding D., Faucher-Giguère C.-A., Quataert E., 2019, , [488](#), [2549](#)
- Stern J., Fielding D., Faucher-Giguère C.-A., Quataert E., 2020, , [492](#), [6042](#)
- Stocke J. T., Penton S. V., Danforth C. W., Shull J. M., Tumlinson J., McLin K. M., 2006, , [641](#), [217](#)
- Stocke J. T., Keeney B. A., Danforth C. W., Shull J. M., Froning C. S., Green J. C., Penton S. V., Savage B. D., 2013, , [763](#), [148](#)
- Stocke J. T., Keeney B. A., Danforth C. W., Oppenheimer B. D., Pratt C. T., Berlind A. A., 2017, , [838](#), [37](#)
- Strickland D. K., Heckman T. M., 2007, , [658](#), [258](#)
- Su M., Slatyer T. R., Finkbeiner D. P., 2010, , [724](#), [1044](#)
- Su K.-Y., Hopkins P. F., Hayward C. C., Faucher-Giguère C.-A., Kereš D., Ma X., Robles V. H., 2017, , [471](#), [144](#)
- Su K.-Y., et al., 2019, , [487](#), [4393](#)

- Su K.-Y., et al., 2020, , [491](#), [1190](#)
- Subrahmanyam R., Cowsik R., 2013, , [776](#), [42](#)
- Suresh J., Nelson D., Genel S., Rubin K. H. R., Hernquist L., 2019, , [483](#), [4040](#)
- Sutherland R. S., Dopita M. A., 1993a, , [88](#), [253](#)
- Sutherland R. S., Dopita M. A., 1993b, , [88](#), [253](#)
- Thom C., et al., 2012, , [758](#), [L41](#)
- Tonnesen S., Bryan G. L., 2021, , [911](#), [68](#)
- Tripp T. M., et al., 2011, [Science](#), [334](#), [952](#)
- Tumlinson J., et al., 2011, [Science](#), [334](#), [948](#)
- Tumlinson J., et al., 2013, , [777](#), [59](#)
- Tumlinson J., Peebles M. S., Werk J. K., 2017, , [55](#), 389–432
- Vogelsberger M., et al., 2014, , [509](#), [177](#)
- Voit G. M., 2018, , [868](#), [102](#)
- Voit G. M., 2019, , [880](#), [139](#)
- Voit G. M., 2021, , [908](#), [L16](#)
- Voit G. M., Donahue M., Bryan G. L., McDonald M., 2015, , [519](#), [203](#)
- Voit G. M., Meece G., Li Y., O’Shea B. W., Bryan G. L., Donahue M., 2017, , [845](#), [80](#)
- Wadsley J. W., Stadel J., Quinn T., 2004, , [9](#), [137](#)
- Walker S. A., Bagchi J., Fabian A. C., 2015, , [449](#), [3527](#)
- Wang Q. D., Immler S., Walterbos R., Lauroesch J. T., Breitschwerdt D., 2001, , [555](#),
[L99](#)
- Wang Q. D., Chaves T., Irwin J. A., 2003, , [598](#), [969](#)

- Wang J., Bose S., Frenk C. S., Gao L., Jenkins A., Springel V., White S. D. M., 2020, , [585](#), [39](#)
- Weinberger R., Springel V., Pakmor R., 2020, , [248](#), [32](#)
- Werk J. K., et al., 2014, , [792](#), [8](#)
- Werk J. K., et al., 2016, , [833](#), [54](#)
- White S. D. M., Frenk C. S., 1991, , [379](#), [52](#)
- Wiener J., Zweibel E., Oh P., 2013, [The Astrophysical Journal](#), 767
- Wiener J., Pfrommer C., Oh S. P., 2017, [Monthly Notices of the Royal Astronomical Society](#), 467, 906
- Wiersma R. P. C., Schaye J., Smith B. D., 2009, , [393](#), [99](#)
- Williams B. F., et al., 2017, , [846](#), [145](#)
- Wu X., McQuinn M., 2022, [arXiv e-prints](#), p. [arXiv:2209.04455](#)
- Yang Y.-P., Li Q.-C., Zhang B., 2020, , [895](#), [7](#)
- Zahedy F. S., Chen H.-W., Johnson S. D., Pierce R. M., Rauch M., Huang Y.-H., Weiner B. J., Gauthier J.-R., 2018, , 484, 2257
- Zhang D., 2018, [Galaxies](#), 6, 114
- Zhang H., Zaritsky D., Zhu G., Ménard B., Hogg D. W., 2016, , [833](#), [276](#)
- Zhang Y., Liu R.-Y., Li H., Shao S., Yan H., Wang X.-Y., 2021, , [911](#), [58](#)
- Zhu G., et al., 2014, , [439](#), [3139](#)
- de Graaff A., Cai Y.-C., Heymans C., Peacock J. A., 2019, , [624](#), [A48](#)
- van de Voort F., Springel V., Mandelker N., van den Bosch F. C., Pakmor R., 2019, , [482](#), [L85](#)

Appendix A

Geometry

Consider two coordinate systems, one for the Milky Way (MW) and another for Andromeda (M31) (See the Figure A.1 for reference). We denote the coordinate system for MW by ‘M’ (XYZ), which is centered at the solar position (O_M). In this coordinate system, the Z-axis points towards the North celestial pole (NCP), X-axis is directed towards the projection of the centre of M31 in the equatorial plane, and the Y-axis is perpendicular to X-axis in the equatorial plane. The coordinate system for M31 is denoted by ‘A’ (X’Y’Z’) and whose origin is at centre of M31 (O_A) with equatorial coordinates, RA= α_0 and DEC= δ_0 respectively. Its axes are aligned with the axes of ‘M’. Consider any point P in the sky with RA and DEC of α, δ . Andromeda’s origin O_A and the point P have position vectors $\vec{r}_{M,0}$ and \vec{r}_M respectively w.r.t the coordinate system ‘M’. Therefore, the position vector of the point P w.r.t M31 coordinate ‘A’ would be $\vec{r}_A = \vec{r}_M - \vec{r}_{M,0}$.

The three components of \vec{r}_M is

$$\begin{aligned}x_M &= r_M \cos(\alpha - \alpha_0) \cos(\delta), \\y_M &= r_M \sin(\alpha - \alpha_0) \cos(\delta), \text{ and} \\z_M &= r_M \sin(\delta).\end{aligned}\tag{A.1}$$

Similarly, the three components of $\vec{r}_{M,0}$ is

$$\begin{aligned}x_{M,0} &= r_{M,0} \cos(\delta_0), \\y_{M,0} &= 0, \text{ and} \\z_{M,0} &= r_{M,0} \sin(\delta_0).\end{aligned}\tag{A.2}$$

$$\text{and } R_{y, \text{clock}}(\theta) = \begin{pmatrix} \cos \theta & 0 & \sin \theta \\ 0 & 1 & 0 \\ -\sin \theta & 0 & \cos \theta \end{pmatrix}$$

A pair of α and δ corresponds to a particular line of sight. Each point along such a line of sight from the M31 has a particular line-of-sight distance from the solar position, from which we get a pair r_A and θ_A in the local M31 coordinate using above method. If r_A lies within our simulation box we find the grid in the simulation box where the coordinate pair (r_A, θ_A) lies. We then use the corresponding density and CR pressure in that grid to calculate the γ -ray emissivity. This is repeated for all points along a given line of sight (corresponding to a given α, δ), and then integrated it along the line of sight. The integrated value at each α, δ then gives the γ -ray flux in that sky coordinate, in order to produce a γ -ray image as shown in Figure 5.4.

Appendix B

Significance Study

It is important to understand how much the difference between cold gas mass is significant in our study. For that reason, we calculated the time evolution of the cold-stripped gas mass for the m10 satellites which are located at the same position of 100 kpc away from the host in two different simulation runs (Figure B.1). This will also give a measure of stochasticity in our simulation. We can see the amount of cold gas is not that different until 2.5 Gyr, however after that, there are some differences between the values. Although at late times, satellites are almost gas-deficit, therefore we should take these differences with a pinch of salt. However, at earlier times, the differences between these two runs are less than a factor of two, which implies our runs are not so stochastic, at least until 2.5 Gyr. Therefore, we can take differences in our runs to be significant and independent of stochasticity if they differ by a factor two.

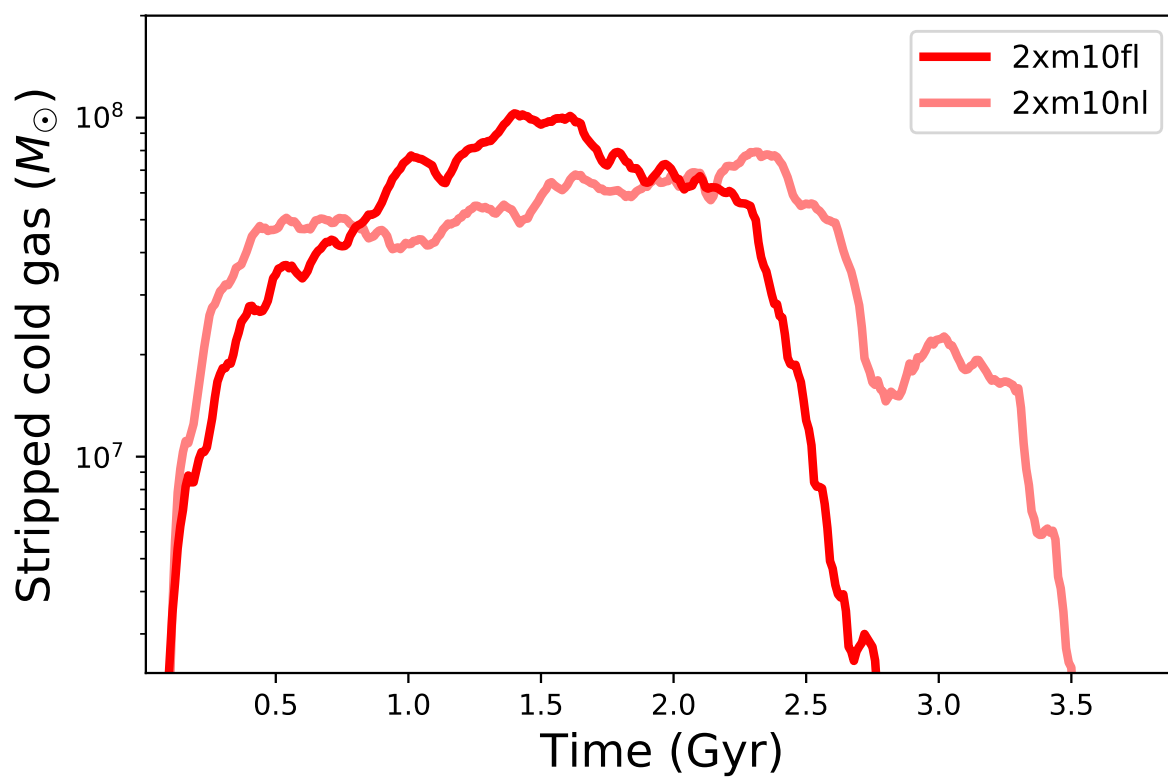


Figure B.1: Time evolution of stripped cold gas from one satellite situated at 100 kpc in the case of two different runs of m10 (2xm10fl and 2xm10nl).